

Design and Fundamental Understanding of Novel Catalysts for Efficient Transformations of Shale Gas Components

By

Yuting Li

Submitted to the graduate degree program in Chemical & Petroleum Engineering and the Graduate Faculty of the University of Kansas in partial fulfillment of the requirements for the degree of Doctor of Philosophy.

Chair: Laurence Weatherley

Raghunath V. Chaudhari

Juan Bravo-Suarez

Kevin Leonard

Michael Rubin

Date Defended: May 7th, 2020

The dissertation committee for Scholar Yuting Li certifies that this is the approved version of the following dissertation:

**Design and Fundamental Understanding of Novel Catalysts
for Efficient Transformations of Shale Gas Components**

Chair: Laurence Weatherley

Date Approved: May 13th, 2020

Abstract

In recent years, due to the abundant storage and development of hydraulic techniques, studies relating to the inexpensive shale gas source have drawn increasing attention among both academic and industrial researchers. Besides the utilization in heating and electricity of ordinary life, the more important application of shale gas is to be used as the raw carbon source in the chemical industry. As a chemical feedstock, it can be converted to various value-added intermediates, such as oxygenates, olefins and heavy hydrocarbons, via distinct catalytic processes.

In this dissertation, there are five significant catalytic processes discussed in detail, including the one-step production of acetic acid by coupling methane with carbon monoxide and oxygen under mild conditions, the complete oxidation of methane at relatively low temperature, the oxidation of ethane to form carboxylic acids (acetic acid and formic acid) at near room temperature and near ambient pressure, the stable dehydrogenation of ethane to produce ethylene, and the synthesis of formic acid directly from carbon monoxide at low temperature.

To improve the efficiency of these catalytic transformations, the design of novel catalysts exhibiting good activity of the activation of methane or ethane and high selectivity of the ideal product is the key. Thus, a variety of novel catalysts were prepared through different synthetic methodologies and were used in these catalytic transformations of short-chain alkanes. Specifically, the singly dispersed rhodium atoms anchored in microporous aluminosilicate materials were employed for the effective conversion of methane and ethane into acetic acid that is one of the most significant chemical materials due to its wide applications. In addition, the coordination-number dependent nickel oxide catalysts were applied in the complete oxidation of methane at relatively low temperatures. Moreover, Pd promoted Zn-based catalysts were used for the enhancement of activity and stability of the production of olefin from ethane dehydrogenation.

Furthermore, the new type of the zeolitic material - nanosheet FAU catalysts, synthesized by using the graphene oxide with confined spaces as a special template, were utilized to produce formic acid from carbon monoxide, which could be formed from methane, reacting with water at low temperature.

As these proposed catalysts presented good performances of the listed catalytic transformations, it is essential to know how these catalysts activate methane or ethane and convert them into ideal products. In this dissertation, fundamental understandings of authentic structures of synthesized catalysts at an atomic level were obtained by using the multiple ex-situ and in-situ characterization techniques. Through the integration of the fundamental understanding of local structures of these catalysts under catalytic conditions and the experimental explorations of their catalytic performances, the correlation between the structure of catalysts and their activities can be built. The establishment of such intrinsic structure-activity correlation is meaningful for the advances of new types of catalysts in science and is beneficial to the future realization of feasible processes.

To conclude, investigations in this dissertation demonstrated the design and fundamental understanding of novel catalysts for efficient transformations of shale gas components under relatively mild conditions. The applied methodologies and achieved results in these studies will provide insights into both essential studies and practical processes involving the activation and conversion of light hydrocarbons (methane and ethane).

Acknowledgment

I would like to express my sincere gratitude to my advisor, Prof. Laurence Weatherley who is the Albert P. Learned distinguished professor and the chair of department of Chemical & Petroleum Engineering in University of Kansas, for his considerable support and facilitation to finish my Ph.D. study smoothly and successfully. He gave many good mentors and precious advice for my studies and also future careers.

I would like to express special thanks to my advisory committee, Prof. Raghunath V. Chaudhari, Prof. Kevin Leonard, Prof. Juan Bravo-Suarez and Prof. Michael Rubin, for their meaningful reviews and insightful suggestions during my preliminary exam and comprehensive exam. The food communication with committee members from distinct research fields has largely broadened my mind and extended my thoughts.

I would like to thank Prof. Franklin (Feng) Tao for his guide and support of my research. The knowledge and capability I learned during the Ph.D. study would be beneficial to my future life.

I would like to thank Prof. Bala Subramaniam, the Dan F. Servey distinguished professor and the director of the CEBC, for his support and facilitation of my Ph.D. study and future career.

I would like to acknowledge my colleagues and friends in the research group, Dr. Luan Nguyen and Dr. Yu Tang, for their considerable assistance in the research. The extensive discussion with them generated many good suggestions for my research works.

I also want to thank the all faculties and staff in the C&PE family and CEBC centers at KU for their strong support and help during my Ph.D. studies.

I would like to acknowledge to the collaborators from other universities and national labs for the exciting work we obtained.

I would like to sincerely thanks to my friends Honghong Shi, Hongda Zhu, Dengpeng Liu, Ziwei Song, Priya Srinivasan, Anoop Uchagawkar, Bhagyasha Patil, Pallavi Bobba, Dylan Jantz, and Lijun Chen for their considerable help in both life and work, making my life in Lawrence colorful and enjoyable.

Last but not least, I would like to express my sincere thanks to my parents and all family members, whom I love always. They support me a lot to accomplish Ph.D. studies overseas and pursue future careers. They always comfort me when I encounter difficulties and encourage me to overcome the challenges.

DEDICATED TO

my mother and father who love me always

Table of Contents

Abstract.....	iii
Acknowledgment.....	v
Table of Contents	viii
List of Figures.....	xiii
Chapter 1.....	xiii
Chapter 2.....	xiii
Chapter 3.....	xiii
Chapter 4.....	xv
Chapter 5.....	xvii
Chapter 6.....	xviii
Chapter 7.....	xix
List of Schemes.....	xxi
Chapter 1.....	xxi
List of Tables	xxii
Chapter 1.....	xxii
Chapter 3.....	xxii
Chapter 5.....	xxii
Chapter 6.....	xxii
Chapter 1 Introduction.....	1
1. The significance of inexpensive source shale gas	1
2. Background information on methane conversion.....	2
2.1 Methane conversion into oxygenates under mild conditions.....	3
2.2 Methane completed oxidation at relatively low temperature	7
3. Background information on ethane conversion	10
3.1 Oxidation of ethane to acetic acid at low temperature.....	11
3.2 Dehydrogenation of ethane to ethylene on a catalyst with reasonable thermal stability.....	13
4. Transformation of hydrocarbon molecules via microporous aluminosilicate	14
4.1 Applications of zeolitic catalysts in small molecules transformation.....	14

4.2	Challenges in the transportation of reactants and products in zeolitic catalysts at low temperature and motivation of this work.....	16
5.	Organization of the dissertation	17
Chapter 2:	Experimental methodology.....	20
1.	Preparation of heterogeneous catalysts	20
1.1	Importance of preparation of heterogeneous catalysts.....	20
1.2	Structural and chemical factors determining the catalytic performance of a catalyst	20
1.3	General methods for the preparation of heterogeneous catalysts related to the works in this dissertation	25
2.	Characterization techniques for the fundamental understanding of catalysts	29
2.1	Transmission electron microscopy.....	29
2.2	X-ray photoelectron spectroscopy.....	32
2.3	X-ray absorption spectroscopy.....	36
2.4	Significance of ex-situ and in-situ characterization studies.....	41
3.	Summary.....	43
Chapter 3:	Single rhodium atoms anchored in micropores for efficient transformation of methane under mild conditions	44
1.	Introduction.....	44
2.	Experiment	46
2.1	Preparation and characterization of catalyst.....	46
2.2	Catalytic reactions	48
2.3	Measurements of products with NMR and GC.....	49
3.	Result and Discussion	50
3.1	Preparation of single Rh atom-based catalytic site	50
3.2	Catalytic performance of Rh ₁ O ₅ @ZSM-5 catalyst at 150°C	54
3.3	Participation of molecular O ₂ in the synthesis of acetic acid.....	57
3.4	Direct participation of CO to the synthesis of acetic acid.....	58
3.5	Direct participation of CH ₄ instead of coupling CH ₄ with formic acid to the synthesis of acetic acid.....	61
3.6	Direct coupling of reactants for the formation of acetic acid	62

3.7	Ready separation of hydrophilic products from a hydrophobic solvent.....	65
3.8	Feature of this chemical transformation in liquid under mild condition.....	66
4.	Conclusion	67
	Contributions of the project:.....	67
Chapter 4: The understanding of coordination number-dependent catalyst – transition metal oxide for methane complete oxidation.....		
		68
1.	Introduction.....	68
2.	Experiment	69
3.	Result and Discussion	71
3.1	Synthesis of NiO catalysts with different surface structures.....	71
3.2	Distinct catalytic performances of NiO(110), NiO(100) and NiO(111).....	74
3.3	The crucial role of the coordination environment of Ni cations on NiO in CH ₄ complete oxidation	79
3.4	Mechanistic understanding of coordination number-dependent catalysis at a molecular level.....	83
4.	Conclusion	90
	Contributions of the project:.....	91
Chapter 5: Catalytic oxidation of ethane to carboxylic acids in the liquid phase at near room temperature and near ambient pressure		
		92
1.	Introduction.....	92
2.	Experiment	94
2.1	Synthesis of catalysts	94
2.2	Characterization of catalysts	94
2.3	Measurements of catalytic performances.....	95
3.	Result and Discussion	98
3.1	Characterization of Rh catalyst structure.....	98
3.2	Identification of the role of Rh atoms	103
3.3	Influence of pressure of ethane on amounts of products and conversion of ethane	106
3.4	Influence of temperature on amounts of products and conversion of ethane...	107
3.5	Reaction pathway and kinetics.....	108

4. Conclusion	111
Contributions of the project:.....	111
Chapter 6: Fundamental understanding of Pd promoted Zn-loaded microporous catalysts for ethane dehydrogenation	112
1. Introduction.....	112
2. Experiment	114
2.1 Catalyst preparation.....	114
2.2 Catalyst characterization	116
2.3 Evaluation of catalytic performances of ethane dehydrogenation.....	117
3. Result and Discussion	119
3.1 Structural characterization of as-synthesized catalysts	119
3.2 Catalytic performance of S-1 supported with Zn and studies of its active sites	121
3.3 Rapid deactivation of catalytic performance of S-1 supported with Zn and intermediate-driven restructuring of Zn-based sites of the catalyst	123
3.4 Enhancement of activity and durability of Zn-base catalyst by adding Pd	127
3.5 Formation of Pd-Zn alloy in the proposed catalyst.....	128
4. Conclusion	136
Contributions of the project:.....	137
Chapter 7: Synthesis of Na@nanoFAU zeolite catalyst and catalysis for production of formic acid with Na@nanoFAU	138
1. Introduction.....	138
2. Experiment	140
2.1 Synthesis and characterizations of Na@nanoFAU.....	140
2.2 The evaluation of catalysis via Na@nanoFAU.....	141
3. Result and Discussion	142
3.1 The formation of Na@nanoFAU.....	142
3.2 The production of formic acid via Na@nanoFAU	147
4. Conclusion	152
Contributions of the project:.....	152
Chapter 8: Summary	153
1. Conclusion	153

1.1	Single rhodium atoms anchored in micropores for efficient transformation of methane under mild conditions	153
1.2	Coordination number-dependent catalysis on transition metal oxide for methane complete oxidation	154
1.3	Catalytic oxidation of ethane to carboxylic acids in the liquid phase at near room temperature and near ambient pressure	155
1.4	Fundamental understanding of Pd promoted Zn-loaded microporous catalysts for ethane dehydrogenation	156
1.5	Synthesis of Na@nanoFAU zeolite catalyst and catalysis for production of formic acid with Na@nanoFAU	157
2.	Recommendations	157
2.1	The improvement of selectivity of ideal products formed by converting methane or ethane via single-atom catalysts in the gas-liquid-solid reaction system	157
2.2	The enhancement of activities of transformations of light alkanes.....	159
2.3	The understanding of reaction mechanisms of ethane transformations	160
	References	162
	Appendix A More experimental results of chapter 3	195
	Appendix B Supplementary information of chapter 4	202
	Appendix C Extra experimental results of chapter 5	204
	Publication List	209

List of Figures

Chapter 1

Figure 1. 1 utilization of light hydrocarbons..... 2

Chapter 2

Figure 2. 1 Schematics of metal nanoparticles in different shapes: cube (a), tetrahedron (b), octahedron (c), cuboctahedron (d) and sphere-like shape (e). Only (100) facets are available on a cube. Only (111) facets are available on a tetrahedron. Both (100) and (111) facets are available on a truncated octahedron. Reproduced with permission from Ref.111. Copyright 2010, American Chemical Society. 23

Figure 2. 2 Schematic representation of some possible mixing patterns: core-shell (a), subcluster segregated (b), mixed (c), three shell (d). The pictures show cross-sections of the clusters. Two certain elements are represented by red particles and yellow particles, respectively. Reproduced with permission from Ref.115. Copyright 2008, American Chemical Society 24

Figure 2. 3 Methods for preparing SACs: mass-selected soft-landing (A) and wet chemistry (B). Reproduced with permission from Ref.108. Copyright 2013, American Chemical Society..... 26

Figure 2. 4 Post-synthesis modifications of layered zeolites. Reproduced with permission from Ref.126. Copyright 2018, the Royal Society of Chemistry. 29

Figure 2. 5 Schematic views of TEM (left) and the basic principle of TEM (right). Reproduced with permission from Ref.127. Copyright 2010, John Wiley and Sons 30

Figure 2. 6 (a)The photoelectric effect, in which an atom absorbs X-ray and emits a core-level electron, creating a photoelectron and leaving behind a hole in the core electron level. (b) XAS occurs because the photoelectron can scatter from a neighboring atom. The scattered photoelectron can return to the absorbing atom, modulating the amplitude of the photoelectron wave-function at the absorbing atom. This, in turn, modulates the absorption coefficient $\mu(E)$, causing the EXAFS. Reproduced with permission from Ref.136. Copyright 2014, Mineralogical Society of America. 38

Figure 2. 7 scheme of a typical XAS experiment setup in synchrotron center. Reproduced with permission from Ref.136. Copyright 2014, Mineralogical Society of America..... 41

Chapter 3

Figure 3. 1 Schematic showing the difference between continuously packed catalytic sites and singly dispersed catalytic sites. (a) Continuously packed cation sites on the surface of an oxide ($\cdots\text{O-M-O-M-O-M-O}\cdots$). (b) Singly dispersed cation sites on the surface of an oxide ($\cdots\text{O-A-O}$).

M₁-O-A-O...). (c) Singly dispersed Rh cation anchored on the internal surface of micropore of aluminosilicate through ion exchange of Rh cations with Brønsted acid sites..... 45

Figure 3. 2 Schematic showing the synthesis and structural feature of isolated Rh atoms in ZSM-5. Schematic (a-c) and pictures (d-f) showing the preparation of 0.10wt%Rh/ZSM-5 catalyst in which Rh₁O₅ sites were formed in the micropores of aluminosilicate. (a) NH₄-ZSM-5 as purchased. (b) Formation of H-ZSM-5 upon calcination of NH₄-ZSM-5 at 400°C for 12h. (c) Formation of ZSM-5 with anchored Rh₁O₅ sites through integrated vacuum pumping and incipient wetness impregnation (IWI) of Rh³⁺ to micropores through ion-exchange in aqueous solution; after impregnation, catalyst precursor was centrifuged; the precipitant was dried in an oven at 80°C for 3h and calcined in air at 550°C for 3h. (d), (e), and (f) are ball-stick model figures of the corresponding schematics (a), (b), and (c). 51

Figure 3. 3 Structural characterizations of ZSM-5 with anchored Rh cations and confirmation of single dispersion of Rh cations in 0.10wt%Rh/ZSM-5. (a) TEM image of particles of 0.10wt%Rh/ZSM-5; (b) TEM image of particles of 0.50wt%Rh/ZSM-5; (c) Rh 3d XPS peak of 0.10wt%Rh/ZSM-5 and 0.50wt%Rh/ZSM-5; (d) Energy space of Rh K-edge of 0.10wt%Rh/ZSM-5 and Rh foil (reference sample) of X-ray absorption spectra; (e) R-space of Rh-K edge of experimental (black) and calculated (red) data of the k²-weighted Rh K-edge EXAFS spectra of used 0.10wt%Rh/ZSM-5; (f) Coordination number of O atoms to a Rh atom and bond length of O-Rh on average of used 0.10wt%Rh/ZSM-5; (g) and (h) R-space of Rh-K edge of experimental (black) and calculated (red) data of the k²-weighted Rh K-edge EXAFS spectra of Rh metal foil and Rh₂O₃ nanoparticles supported on Al₂O₃, respectively..... 52

Figure 3. 4 Yields of acetic acid, formic acid, and methanol (left vertical axis) as well as the selectivity to acetic acid (the right vertical axis) were plotted as a function of different pressures of CH₄ (10 or 50 bars) and different reaction times (2 h or 12 h). 28 mg of 0.10wt%Rh/ZSM-5 was used for each catalysis. Each catalysis consists of 10 bar CO and 8 bar O₂ and certain pressure of CH₄ as noted on the X-axis (10 or 50 bars). The catalysis temperatures of all studies here are 150°C here. 55

Figure 3. 5 Yields of methanol (black), formic acid (blue) and acetic acid (red) in the chemical transformation of CH₄ at 150°C in aqueous solutions at different pressure of (a) O₂, (b) CO, (c) CH₄. (a) 30 bar CH₄, 10 bar CO and different pressure of O₂ at 150°C for 2h. (b) 50 bar CH₄, 8 bar O₂ and different pressure of CO at 150°C for 2h. (c) 10 bar CO, 8 bar O₂ and different pressure of CH₄ at 150°C for 2h. 58

Figure 3. 6 ¹³C NMR spectra of products of acetic acid, formic acid and methanol on 28 mg 0.10wt%Rh/ZSM-5 at 170°C for 10h in gas mixture :(a) mixture of 0.7 bar ¹³CO, 6.3 bar CO, 14 bar CH₄ and 8 bar O₂, (b) mixture of 7 bar CO, 14 bar CH₄ and 8 bar O₂, (c) mixture of 7 bar CO, 0.7 bar ¹³CH₄, 13.3 bar CH₄ and 8 bar O₂, and (d) mixture of 7 bar CO, 14 bar CH₄ and 8 bar O₂. (a) and (b) are isotope experiments; (c) and (d) are their corresponding contrast experiments. 60

Figure 3. 7 Isotope-labelled studies for elucidating whether acetic acid could be formed through coupling methanol with CO. (a) Two potential pathways α and β for production of acetic acid; in pathway α , CH_3OH is not an intermediate for formation of CH_3COOH ; in pathway β , CH_3OH is an intermediate for formation of CH_3COOH . (b) Potential catalytic products formed from 0.10wt%Rh/ZSM-5 in the mixture of $^{13}\text{CH}_3\text{OH}$ and H_2O in solution under mixture of CH_4 , CO and O_2 if the transformation of CH_4 , CO and O_2 follows pathway α , β , or both α and β . (c) NMR spectra of the products formed from 28 mg of 0.10wt%Rh/ZSM-5 after reaction in 10 bar CH_4 , 5 bar CO, and 4 bar O_2 at 150°C for 1h; there was no any isotope-labelled methanol, $^{13}\text{CH}_3\text{OH}$ added to the reactor before catalysis. (d) NMR spectra of the products formed from 28 mg of 0.10wt%Rh/ZSM-5 after reaction in 10 bar CH_4 , 5 bar CO, and 4 bar O_2 at 150°C for 1h.; notably, 1.0 mmol $^{13}\text{CH}_3\text{OH}$ was added to H_2O before catalysis. 63

Figure 3. 8 Yields of acetic acid, formic acid and methanol from 28 mg 0.10wt%Rh/ZSM5 in 10 ml dodecane at 150°C in the mixture of 30 bar CH_4 , 10 bar CO and 5 bar O_2 for 2h. 65

Chapter 4

Figure 4. 1 HAADF-STEM studies of morphology and lattice fringes of planar sheet NiO, cubic NiO, and octahedral NiO. (a) HAADF-STEM images of planar sheets NiO; the exposed face is (110). (b) HAADF-STEM image of planar sheets NiO (side view). (c) HAADF-STEM image of a single planar sheet along the (110) direction which show the side view of a planar sheet. (d-f) HAADF-STEM images of planar sheet NiO; the exposed face is (110). (g, h) HAADF-STEM images of cubic NiO; the exposed face is (100). (i, j) HAADF-STEM images of octahedral NiO; the exposed face is (111). 73

Figure 4. 2 Surface structures of NiO(110), NiO(100) and NiO(111) and experimentally measured catalytic performances of NiO. (a) (110) surface of planar sheet NiO; each Ni cation of (110) surface coordinates with four oxygen atoms. (b) (100) surface of cubic NiO; each Ni cation of (100) surface coordinates with five oxygen atoms. (c) (111) surface of octahedral NiO; each Ni cation of (111) surface coordinates with six oxygen atoms. (d) Conversion of planar sheets of NiO, cubic NiO and octahedral NiO as a function of temperature for complete oxidation of CH_4 in the temperature range of $250\text{-}500^\circ\text{C}$; 100 mg of planar sheet NiO and 500 mg of octahedral NiO was used in the measurement of catalytic performances. 75

Figure 4. 3 Catalysis on the partially reduced surface of cubic NiO and their catalytic activity. (a) Catalytic performances of 100 mg of cubic NiO catalyst which was pre-reduced in 5% H_2 for 1 hour at different temperatures (225°C , 250°C , 275°C , and 300°C); thus, the four catalysts are named, cubic NiO- H_2 - 225°C (green), NiO- H_2 - 250°C (blue), NiO- H_2 - 275°C (cyan), and NiO- H_2 - 300°C (magenta). (b) Measured atomic ratios of O/Ni of the four catalysts. (c) List of TOFs of the four catalysts at catalysis temperatures 425°C and 450°C ; these TOFs were calculated with Method 1 by dividing the number of consumed CH_4 molecules at a specific temperature such as

400°C or 450°C with the number of Ni atoms in oxygen vacancies on the surface measured with XPS; green and red bars are TOFs at 425°C and 450°C, respectively. (d) List of TOFs of the four catalysts at catalysis temperatures 425°C and 450°C; these TOFs were calculated with Method 2 by dividing the number of consumed CH₄ molecules at a specific temperature such as 400°C or 450°C with the number of all nickel cations on the surface measured with XPS..... 78

Figure 4. 4 Operando studies of the surface of planar sheet NiO and cubic NiO during catalysis. (a) Ni 2p of planar sheet NiO in the temperature range of 25°C-400°C in the mixture of CH₄ and O₂. (b) O 1s of planar sheet NiO in the temperature range of 25°C-400°C in the mixture of CH₄ and O₂; the shoulders were marked with red dash-line. (c) C 1s of planar sheet NiO in the temperature range of 25°C-400°C in the mixture of CH₄ and O₂. Spectra were deconvoluted to peaks 1 and 2 and a minor peak at 284.3eV. (d) Plot of fraction of area of O 1s shoulder to the total area of O 1s photoemission feature. (e) Fractions of areas of peaks 1 and 2 of C 1s in total areas of peaks 1 and 2 as a function of reaction temperature. (f-h) Ni 2p, O 1s and C 1s of cubic NiO in the same temperature range of 25°C-400°C in the same mixture of CH₄ and O₂ as planar NiO sheets..... 80

Figure 4. 5 Geometries of transition states and final states of the transformation of CH₄ and O₂ to CO₂ and H₂O on (110) surface of planar sheet NiO. (a1 and a2) Structures of transition state and final state for cleaving the first C-H of CH₄. (b1 and b2) Structures of transition state and final state for dissociating CH₃ to CH₂ and H. (c1 and c2) Structures of transition state and final state for oxidizing CH₃ to CH₃O. (d1 and d2) Structures of transition state of hydrogen transfer and final state of water desorption and oxygen molecule adsorption. (e1 and e2) Structures of transition state and final state for dissociating CH₂ to CH and H. (f1 and f2) Structures of transition state and final state for oxidizing CH₂ to CH₂O. (g1 and g2) Structures of transition state and final state for CH₂O dehydrogenation to CHO. (h1 and h2) Structures of transition state and final state for CHO dehydrogenation to CO and H. (i1, i2, and i3) Structures of transition state and final state for water desorption and oxygen molecule adsorption, and transition state of CO oxidation to form CO₂. 84

Figure 4. 6 The most favorable reaction pathway of CH₄ complete oxidation on (110) surface of planar sheet NiO proposed by DFT calculations (a) and its corresponding energy profile (b). ... 86

Figure 4. 7 Geometries of transition states and final states of CH₄ complete oxidation on (100) surface of cubic NiO. (a1 and a2) Structures of transition state and final state for activation of CH₄. (b1 and b2) Structures of transition state and final state for dissociating CH₃ to CH₂ and H. (c1 and c2) Structures of transition state and final state for oxidizing CH₃ to CH₃O. (d1 and d2) Structures of transition state of hydrogen transfer and final state of CH₃O dehydrogenation. (e1 and e2) Structures of transition state and final state for oxidizing CH₂ to CH₂O. (f1 and f2) Structures of transition state and final state for dehydrogenation of CH₂O. (g1, g2 and g3) Structures of transition state of CHO dehydrogenation, final state of water desorption and oxygen molecule adsorption, and transition state of CO oxidation of pathway A (h1, h2 and h3)

Structures of transition state and final state of CHO oxidation, and transition state of CHO₂ dehydrogenation..... 87

Figure 4. 8 The most favorable pathway of CH₄ complete oxidation on (100) surface of cubic NiO proposed by DFT calculations (a) and its corresponding energy profile (b). 89

Chapter 5

Figure 5. 1 XRD patterns of (a) pure H-ZSM-5 and (b) 0.10wt%Rh/ZSM-5. No any diffraction peaks of rhodium oxide nanoclusters were observed. 99

Figure 5. 2 Photoemission features of (a) H-ZSM-5, (b) 0.10wt%Rh/ZSM-5 and (c) 2.0wt%Rh/ZSM-5. Rh 3d photoemission features were not observed from 0.10wt%Rh/ZSM-5, but clearly shown on 2.0wt%Rh/ZSM-5. 99

Figure 5. 3 TEM images of 0.10wt%Rh/ ZSM-5 (a and b) and 2.0wt%Rh/ZSM-5 (c-f). There are no dark spots on the external surface of 0.10wt%Rh/ZSM-5. Rhodium oxide nanoclusters on 2.0wt%Rh/ZSM-5 were readily observed in Figures 5.6c-f. 100

Figure 5. 4 XANES and EXAFS studies of 0.10wt%Rh/ZSM-5, Rh foil and Rh₂O₃ nanoparticles supported on Al₂O₃. (a) Energy space of 0.10wt%Rh/ZSM-5 in flowing He at 150°C obtained by XANES technique. (b) R-space of Rh K-edge of Rh metal foil obtained by EXAFS technique. (c) R-space of Rh K-edge of 0.10wt%Rh/ZSM-5 in flowing He at 150°C obtained by EXAFS technique; obviously, there is a lack of the second shell of Rh K-edge of Rh-O-Rh. (d) R-space of Rh-edge of Rh₂O₃/Al₂O₃ obtained by EXAFS technique. The lack of peak of Rh-Rh bond and the lack of Rh-O-Rh (the second coordination shell of rhodium oxide) in the R-space of Rh K-edge of 0.10wt%Rh/ZSM-5 suggests the lack of formation of rhodium oxide or metal rhodium nanoclusters..... 103

Figure 5. 5 Influence of amount of H₂O₂ dissolved in deionized water (the volume of the H₂O₂ solution is always 10 ml) on the amounts of formed acetic acid and formic acid on 30 mg of pure H-ZSM-5 or 30 mg of 0.10wt%Rh/ZSM-5. (a) Amounts of formic acid and acetic acid formed on 30 mg of pure H-ZSM-5 in 15 bar ethane by oxidation with different amounts of H₂O₂ at 50°C for 2h. (b) Amounts of acetic acid and formic acid formed on pure 0.10wt%Rh/ZSM-5 in 15 bar ethane by oxidization with different amounts of H₂O₂ at 50°C for 2h. (c) The molar fraction of all products generated by 30 mg of pure H-ZSM-5 among all products formed by 30 mg of 0.10wt% Rh/ZSM-5. The contribution of H-ZSM-5 in formation of acetic acid and formic acid is minor in contrast to Rh₁O₅ sites of 0.10wt% Rh/ZSM-5 when the amount of H₂O₂ is 10 mmol or less. Thus, the amount of H₂O₂ is 10 mmol in 10 ml H₂O. 104

Figure 5. 6 Influence of pressure of ethane on amounts of acetic acid and formic acid formed by oxidizing ethane at 1.5, 5, or 15 bar with 10mmol H₂O₂ in 10ml H₂O at 50°C for 2h. 30mg 0.1%Rh/ZSM-5 was used as the catalyst in each experiment. 107

Figure 5. 7 Influence of temperature of catalysis on conversion of ethane and amounts of acetic acid and formic acid formed by oxidizing 15 bar ethane with 10mmol H ₂ O ₂ in 10ml DI H ₂ O at 50°C, 57.5°C, 65°C, and 80°C for 2h. Fresh 30mg 0.1%Rh/ZSM-5 was used in catalysis at each temperature.	108
Figure 5. 8 Amounts of acetic acid and formic acid formed from 15bar C ₂ H ₆ oxidized by 10mmol H ₂ O ₂ at 50°C in different duration. The data of at each time (30 min, 60 min, 90 min, 12 min, 180 min, or 360 min) was achieved from an independent experiment using the same amount of fresh catalyst (30 mg 0.10wt%Rh/ZSM-5). In other words, six experiments with different reaction times were performed. Each of the six experiments was performed under the same condition on fresh 30 mg of 0.10wt%Rh/ZSM-5.	109
Figure 5. 9 Arrhenius plot of Ln r (reaction rate) versus 1/T in the temperature range of 50°C-72°C. The activation barriers for productions of (a) acetic acid and (b) formic acid are 32.5 kJ/mol and 35.5 kJ/mol, respectively.....	110

Chapter 6

Figure 6. 1 XRD patterns of S-1 (black), 1.0wt%Pd/S-1 (red) 2.0wt%Zn/S-1 (blue), and 2.0wt%Zn/1.0wt%Pd/S-1 (purple).....	120
Figure 6. 2 Catalytic performance of (a) S-1, (b) 2.0wt%Zn/S-1, (c) 1.0wt%Pd/S-1 and (d) 2.0wt%Zn/1.0wt%Pd/S-1 in the temperature range of 500-650°C. 100 mg of the catalyst was used. It was diluted by 500 mg purified quartz 10 ml/min 10% ethane was flowing through the catalyst bed.....	121
Figure 6. 3 Operando studies of Zn K-edge of 2.0wt%Zn/ S-1 using XANES and EXAFS. (a) Energy space spectra of Zn K-edge of Zn foil (as reference), 2.0wt%Zn/ S-1 at 25°C before catalysis and catalyst during catalysis at 650°C. (b) R-space spectra of Zn K-edge of 2.0wt%Zn/ S-1 before catalysis at 25°C. (c) R-space spectrum of Zn K-edge of 2.0wt%Zn/ S-1 during catalysis at 650°C. (d) List of parameters used in fitting R-space spectra of Zn K-edge in (b). (e) List of parameters used in fitting R-space spectra of Zn K-edge in (c).....	123
Figure 6. 4 Durability of catalytic performance based on time-on-stream examination under the same catalytic condition at 650°C. (a) 0.200 gram of 2.0wt%Zn/S-1 at 650°C, and (b) 0.200 gram of 2.0wt%Zn/1.0wt%Pd/S-1 at 650°C.	124
Figure 6. 5 Sequential R-space spectra of Zn K-edge of 2.0wt%Zn/S-1 studied with EXAFS technique during catalysis at 650°C (Scan #1 is the first spectrum and scan #4 is the last one).126	
Figure 6. 6 Operando studies of Pd K-edge of 2.0wt%Zn/1.0wt%Pd/S-1 using XANES and EXAFS. (a) Energy space spectra of Pd K-edge of Pd foil, catalyst before catalysis at 25°C and catalyst during catalysis at 650°C. (b) R-space spectra of Pd K-edge before catalysis at 25°C. (c) R-space spectrum of Pd K-edge of the catalyst during catalysis at 650°C. (d) List of parameters	

used in fitting R-space spectra of Pd K-edge in (b). (e) List of parameters used in fitting R-space spectra of Pd K-edge in (c).	130
Figure 6. 7 Operando studies of Zn K-edge of 2.0wt%Zn/1.0wt%Pd/S-1 using XANES and EXAFS. (a)Energy space spectra of Zn K-edge of Zn foil, the catalyst before catalysis at 25°C and the catalyst during catalysis at 650°C. (b)R-space spectra of Zn K-edge of the catalyst before catalysis at 25°C. (c)The R-space spectrum of Zn K-edge of the catalyst during catalysis at 650°C. (d)List of parameters used in fitting R-space spectra of Zn K-edge in (b). (e)List of parameters used in fitting R-space spectra of Zn K-edge in (c).	130
Figure 6. 8 Evolutions of energy space spectra of (a) Zn K-edge and (b) Pd K-edge of 2.0wt%Zn/1.0wt%Pd/S-1 before catalysis at 25°C (red), during catalysis at 500°C (yellow), during catalysis at 600°C (green), and during catalysis at 650°C (blue) studied with operando XANES.	132
Figure 6. 9 Evolutions of R-space spectra of Pd K-edge of 2.0wt%Zn/1.0wt%Pd/S-1 (a) during catalysis at 500°C, (b) during catalysis at 600°C, and (c) during catalysis at 650°C. (d) List of parameters used in fitting R-space spectra of Pd K-edge in (a). (e) List of parameters used in fitting R-space spectra of Pd K-edge in (b). (f) List of parameters used in fitting R-space spectra of Pd K-edge in (c).....	134
Figure 6. 10 Evolutions of R-space spectra of Zn K-edge of 2.0wt%Zn/1.0wt%Pd/S-1 (a) during catalysis at 500°C, (b) during catalysis at 600°C, and (c) during catalysis at 650°C. (d) List of parameters used in fitting R-space spectra of Zn K-edge in (a). (e) List of parameters used in fitting R-space spectra of Zn K-edge in (b). (f) List of parameters used in fitting R-space spectra of Zn K-edge in (c).	134

Chapter 7

Figure 7. 1 Schematic showing molecular diffusion in micropores of FAU (a and b) and nanoFAU (c and d). At a relatively low temperature, there could be a diffusion limit of reactant and product molecules in regular FAU particles (a and b) due to both the small micropores with a diameter of subnanometer and the long channels with a length of a few hundreds of nm. Such diffusion (a and b) could be minimized by the synthesis of nanoFAU (c and d) which has a thickness of a few nanometers.	139
Figure 7. 2 Schematic of synthesis and SEM images of nanocomposite of graphene oxide and precursor of synthesizing aluminosilicate. (a) Schematic showing the formation of nanosheets of FAU by filling precursor to the limited space confined by graphene oxide layers. (b and c) SEM image and XRD of the nanocomposite of graphene oxide and precursor before calcination at 400°C. (d and e) SEM image and XRD of as-synthesized Na@nanoFAU formed after calcination at 400°C in air to remove graphene oxide flake.....	143

Figure 7. 3 TEM images and structural model of Na@nanoFAU. (a-c) Representative SEM images of the sonicated dilute colloidal suspension of Na@nanoFAU (after graphene oxide was removed) after being dried on the TEM grid and then being sputtered with a gold film (60 seconds sputtering, ~5-10 nm thickness). These images show that these well-defined Na@nanoFAUs were successfully synthesized. (d) Representative SEM image of the commercial FAU crystals with a lateral dimension and thickness of 300-500 nm. (e-g) View of a Na@nanoFAU with a thickness of a single unit cell (2-3 nm) along Z-direction. 144

Figure 7. 4 Size and thickness of Na@nanoFAU studied with AFM. (a) AFM images of three pieces of Na@nanoFAU; their two-dimensional size is in the range of 200-300 nm. (b) Line profile of the height of the three Na@nanoFAUs of (a); the Y-axis of (b) gives the thickness of these Na@nanoFAUs; it is about 2-3 nm, only a unit cell of a regular FAU crystal. 145

Figure 7. 5 HAADF-STEM images of Na@nanoFAU. (a) Image consisting of several Na@nanoFAU aggregates (or called nanoparticles); in each aggregate, several Na@nanoFAU sheets are stacked in parallel; the green circles mark aggregates; morphologies of these nanosheets can be seen well. (b) Enlargement of the section marked with red box in (a); each dashed line marks a nanosheets. The distance between two nanosheets is about 2.5 nm. The successful observation of these nanosheets shows the successful synthesis of Na@nanoFAU with a thickness of a single unit cell of a FAU crystal. 146

Figure 7. 6 Dynamic light scattering profile of dilute colloidal suspension of Na@nanoFAU (a) and N₂ physisorption isotherm on Na@nanoFAU (b). 146

Figure 7. 7 Catalytic performance of 30 mg Na@nanoFAU (10wt%Na@nanoFAU) at 150°C dispersed in 10 ml deionized water under 10 or 50 bar CO sealed in a Parr reactor. (a) Yields of formic acid formed on 30 mg 10wt%Na@nanoFAU at 10 bar and 50 bar CO; 10 bar or 50 bar CO was introduced into a Parr reactor which loaded with 10 ml deionized water, respectively. Each reaction was performed at 150°C for 3 h; the catalyst was vigorously stirred during catalysis. (b) Yields of formic acid catalyzed by 30 mg 10wt%Na@nanoFAU in 10 ml deionized water under 10 bar CO for 3 h and 9 h; the reaction was performed at 150°C..... 149

Figure 7. 8 Kinetics studies of the formation of formic acid from CO and H₂O on 30 mg Na@nanoFAU in the temperature range of 150-180°C. (a) Amount of formic acid formed through catalysis on 30 mg Na@nanoFAU (10wt%Na@nanoFAU) at different temperatures. (b) Arrhenius plot for the formation of formic acid under kinetics control regime. 151

List of Schemes

Chapter 1

- Scheme 1. 1** Production of acetic acid (BASF process)²³. a) Preheater; b) Reactor; c) Cooler; d) High-pressure separator; e) Intermediate pressure separator; f) Expansion chamber; g) Separation chamber; h) Degasser column; i) Catalyst separation column; k) Drying column; l) Pure acid column; m) Residue column; n) Auxiliary column; o) Wash column; p) Scrubbing column..... 4
- Scheme 1. 2** Production of acetic acid (Monsanto process)²⁴. a) Reactor; b) Flasher; c) Light-ends column; d) Dehydration column; e) Heavy-ends column. 5

List of Tables

Chapter 1

<i>Table 1. 1</i> Composition of shale gas ⁹	1
---	---

Chapter 3

<i>Table 3. 1</i> Comparison of turn-over frequency (TOF) for formation of acetic acid or oxygenates including acetic acid, formic acid and methanol on 0.10wt%Rh/ZSM-5 and homogeneous catalyst	56
--	----

<i>Table 3. 2</i> Catalytic performances of 28 mg catalysts of 0.10wt%Rh supported on different supports in a mixture of 10 bar CH ₄ , 10 bar CO, and 8 bar O ₂ at 150 °C for 3 h with 10 mL H ₂ O in a high-pressure reactor	57
--	----

Chapter 5

<i>Table 5. 1</i> Surface area and pore volume of the catalysts	100
---	-----

<i>Table 5. 2</i> Rhodium concentration of fresh and used 0.10wt%Rh/ZSM-5	101
---	-----

<i>Table 5. 3</i> Coordination number and bond length of Rh atoms in 0.10wt%Rh/ZSM-5 at 150oC in flowing helium	102
---	-----

Chapter 7

<i>Table 7. 1</i> Control experiments performed under specific reaction parameters described in the following	148
---	-----

Chapter 1 Introduction

1. The significance of inexpensive source shale gas

Recently, the development of novel catalytic processes for transforming inexpensive carbon-containing resources to value-added chemicals or commodities has drawn significant attention due to the increasing emission of CO₂ in petrochemical industries^{1, 2}, limited reservoirs of petroleum or coal³ and burgeoning energy demand⁴. Among potential alternatives, the shale gas progressively becomes the most promising energy and chemical feedstock⁵, given its abundant storage, global availability and quite low cost.

Shale gas is one of the most important unconventional reservoirs of light alkanes that are essential raw materials of chemical and energy industries. The global storage of shale gas has been estimated to reach approximately 456×10^{12} cubic meters⁶. In the last decade, innovative methods in the extraction of shale gas from shale rock have made a vast amount of shale gas resource technically accessible to the world. Notably, the well-developed hydraulic fracturing technology has primarily increased the availability of shale gas in the United States^{7, 8}.

Table 1. 1 Composition of shale gas⁹

Component	CH ₄	C ₂ H ₆	C ₃ H ₈	C ₄ H ₁₀	C ₅ H ₁₂	CO ₂	H ₂ S	N ₂	He
Volume fraction (%)	70-90	0-20	0-10	1-2	1-5	1-2	1-2	1-5	<0.5

Table 1.1 demonstrates the composition of shale gas. The main components of shale gas are methane, ethane, and propane, whose volume fractions vary at different locations. As illustrated in Figure 1.1, other than the substitution of coal for household heating supplies and electricity generation in power plants, light hydrocarbons, especially methane and ethane, are significant building blocks in chemical industries. These short-chain alkanes can be converted to

numerous important chemical intermediates used in the production of commodities of daily life¹⁰⁻¹³. There are numerous efforts devoted in the field of heterogeneous catalysis toward the development of new catalytic processes.

This dissertation will conclude research works involving methane conversion into oxygenates (acetic acid and formic acid), complete oxidation of methane, oxidation of ethane to produce acetic acid and dehydrogenation of ethane to form ethylene. Compared to engineering-oriented efforts in formulating any catalytic processes, this research dissertation is interested in how shale gas molecules could be chemically transformed through distinct chemical reactions. In short, the objectives of this dissertation are to design novel catalysts for efficient utilization of light hydrocarbons and to fundamentally understand the reaction mechanisms in transformations of short-chain hydrocarbons at a molecular level by using multiple characterization methods.

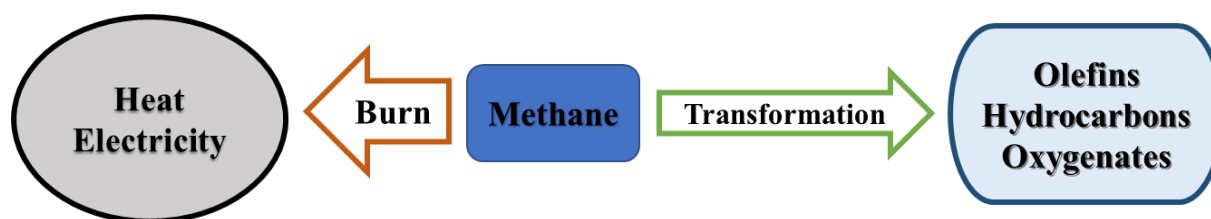


Figure 1. 1 utilization of light hydrocarbons

2. Background information on methane conversion

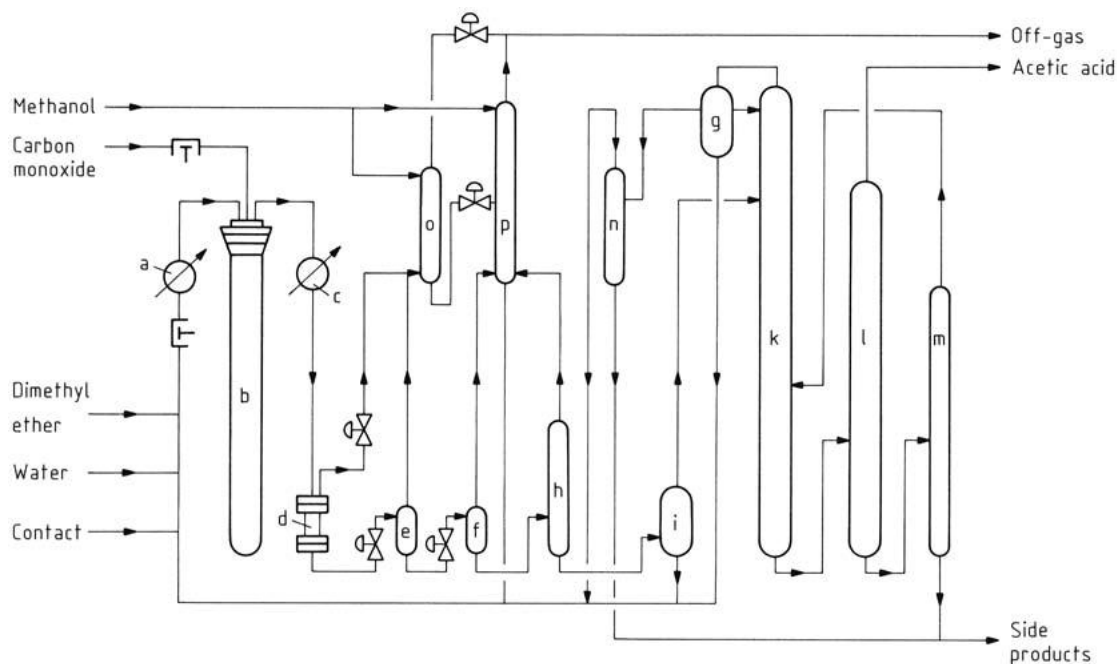
Methane, the primary component of shale gas, is the most stable molecule in the library of hydrocarbons. The four strong and localized C-H bonds ($\Delta H_{C-H} = 413\text{kJ/mol}$) and the absence of low-energy unoccupied orbitals and high-energy occupied orbitals make it barely possible to participate in a chemical reaction without the presence of a catalyst¹⁴. Such inertness has made methane-based chemical processes to operate at intermediate temperature (400°C-500°C) or high temperature (>500°C). To increase the efficiency of these thermal catalytic processes involving

methane activation, effective catalysts and optimized catalytic conditions are necessary. A vast amount of investigations relating to these aspects could be found in literature^{11, 12, 15-18}. In terms of fundamental studies of chemical transformations of methane, tremendous efforts have been made in the last decades^{12, 17-20}. Two projects in this dissertation are aiming to the fundamental understanding of methane transformation relevant to the conversion of methane into oxygenates and methane combustion. Thus, in the following section, the background information and current challenges of these two projects are briefly reviewed, which include practical transformations of methane to produce acetic acid and complete oxidation of methane at different temperatures.

2.1 Methane conversion into oxygenates under mild conditions

2.1.1 Industrial production of acetic acid

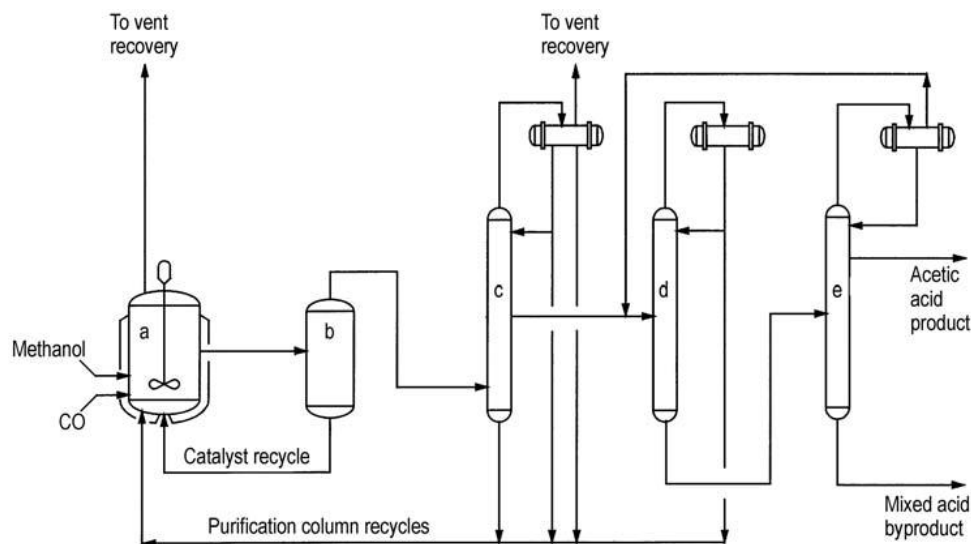
In the 1940s, the German chemical corporation, Badische Anilin und Soda Fabrik (BASF), firstly reported the process of acetic acid manufactured from methanol and carbon monoxide at high temperature and high pressure with cobalt-based catalysts²¹. In the late 1960s, the low-pressure carbonylation of methanol process was developed by Monsanto with a rhodium iodide promoted catalyst system which provides significantly higher activity and selectivity than the previous cobalt-based process^{21, 22}, resulting in over 90% yield of acetic acid referring to methanol. Methanol carbonylation is currently the dominant process for production of acetic acid. According to literatures^{21, 22}, the percentage of produced acetic acid through this low-pressure methanol carbonylation, developed in the 1960s, in the total annual production of acetic acid in the United States has increased from less than 10% in the 1970s to approximately 46% in the 1990s, and recently it has been more than 90%²¹.



Scheme 1.1 Production of acetic acid (BASF process)²³. a) Preheater; b) Reactor; c) Cooler; d) High-pressure separator; e) Intermediate pressure separator; f) Expansion chamber; g) Separation chamber; h) Degasser column; i) Catalyst separation column; k) Drying column; l) Pure acid column; m) Residue column; n) Auxiliary column; o) Wash column; p) Scrubbing column.

The BASF process of methanol carbonylation is schematically shown in Scheme 1.1²³. In the beginning, both carbon monoxide and methanol (containing up to 60% dimethyl ether), with the recycle and the makeup of catalysts will be introduced into the high-pressure reactor (b in Scheme 1.1). After the occurrence of the reaction, products will be cooled and sent to the high-pressure separator (d). The liquid product will be expanded to a relatively lower pressure of 0.5-1.0 MPa in the intermediate-pressure separator (e) and then will go through the expansion chamber (f) to generate the raw acid. The gas from two separators flowing to the wash column (o), and the gas from the chamber flowing to the scrubber (p), will be discarded as the off-gas containing 65-75 vol% CO, 15-20 vol% CO₂, 3-5 vol% CH₄, and the balance CH₃OH. The methyl iodide and other iodine-containing volatile compounds in both scrubber and wash column will be recovered via methanol feed to form a methanolic solution that will be returned to the reactor (b). The raw

acid containing 45 wt% acetic acid, 35 wt% water, and 20 wt% esters (mainly methyl acetate) will be purified in five distillation towers.



Scheme 1. 2 Production of acetic acid (Monsanto process)²⁴. a) Reactor; b) Flasher; c) Light-ends column; d) Dehydration column; e) Heavy-ends column.

Other than the BASF process, the Monsanto process is described in Scheme 1.2²⁴. To start the reaction, carbon monoxide and methanol will be continuously introduced to a back-mixed liquid phase reactor (a) at conditions of 150-200°C and 30-60bar. While the non-condensable byproducts (CO₂, H₂, and CH₄) are emitted from the reactor to maintain the carbon monoxide partial pressure in the reactor, the liquid products from the reactor will be forwarded to the flasher (b). Here, the catalyst will be separated as a residue stream from the crude acetic acid product and recycled to the reactor. The crude acetic acid, including methyl iodide, methyl acetate, and water will be taken from the head of the flasher to the light-ends column(c). Here, the light components (methyl iodide, methyl acetate, and water) will be recycled to the reactor as a two-phase overhead stream, while wet acetic acid will be removed as a side stream and sent to the dehydration column (d). An aqueous acetic acid overhead stream from (d) will also be recycled to the reactor, and a dry acetic acid product residue stream will be forwarded to a heavy-ends column (e). As a residue

stream in column (e), propionic acid, the major liquid byproduct of the process, will be sent out with other higher boiling carboxylic acids. Product acetic acid will be obtained in column (e) as a side stream, and the overhead stream will be recycled to the purification section of the process. The off-gas from the reactor and the purification section will be combined and sent to a vent recovery system in which the light ends, including organic iodides such as methyl iodide, will be scrubbed before the non-condensable gases are flared.

2.1.2 Challenges in the current industrial processes and motivation of the work

Other than being an important ingredient of foods, acetic acid is one of the important intermediates of chemical industries. The global demand of acetic acid is over 10 million metric tons per year (Mt/a)^{21, 25}. Currently, it is produced from methanol carbonylation, in which CO reacts with methanol to form acetic acid. However, methanol is synthesized from syngas (CO and H₂) at a temperature range of 250-300°C²⁶; the mixture of CO and H₂ is commonly produced from steam reforming processes of natural gas²⁷ or partial oxidation of coal²⁸ at quite high temperatures, 600-800°C. The production process from raw materials natural gas or coal to acetic acid significantly involves high-temperature catalysis, which makes it a high energy-demanded and high-cost process. In addition, to reuse the pricy rhodium-based homogeneous catalysts, the separating and recycling during the process are required. Thus, it would be ideal if a catalytic reaction could directly transform methane to acetic acid through one-step heterogeneous catalysis under mild condition by using cost-effective catalysts instead of the high concentration of precious metal complexes.

Motivated by these challenges, this work prepared a single-atom based catalyst which efficiently uses precious metal, Rh. Carbon addition reaction, CH₄+CO+O₂, was applied to produce acetic acid. Experimental findings of this work confirmed that the single-atom Rh catalyst is active

for activation of CH₄ and further oxidation of intermediate to form acetic acid at a low temperature of 150°C. Chemical and coordination environment of Rh atoms of catalytic sites were identified through a variety of characterization techniques such as electron microscopy and XANES as well as EXAFS spectra.

2.2 Methane completed oxidation at relatively low temperature

2.2.1 Processes of methane complete oxidation at different temperatures

In modern times, unburned hydrocarbons are commonly generated from power plants or exhausted from engines of vehicles that use gasoline, diesel, natural gas, or even liquid petroleum gas^{2,4}. These remained hydrocarbons must be oxidized to CO₂ and H₂O before being released into the atmosphere. In addition, as the significantly increased application of natural gas in the generation of electricity and heat, the complete combustion of methane is necessary to produce more energy. Thus, the complete oxidation of light hydrocarbons, particularly methane, has been a significant topic in the field of heterogeneous catalysis for decades.

Currently, the combustion process of methane is usually operated at high temperatures by using highly thermal stable catalysts. For example, barium hexaaluminate anchored on CeO₂ nanoparticles was reported to exhibit high thermal stability and good catalytic performance of methane complete oxidation at a quite high temperature (>1000°C)²⁹. Mixed oxides catalysts have been reported in publications to be active for the oxidation of methane³⁰⁻³³. In the 1960s, the mixed oxides Co_{3-x}Cu_xO₄, Co_{3-x}Zn_xO₄, and Co_{3-x}Ni_xO₄ were firstly found to be active for the oxidation of hydrocarbons and were investigated continuously in the following studies^{34, 35}. A very recent study demonstrated that high activities of these oxides in the oxidation of a mixture of liquefied petroleum gas with or without CO³⁶. Noble metals (Pt or Pd) supported on support such as Al₂O₃

is another type of well-studied catalysts³⁷. Recently, a catalyst of Pd nanoparticles caged in a porous CeO₂ shell supported on Al₂O₃ was found to be remarkably active for the complete oxidation of methane at high temperature up to 850°C^{38, 39}. In addition, in the last decades, mechanisms of complete oxidation of methane over these noble metal catalysts have been conclusively studied^{37, 40} and catalytic performances of these Pt- or Pd-based catalysts have been optimized³⁶. For instance, distinct mechanisms of the activation of C-H bonds on Pd-based catalysts were investigated at a molecular level, illustrating the involvement of Pd and O active centers in the complete oxidation of methane⁴⁰.

Besides operating at high-temperature, catalytic conversion of CH₄ is needed to be performed at a relatively lower temperature range for the removal of the exhausted methane from engines that use natural gas as the fuel. The exhausted gas from engines using methane normally contains CH₄ (about 1,000ppm.)^{37, 41}. Thus, the highly efficient complete oxidation of methane is significant for the abatement of the unburned methane in the exhaust of engines and the mitigation of greenhouse gases in the ambient environment^{37, 41, 42}. As the combustion temperature in this application is typically lower than 550°C, catalysts with high activity at intermediate temperatures are requested.

2.2.2 Challenge in the fundamental understanding of methane complete oxidation and motivation of this work

The high cost of catalysts composed of precious metals has driven the development of catalysts composed of earth-abundant elements. Compared to Pd and Pt, early transition metals are much more inexpensive due to their relatively high abundance. Thus, the catalyst consisting of transition metal oxides, a promising alternative to the noble metal catalysts, has been considerably investigated to enhance the activity of methane complete oxidation at relatively low temperatures³³,

⁴³. Transition metal oxide (TMO) based catalysts play significant roles in the transformations of short-chain alkanes in chemical and energy industries^{44, 45}. A recent report in the literature illustrated that Ni cations are active for activation of CH₄ at a temperature as low as 60°C³³. To develop a transition metal oxide-based catalyst with high activity at a low-temperature regime, the fundamental understanding of its active sites is crucial. The chemical and coordination environment of a transition metal cation is proposed to be correlated with the activity of the catalyst for methane activation and oxidation since the cation of early transition metal in the surface acts as the center of a catalytic site.

However, in contrast to a vast number of explorations of metal catalysts in the last few decades^{37, 45-48}, there has been a significant lack of fundamental studies of TMO-based catalysts. A primary reason is that the intrinsic complexity of TMO-based catalysts resulting from the coexistence of multiple valences of most transition metal cations, the presence of multiple phases at the catalytic temperatures, the richness in surface defects of catalysts in terms of oxygen vacancies. The coexistence of cations and anions on the surface of TMO-based catalysts increases the difficulty of revealing their local structures. From the characterization technique point of view, the low conductivity and magnetic properties of TMO have made characterizations of surface and structure of TMO catalysts more challenging to some extent. It is well acknowledged that a catalyst can only be well designed after the fundamental understanding of the reaction mechanism on a related catalyst is achieved. Consequently, the objectives of this work are to achieve the synthesis of different transition metal oxide catalysts exhibiting distinct catalytic performances and to obtain an atomic-scale understanding of the catalytic mechanism of complete oxidation of methane on a transition metal oxide.

To explore the chemical and coordination environments of cations on surface of TMO and build an intrinsic correlation between authentic surface chemistry of TMO and their corresponding catalytic performances, NiO was chosen as a probe catalyst since Ni cations were reported to be active in the activation of CH₄ at a relatively low temperature³³. In this project, NiO with different surface structures including planar sheet NiO with mainly exposed (110) surface, cubic NiO with mainly exposed (100) surface, and octahedral NiO with mainly exposed (111) surface were synthesized. These catalysts exhibited distinct catalytic performances, suggesting that coordination environment-dependent catalytic performances were uncovered. Through operando AP-XPS studies and computational studies, an intrinsic correlation between surface chemistry of NiO and their corresponding catalytic predominance was built.

3. Background information on ethane conversion

Ethane, the second main component of shale gas, is one of the most important feedstocks to produce commodity chemicals. Due to the relatively lower C-H bond enthalpies ($\Delta H_{C-H} = 423.3$ kJ/mol) than methane⁴⁹, C-H of ethane can be activated at a relatively mild condition¹⁴. To this extend, ethane is a more promising material to be used as chemical feedstocks in industries. A variety of value-added chemical intermediates, including olefins^{50, 51}, oxygenates⁵²⁻⁵⁴ and heavy hydrocarbons^{55, 56}, can be formed by converting ethane through different catalytic processes. In recent years, enormous efforts have been devoted in efficient transformations of ethane^{13, 50, 57}. Two projects in this dissertation aim to the fundamental investigations of ethane transformations relating to oxidation of ethane to produce acetic acid and dehydrogenation of ethane to form ethylene. Thus, in the following section, the background information and challenges of these

projects are concisely reviewed, including current oxidation process of ethane and ethane catalytic dehydrogenation.

3.1 Oxidation of ethane to acetic acid at low temperature

3.1.1 Industrial production of acetic acid from ethane oxidation

The oxidation of ethane is another economically potential process for the synthesis of acetic acid due to the low cost of ethane as the raw material²¹. As shown in the following, the oxidation of ethane is exothermic and thermodynamically favorable at room temperature, $C_2H_6 + 1.5 O_2 \rightarrow CH_3COOH + H_2O$ $\Delta H_{298K}^0 = -478kJ/mol$. A number of efforts were made for synthesis of acetic acid through direct oxidation of ethane with the most inexpensive oxidant, O_2 ²¹. For instance, the Ethoxene process⁵⁸ was developed for the production of acetic acid with less by-product ethylene through the addition of water in the feedstock of this catalysis. In this process, a catalyst comprised of molybdenum, vanadium, niobium, calcium, and antimony was used for the coproduction of ethylene and acetic acid, and an ethylene hydration catalyst was added for the promotion of selectivity of acetic acid. Moreover, the process with catalyst of vanadium oxide or vanadyl pyrophosphate supported on titanium dioxide is patented by Rhône-Poulenc to make acetic acid from ethane oxidation^{59, 60}. It has demonstrated that the yield of acetic acid was favored over ethylene and carbon oxides when the catalysis was conducted at 300°C. They also claimed that the addition of molybdenum enhances acetic acid selectivity, and the rate-determining step is speculated to be the desorption of acetic acid from the catalyst surface. Moreover, it is reported that the addition of other metals such as niobium, rhenium or palladium to mixed metal oxide catalysts can enhance selectivity for the production of acetic acid^{54, 60-62}. Notably, the mixed metal oxide (MMO) Mo-V-Nb catalysts doped with Pd exhibited the best performance, obtaining yields

to acetic acid as high as approximately 3-5% at 300°C⁶³. A two-site mechanism was proposed for this catalyst for the formation of acetic acid: ethane reacts with lattice oxygen of the MMO at reactive V⁵⁺ sites to form ethylene and then ethylene will diffuse to dispersed Pd²⁺ atoms forming acetic acid through a Wacker-like reaction⁶⁴. Additionally, the role of water was reported to be crucial for the assistance in the Wacker-like process at the Pd²⁺ active sites by facilitating acetic acid to deposit from the surface.

3.1.2 Challenges in direct oxidation of ethane to acetic acid and motivation of this work

The transformation of ethane to acetic acid through direct oxidation using molecular O₂ is not competitive as the mature methanol carbonylation process. The challenge is the extremely low yield at a level of a few percentages, which is far lower than the requested conversion of a potential candidate for replacement of the current methanol carbonylation. On the other hand, the current oxidation of ethane with O₂ requests activation of molecular O₂ at a relatively high temperature, 300°C or even higher. At 300°C or higher, it is challenging to control the extent of oxidation, since multiple by-products can be activated at a relatively high temperature and thus be further oxidized. In addition, at a relatively high temperature, intermediates in the pathway to the formation of acetic acid can gain enough energy to across energy barriers of alternative pathways to form by-products. Particularly, at a relatively high temperature, intermediate could be completely oxidized into CO₂ and H₂O since complete oxidation of intermediate to CO₂ and H₂O is the most thermodynamically favorable process⁶⁵.

Compared to these reported channels to form acetic acid through aerobic oxidation of ethane at high temperatures, oxidation of ethane at low temperatures would be more attractive to be developed. A near room temperature process would be ideal if possible since it could save a significant amount of energy and avoid a side-reaction of complete oxidation. Thus, in this work,

the synthesis of acetic acid at near room temperature was achieved through direct oxidation of ethane by using singly dispersed Rh sites anchored to micropores of zeolite as the catalyst and H_2O_2 as an oxidizing agent.

3.2 Dehydrogenation of ethane to ethylene on a catalyst with reasonable thermal stability

3.2.1 Different routes for production of ethylene

Ethylene is one of the most significant materials owing to the wide applications in chemical industries. The production of ethylene in the petroleum industry is the steam cracking of ethane at quite high temperatures, typically 750-950°C, which is an intensive energy-consumption process.⁶⁶ Oxidative dehydrogenation (ODH) of ethane is another channel to transform ethane to ethylene.^{50, 51, 58} With the participation of O_2 to oxidize H to H_2O , the dehydrogenation of ethane to ethylene becomes more thermodynamically favorable than the non-catalysis thermal dissociation of ethane to ethylene and hydrogen⁵⁰. ODH of ethane can be performed at a temperature as low as 500-650°C. However, to obtain high yield for producing ethylene through ODH is challenging. Side reactions involving the formation of oxygenates from ethane oxidation or further oxidation of ethene must be suppressed. An additional route of producing ethylene is the oxidative coupling of methane (OCM) at high temperatures of 700-850°C^{11, 12, 67-70}. The limit of low activity and selectivity and a quite high catalysis temperature have made this reaction channel unrealistic in the production of ethylene.

3.2.2 Challenges of catalytic dehydrogenation of ethane with good activity and thermal stability and motivation of this work

Catalytic dehydrogenation of ethane process can be operated at relatively low temperatures since the participation of catalytic sites can create a new pathway with the lower activation barrier.

It has been found that Zn-based catalysts are active for catalyzing the dehydrogenation of ethane to ethylene⁷¹⁻⁷³. It exhibits good activity at relatively low temperatures <700°C, although the selectivity of ethylene decreases along with the increase of temperature. Additionally, its catalytic activity obviously decays within ten hours. The experimental findings indicated that the addition of noble metals such as Pt on the Zn-based catalysts could enhance the activity of ethylene production and prevent the deactivation of Zn-based catalysts⁷⁴. There is a lack of insights into the complete deactivation of Zn active sites and the promotion effect of the second metals in catalysts. Thus, in this work, fundamental investigations were conducted to understand the deactivation of Zn-based catalysts and the role of palladium in promoted catalysts. Catalytic performances were evaluated by using three series of catalysts including microporous materials supported Zn only, Pd only and both Zn and Pd, respectively. In-situ XANES and EXAFS characterization techniques were engaged in building the intrinsic correlation between the local structures of proposed catalysts and their catalytic performance.

4. Transformation of hydrocarbon molecules via microporous aluminosilicate

4.1 Applications of zeolitic catalysts in small molecules transformation

In past years, along with the development of synthetic methodologies of zeolites, these microporous aluminosilicate materials are increasingly applied in chemical and energy industries^{56, 66, 75-82}. Sizes of particles of porous aluminosilicate are typically a few hundreds of nanometers or even larger. In other words, the lengths of these porous channels are typically a few hundreds of nm or longer. In petrochemical industries, this type of microporous material was used to catalyze reactions performed at high temperatures (>500°C), e.g., the cracking process^{16, 78, 83, 84}. Such broad applications of zeolites result from their unique property of shape selection and good thermal

stability derived from their high crystalline structure. The elevation of the molar ratio of silicon and aluminum can enhance the thermal stability of zeolite. The high silica zeolites can be achieved by adjusting the composition of Si and Al sources in hydrothermal gel, while low silica zeolites are usually obtained through post-synthesis treatments.

Another main feature of the classical zeolites is acidic properties, resulting from the extra negative charge corresponding to the Al tetrahedral sites. The microporous aluminosilicate usually contains both Brønsted acid sites associated with proton located in Al sites of the framework and relatively less amounts of Lewis acids sites assigned to the dehydroxylated Al species left or linked in the external framework, probably coming from high temperature annealing. By substituting Al or Si atoms with other species or cations such as Ti or Ge, different families of zeolitic materials could be developed, exhibiting distinct properties. This strategy makes it possible to synthesize the microporous materials with controllable acidity. For example, the materials that make replacement of aluminum by tetravalent cations have presented very specific Lewis acidity and redox properties.

The ion exchange property of zeolitic material is found to be critical in the utilization of zeolites in various catalytic reactions^{78, 85}. Some unique properties could be generated by ion exchange with alkali cations or by the incorporation of basic metals and metal oxides. As reported in literature⁸⁶⁻⁹³, these microporous supports can be used to anchor catalytic metal atoms/sites for the transformation of CH₄ to intermediates of chemical industries such as acetic acid in the liquid phase at a relatively low temperature. Typically, anchoring cations on zeolites can be achieved through ionic exchange between proton and cations. As the acidic sites are singly dispersed, the anchored cations are singly dispersed. It is one method to develop single-atom catalysts. The anchored cations have specific chemical and coordination environments. Compared to the

periodically packed M cations in the surface lattice of oxide particle M_xO_y ($\cdots M-O-M-O-M-O \cdots$), these singly dispersed cations, M^{n+} anchored in microporous aluminosilicate exhibit distinguish chemical and coordination environments^{86, 90, 94}. These catalytic sites presenting unique chemical and coordination environments are expected to provide quite different catalytic performances.

4.2 Challenges in the transportation of reactants and products in zeolitic catalysts at low temperature and motivation of this work

Recently, amounts of studies have suggested that wide applications of metal modified microporous materials in the activation and conversion of light hydrocarbons^{53, 55, 90-92, 95-98}. The commercial microporous aluminosilicate particles engaged in different catalytic processes usually have sizes of 0.5-10 μm . Thus, the diffusion of molecules in these zeolitic materials is an affecting factor of the reaction rate. It is not a problem for the utilization of microporous aluminosilicate in industrial hydrocracking because these reactions are performed at high temperatures in the gas phase. Unfortunately, for production of chemicals at low temperatures through zeolite-based catalysts, a significant limit in the diffusion of reactant and product molecules can be seen.

The limit of molecular diffusion in the catalytic process results from the long diffusion path of molecules in channels of aluminosilicate with the size of a few hundreds of nanometers and very limited pore diameter at a sub-nanometer scale. Thus, the kinetics of a catalytic reaction could be reduced when it is performed on active sites anchored in the microporous aluminosilicate buried in the liquid phase at a low temperature ($< 200^\circ\text{C}$). To avoid such diffusion limit, in this work, FAU at the nanoscale (nanoFAU) was synthesized by growing the layered porous aluminosilicate in confined space between adjacent graphene oxide layers and sequentially removing the graphene oxide through calcination at a high temperature. The synthesized nanosheet FAU exhibits a lateral

dimension of tens of nanometers but a thickness of only 2-3 nm in terms of a single unit cell of zeolite. The Na⁺ cations anchored on Brønsted site in micropores of the synthesized nanosheet FAU, namely Na@nanoFAU, is active for the synthesis of formic acid from CO and H₂O in aqueous solution at 150°C under the gas phase of 10 bar CO.

5. Organization of the dissertation

This dissertation started with this introductory chapter (Chapter 1). In the introduction chapter, the background of each project was briefly reviewed. The challenges and motivation of the work performed in the research activity of this dissertation were presented. After the introduction chapter, experimental approaches used in the experimental work of projects in this dissertation were described in Chapter 2 entitled experimental methodology. The key attributes for the design of distinct catalysts were illustrated in this chapter. These defined catalysts can be obtained through distinguished synthesized methodologies. The emphasis of this chapter is the description of operando characterization techniques, including the use of ambient pressure X-ray photoelectron spectrometer (AP-XPS) and the application of X-ray absorption spectroscopy namely X-ray absorption near edge structure (XANES) and extended x-ray absorption fine structure (EXAFS). These techniques are widely used by numerous research groups of catalysis worldwide, allowing to characterize the authentic surface chemistry of catalysts and chemical or coordination environments of catalysts during catalysis. Through such authentic information of catalysts during catalysis, intrinsic correlations between structures of catalytic sites at the atomic scale and their corresponding catalytic performances were established in this dissertation. With these intrinsic correlations, fundamental understandings of the mechanisms of these reactions were

achieved. Moreover, five different research projects of this dissertation were presented in chapter 3-7.

Chapters 3 and 4 are transformations of CH₄ at low temperature (150°C) or relatively low temperature (300°C). Chapter 3 entitled *single rhodium atoms anchored in micropores for efficient transformation of methane under mild conditions* focuses on the catalytic synthesis of acetic acid from methane at 150°C or lower through a carbon addition reaction using O₂ as the oxidizing agent ($2\text{CH}_4 + 2\text{CO} + \text{O}_2 \rightarrow 2\text{CH}_3\text{COOH}$). The catalyst for this carbon addition reaction is the singly dispersed Rh atoms anchored in microporous aluminosilicate. Fundamental understanding of the catalytic mechanism of this carbon addition reaction was achieved through DFT calculations. Chapter 4 entitled *the understanding of coordination number-dependent catalyst - transition metal oxide for methane complete oxidation* uses CH₄ complete oxidation as a probe reaction and NiO as a model catalyst. Three types of NiO, including planar sheet NiO, cubic NiO and octahedral NiO, exposing faces of (110), (100) and (111), respectively, were prepared and they exhibited distinct catalytic performances. Experimental findings indicate that the coordination number of oxygen anions around a Ni cation plays a crucial role in the activation of CH₄. Only Ni cations on NiO(110) coordinating with four oxygen atoms exhibited high activity. Computational studies rationalized the observed difference in activities of complete oxidation of CH₄. In addition, this work demonstrates that catalytic activity of an inert surface such as (100) of cubic NiO could be triggered by manipulation of the coordination environment of Ni cations to a favorable coordination environment.

Chapters 5 and 6 are catalytic transformations of ethane into value-added chemicals. Chapter 5 entitled *Catalytic oxidation of ethane to carboxylic acids in the liquid phase at near room temperature and near ambient pressure* presents the catalysis of oxidation of ethane to acetic

acid. The feature of this catalytic process is its operational temperature, near to room temperature. At such a low temperature, ethane can be transformed into acetic acid with relatively high conversion. It suggests a promising channel of producing acetic acid from the second richest component of shale gas, ethane at near ambient temperature and ambient pressure. Chapter 6 entitled *Fundamental understanding of Pd promoted Zn-loaded microporous catalysts for ethane dehydrogenation* focuses on the experimental exploration of how catalytic performance of Zn-based catalysts can be promoted and stabilized with the addition of Pd. In this study, through extensive in-situ characterizations using XANES and EXAFS, the mechanism of the promoting effect and stability of Pd to Zn catalyst was uncovered. Operando studies suggest that the formation of Pd-Zn alloy by adding Pd to Zn-based catalysts can suppress the vaporization of metal Zn anchored to microporous supports.

Chapter 7 entitled *Synthesis of Na@nanoFAU zeolite catalyst and catalysis for the production of formic acid with Na@nanoFAU* is the last project of the dissertation work. It illustrates the synthesis of the new type of zeolite – nanosheet FAU that is expected to exhibit a minimum limit in the diffusion of molecules. The Na cations anchored in the nanosheet of microporous aluminosilicate are proposed as active sites in the coupling of CO and H₂O to form formic acid.

Chapter 2: Experimental methodology

1. Preparation of heterogeneous catalysts

1.1 Importance of preparation of heterogeneous catalysts

Heterogeneous catalysis plays a crucial role in energy and chemistry industries worldwide since most transformations of raw materials to value-added chemicals involve heterogeneous catalysis⁹⁹. In order to improve activities of heterogeneous catalysis, novel heterogeneous catalysts are essential to be designed and developed.

The preparation of catalysts is the key to the function of catalysts for efficient transformations of reactants to ideal products with good activity and high selectivity and long durability. From the fundamental understanding point of view, the preparation of a catalyst with well-controlled structural and chemical specifications is crucial as well since these specifications are essential for the activity of a catalyst. Even if a catalytic reaction is performed in the micropores of a zeolitic material, the internal surface of the micropore is essential for understanding the catalytic performance of this microporous aluminosilicate. Literatures reported a variety of synthesis methodologies that can be used in the preparation of heterogeneous catalysts¹⁰⁰⁻¹⁰². To achieve a proper catalyst consisting of specific active sites and structures, the selection of appropriate synthetic approaches is significant. This section will introduce factors of catalysts affecting catalytic performances and briefly review the basic preparation methods of proposed catalysts used in transformations of shale gas constitute.

1.2 Structural and chemical factors determining the catalytic performance of a catalyst

In principle, typical heterogeneous catalysis normally involves the following steps⁹⁹:

- a) The reactants diffuse through external areas surrounding the catalyst particle.

- b) The reactants diffuse into internal pores of catalysts reaching to the active sites.
- c) The reactants are adsorbed onto the active sites.
- d) Surface reactions occur on the active sites, including activation of reactants, formation or conversion of various adsorbed intermediates and production of products, and possibly involving surface diffusion steps.
- e) The products desorb from the catalyst sites.
- f) The products diffuse out the internal pores of catalysts.
- g) The products diffuse through the external areas surrounding the catalyst particle.

Here the rate of heterogeneous catalytic reaction could be controlled by different regions during these steps, namely (i) film diffusion (Steps a and g); (ii) pore diffusion (Steps b and f); and (iii) intrinsic reaction kinetics (Steps c to e)⁹⁹. And the overall reaction rate is usually determined by the surface reaction rate related to the activity of a catalyst. Thus, it is essential to design catalysts exhibiting good performance to improve the efficiency of the heterogeneous catalytic process. To obtain a good heterogeneous catalyst, several key attributes need to be considered⁹⁹:

- 1) Good selectivity of a catalyst for high yield of desired products and minimal formation of undesirable byproducts.
- 2) Adequate rate of a reaction under desired conditions of the process.
- 3) Stable performance at reaction conditions for a long time.
- 4) Good accessibility of reactants and products diffusing to the active sites.

To achieve these essential characteristics, the design of catalytic sites and catalyst particles are of vital importance. Especially, the first three characteristics are primarily relevant to the interaction between reactants/products with active sites of a catalyst. As enormous efforts have been devoted to insightfully exploring active sites exhibiting exceptional efficiency in reactions,

various descriptors of active sites are introduced and proposed for the good design. From literatures^{83, 103}, the key aspects include the particle size, shape, chemical composition, interaction between metal and support, and metal-reactant/solvent interaction.

The size of active sites is the first primary factor having a significant influence on the performance of a catalyst. For example, metal catalysts in the form of single atoms, nanoclusters, nanoparticles exhibit distinct catalytic performances for the same reaction. Based on the literature¹⁰³, the electronic state of a catalytic site can largely vary along with the decrease of the size of a catalyst particle, leading to an obvious change of adsorption energy to a reactant molecule or intermediate. The size-dependent variation of electronic state intrinsically results from the size-dependent coordination environment of metal atoms. It has been found from some perceptive studies that this relationship between the size of catalytic species and activity of catalysis is related to the distinct coordination environment of active sites with different sizes. As summarized in literatures^{12, 104-109}, single-atom catalysts are recently discovered to present good performances in multiple catalytic reactions, including thermal catalysis such as CO oxidation or water-gas shift, photocatalysis and electrocatalysis. Especially, single-atom catalysts exhibit high activities in the activation of small molecules, resulting from the unique electronic and geometric properties of single-atom catalysts. Thus, in the work of this dissertation, the single-atom catalysts are proposed to active small molecular alkanes including methane and ethane.

Besides the size of sites on a catalyst, another key characteristic is the shape of the catalytic species. Most of the heterogeneous catalysts used nowadays are existed in crystalline structures exposing multiple facets. Which facets the metal nanoparticles could expose is dependent on the shape of the catalyst particle. As well documented in the literature^{103, 110}, the shape of catalyst particles can be controlled through dedicated synthesis. For example, as illustrated in Figure 2.1,

metal nanoparticles could form cube, tetrahedron, octahedron, truncated octahedron and sphere, presenting different facets in the surface. A uniform surface structure of a metal catalyst can be obtained by controlling the shape of its crystal during the preparation process. By forming a different shape of catalyst particles, the coordination number of atoms on a certain facet of metal nanoparticles can be distinct, leading to the variation of the adsorption energy of reactant molecules or intermediates on the surface of a catalyst. It is suggested that this difference could largely affect the selectivity and activity of a heterogeneous catalyst in reactions. Thus, in the work of this dissertation, transition metal oxide catalysts with distinct shapes in terms of different exposed surfaces are proposed for the complete oxidation of methane.

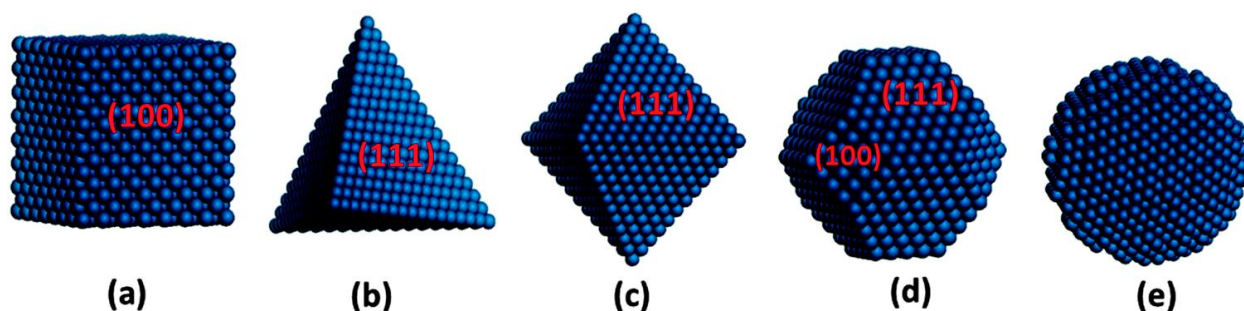


Figure 2. 1 Schematics of metal nanoparticles in different shapes: cube (a), tetrahedron (b), octahedron (c), cuboctahedron (d) and sphere-like shape (e). Only (100) facets are available on a cube. Only (111) facets are available on a tetrahedron. Both (100) and (111) facets are available on a truncated octahedron. Reproduced with permission from Ref. **111**. Copyright 2010, American Chemical Society.

The composition and the phase of active sites often significantly vary the performance of a catalyst. The best example is the bimetallic catalysts that are one of the most critical types of catalysts in petrochemistry due to the tunability of the electronic and geometric structures of bimetallic species derived from the contribution of the second metal¹¹²⁻¹¹⁴. As demonstrated in literature¹¹⁵, four general structures are proposed to describe the mixing pattern between two elements of a bimetallic species, including core-shell structures^{116, 117}, sub-cluster segregated nanoalloys, homogeneously mixed structures¹¹⁸, and multi-shell nanoalloys¹¹⁹, schematically

shown in Figure 2.2. Moreover, mixed metal oxides with or without supports are also conclusively investigated in enormous researches. For example, the vanadium pyrophosphate (VPO) catalyst was a well-studied metal oxide catalyst for oxidations of C₁-C₄ alkanes. According to the studies in literatures^{13, 30}, catalysts consisting of multiple compositions exhibit enhanced activities of different reactions, presumably resulting from their different electronic states and synergetic effect of the active sites. In the work of this dissertation, catalysts with multi compositions are designed and fundamentally investigated for transformations of ethane.

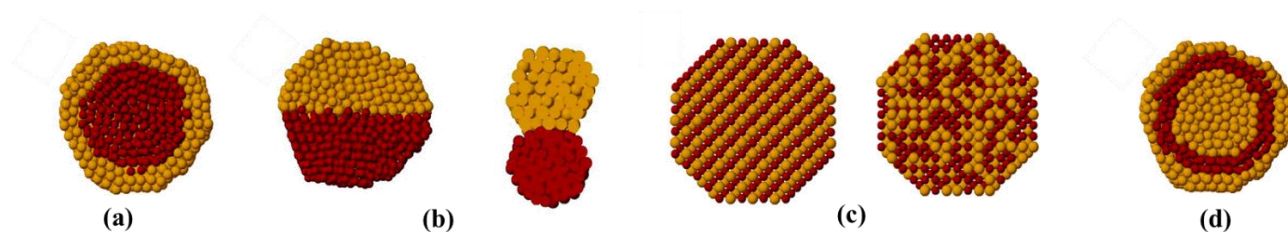


Figure 2. 2 Schematic representation of some possible mixing patterns: core-shell (a), subcluster segregated (b), mixed (c), three shell (d). The pictures show cross-sections of the clusters. Two certain elements are represented by red particles and yellow particles, respectively. Reproduced with permission from Ref. **115**. Copyright 2008, American Chemical Society

Other than the above three factors, the porous structure within a catalyst particle is another crucial factor that largely impacts the activation of reactants because of the confinement effect and specific coordination environment of an active site. Microporous materials, namely zeolite, are commonly utilized in the industrial catalytic process such as cracking, due to its shape selectivity and molecular sieving properties. Diameters of zeolite micropores are very close to the size of many molecules, so they are capable of distinguishing among compounds with even a small variety of sizes. This feature makes the zeolites are favored in product distribution leading to the outstanding selectivity in many reactions.

However, the zeolite channels with small diameters also limit the diffusion of reactants and products inside of zeolites, restricting the overall rate of heterogeneous catalysis. Therefore, in

recent research, the exploration of a promising alternative of conventional three-dimensional zeolites has been attracted considerable interest. New zeolitic materials have been developed, including nano-sized, hierarchical, and two-dimensional zeolites. Here a 2D zeolite is defined as a zeolite with a thickness in one dimension less than several nanometers corresponding to about one- or two- unit cells. It has been reported that there are significant advantages associated with new zeolitic materials. These new types of zeolite exhibit enhanced accessibility of basic properties such as porosity or acidity, and also have developed external/mesopore surface area. One obvious advantage of 2D zeolites in contrast to conventional microporous aluminosilicate is the largely enhanced diffusion of reactant and product molecules, intermediates and products. Thus, in the work of this dissertation, the new type of zeolitic catalyst is proposed for the conversion of short-chain alkanes, especially at low temperatures.

1.3 General methods for the preparation of heterogeneous catalysts related to the works in this dissertation

As activities of heterogeneous catalysts in multiple reactions are conclusively dependent on the structure of the catalyst, the structure-orientated synthesis methods are of essential importance in the formation of a specialized structure providing necessary properties. Here, several general synthesis strategies for preparing the proposed catalysts are concisely summarized.

One necessity of applying a single-atom catalyst in heterogeneous catalysis is to sustain the atoms of an ideal species to singly dispersed on proper supports. However, it is challenging to achieve the stable structure of such SACs, because the aggregation of single metal atoms is intended to occur, especially under high-temperature circumstances. As reviewed in literature¹⁰⁸, the mass-selected soft-landing techniques and improved wet chemistry methods are the most

promising methods employed to obtain atomic dispersion of the metal species on specific supports, illustrated in Figure 2.3.

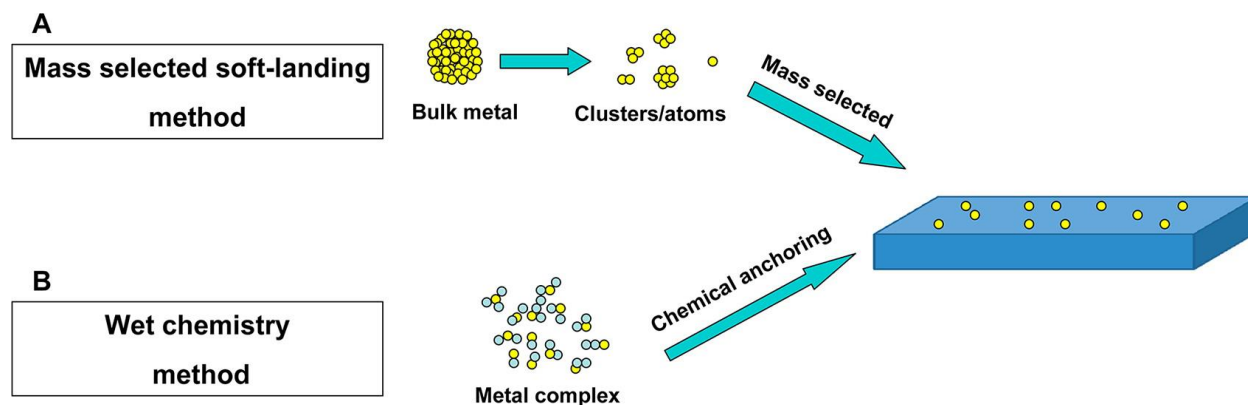


Figure 2. 3 Methods for preparing SACs: mass-selected soft-landing (A) and wet chemistry (B). Reproduced with permission from Ref. **108**. Copyright 2013, American Chemical Society

The mass-selected soft-landing technique is able to exactly control the size of metal species by manufacturing mass-selected molecular/atomic beams on the precisely adjusted surface structure of the support and combining ultrahigh vacuum surface science procedures¹²⁰⁻¹²². By using this technique, model catalysts with a range of sizes from single atoms to nanoclusters could be provided for fundamental studies to establish the relation of catalytic performance and the size of catalytic sites. However, this strategy is expensive and inefficient to be widely applied in practical industrial heterogeneous catalysis. As a good alternative, the modified wet chemistry has been significantly investigated and improved for the preparation of single-atom catalysts. A general protocol is to anchor the single atoms of defined metal species from precursors to the supports via chemical reactions. The anchoring of isolated atoms can be achieved through appropriate chemical interaction between the metal complex and the surface of supports. Here a strong metal-support binding is a crucial attribute to prevent atoms aggregating on the surface during the post-treatment processes. To offer singly dispersed active sites needed in heterogeneous catalysis, the selection of precursors of metal species such as organometallic ligands and the removal of useless or even

poisonous ligands/ions are necessary. Additionally, to stabilize the isolated atoms of metal species, some strategies, for example, introducing alkali-ion contaminants as aggregation inhibitors or remaining organic ligands during the preparation process, are applied. Moreover, to provide sufficient single-atom active sites, the high-surface-area supports are generally required. In short, the combination of all these strategies allows the formation and application of single-atom catalysts.

In terms of shape- or surface- dependent catalysts, different preparation routes of the metal or oxide nanoparticles with controlled shapes or surfaces have been reported in literatures^{103, 110, 123, 124}. The solid-state methods are the general routes to synthesize the oxide nanoparticles and are applicable for large-scale production. The drawbacks of such routes are the high cost from high-temperature annealing and the aggregation of nanoparticles due to the uncontrolled nucleation and growth processes. To address these challenges, new wet-chemistry methods have been explored in the last decade, including the hydro-solvothermal route, the two-phase route, thermolysis, and reverse micelle colloidal process. These new wet-chemistry synthetic routes can form the nucleus with a similar size by regulating the homogenous nucleation processes under the same conditions. After growing at the same rate, these nuclei eventually form the uniform oxide nanoparticles existing in a specific shape.

To prepare designed catalysts consisting of multi-species, the selection of precursors and the control of preparing conditions are critical. These controlled attributes will affect the interaction between the precursors of different elements and supports that may occur in a gas-solid/liquid-solid interface or a solid matrix, resulting in the various structures of the multiple compositions on catalysts. From the intensive studies of synthetic methodologies, co-impregnation, coprecipitation and co-deposition are common approaches to introduce the various species into supports to form oxide compositions. In terms of a bimetallic catalyst, a variety of methods are

available in literature^{114, 125}. Among the potential synthetic approaches, the chemical After introducing the metal species into support, a followed reduction, such as co-reduction or successive reduction, will be carried out to produce the bimetallic structures. Different steps will determine the distinct final structure of a bimetallic catalyst due to the complexity of two metal components present in the preparation process. Consequently, an appropriate approach is required to form catalysts containing ideal species with a defined structure and properties of interest.

Regarding zeolitic materials, hydrothermal synthesis is the basic method. For achieving the new types of microporous catalysts, special templates and post-synthesis modification protocols are required. According to the crucial review article¹²⁶, there are three general approaches for the synthesis of 2-dimensional zeolites, demonstrated in Figure 2.4. Firstly, an ADOR representing assembly, disassembly, organization and reassembly mechanism is engaged in the top-bottom synthetic procedure by introducing Ge to form germanosilicate zeolites with anisotropic structures. After hydrolysis of Ge-O, the layers will be reconnected in different ways, coming out as layered zeolite with various framework structures. In addition, some zeolites with a framework of FER, MWW, NSI, SOD, and several others can be directly prepared as lamellar precursors by using the special template such as the large molecular surfactant $C_{22}H_{45}-N^+(-CH_3)_2-C_6H_{12}-N^+(-CH_3)_2-C_6H_{13}$, namely C₂₂₋₆₋₆, to create mesoporous bridges between two sheets consisting of micropores at a thickness of several nanometers. These lamellar can be subsequently processed or modified through various routes such as swollen or pillared protocols to form the nanosheet zeolites with the preserved 2D structure. Moreover, the restricted crystal growth mechanism is carried out to realize the formation of 2D zeolites. In this procedure, the precursor agents will be inserted into a surfactant such as graphene oxide thin films with a specially designed structure to block the crystal

growth in one of the crystallographic directions, thereby, resulting in the synthesis of sheet-like single crystals.

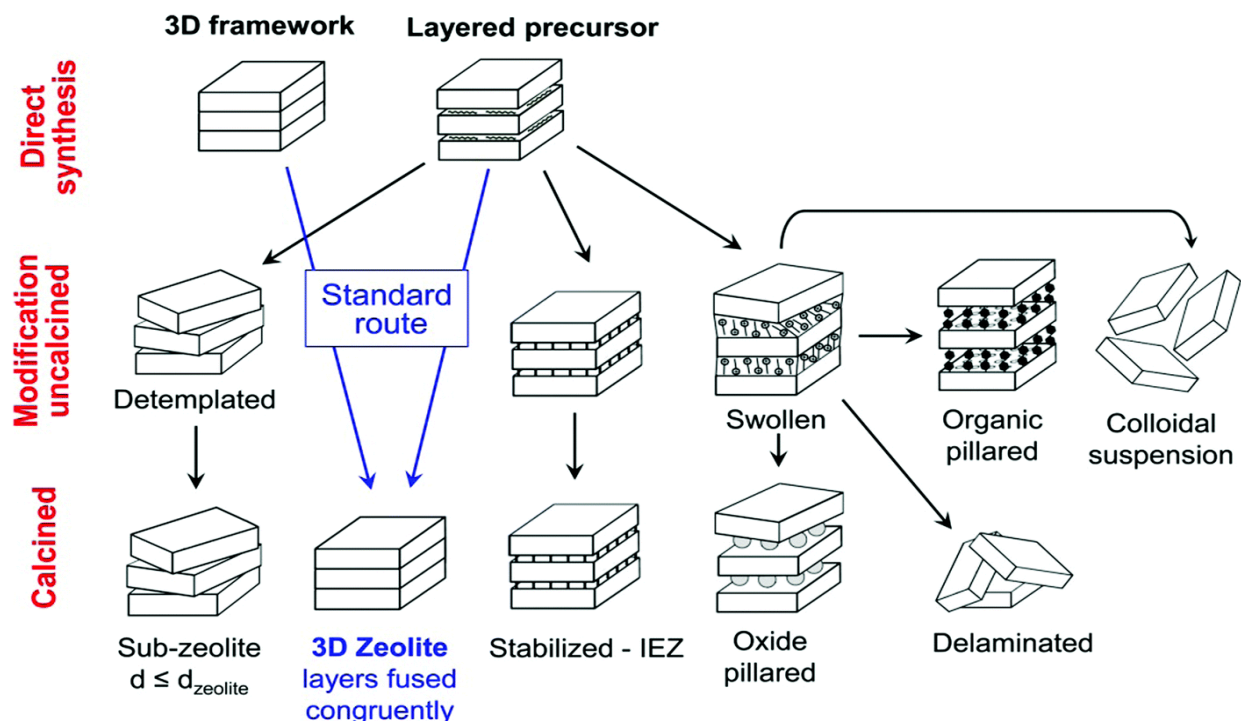


Figure 2. 4 Post-synthesis modifications of layered zeolites. Reproduced with permission from Ref.126. Copyright 2018, the Royal Society of Chemistry.

2. Characterization techniques for the fundamental understanding of catalysts

2.1 Transmission electron microscopy

The transmission electron microscopy (TEM) is a feasible technique to acquire the local structure of catalysts owing to its capability in capturing images of material microstructures. In the work of this dissertation, to understand prepared catalysts at an atomic level, high-resolution transmission electron microscopy (HR-TEM) and scanning transmission electron microscopy (STEM) are employed. TEMs used in this the works of this dissertation were commercial products owned by university electron microscopic centers or the university collaborators worked.

2.1.1 HR-TEM

A transmission electron microscopy includes electron source, condenser lens, specimen stage, objective lens and projector lens along its optical path, as in Figure 2.5 left. When an electron beam accelerated by high voltage hits the solid sample located in the specimen stage under the high vacuum, the multiple interactions, mainly transmission and diffraction, as shown in Figure 2.5 right, between the electron beam and the sample will occur. After the interaction, a bright-field image will be generated when the transmitted beam passes the objective aperture; in contrast, a dark-field image will be obtained by allowing one diffraction beam to pass the objective aperture.

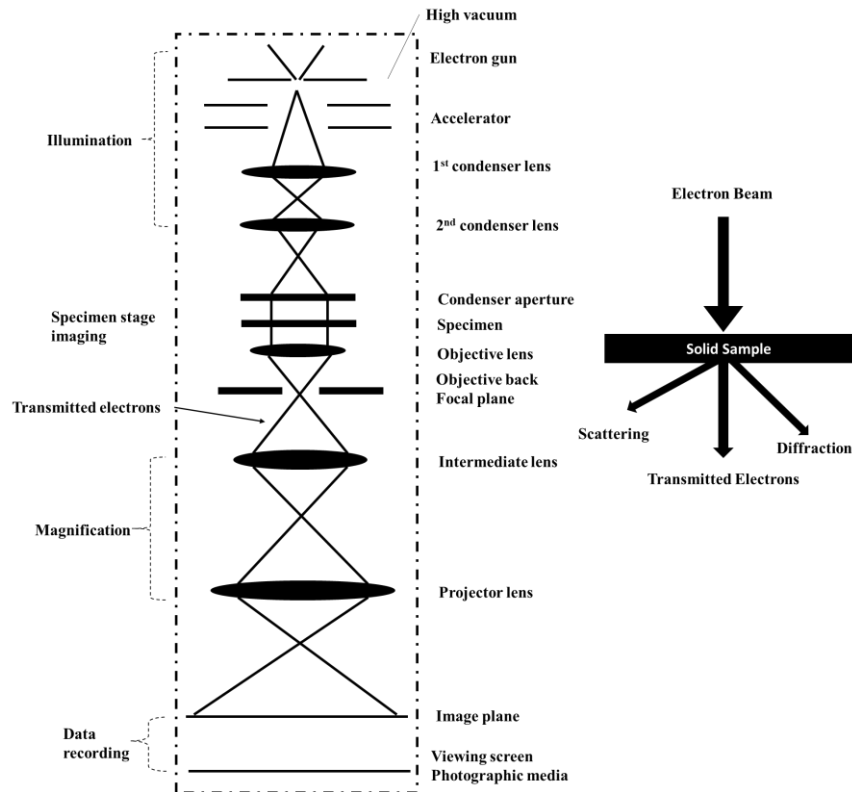


Figure 2. 5 Schematic views of TEM (left) and the basic principle of TEM (right). Reproduced with permission from Ref.127. Copyright 2010, John Wiley and Sons

Among the different types of electron microscopies, the high-resolution transmission electron microscopy (HR-TEM) is powerful to provide structural information of materials at the

atomic scale, such as lattice or unit cell of the crystalline material, because its highest resolution can realize around 0.5\AA . The principle of HR-TEM is referred to the phase contrast of TEM, which must involve at least two electron waves that are different in the wave phase. These minimum two beams (the transmitted beam and a diffraction beam) must participate in image formation. A phase difference between these two beams will be generated from the periodic lattice structure of a crystalline specimen. And during the propagation of the objective lens, the transmitted beam and the diffracted beam will interfere with itself to generate additional phase difference. Eventually, an interference pattern with periodic dark–bright changes on the image plane will be formed from the recombination of transmitted and diffracted beams.

2.1.2 STEM

The scanning transmission electron microscopy (STEM) is another type of TEM equipped with scanning coils to be used in the understanding of the atomic level structure of a catalyst. Unlike the conventional TEM, the electron beam of STEM will scan over the sample in a raster illumination system by focusing on a fine spot (typically at a size of $0.05\text{--}0.2\text{ nm}$) with the beam parallel to the optical axis. This process allows STEM to be feasible for analytical techniques such as Z-contrast annular dark-field imaging, and spectroscopic mapping by energy-dispersive X-ray (EDX) spectroscopy. The direct correlation of images and spectroscopic data through the simultaneous collection of both signals could be established.

The high-angle annular dark-field scanning transmission electron microscopy is possible to form atomic resolution images by collecting scattered electrons via an annular detector that is located outside of the path of the directly transmitted beam. The contrast of the image from HAADF-STEM is directly related to the atomic number and atom density, so it is a sensitive tool to detect low concentration species of a catalyst and to identify multiple elements with distinct

atomic numbers on support. In addition, by combining the EDX spectroscopy, it is available to investigate the location of a certain species or distribution of elements by estimating the element concentrations spatially in the selected area of a catalyst.

2.2 X-ray photoelectron spectroscopy

X-ray photoelectron spectroscopy, as known as element surface chemical analysis (ESCA), is a surface-sensitive technique to detect the composition and chemistry of surficial sites of a catalyst both qualitatively and quantitatively. The XPS instruments were invented by Kai Siegbahn in the early 1970s¹²⁸. There are numerous instrumentation corporations mainly in Germany, Japan, UK and Sweden producing whole systems of XPS and parts of XPS systems such as various types of energy analyzers, X-ray sources, pumps, sample manipulators, and reaction cell. To fundamentally understand the chemical and electronic status of active sites on the surface of a catalyst, XPS experiments conducted in the vacuum and during catalysis are applied in the work of this dissertation.

2.2.1 Ultrahigh vacuum X-ray photoelectron spectroscopy

The basic principle of X-ray photoelectron spectroscopy (XPS) is the photoelectric effect, which is described as the emission of electrons or other free carriers when electromagnetic radiation hits a material. Specifically, the X-ray photoelectron is the electron ejected from an electron shell of an atom when the atom is irradiated by X-ray photons. Thus, by using soft X-ray sources such as Mg K α and Al K α invented in the 1960s to “kick out” electrons from subshells of an atom, X-ray photoelectron spectroscopy could collect these photoelectrons with certain kinetic energy E_K by using energy analyzer which was designed and first manufactured by Siegbahn in

1960's-1970's and offered him the Nobel Prize in Physics. Given the kinetic energy E_K , the binding energy E_B of an element can be calculated on the basis of the following relationship:

$$E_K = h\nu - E_B - \phi$$

where $h\nu$ is the energy of the incident photon (h is Planck's constant and ν is the frequency), ϕ is work function representing the energy required for an electron to escape from the surface of a material, E_B is the binding energy of the electron shell, and E_k is the kinetic energy of ejected photoelectron.

Among the various characterization methods of solid materials, XPS plays an essential role in the study of chemistry and structures of a catalyst whose active sites are normally on the surface. This advantage results from the short mean free path of photoelectron when passing through a condensate material. Here the mean free path of the electron is defined as the average distance when the electron travels between collisions. For example, the mean free path of a photoelectron with kinetics energy in the range of 0.1-1.4 keV is about a few nanometers when it travels a solid material. The following equation presents the signal intensity of photoelectron $I(x)$ after traveling through a material with profile distance x :

$$I(x) = I_0 * e^{-x/\lambda}$$

where λ is the mean free path, and I_0 is the initial intensity. It can be clearly seen that the intensity of photoelectron decreases exponentially, along with the increase of x . After integration, the total photoelectron signal collected from the surface of material could be obtained:

$$I = \int_{x=0}^{x=infinite} I(x)dx = \int_{x=0}^{x=infinite} I_0 * e^{-\frac{x}{\lambda}} dx = \lambda * I_0$$

And the proportion of the signal contributed from the depth between x_1 and x_2 over the total signal could be gained:

$$P = \frac{\int_{x_1}^{x_2} I(x) dx}{\int_0^{\infty} I(x) dx} = e^{-\frac{x_1}{\lambda}} - e^{-\frac{x_2}{\lambda}}$$

Typically, when $x_1=0$, $x_2=3\lambda$, the signal portion is 95%. This indicates the surface layer in a thickness of 3λ contributes to 95% of the total XPS signal. Therefore, XPS is a highly surface-sensitive technique. Usually, XPS is conducted under ultrahigh vacuum conditions (10^{-9} mbar) to collect more photoelectrons from atoms of a sample.

In photoelectron spectroscopy, a certain element can be identified from the analysis of binding energies, as binding energies of atomic electrons are characteristic values. Thus, the qualitative information of a catalyst, such as surface composition, could be investigated by scanning a wide range of spectra to measure all characteristic features of surface elements. In addition, the oxidation state of a target element could be revealed from the shifting of binding energy in XPS. Owing to the shielding effect, the apparent binding energy of the photoelectron can be affected by the local electron density. Specifically, atoms at higher oxidation state have higher binding energy because of the reduced electron density. The coordination environment of an ideal element is also possible to be found by comparing it with the reference database¹²⁹. Moreover, quantitative information of a catalyst such as the relative surface atomic ratio of elements could be explored from high-resolution spectra of the most intensive features of elements, such as 2p feature for 3d transition metal, 3d feature for 4d transition metal and 4f feature for 5d transition metal. The intensity of a photoelectron I is given by $I = n * S$ where n is the surface atom number in unit volume and S is the surface sensitivity factors; thereby, the percentage of an ideal element in the total composition of a catalyst could be estimated.

2.2.2 Ambient pressure X-ray photoelectron spectroscopy (AP-XPS)

It is promising to study the catalyst surface under real catalytic conditions by performing operando XPS experiments due to its superior surface sensitivity. Atoms on the top few layers of a catalyst contribute a large portion of total signals that can be detected by XPS. These atoms are directly relating to the catalytic activity of a catalyst. In contrast, atoms in deeper layers or in the bulk of material contribute a negligible signal in XPS spectra. Thus, the peak shift in XPS spectra detected under catalytic conditions is associated with the change of active sites of a catalyst during catalysis.

A significant challenge of achieving the XPS of a sample during catalysis is the pressure gap. The ultrahigh vacuum (UHV) is required in conventional XPS because the expensive devices, such as electron energy analyzer and X-ray source, can only work under UHV conditions (10^{-9} mbar). Moreover, the UHV circumstance is beneficial for the collection of sufficient signals by avoiding the depletion of photoelectrons through collision. Nevertheless, heterogeneous catalytic reactions involve the interface between solid with gas or liquid. The existence of the gas or liquid phase above solid catalysts will dramatically decrease the signal of photoelectrons, because of the collision with gas or liquid molecules. Thus, to assemble a reactor on the UHV system, many efforts in instrumental development have been made in handling the pressure, temperature and flow of the fluidic reactant.

In the 1970s-1980s, Kai Siegbahn started the use of XPS to studies of surfaces of various samples in the gaseous phase^{128, 130, 131}. Significant progress of ambient pressure X-ray photoelectron spectroscopy (AP-XPS) in heterogeneous catalysis has been achieved. As reported in literatures¹³²⁻¹³⁵, some strategies were applied to address the challenge of pressure gap, such as, the installation of the in-situ reactor cell, the use of the high focusing lens system and the utilization

of high flux density X-ray source which could be achieved in synchrotron light source in a national lab. AP-XPS systems are available in many research groups around the world. The AP-XPS systems can be purchased from companies in the form of whole systems or different parts including X-ray source, energy analyzer, UHV chamber, sample manipulator, sample holder, vacuum pumps, reaction cell, gas-introduction manifold and others, which could be assembled in-house. In recent research, many useful instrumental parts were designed from manufactures to provide more functions of the XPS systems.

2.3 X-ray absorption spectroscopy

X-ray absorption spectroscopy (XAS), including X-ray absorption near edge structure (XANES) and extended X-ray absorption fine structure (EXAFS), is a crucial technique to investigate the coordination environment of atoms in a catalyst. To fundamentally understand the nature of atoms in a catalyst at molecular levels, both ex-situ and in-situ experiments of X-ray absorption spectroscopy are used in this dissertation work.

2.3.1 Basic principle

XAS is developed on the basis of the phenomenon of inelastic scattering, in which the intensity of an incident beam of X-ray photons decreases when it passes through a substance. As shown in Figure 2.6 (a), by adsorbing the sufficient energy $E = h\nu$ of a photo, an electron can be emitted from the internal shells, such as 1s at the K edge, 2s for the LI edges, 2p for the LII and LIII edges, of a core atom. By passing through the material, the intensity of the X-ray beam is attenuated according to a Beer–Lambert-type absorption law; thereby, the loss of intensity ΔI is a function of the initial intensity I_0 and the thickness x crossed:

$$\Delta I(E) = -\mu(E) \cdot I(E)dx,$$

where $\mu(E)$ is the linear absorption coefficient. And the integration format is:

$$I/I_0 = e^{-\mu x} ,$$

where I_0 and I are the incident intensity and the intensity transmitted after crossing through the homogeneous sample. After the excitation of an electron in core shell of an atom, the electrons in outer shells of the atom could relax to fill the hole left by ejected electron, thus emitting fluorescence. Fluorescence is also a characteristic of a specific element, which can be collected in the XAS experiment. The absorption coefficient of the sample $\mu(E)$ can be plotted as a function of X-ray photon energy to form the XAS spectrum, as displayed in Figure 2.6 (b). A sharp absorption edge jump in the XAS spectrum is observed when the energy of an incident X-ray photon equals to the binding energy of a core level electron. Then, the emitted photoelectron from the absorbing atoms could scatter with surrounding atoms and interfere with the original X-ray photons. The combination of constructive and destructive interference leads to the oscillation feature after the absorption edge in the XAS spectrum. In the XAS spectrum, the X-ray absorption near edge structure (XANES) is assigned to the region from the edge jump to ~ 100 eV above the absorption edge, while the extended X-ray absorption fine structure (EXAFS) is associated to the region of oscillation features after XANES. These two structures provide different aspects of the absorption atoms.

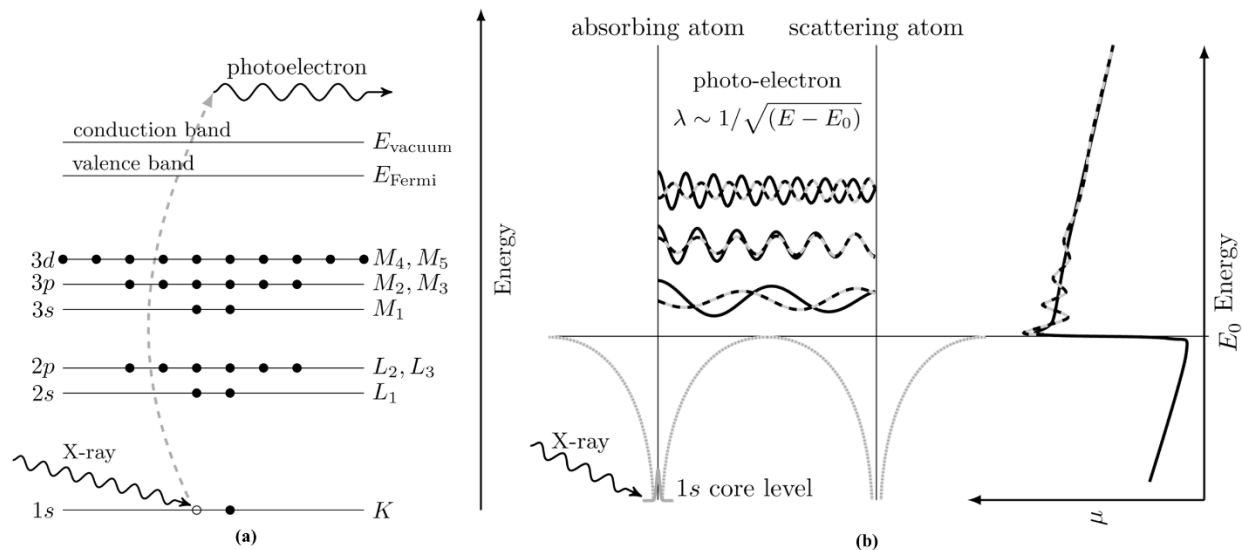


Figure 2. 6 (a)The photoelectric effect, in which an atom absorbs X-ray and emits a core-level electron, creating a photoelectron and leaving behind a hole in the core electron level. (b) XAS occurs because the photoelectron can scatter from a neighboring atom. The scattered photoelectron can return to the absorbing atom, modulating the amplitude of the photoelectron wave-function at the absorbing atom. This, in turn, modulates the absorption coefficient $\mu(E)$, causing the EXAFS. Reproduced with permission from Ref. **136**. Copyright 2014, Mineralogical Society of America.

The oxidation status of the core atom could be deduced from the XANES spectrum. The edge jump energy of the absorption coefficient in the XANES spectrum is the energy for the excitation of a core shell electron. This main feature of the edge jump is related to the electric-dipole allowed transitions ($\Delta l = \pm 1$) following the selection rule, such as $1s \rightarrow (n+1)p$ in K edge. A weak pre-edge is also possibly formed from the selection rule forbidden transition, such as $1s \rightarrow nd$ for K edge if there is p-d hybridization. Additionally, XAS could sensitively analyze chemical state change and electron density difference of a catalyst, due to the shielding effect. For instance, the atom with higher oxidation state and lower electron density will exhibit an upshifted energy of the edge adsorption. By comparing the shape and position of peaks in a sample with references, more detailed information of the absorbing atom could be uncovered, such as coordination geometry, the unoccupied state and orbital hybridization.

On the other hand, the coordination information of the adsorbing atom can be deduced from the EXAFS spectrum. The main feature of oscillation is considerably affected by surrounding atoms. By performing the simulation of the oscillation spectrum, the structural parameters including the number of coordinating atoms N_j , the respective distance between the core atom and coordinating atoms R_j and the Debye-Waller factor σ_j relating to the thermal disorder and static disorder, can be obtained with following EXAFS equation:

$$\chi(k) = \sum_j N_j S_0^2 f_j(k) \left(\frac{1}{k} R_j^2\right) \exp(-2R_j/\lambda) \exp(-2k^2 \sigma_j^2) \sin[2kR_j + \phi_{i,j}(k)]$$

where S_0 is a scaling factor (amplitude reduction factor), generally at 0.7-1, created when a valence electron fills the hole emitting the excited atoms. It is necessary to take two damping factors into account; one refers to the mean free path of an electron and another is related to the disorder on the distribution of neighbors j . The structural information generated from the interference function is limited to a maximum of 10\AA around the absorbing atom.

In a typical processing protocol, the energy space spectrum of EXAFS is firstly converted to k-space, and then Fourier transferred to the R-space spectrum, also known as the radial function of EXAFS. The peaks in R-space are associated with the specific bonding path between the core atom and surrounding atoms. The data of energy space and R-space will be analyzed through the Athena and Artemis software in the IFEFFIT package¹³⁷. The spectra energy will be calibrated using metal foils of each element as references, and data will be normalized by subtracting the background. The distance of a certain path will be gained from the atomic cluster built via the FEFF6.0 code (running within Artemis) by introducing the atomic positions from crystallographic data of standard materials. The amplitude reduction factor (S_0^2) of each element will be obtained by refining the spectrum of a standard metal foil. The fitting procedure is typically performed on

the k^2 -weighted Fourier transformed EXAFS spectra (Hanning window) using a k range of 2-13 \AA^{-1} and an R range of 1-3 \AA .

2.3.2 In-situ X-ray absorption spectroscopy

X-ray absorption near edge structure (XANES) and extended X-ray absorption fine structure (EXAFS) are promising techniques to characterize heterogeneous catalysts under realistic catalytic conditions. Thus, the oxidation state and coordination environment of interested elements of catalysts during catalysis can be obtained. Numbers of efforts have been devoted to the development of this in-situ study. Inspired by the creation of reaction cells in other X-ray techniques such as X-ray diffraction, the quartz tube cells were broadly engaged in XAS studies, allowing the XAS experiments carried out under catalytic conditions. In a typical in-situ experiment, the catalyst powder will be located in the middle of a quartz tube cell and remained under reaction conditions by flowing the reactant gasses into the reaction cell and heating to the whole cell to catalytic temperature. h-BN and Kapton can be the substitution of quartz because of their low X-ray absorption. These materials will be used in different conditions of the in-situ XAS experiments due to their own advantages and disadvantages. Firstly, a quartz tube can stand very high temperature ($>950^\circ\text{C}$) in most gaseous reactants, but it only works best for elements with the higher absorption edge energy ($>10\text{keV}$), due to the self-absorption of lower energy photons. In terms of the h-BN tube, the relatively smaller adsorption of lower energy is beneficial to using the h-BN tube as the complimentary of the quartz tube. It is also stable and inert in an oxidizing environment at high temperatures up to 850°C . The drawback of h-BN is the difficulty of it being machined into a thin wall tube. On the other hand, Kapton is feasible to be used in studies of an element with lower energies ($<10\text{keV}$) owing to its much better capability of X-ray transmission, although it can only be used at lower temperatures ($<400^\circ\text{C}$).

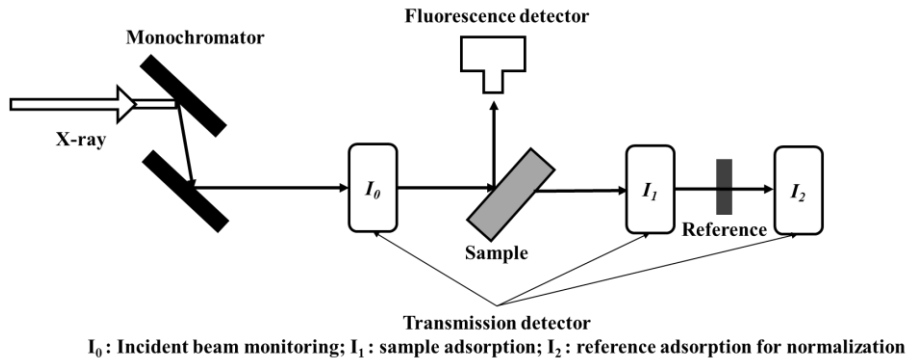


Figure 2. 7 scheme of a typical XAS experiment setup in synchrotron center. Reproduced with permission from Ref. **136**. Copyright 2014, Mineralogical Society of America.

A typical XAS experiment setup is displayed in Figure 2.8. After being focused by a monochromator, the incident X-ray beam will sequentially pass through the sample, installed between the gas ionic detector I_0 and I_1 , and the reference (normally metal foil), located between the gas ionic detector I_1 and I_2 . The intensities of the incident X-ray beam and transmitted signals will be monitored by I_0 , I_1 and I_2 , respectively. Meanwhile, the fluorescence signal I_f released from the sample can be collected by a dedicated detector such as a Ge-13 detector. The absorption coefficients for the sample collected by transmission mode (μ_t) and fluorescence mode (μ_f) can be calculated by equations $\mu = \ln \left(\frac{I_0}{I_t} \right)$ and $\mu = \ln \left(\frac{I_0}{I_f} \right)$, respectively. In recent researches, many revised or updated reaction cells have been proposed and tested for the in-situ XAS studies to present better capability of various catalytic conditions, different reactants and products, and a wider range of studied elements.

2.4 Significance of ex-situ and in-situ characterization studies

As described previously, the heterogenous catalysis refers to a surface reaction that is conclusively dependent on the surface interaction between reactant/product molecules with the active sites on the surface of a catalyst. On active sites of the surface, the reactants will be adsorbed

and converted to a series of intermediates in numbers of elementary steps, eventually forming products that will desorb from the catalytic sites. Thus, to understand the mechanism of a catalytic process, the investigation of the nature of the catalytic structure, especially active sites, is required. The conventional ex-situ studies can characterize the local structure of the active sites of a catalyst. For example, the formation of single-atom catalysts or bimetallic catalysts can be identified by high-resolution TEM, HAADF-STEM and ex-situ EXAFS. The shape and surface of metal oxide particles or nanosheet zeolites can be recognized by high-resolution TEM. And the XPS can provide information on the composition and oxidation states of a prepared catalyst.

However, these ex-situ studies can only provide information on a heterogeneous catalyst before or after reactions. It has been found that the authentic catalyst structure before or after reactions is different from the catalyst under catalytic conditions in many cases. And this difference results from various factors due to the complexity of the catalytic process. Specifically, the partial pressure of reactants and products around the catalyst surface is reported to affect the chemical potential of the system; thereby, it changes the chemical state of the catalyst under reaction conditions. For instance, the study of supported metal nanoparticle catalysts for CO oxidation has demonstrated that the surface structure of the metal nanoparticle is altered due to the coordination with carbon monoxide. Thus, to investigate the nature of active sites on the catalyst surface, techniques allowing to characterizing catalysts under catalytic conditions such as the presence of reactant/product gasses, high temperature and a certain pressure are needed. In the field of catalysis and surface science, the in-situ studies are proposed in many publications to describe the studies that aim to obtain information on structures of catalyst surface or bulk when it is in a gas or liquid phase composed of reactants at catalytic temperature and pressure. In principle, the amounts of reactants and yields of products should be monitored during the characterizing process to guarantee

that the signal is collected from the catalysts under working conditions. Here, the AP-XPS and in-situ XAS experiments can be conducted through designed instruments in worldwide institutions to provide the surface chemistry and coordination information of a catalyst in a similar circumstance where it performs the catalysis.

In short, both ex-situ and in-situ studies of a heterogeneous catalyst through techniques at molecular or atomic levels are essential for the fundamental understanding of the catalysis mechanism and identification of the authentic active sites, leading to the design of novel catalysts.

3. Summary

This section has briefly reviewed the appropriate synthetic approaches of proposed heterogeneous catalysts and introduced important characterization methods for fundamentally understanding local structures and the nature of active sites of a catalyst. Enormous efforts have been devoted to the significant advances in preparation methodologies of heterogeneous catalysts in literature. Correlation between the structure of a catalyst and catalytic performance of the catalyst can be established through the integration of advanced characterizing explorations of the catalyst during catalysis and careful investigations of catalytic performance. Such establishment of the structure-function relationship is vital for providing a guideline for the deep understanding of reaction mechanisms of ideal catalysis performed on well-defined catalysts and potential development of catalysts with high activity and selectivity.

Chapter 3: Single rhodium atoms anchored in micropores for efficient transformation of methane under mild conditions

1. Introduction

CH₄ has been one of the inexpensive energy resources since the maturation of hydraulic fracturing technology. So far, most processes of chemical transformation of CH₄ to intermediate compounds of chemical industries including steam or dry reforming, partial oxidation and oxidative coupling are performed at quite high temperatures¹⁹. One side effect of these high-temperature catalytic processes is the deactivation of catalysts due to carbon deposition¹³⁸. For example, coke-like carbon layers are readily formed to cover catalyst sites at a high temperature^{138, 139}. Another is the input of a huge amount of energy to process these catalytic reactions at quite high temperatures. Thus, activation of C-H of CH₄ at a low temperature is necessary in order to transform shale gas to intermediate compounds for the chemical industry in an energy-efficient manner^{53, 88, 97, 140-144}.

Acetic acid is one of the important chemical intermediates due to its wide applications. The global demand is 6.5 million metric tons per year (Mt/a). Most of them are produced from methanol carbonylation, in which CO reacts with methanol to form acetic acid. Unfortunately, methanol is synthesized from CO and H₂ which are produced from steam reforming of methane or coal at a quite high temperature (>700°C).¹⁴⁵ Replacement of the current high-temperature catalysis step toward the production of acetic acid with catalysis at low temperature would be feasible if a catalytic process could efficiently, directly transform CH₄ to acetic acid under a mild condition. Direct transformation of methane to acetic acid at a low temperature through a homogeneous catalytic process on free Rh³⁺ cations in solution was reported¹⁴⁶⁻¹⁴⁸, in which oxidation of CH₄ and CO with H₂SO₄ or superacid, or O₂ produces oxygenates at 140-180°C in a liquid phase.

Challenges in this transformation of homogeneous catalysis are (1) the separation of oxygenates from homogeneous catalysts in the same phase, (2) the extremely low catalytic activity, only 5.6×10^{-6} - 1.7×10^{-5} oxygenate molecules formed on per Rh active site per second, and (3) requirement of highly efficient recycling and reusability of the precious metal.

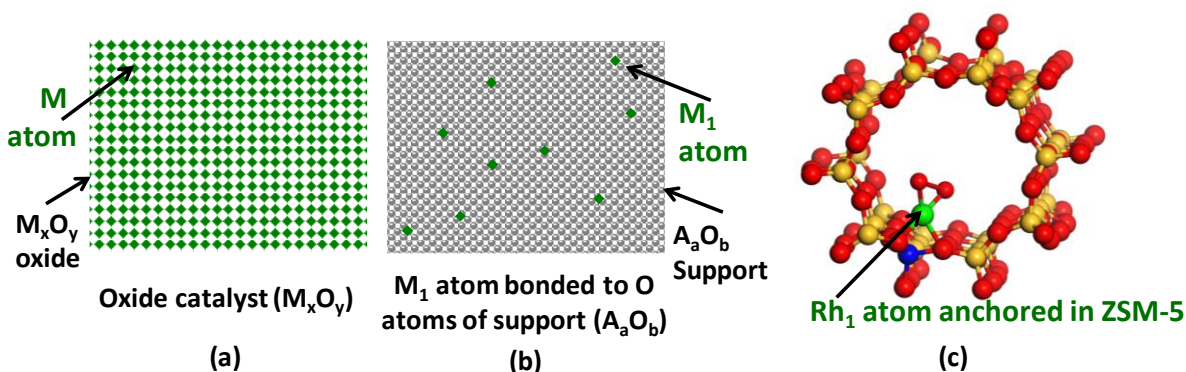


Figure 3. 1 Schematic showing the difference between continuously packed catalytic sites and singly dispersed catalytic sites. (a) Continuously packed cation sites on the surface of an oxide ($\cdots\text{O-M-O-M-O-M-O}\cdots$). (b) Singly dispersed cation sites on the surface of an oxide ($\cdots\text{O-A-O-M}_1\text{-O-A-O}\cdots$). (c) Singly dispersed Rh cation anchored on the internal surface of micropore of aluminosilicate through ion exchange of Rh cations with Brønsted acid sites.

The formation of single sites is a significant approach of the development of a catalyst toward high catalytic activity and selectivity^{90, 149-154}. Separately anchoring catalytic sites (M_1) on the oxide support (M_1/A_xO_y) could tune the electronic state of catalytic sites of M which are typically continuously packed on the surface of metal nanoparticles (M-M) or periodically packed on the surface of a metal oxide (M-O) nanoparticle. Through singly immobilized active sites on the oxide substrate, the “coordination ligands” of an isolated singly dispersed cation site (M_1), such as oxygen atoms, could largely tune the catalytic performance of the cation sites (M_1). Thus, compared to continuously packed M atoms on the surface of metal nanoparticles ($\cdots\text{M-M-M}\cdots$) and periodically packed M cations on the surface lattice of a metal oxide nanoparticle ($\cdots\text{O-M-O-M-O-M-O}\cdots$) (Figure 3.1a),^{150, 155} these isolated cation sites (M_1^*) anchored on the surface of a

substrate oxide (A_aO_b) could have distinct coordination environments ($\cdots O-A-O-M_1^*-O-A-O-A\cdots$) as shown in Figure 3.1b. Thus, those isolated cations (M_1) could exhibit a catalytic performance different from a metal oxide nanoparticle (M_xO_y) or a metal nanoparticle (M_n). Compared to Rh^{3+} freely moving without a closely packed coordination shell, the distinguished coordination of Rh atoms anchored in micropores of an aluminosilicate support offers higher activity in transforming methane to oxygenates such as methanol in published works^{90,93}.

Here we separately anchored Rh cations on the internal surface of micropores of an aluminosilicate, ZSM-5 (Figure 3.1c) through ion exchange between Rh^{3+} in solution and H^+ on the internal surface of micropore. As these Bronsted sites are typically isolated, Rh^{3+} cations can be separately anchored on Bronsted sites. Production of acetic acid through coupling CH_4 with CO and O_2 ($2CH_4+2CO+O_2=2CH_3COOH$) is efficiently catalyzed by these singly dispersed Rh sites, Rh_1O_5 . This heterogeneous catalyst exhibits good activity in transforming CH_4 to acetic acid, 0.07 CH_3COOH molecules per Rh site per second with a selectivity of ~70% for production of acetic acid. Isotope-labeled experiments using $^{13}CH_4$ and ^{13}CO show that CH_3 of CH_3COOH results from activation of CH_4 and $C=O$ of CH_3COOH from the insertion of CO. The reaction pathway referring to one-step synthesis of acetic acid from methane was proposed in this work.

2. Experiment

2.1 Preparation and characterization of catalyst

Two steps were involved in the preparation of a Rh/ZSM-5 catalyst. The first step is the preparation of H-ZSM-5 by calcining commercial NH_4 -ZSM-5 with a molar ratio of $SiO_2/Al_2O_3 = 23$ (Alfa Aesar) in air at $400^\circ C$ for 12h, as reported in publications⁸⁵. Four Rh/ZSM-5 catalysts with different Rh concentrations (0.01wt%, 0.05wt%, 0.10wt%, 0.50wt%) were synthesized

through a method integrating vacuum pumping and incipient wetness impregnation (IWI) of an aqueous solution containing a certain amount of rhodium(III) nitrate hydrate (~36%Rh basis, Sigma-Aldrich) at room temperature. Typically, 500 mg of H-ZSM-5 was placed in a 50ml three-port flask. The three ports were sealed with three corks. One port was connected to a vacuum pump. Before injecting $\text{Rh}(\text{NO}_3)_3$ solution, air in the flask containing 100 mg H-ZSM-5 was purged for 3-5h by a vacuum pump when the H-ZSM-5 powder was being stirred. The size of the stirring bar is about 5mm for maximizing the amount of H-ZSM-5 to be stirred. Then, 0.30 ml of 1.0 mg/ml $\text{Rh}(\text{NO}_3)_3$ aqueous solution was added to the H-ZSM-5. The injection needle quickly reached the powder to avoid the dispersion of the solution to the flask wall since the flask is in a vacuum. In addition, the tip of the needle needs to reach H-ZSM-5 powders as close as possible during injection, minimizing diffusion of the solution to the flask wall. After adding solution consisting of Rh^{3+} precursor, the H-ZSM-5 should be continuously, vigorously stirred for sufficient ion exchange. Then, the samples were further dried in an oven at 80°C for 3h and calcined in air at 550°C for 3 h. Figure 3.2 schematically shows the evolution of the structure of the anchored Rh atoms in ZSM-5 of 0.10wt%Rh/ZSM-5.

Actual Rh concentration of prepared catalysts before and after the reaction were determined by inductively coupled plasma atomic emission spectrometry (ICP-AES), as described in Appendix A. Figure S3.2 is the standard curve of ICP-AES for the measurement of Rh concentrations. TEM (FEI, Titan 80-300) was used to characterize the morphology of the catalyst. Extended X-ray adsorption fine structure (EXAFS) studies of Rh K-edge of prepared catalysts were taken at SPring-8 synchrotron center. The adsorption fine structure spectra of Rh K-edge were fitted using the IFEFFIT package and FEFF6 theory. Reference samples including Rh metal foil and Rh_2O_3 nanoparticles supported on Al_2O_3 were also studied with EXAFS. Their R-space

spectra of these reference samples were fitted with the same software. XPS was performed using a PHI5000 VersaProbe Spectrometer with monochromated Al K α as an X-ray source.

2.2 Catalytic reactions

Transformation of methane to acetic acid on 0.10wt%Rh/ZSM-5 was performed in a Parr high-pressure reactor (Series 4790, Parr) containing a Teflon liner vessel (Figure S3.1 in Appendix A). 28 milligram 0.10wt%Rh/ZSM-5 was added to 10 mL H₂O in the reactor. After evacuating the air left in the reactor by flowing CH₄ (99.9%, Matheson) and purging for five times, the system was pressurized with reactant gases in a sequence of CH₄, CO (99.9%, Matheson) and O₂ (99.9%, Matheson) to their desired pressures. The ratios of methane and carbon monoxide in oxygen were controlled below the lower explosive limit or above the upper explosive limit^{156, 157}. The high-pressure reactor was completely sealed and then heated to the desired reaction temperature (typically 150°C) by placing it in an oil bath. The temperature controller of the heating plate (VWR International) was used to measure the temperature of the solution in the Parr reactor through the thermocouple placed inside of the reaction solution and to control the temperature through outputting tunable power to the heating plate. Once the desired catalysis temperature was reached, the solution was vigorously stirred at 1200 rpm and was maintained at the reaction temperature for a certain amount of time. After completion of the reaction, the vessel was cooled in an ice bath to a temperature below 10°C to minimize the loss of volatile products. The solution with liquid products was filtered from the catalyst powder. The clean liquid containing acetic acid, formic acid, and methanol was analyzed by ¹H-NMR or ¹³C-NMR.

2.3 Measurements of products with NMR and GC.

^1H NMR spectra were collected at room temperature on a Bruker AVANCE III HD 400 spectrometer. The measurements were calibrated by using 3-(trimethylsilyl)-1-propanesulfonic acid sodium salt (DSS) residual signal at $\delta = 0.0$ ppm. Figure S3.3 in Appendix A is a typical NMR spectrum of products formed from CH_4 transformation. Obviously, the peak of DSS can be identified. Typically, 0.7 ml collected filtrate and 0.1 ml of D_2O (with 0.02wt% DSS) were mixed in an NMR tube for analysis. The identified oxygenated products were acetic acid ($\delta = 2.08$ ppm), formic acid ($\delta = 8.24$ ppm) and methanol ($\delta = 3.34$ ppm). A solvent suppression program was applied in order to minimize the signal originating from H_2O , similar to previous published studies⁹⁰. Standard curves were built for the quantitative analysis of major products. To establish a standard curve of a specific product such as acetic acid, a series of standard solutions with different concentrations of acetic acid were prepared. For instance, to establish a standard curve acetic acid, a series of standard solutions with different concentrations of acetic acid were prepared. NMR spectra of these standard solutions were collected with the exact same parameters of NMR measurements. The ratio of the area of peak of acetic acid ($\delta = 2.08$ ppm) to the area of DSS of the same solution was calculated. These ratios of solutions with different concentrations of acetic acid were plotted as a function of the concentrations of acetic acid. Thus, as demonstrated in Figures S3.4 a, b and c in Appendix A, standard curves of acetic acid, formic acid, and methanol were created with the similar protocol. The concentration of a product (such as acetic acid) in a reaction solution was determined by locating the ratio of the peak area of the product to the area of DSS (y-axis) in the standard curve and then finding the corresponding value (x-axis) representing the amount of the product in the unit of μmol . Gases in the head of the Parr reactor after catalysis were analyzed with GC. Table S3.2 in Appendix A presents the amounts of all reactants before catalysis

and all products as well as left reactants after the catalysis; this catalysis was performed on 28 mg 0.10wt%Rh/ZSM-5 dispersed in 10 mL deionized H₂O under 50 bar CH₄, 10 bar CO, and 8 bar O₂ for 3h. Bruker Topspin 3.5 software was used to acquire, process, and visualize the NMR data.

3. Result and Discussion

3.1 Preparation of single Rh atom-based catalytic site

Rh cations were introduced to the internal surface of micropores of ZSM-5 through a method integrating vacuum pumping and incipient wetness impregnation (IWI). To minimize the amount of Rh cations to be deposited on the external surface of a ZSM-5 particle, solution of Rh³⁺ with the same volume as the pore volume of ZSM-5 was slowly dropped to ZSM-5 powder with a syringe pump when the catalyst powder was continuously stirred and remained in a vacuum. During IWI, Rh cations exchanged with singly dispersed Brønsted acid sites of H-ZSM-5, which was prepared through calcining NH₄-ZSM-5 at 400°C for 12h. After the introduction of Rh³⁺, the samples were further dried in an oven at 80°C for 3h and calcined in air at 550°C for 3h, forming the catalyst, Rh/ZSM-5. The evolution of the chemical environment of Rh cations in ZSM-5 was schematically shown in Figure 3.2. The concentration of Rh cations in a synthesized catalyst was measured through inductively coupled plasma atomic emission spectroscopy (ICP-AES). Before an ICP-AES measurement, 28 mg of 0.10wt%Rh/ZSM-5 was dissolved in aqua regia. For catalyst with a nominal mass ratio of Rh to aluminosilicate, 0.10wt%, the measured weight percent was 0.10wt%, which suggests no obvious loss of Rh atoms during the preparation. X-ray photoelectron spectroscopy (XPS) studies of the synthesized 0.10wt%Rh/ZSM-5 displayed a lack of Rh atoms in the surface region of catalyst particles (red spectrum in Figure 3.3c) since the XPS is a surface sensitive technique. The lack of Rh atoms in the surface region revealed with XPS together with the 0.10wt%Rh in the synthesized catalyst measured with ICP-AES suggests that these introduced

Rh atoms were only anchored in micropores of ZSM-5 particles instead of the external surface of ZSM-5 particles. In terms of the catalyst sample with a high loading (0.50wt%Rh/ZSM-5), however, rhodium oxide nanoparticles at a size of around 2-4 nm were formed on the external surface of ZSM-5 as evidenced by the low contrast patches in transmission electron microscopy (TEM) images (Figure 3.3b), which is consistent with the observed Rh 3d photoemission feature in studies of the sample 0.5wt%Rh/ZSM-5 using XPS (black spectrum in Figure 3.3c)¹⁵⁸.

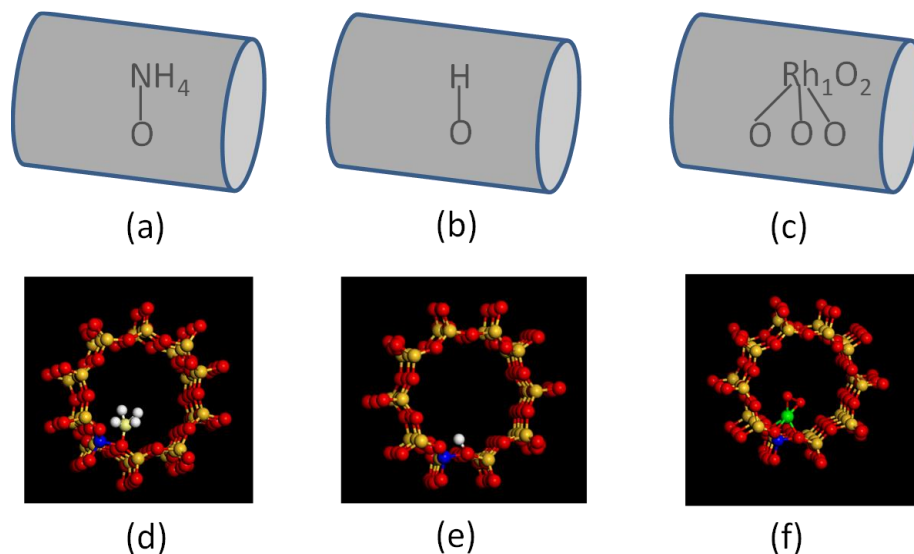


Figure 3. 2 Schematic showing the synthesis and structural feature of isolated Rh atoms in ZSM-5. Schematic (a-c) and pictures (d-f) showing the preparation of 0.10wt%Rh/ZSM-5 catalyst in which Rh_1O_5 sites were formed in the micropores of aluminosilicate. (a) NH_4 -ZSM-5 as purchased. (b) Formation of H-ZSM-5 upon calcination of NH_4 -ZSM-5 at 400°C for 12h. (c) Formation of ZSM-5 with anchored Rh_1O_5 sites through integrated vacuum pumping and incipient wetness impregnation (IWI) of Rh^{3+} to micropores through ion-exchange in aqueous solution; after impregnation, catalyst precursor was centrifuged; the precipitant was dried in an oven at 80°C for 3h and calcined in air at 550°C for 3h. (d), (e), and (f) are ball-stick model figures of the corresponding schematics (a), (b), and (c).

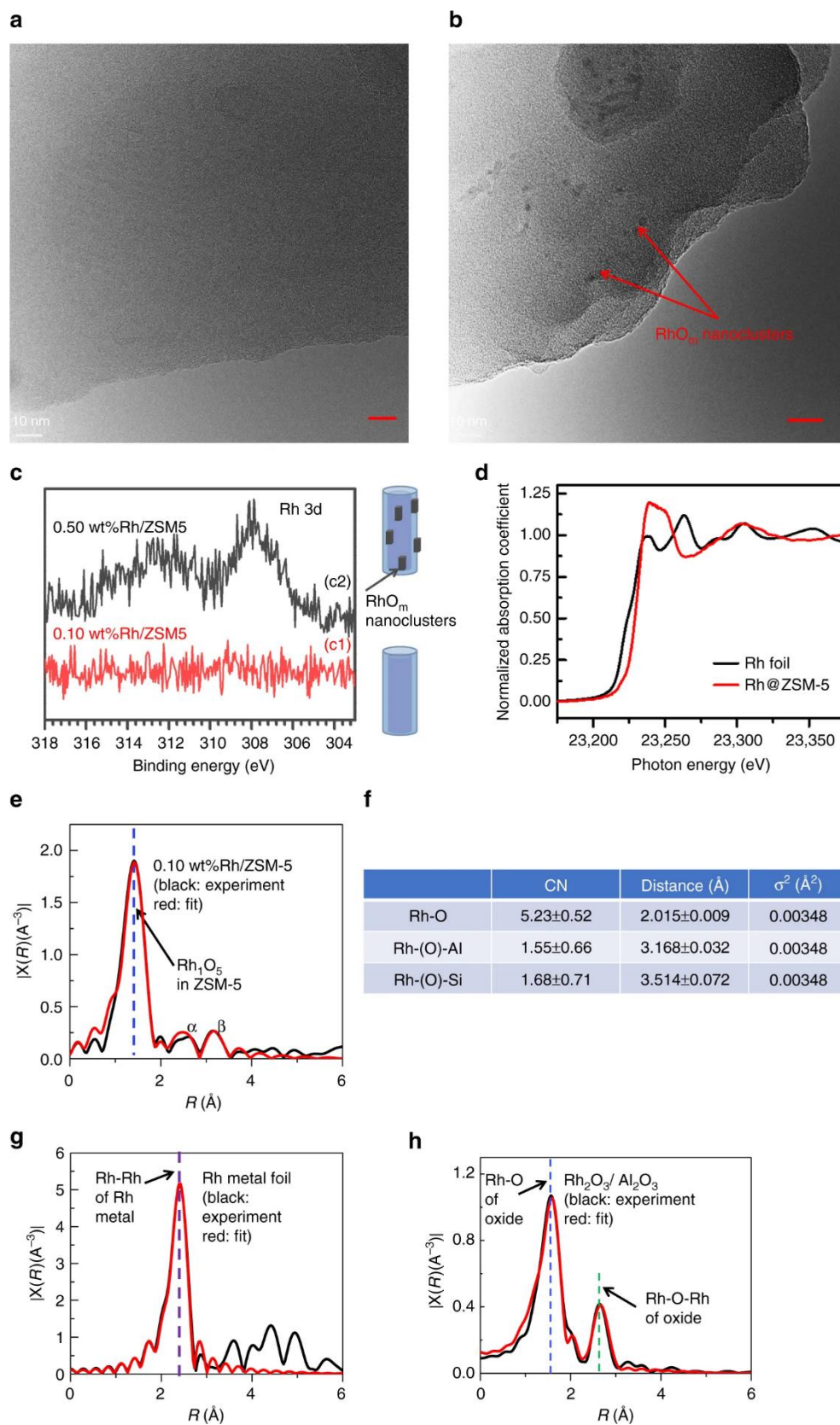


Figure 3. 3 Structural characterizations of ZSM-5 with anchored Rh cations and confirmation of single dispersion of Rh cations in 0.10wt%Rh/ZSM-5. (a) TEM image of particles of 0.10wt%Rh/ZSM-5; (b)

TEM image of particles of 0.50wt%Rh/ZSM-5; (c) Rh 3d XPS peak of 0.10wt%Rh/ZSM-5 and 0.50wt%Rh/ZSM-5; (d) Energy space of Rh K-edge of 0.10wt%Rh/ZSM-5 and Rh foil (reference sample) of X-ray absorption spectra; (e) R-space of Rh-K edge of experimental (black) and calculated (red) data of the k^2 -weighted Rh K-edge EXAFS spectra of used 0.10wt%Rh/ZSM-5; (f) Coordination number of O atoms to a Rh atom and bond length of O-Rh on average of used 0.10wt%Rh/ZSM-5; (g) and (h) R-space of Rh-K edge of experimental (black) and calculated (red) data of the k^2 -weighted Rh K-edge EXAFS spectra of Rh metal foil and Rh₂O₃ nanoparticles supported on Al₂O₃, respectively.

The existence of Rh atoms in the micropores of ZSM-5 after catalysis was confirmed by the measured concentration of Rh atoms remained in micropores with ICP-AES, which was 0.098%. Extended X-ray absorption fine structure spectroscopy (EXAFS) was used to characterize the chemical environment of anchored Rh atoms of used 0.10wt%Rh/ZSM-5 (the catalyst after reaction). After catalysis, the used catalyst powder was centrifuged and thus washed with deionized H₂O several times and then dried in an oven at 200 °C. The obtained powder was used for EXAFS studies in flowing He at 150 °C. the R-space spectrum of K-edge of Rh atoms of the used catalyst shows that Rh atoms bond with oxygen atoms and the average coordination number of oxygen atoms to a Rh atom is CN(Rh-O) of 5.23 ± 0.52 (Figure 3.3e, f). Notably, no contribution of Rh–Rh metal bonds needed to fit the R-space spectrum of Rh K-edge (Figure 3.3e), suggesting that there is no evidence for the formation of Rh–Rh metal bonds. This is consistent with the oxidization state of Rh shown in Figure 3.3h. Similar to literature¹⁵⁹⁻¹⁶¹, the second shell of rhodium oxide at 2.60 Å in the R-space spectrum (Figure 3.3h) was clearly observed in our reference sample Rh₂O₃ nanoparticles. However, there is a lack of Rh-O-Rh peak at 2.60 Å in the R-space spectrum of 0.10wt%Rh/ZSM-5 (black line in Figure 3.3e). It shows Rh atoms of our used catalyst do not have the second coordination shell of Rh atoms in terms of lack of Rh-O-Rh and thus there are no rhodium oxide nanoclusters formed in our used catalyst (0.10wt%Rh/ZSM-5). Inspired by work of Gates group, particularly the assignment of intensity at about 2.7 Å in the R-space spectrum of Rh K-edge to Rh-O-Al with a Rh-(O)-Al distance of 3.02 Å, we fit the small

peak (α) at about 2.7 Å in Figure 3.3e to Rh-O-Al. In addition, we fit the intensity at about 3.3 Å (β) in the R-space of Rh K-edge to Rh-O-Si (Figure 3.3e); the coordination numbers of Al to Rh through O atom and Si to Rh through O atom are 1.55 ± 0.66 and 1.68 ± 0.71 , respectively; the distances of Al and Si atoms to the Rh atoms are 3.168 ± 0.032 Å and 3.514 ± 0.072 Å, respectively. Thus, these EXAFS studies show that Rh atoms of 0.10wt%Rh/ZSM-5 are singly dispersed in micropores of ZSM-5, and each Rh atom bond with about five oxygen atoms on average. In the following paragraphs, sometimes we used Rh₁O₅@ZSM-5 when we need to point out the coordination environment of the Rh atoms on average. Figure 3.2 schematically shows the structure of a catalytic site of Rh₁O₅ anchored in micropores of ZSM-5.

3.2 Catalytic performance of Rh₁O₅@ZSM-5 catalyst at 150°C

Experiments for the synthesis of acetic acid were conducted by using same amount of different catalysts under identical catalytic conditions. With 28 mg of 0.10wt% Rh/ZSM-5, about 246 μmol of total products (acetic acid, formic acid, and methanol) were produced at 150°C in the first hour (entry 4 in Table S3.1 in Appendix A). Under the same condition, the yields of the total organic compounds formed from 0.50wt%Rh/ZSM-5 (entry 5 in Table S3.1 in Appendix A) are similar to 0.10wt%Rh/ZSM-5. This similarity in catalytic performances shows that the rhodium oxide nanoparticles formed in 0.50wt%Rh/ZSM-5 are not active for this transformation. In other words, the catalytic activity of 0.10wt%Rh/ZSM-5 in this chemical transformation is contributed from the Rh₁O₅ sites anchored in micropores of ZSM-5 instead of rhodium oxide nanoparticles. As calculated in Appendix A, the conversions of CH₄ in studies of Figure 3.4 and Table S3.1 are lower than 20%. Thus, we used these conversions to calculate the turn-over frequency with the equation

$$TOF = \frac{\text{number of produced molecules of products}}{\text{time of catalytic reaction (s)} \times \text{number of active sites (Rh}_1\text{O}_5)}$$

This calculation is based on the assumption that all loaded Rh atoms are active sites, as described in Appendix A. The activities for production of acetic acid and total oxygenates at 150°C are 0.070 and 0.10 molecules per Rh atom per second (entry 3 of Table 3.1), respectively.

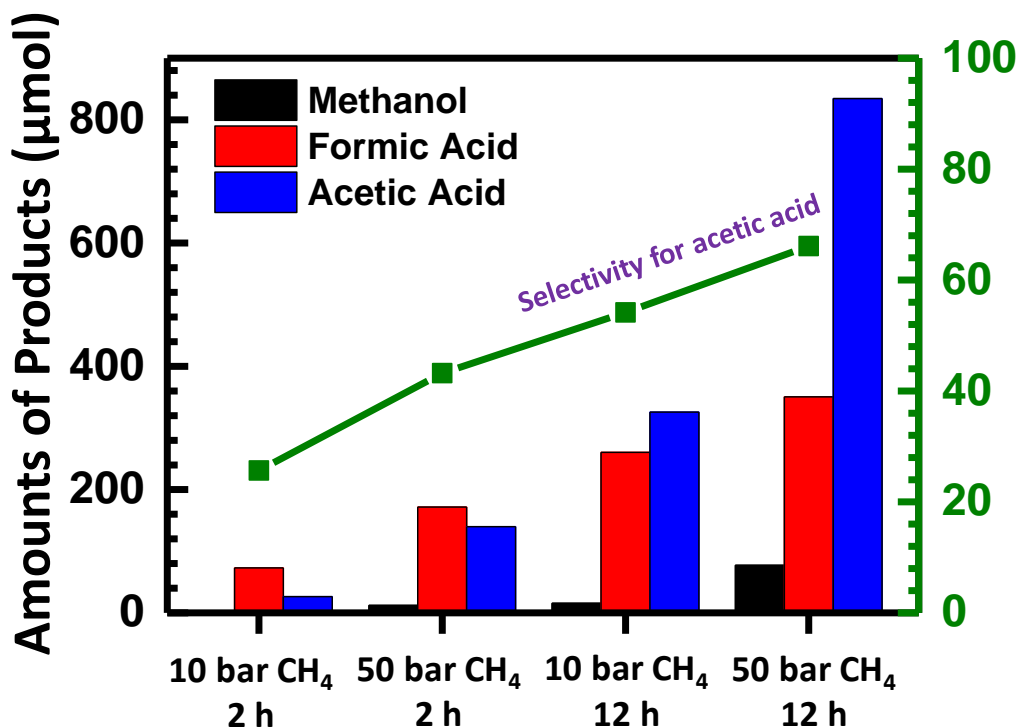


Figure 3. 4 Yields of acetic acid, formic acid, and methanol (left vertical axis) as well as the selectivity to acetic acid (the right vertical axis) were plotted as a function of different pressures of CH₄ (10 or 50 bars) and different reaction times (2 h or 12 h). 28 mg of 0.10wt%Rh/ZSM-5 was used for each catalysis. Each catalysis consists of 10 bar CO and 8 bar O₂ and certain pressure of CH₄ as noted on the X-axis (10 or 50 bars). The catalysis temperatures of all studies here are 150°C here.

To check whether Rh atoms anchored in micropores of ZSM-5 could detach from ZSM-5, the clear solution was obtained by filtration for removal of Rh/ZSM-5 catalyst particles from the solution after catalysis at 150°C for 12h. ICP-AES test of this solution shows that only 2% of the total Rh atoms of 28 mg of 0.10wt%Rh/ZSM-5 detached from ZSM-5 to the solution. Thus, most Rh atoms remained in ZSM-5 after catalysis. Due to the negligible amount of Rh³⁺ detached from 0.10wt%Rh/ZSM-5 and the extremely low TOF of free Rh³⁺ in solution evidenced in entry 1 in

Table 3.1, the contribution of the detached Rh^{3+} to the measured catalytic activity in the formation of acetic acid is negligible. It suggests that the anchored Rh atoms are active sites.

Table 3. 1 Comparison of turn-over frequency (TOF) for formation of acetic acid or oxygenates including acetic acid, formic acid and methanol on 0.10wt%Rh/ZSM-5 and homogeneous catalyst

Note: the unit of TOR here is number of product molecules formed from per site per second.

Entry	Catalyst	Catalytic temperature	TOF of acetic acid (molecule per site per second)	TOF of total oxygenates ^[a] (number of molecules per site per second)	Selectivity for production of acetic acid
1	$\text{Rh}(\text{NO}_3)_3$ ^[a]	150°C	6.3×10^{-6} ^[b]	2.4×10^{-5} ^[b]	26.3%
2	0.10wt% Rh/ZSM-5 ^[a]	150°C	0.040 ^[c]	0.099 ^[c]	40.0%
3	0.10wt% Rh/ZSM-5 ^[a]	150°C	0.070 ^[d]	0.10 ^[d]	70.1%

[a]: Here, oxygenates include acetic acid, formic acid and methanol (CO_2 was not included). Calculations of TOFs of these catalysts were described in Appendix A.

[b]: Five milliliters of 0.01 mol/L $\text{Rh}(\text{NO}_3)_3$ was added in Parr reactor and 50 bar CH_4 , 10 bar CO , and 8 bar O_2 were introduced to the Parr reactor and then the Parr reaction was sealed; the reaction was performed at 150°C for about 90h. This measurement was done for comparison with 0.10wt%Rh/ZSM-5 in which Rh_1 cations were anchored in micropores

[c]: The catalysis condition of 0.10wt%Rh/ZSM-5: a mixture of 50 bar CH_4 , 10 bar CO , 8 bar O_2 , 2h; the yields of acetic acid and all oxygenates were listed in Figure 3.4.

[d]: The catalysis condition of 0.10wt%Rh/ZSM-5: a mixture of 50 bar CH_4 , 10 bar CO , 8 bar O_2 , 12h; the yields of acetic acid and all oxygenates were listed in Figure 3.4.

To further confirm the contribution of Rh_1O_5 sites to the formation of acetic acid, control experiments were performed on these catalysts including 28 mg of H-ZSM-5, 28 mg of 0.10wt%Rh/ SiO_2 and 28 mg of 0.10wt%Rh/ Al_2O_3 under the exactly same condition as that of 28 mg 0.10wt%Rh/ZSM-5 at 150°C in the mixture of 50 bar CH_4 , 10 bar CO and 8 bar O_2 for 2h. As shown in Table 3.2, the amounts of acetic acid, formic acid, or methanol produced on 28 mg of 0.10wt%Rh/ SiO_2 and 28 mg of 0.10wt%Rh/ Al_2O_3 are lower than 10 μmol , which are at the level of the error bar. All the reported yields in this work are the measured products formed from 28 mg catalyst. In conclusion, these control samples in terms of Rh supported on these nonporous oxides and even on a couple of commonly used reducible oxides are not active for the production of acetic

acid or methanol from the coupling of CH₄ with CO and O₂. Thus, these studies suggest the significant contribution of Rh₁O₅ sites encapsulated in ZSM-5 to the formation of acetic acid.

Table 3. 2 Catalytic performances of 28 mg catalysts of 0.10wt%Rh supported on different supports in a mixture of 10 bar CH₄, 10 bar CO, and 8 bar O₂ at 150 °C for 3 h with 10 mL H₂O in a high-pressure reactor

Entry	Catalyst	Methanol (μmol)	Formic acid (μmol)	Acetic acid (μmol)	Total products (μmol)
1	H-ZSM-5	3.67	2.28	1.87	7.82
2	0.10wt%Rh/SiO ₂	8.71	4.62	6.13	19.46
3	0.10wt%Rh/Al ₂ O ₃	5.68	0.91	3.05	9.64

Acetic acid, formic acid, and methanol were identified as products. Reactants on pure H-ZSM-5 was also performed at the same conditions as a blank experiment (entry 1)

The participation of all these three reactants (CH₄, CO, and O₂) was confirmed with three parallel studies on 0.10wt%Rh/ZSM-5 under the exactly same catalytic condition as displaced in Figure S3.5 a, b, c; in each of these studies, only two of the three reactants were introduced to the Parr reactor; none of these studies produced acetic acid, formic acid, or methanol due to the lack of the third reactant gas. Those studies clearly show that all three gases (CH₄, CO, and O₂) are necessary reactants for the formation of CH₃COOH.

3.3 Participation of molecular O₂ in the synthesis of acetic acid

Here we used low-cost molecular oxygen (O₂) or compressed air as an oxidant in the oxidative transformation of CH₄ and CO to acetic acid. To further confirm the direct participation of molecular O₂, we performed catalysis at different pressures of O₂ (2 bar, 4 bar, 8 bar, 12 bar, and 16 bar) but all other conditions are the same in these parallel studies; in each of these parallel studies, 28 mg of 0.10wt%Rh/ZSM-5 was added to 10 ml H₂O. The reaction was performed at 150°C for 2 h in a mixture of 30 bar CH₄, 10 bar CO and different pressures of O₂, investigating the correlation of yields of products (acetic acid, formic acid and methanol) with the pressure of O₂. As shown in Figure 3.5a, the highest yields of acetic acid and formic acid were obtained from

the catalysis using 8 bar O₂. The increase of yield of acetic acid and formic acid along with the increase of O₂ pressure shows that O₂ does participate in the formation of acetic acid and formic acid. It is expected that high coverage of oxygen atoms on a Rh atom formed at high pressure of O₂ could saturate the coordination of Rh₁ atom and thus poison the catalyst sites at high pressure of O₂, resulting in a low yield of oxygenates at high pressure of O₂.

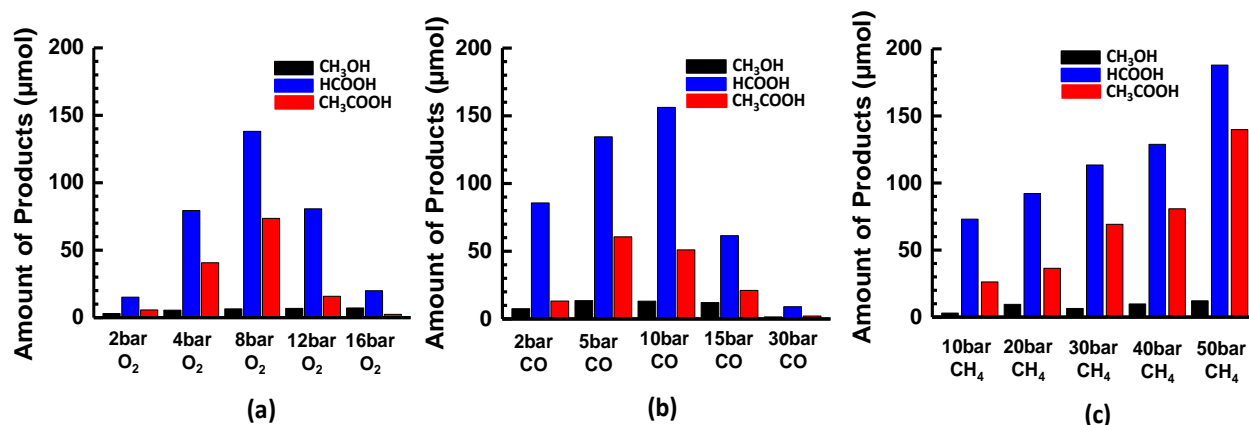


Figure 3. 5 Yields of methanol (black), formic acid (blue) and acetic acid (red) in the chemical transformation of CH₄ at 150°C in aqueous solutions at different pressure of (a) O₂, (b) CO, (c) CH₄. (a) 30 bar CH₄, 10 bar CO and different pressure of O₂ at 150°C for 2h. (b) 50 bar CH₄, 8 bar O₂ and different pressure of CO at 150°C for 2h. (c) 10 bar CO, 8 bar O₂ and different pressure of CH₄ at 150°C for 2h.

3.4 Direct participation of CO to the synthesis of acetic acid

To further confirm the participation of CO in the formation of acetic acid, the influence of the partial pressure of CO on both the conversion of CH₄ and selectivity for the production of acetic acid was investigated through parallel studies (Figure 3.5b). In each of these studies, the partial pressures of CH₄ and O₂ were fixed at 15 bar and 8 bar, respectively. However, the pressures of CO in the five studies are 2 bar, 5 bar, 10 bar, 15 bar, and 30 bar. The increase of the amount of acetic acid while CO pressure was increased from 2 bar to 10 bar, suggesting that CO directly participates in the formation of acetic acid. The lack of activity for production of acetic acid at 30 bar CO showed that catalyst sites are blocked at such a high pressure of CO. CO molecules must have directly interacted with the Rh cations. At high pressure of CO, high coverage of CO could

saturate the coordination of CO molecules to a Rh₁ atom and deactivate the catalyst. We measured the concentrations of Rh in the liquid (α) after filtering the catalyst experienced catalysis at 10 bar CO, 15 bar CH₄ and 8 bar O₂, and in another liquid (β) after filtering the catalyst experienced catalysis at 30 bar CO, 15 bar CH₄ and 8 bar O₂. The amounts of Rh atoms in the liquids α and β are 3.1% and 13.0% of Rh atoms of 28 mg of 0.10wt%Rh/ZSM-5, respectively. Thus, the much larger loss of Rh atoms at high pressure of CO (30 bar) suggests that Rh atoms form carbonyl at high pressure of CO and some of these formed rhodium carbonyl species desorb and dissolve in solution. Thus, Rh species detached at high pressure of CO.

One molecular-level evidence on the direct participation of CO is the following isotope experiment. 0.7 bar ¹³CO (Aldrich, 99 atom%) was mixed with 6.3 bar of CO, 14 bar CH₄ and 4 bar O₂ for catalysis of 10 hours (Figure 3.6a). 40 μ mol of ¹³CH₃OH (Aldrich, 99 atom%) was added to the collected solution after catalysis as a reference to quantify the amount of potential isotope products ¹³CH₃COOH, CH₃¹³COOH, or H¹³COOH. As (1) the amount of produced CH₃OH is negligible and (2) the chemical shift of ¹³CH₃OH in ¹³C spectrum can be readily distinguished from reactants and acetic acid and formic acid, 40 μ mol of ¹³CH₃OH (Aldrich, 99 atom%) was added as a reference to quantify the amount of isotope products CH₃¹³COOH, H¹³COOH, and ¹³CH₃COOH. Due to the natural existence of ¹³C in regular CO with a natural abundance of ¹³C of 1.1%, contrast experiments (Figure 3.6b) are necessary for elucidating the chemical bonding of ¹³C in the formed products. Contrast experiments using the mixture of 7 bar of CO, 14 bar CH₄ and 8 bar O₂ were performed. As shown in Figure 3.6b, the intensity ratio of CH₃¹³COOH to ¹³CH₃OH of the solution of isotope experiment (Figure 3.6a) is obviously larger than that in the contrast experiment (Figure 3.6b) by about 6.4 times. In addition, the intensity ratio of H¹³COOH to ¹³CH₃OH in the isotope experiment is higher than the contrast experiment by about

2.6 times. Notably, the intensity ratio of $^{13}\text{CH}_3\text{COOH}$ to $^{13}\text{CH}_3\text{OH}$ in isotope experiment (Figure 3.6a) is similar to the ratio of the contrast experiment. It suggests that the C atoms of CH_3 of CH_3COOH do not come from the reactant CO.

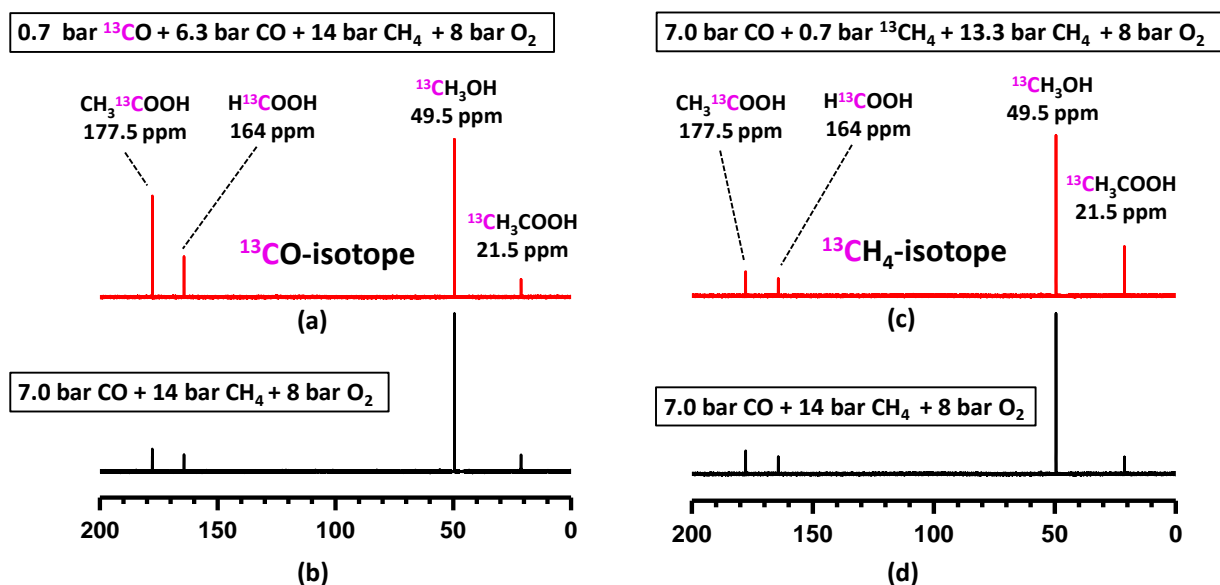


Figure 3. 6 ^{13}C NMR spectra of products of acetic acid, formic acid and methanol on 28 mg 0.10wt%Rh/ZSM-5 at 170°C for 10h in gas mixture :(a) mixture of 0.7 bar ^{13}CO , 6.3 bar CO, 14 bar CH_4 and 8 bar O_2 , (b) mixture of 7 bar CO, 14 bar CH_4 and 8 bar O_2 , (c) mixture of 7 bar CO, 0.7 bar $^{13}\text{CH}_4$, 13.3 bar CH_4 and 8 bar O_2 , and (d) mixture of 7 bar CO, 14 bar CH_4 and 8 bar O_2 . (a) and (b) are isotope experiments; (c) and (d) are their corresponding contrast experiments.

One potential pathway to form acetic acid is the coupling of CO with a formed formic acid molecule; if so, the yield of acetic acid should increase along with the increase of CO pressure. However, as shown in Figure 3.5b yield of acetic acid decreases along with the increase of CO pressure (≥ 10 bar). Thus, coupling formic acid with CO to form acetic acid is not a pathway. To further check the possibility of reaction between HCOOH and CO to form acetic acid, we performed three control experiments at 150°C for 3h under the following conditions including a mixture of 28 mg 0.10wt%Rh/ZSM-5, 108 μmol HCOOH , and 10 mL DI H_2O without any CO,

with 5 bar CO, and with 10 bar CO, respectively. As shown in Figure S3.6 in Appendix A, no acetic acid was formed in these experiments.

3.5 Direct participation of CH₄ instead of coupling CH₄ with formic acid to the synthesis of acetic acid

The influence of CH₄ pressure on the catalytic performance was explored at 150°C under a mixture of 10 bar CO and 8 bar O₂ and different pressure of CH₄ (10 bar, 20 bar, 30 bar, 40 bar and 50 bar) for 2 hours (Figure 3.5c). The progressive increase of yield of acetic acid shows that CH₄ directly participates in the formation of acetic acid. The apparent increase of yield of acetic acid along the increase of CH₄ pressure demonstrates that CH₄ directly participates in the formation of acetic acid (Figure 3.5c), which excluded a pathway in which CH₄ couples with formic acid to form acetic acid. If acetic acid was formed from a coupling of formic acid with CH₄, the amount of formic acid should have decreased along the increase of pressure of CH₄ since more formic acid should have been consumed along with the increased amount of CH₄ to form acetic acid.

To elucidate the source of carbon atoms at the molecular level, ¹³CH₄ isotope experiments were performed. 0.7 bar ¹³CH₄ (Aldrich, 99 atom%) was mixed with 13.3 bar of CH₄, 7.0 bar CO, and 4.0 bar O₂ for isotope experiment on 28 mg of 0.10wt% Rh/ZSM-5 at 170°C for 10 hours (Figure 3.6c). As shown in Figure 3.6c, CH₃¹³COOH, H¹³COOH and ¹³CH₃OOH were observed. A contrast experiment using the mixture of 14 bar unlabeled CH₄, 7.0 bar of CO, and 8 bar O₂ was performed at exactly the same catalytic conditions (Figure 3.6d). ¹³CH₃COOH were formed in the two experiments. However, the ratio of ¹³CH₃COOH to reference (¹³CH₃OH) when ¹³CH₄ was used (Figure 3.6c), is much larger than that when unlabeled CH₄ was used (Figure 3.6d). This

difference shows that the carbon atom of CH₃ of acetic acid comes from CH₄ instead of CO. If C atoms of C=O of CH₃COOH could come from CH₄, the ratio of CH₃¹³COOH to reference (¹³CH₃OH) in Figure 3.6c would be much larger than the ratio in Figure 3.6d since the isotope experiment contains a significant amount of ¹³CH₄. In fact, in both regular and isotope experiments, we did observe a small amount of CH₃¹³COOH but there is no large difference between their ratios to reference (¹³CH₃OH) in the experiments of both Figures 3.6 c and d. Here, the formation of CH₃¹³COOH is due to the natural abundance of ¹³CO in unlabeled CO. Thus, CO does not contribute to the formation of CH₃ of CH₃COOH.

3.6 Direct coupling of reactants for the formation of acetic acid

It is noted that the amount of methanol in any of our studies is always much lower than acetic acid and formic acid. One potential argument for the low yield of methanol could be that methanol has been formed but it could have acted as an intermediate compound in the formation of acetic acid; in other words, formic acid could have been consumed through coupling with CO to form acetic acid. Depending on whether CH₃OH could act as an intermediate product in the formation of acetic acid or not, two categories of potential pathways α and β were proposed in Fig. 3.7a. In potential pathway α , CH₄ couples with CO to directly form acetic acid; methanol is not an intermediate product of this type of reaction pathway. In potential pathway β , however, CH₃OH is an intermediate product and then be consumed in the formation of acetic acid; CH₄ is first oxidized to CH₃OH (the first step) and then CH₃OH couples with CO to form acetic acid (the second step); the second step of the potential pathway β is called carbonylation of methanol by CO; it is in fact the Monsanto process^{162, 163}. In order to identify whether methanol carbonylation (pathway β)

could be a pathway for the production of acetic acid on our catalyst Rh₁O₅@ZSM-5, carefully designed isotope experiments described in Appendix A were performed.

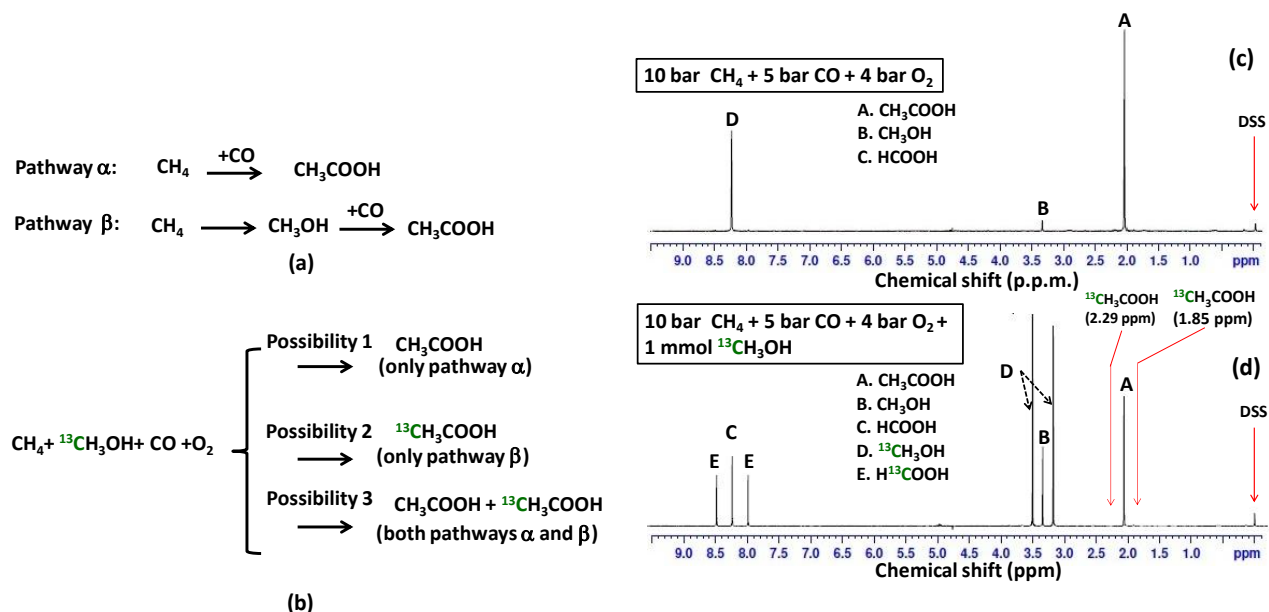


Figure 3. 7 Isotope-labelled studies for elucidating whether acetic acid could be formed through coupling methanol with CO. (a) Two potential pathways α and β for production of acetic acid; in pathway α , CH_3OH is not an intermediate for formation of CH_3COOH ; in pathway β , CH_3OH is an intermediate for formation of CH_3COOH . (b) Potential catalytic products formed from 0.10wt% Rh/ZSM-5 in the mixture of ${}^{13}\text{CH}_3\text{OH}$ and H_2O in solution under mixture of CH_4 , CO and O_2 if the transformation of CH_4 , CO and O_2 follows pathway α , β , or both α and β . (c) NMR spectra of the products formed from 28 mg of 0.10wt% Rh/ZSM-5 after reaction in 10 bar CH_4 , 5 bar CO , and 4 bar O_2 at 150°C for 1h; there was no any isotope-labelled methanol, ${}^{13}\text{CH}_3\text{OH}$ added to the reactor before catalysis. (d) NMR spectra of the products formed from 28 mg of 0.10wt% Rh/ZSM-5 after reaction in 10 bar CH_4 , 5 bar CO , and 4 bar O_2 at 150°C for 1h.; notably, 1.0 mmol ${}^{13}\text{CH}_3\text{OH}$ was added to H_2O before catalysis.

These isotope experiments show that acetic acid cannot be formed from carbonylation of methanol by CO on our catalyst. In one isotope-labeled experiment, 1.0 mmol isotope-labeled ${}^{13}\text{CH}_3\text{OH}$ (99 atom% ${}^{13}\text{C}$, Aldrich) was added to 10 ml deionized H_2O before the introduction of 10 bar CH_4 , 5 bar CO , and 4 bar O_2 to the Parr reactor. If CH_3OH could not be an intermediate for the formation of acetic acid, the added ${}^{13}\text{CH}_3\text{OH}$ would not participate into the formation of isotope-labeled acetic acid, ${}^{13}\text{CH}_3\text{COOH}$. Thus, no ${}^{13}\text{CH}_3\text{COOH}$ could be observed if carbonylation of methanol by CO would not be involved (possibility 1 in Figure 3.7b). The NMR

spectrum of the solution of products formed in the reactor having $^{12}\text{CH}_4$, ^{12}CO , and O_2 in H_2O ($^{13}\text{CH}_3\text{OH}$ was not added) after the reaction of 2h was presented in Figure 3.7c. Figure 3.7d is the NMR spectrum of the products formed after the catalysis for 1 h under a condition of a mixture of $^{13}\text{CH}_3\text{OH}$, $^{12}\text{CH}_4$, ^{12}CO , and O_2 at 150°C . The observed peaks A, B, C, D, and E in Figure 3.7d were assigned to CH_3COOH , CH_3OH , HCOOH , $^{13}\text{CH}_3\text{OH}$, and H^{13}COOH , respectively. As neither peak of H atoms of $^{13}\text{CH}_3$ of $^{13}\text{CH}_3\text{COOH}$ in ^1H spectrum nor peak of ^{13}C atoms of $\text{CH}_3^{13}\text{COOH}$ in the ^{13}C spectrum was observed in the NMR, pathway β is not a pathway for the formation of acetic acid. Thus, these isotope studies showed that acetic acid is not formed from carbonylation of methanol by CO. Additionally, H^{13}COOH was observed clearly in Figure 3.7d, suggesting that $^{13}\text{CH}_3\text{OH}$ can be oxidized to H^{13}COOH under the current catalytic condition.

Directly reforming CH_4 with CO_2 to produce acetic acid at a temperature $\geq 250^\circ\text{C}$ was reported in literatures¹⁶⁴⁻¹⁶⁹. Presumably, one potential reaction pathway for the formation of acetic acid on our catalyst is that CO is first oxidized by O_2 to form CO_2 and then CO_2 couples with CH_4 to form acetic acid. To check this possibility, 30 bar CH_4 and 30 bar CO_2 were introduced to the Parr reactor and the reaction was performed under the same catalytic condition on 28 mg 0.10wt%Rh/ZSM-5 (at 150°C for 4h). As shown in Figure S3.7, no acetic acid, formic acid or methanol was formed. Thus, the pathway involving CO oxidation to form CO_2 and then reforming CH_4 with CO_2 to form acetic acid was excluded.

The mechanism of one-step synthesis of acetic acid by coupling methane with carbon monoxide and oxygen through homogeneous catalysts was proposed in literatures^{147, 148}. Nevertheless, the reaction pathway was uncovered due to the lack of fundamental understanding of the authentic structure of heterogeneous catalysts at atomic level. It is challenging to characterize the structure of the single-atom Rh catalyst under catalytic conditions for the one-step

synthesis of acetic acid from methane owing to the complexity of the gas-liquid reaction system. Thus, it is expected to overcome the difficulty of in-situ studies in the future research to explore the mechanism of producing the acetic acid through methane direct transformation.

3.7 Ready separation of hydrophilic products from a hydrophobic solvent

The above chemical transformation was performed in aqueous solution. As the products of this chemical transformation, acetic acid, formic acid, and methanol are hydrophilic, it is not feasible to separate these hydrophilic products from water. Thus, a hydrophobic solvent, *n*-dodecane, was used to attempt to make hydrophilic products automatically separate from the solvent after synthesis.

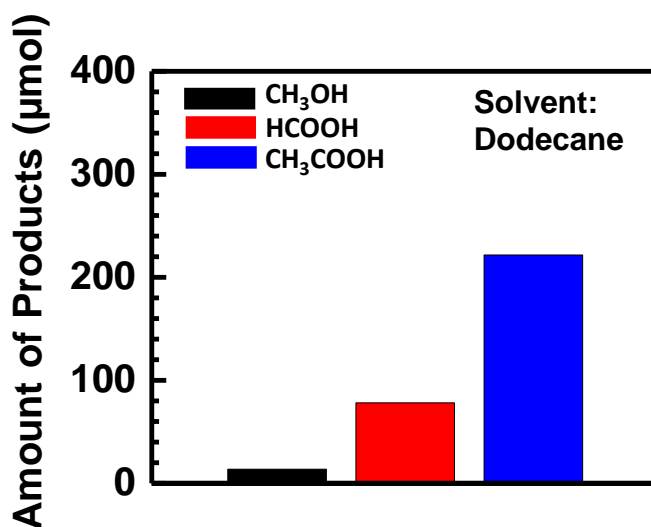


Figure 3. 8 Yields of acetic acid, formic acid and methanol from 28 mg 0.10wt%Rh/ZSM5 in 10 ml dodecane at 150°C in the mixture of 30 bar CH₄, 10 bar CO and 5 bar O₂ for 2h.

As shown in Figure 3.8, the yields of catalysis at 150°C on 28 mg 0.10wt%Rh/ZSM-5 in 10 ml *n*-dodecane in the mixture of 50 bar CH₄, 10 bar CO and 8 bar O₂ for 2 hours are slightly higher than that using 10 ml DI water under the same catalytic conditions as shown in Figure 3.4. The significant advantage of using an organic solvent is that the hydrophilic products of this

reaction (acetic acid and formic acid) can readily separate from the hydrophobic solvent, without energy cost.

3.8 Feature of this chemical transformation in liquid under mild condition

CH₄ and CO can be oxidized with different oxidants including O₂, concentrated H₂SO₄, or a superacid by using the homogeneous catalyst RhCl₃,^{147, 148, 170, 171} in which acetic acid and other products (formic acid and methanol) were formed. One control experiment using Rh(NO₃)₃ was done (entry 1 in Table 3.1); the turn-over-frequency (TOF) of the homogenous catalyst, Rh(NO₃)₃ without a promoter, is only 6.3 x 10⁻⁶ molecules per rhodium cation per second at 150°C. Here, the Rh₁O₅@ZSM-5 catalyzes the oxidation of CH₄ and CO with a low-cost oxidant, molecular oxygen or even air at 150°C at a solid-liquid-gas interface. TOF of the catalytic sites Rh₁O₅ anchored in microporous aluminosilicates reaches 0.070 CH₃COOH molecules per Rh₁O₅ site per second in a mixture of 50 bar CH₄, 10 bar CO, and 8 bar O₂ (entry 3 of Table 3.1). The TOF for production of acetic acid on singly dispersed Rh₁O₅ sites is much higher than those reported homogenous catalysts by >1000 times. As shown in Figure 3.4, 840 μmol of acetic acid, 352 μmol of formic acid, and 82 μmol of methanol were produced from 28 mg 0.10wt%Rh/ZSM-5 at 150°C for 12h under a catalytic condition of 50 bar CH₄, 10 bar CO and 8 bar O₂, which correspond to conversion of 10.2% of CH₄ under this condition. Selectivity for production of acetic acid among all organic products reaches about 70% under this condition. Other than the highest catalytic efficiency on Rh₁O₅@ZSM-5, a significant advantage of this catalytic process is the ready separation of liquid products from the solid catalyst and solvent.

4. Conclusion

In this work, the heterogeneous single-atom catalyst, 0.10wt% Rh/H-ZSM-5 consisting of single dispersed Rh_1O_5 sites anchored in the microporous aluminosilicate, was synthesized. The anchored Rh_1O_5 sites exhibited unprecedented catalytic activity in the production of acetic acid from carbon monoxide addition. The TOF for the formation of acetic acid over the single-atom Rh catalyst is 0.70 moles acetic acid per mole Rh_1O_5 sites per second, higher than that of free Rh^{3+} in aqueous solution by >1000 times under mild conditions. The mechanism of the synthesis of acetic acid was proposed to be the coupling of three reactants (methane, carbon monoxide and oxygen) over Rh_1O_5 sites. This heterogeneous catalytic process suggests a new route for the one-step synthesis of acetic acid through direct utilization of methane under a mild condition at 150°C or lower by using a low-cost oxidant O_2 , in place of the current industrial process based on carboxylation of methanol.

Contributions of the project:

The synthesis of catalysts and catalytic performances of prepared catalyst were mainly done by Yuting Li; Characterizations of catalysts were done by Yu Tang and collaborators.

Chapter 4: The understanding of coordination number-dependent catalyst – transition metal oxide for methane complete oxidation

1. Introduction

The extensive studies of metal catalysts in the last four decades have uncovered that the packing of metal atoms on the surface of a metal particle is essential for the catalytic performance of metal catalysts^{99, 172}. Compared to metal catalysts, transition metal oxide (TMO) and TMO-based catalysts catalyze more than half of the reactions of chemical and energy transformations in industries. However, much less understanding of the reaction mechanisms on TMOs and TMO-based catalysts at a molecular level has been achieved in contrast to catalysis on metals. Compared to the considerable fundamental studies of surface structures of metal catalysts and their corresponding catalytic performances^{99, 172-175}, very few intrinsic correlations between different surface structures of a TMO catalyst and their corresponding catalytic performances have been established. That is partially due to the high complexity of surface structures of TMO catalysts. Such structural complexity results from the coexistence of cations with different coordination environments, the coexistence of cations of different valences, and the coexistence of different surface defects. In addition, a dramatic restructuring of surfaces of a TMO catalyst could happen along with a transition of bulk phase from a low-temperature phase to high-temperature one when the temperature of catalysis is increased since a TMO often exists in forms of more than one phase. These complicated, interacting factors have made the establishment of an intrinsic correlation between an atom-scale surface structure of a TMO catalyst and its corresponding catalytic performance extremely challenging.

To explore the correlation of surface structures of a TMO and their corresponding catalytic performances, NiO was chosen as a probing TMO since a Ni cation anchored on Co₃O₄ surface

lattice plays a significant role in the activation of C-H bond of CH₄ in methane complete oxidation^{33, 176-178}. In this study, planar sheet NiO, cubic NiO and octahedral NiO were synthesized, whose exposed surfaces are (110) facet, (100) facet and (111) facet, respectively. Ni²⁺ cations in surfaces of these three catalysts were found to coordinate with 4, 5, and 6 oxygen atoms, respectively. Experimental studies demonstrated that a Ni cation coordinating with four oxygen atoms on (110) of planar sheet NiO is highly active for activation of CH₄ and CH₄ complete oxidation in contrast to the inertness of both (100) of cubic NiO and (111) of octahedral NiO at temperatures lower than 400°C. It suggests that the coordination environment of a Ni cation plays a crucial role in determining the catalytic activity of NiO catalysts. It is also found that the catalytic activity of inert (100) surface of cubic NiO for CH₄ complete oxidation was improved by decreasing the coordination number of O atoms surrounding a Ni atom [CN(Ni-O)] through the H₂ reduction at a temperature $\geq 225^\circ\text{C}$. The combination of experimental explorations and theoretical studies indicates an intrinsic correlation between the coordination environment of the Ni²⁺ active sites and their catalytic activities. In short, this work demonstrated (1) coordination environment of cations on surface of a transition metal oxide is crucial for catalytic performance on TMO, and (2) catalytic activity on an inert TMO surface can be triggered through manipulation of coordination environment of cations on the surface if the ideal coordination environment of cation for a catalytic reaction is revealed.

2. Experiment

Planar sheet NiO was prepared through the calcination of hexagonal plates of nickel hydroxide, Ni(OH)₂ synthesized with a hydrothermal reaction. 0.540 gram of Ni(NO₃)₂ 6H₂O and 1.2 gram of dodecylbenzenesulfonate were dissolved in 120 ml deionized water completely. 0.250

of NaOH was added to the prepared solution. The well-mixed solution was stored in an autoclave. The hydrothermal reaction was performed at 150°C for 36h. After the reaction, the formed nanocrystals were washed with deionized water and then ethanol with the following drying in air at 60°C for 6h, forming crystallized hexagonal plates of Ni(OH)₂. Then, the well-crystallized Ni(OH)₂ was calcinated at 400°C for 2h in air. The formed NiO appears as planar sheets.

Cubic NiO was purchased from Aldrich (99.99%) without further treatment. The crystalline structure of the commercial cubic NiO was confirmed. In addition, cubic NiO was also synthesized with a method called one-step spray pyrolysis reported in literature.^{179, 180} In a basic process, Ni(NO₃)₂•6H₂O was dissolved in distilled water to form the spray solution. Then, the aqueous spray solution consisting of nickel components was introduced into the high-temperature diffusion flame at a flow rate of 150 ml/h. Citric acid was added to be the chelating agent forming the clear spray solutions. The synthetic cubic NiO particles have very similar size and surface area as those of commercial NiO.

Octahedral NiO was prepared by thermal decomposition of hexagonal nanoplate of Ni(OH)₂, a method reported in literature.^{181, 182} In a typical synthesis, NiCl₂•6H₂O (0.808g, 3.4 mmol) and 0.5 g polyvinylpyrrolidone (PVP) was dissolved in a prepared mixture of 5 ml DI water and 40 mL anhydrous ethanol. Then, 0.10 gram of NaOH was added to the solution under vigorous stirring. The mixture was transferred to a Teflon lined stainless steel autoclave and kept at 200°C-250°C for 4h. After the hydrothermal treatment, the solid product was collected and washed with DI water and ethanol. Then it was dried in the oven at 60°C for 12h. Octahedral NiO was finally obtained by annealing the solid at 450°C in air for half hour.

The high-resolution transmission electron microscope (HR-TEM) images and high angle annular dark-field (HAADF) imaging technique in STEM mode (HAADF-STEM) were used to

take images from these NiO catalysts on FEI Tecnai F20 XT located at John M. Cowley Center for High-Resolution Electron Microscopy at Arizona State University and Department of Inorganic Chemistry at Fritz Haber Institute. Powder X-ray diffraction (XRD) patterns of used catalysts were recorded with a Rigaku Ultimate IV operating in reflection mode with Cu K α radiation that was monochromatic with a secondary graphite monochromator. The surface of catalysts during catalysis of complete oxidation of methane was characterized when a catalyst was under a catalytic condition by ambient pressure X-ray photoelectron spectroscopy (XPS). Details of how AP-XPS was used for operando studies of the surface of catalysts were reviewed in recent reviews¹⁸³.

All the DFT calculations were carried out with a periodic slab model using the Vienna ab initio simulation program (VASP) by Hu group at The Queen's University, Belfast.¹⁸⁴⁻¹⁸⁷ The generalized gradient approximation (GGA) was used with the Perdew-Burke-Ernzerhof (PBE)¹⁸⁸ exchange-correlation functional. The projector-augmented wave (PAW) method^{189, 190} was utilized to describe the electron-ion interactions; the cut-off energy for the plane-wave basis was 450eV.

3. Result and Discussion

3.1 Synthesis of NiO catalysts with different surface structures

Planar sheet NiO with a surface area of 127 m²/g was prepared through the calcination of hexagonal plates of Ni(OH)₂ that were synthesized with the hydrothermal method. As shown in Figures 4.1a and b, the average size of a planar sheet NiO is 50-100nm \times 50-100nm with a thickness of 3-4 nm. The exposed planar face is (110), evidenced by HAADF-STEM studies in Figure 4.1a-f. For instance, the measured lattice fringes crossing the thickness of the sheet in Figure

4.1c is the interplanar distance of (110) facets; thus, the surface of the planar sheet is (110). In addition, in Figure 4.1f, measured lattice fringes marked with red lines are the interplanar distance of two adjacent (200) faces; measured lattice fringes marked with blue lines are the interplanar distance of two adjacent (111) faces in the same HAADF-STEM image; these lattice fringe measurements show that the large plane of the planar sheet is the (110) facet.

Figures 4.1g and 4.1h are HAADF-STEM images of cubic NiO particles. The (100) surface was on the exposed surface of a cubic NiO particle, evidenced by the measured interplanar distances of (002) and (200) marked with yellow lines of the same cube in the same image (Figure 4.1h). As both (002) and (200) are parallel to the beam direction, the exposed surface of the cubic NiO particle is (100). The surface area of cubic NiO is quite low, 5-6 m²/g.

Figures 4.1i and 4.1j are images of octahedral NiO. The interplanar distances along (111) are 2.08Å. It suggests that the exposed surfaces of the octahedron are (111). The observed morphology of octahedral NiO is consistent with literature^{182, 191, 192}. The surface area of octahedral NiO is about 21.5 m²/g.

Obviously, the three types of NiO particles exhibit different but specific surface structures, i.e. (110) face on planar sheet NiO, (100) face on cube NiO and (111) face on octahedron NiO. Extensive studies of catalytic performances showed that these surfaces exhibit distinct catalytic performances, as discussed in the following sections.

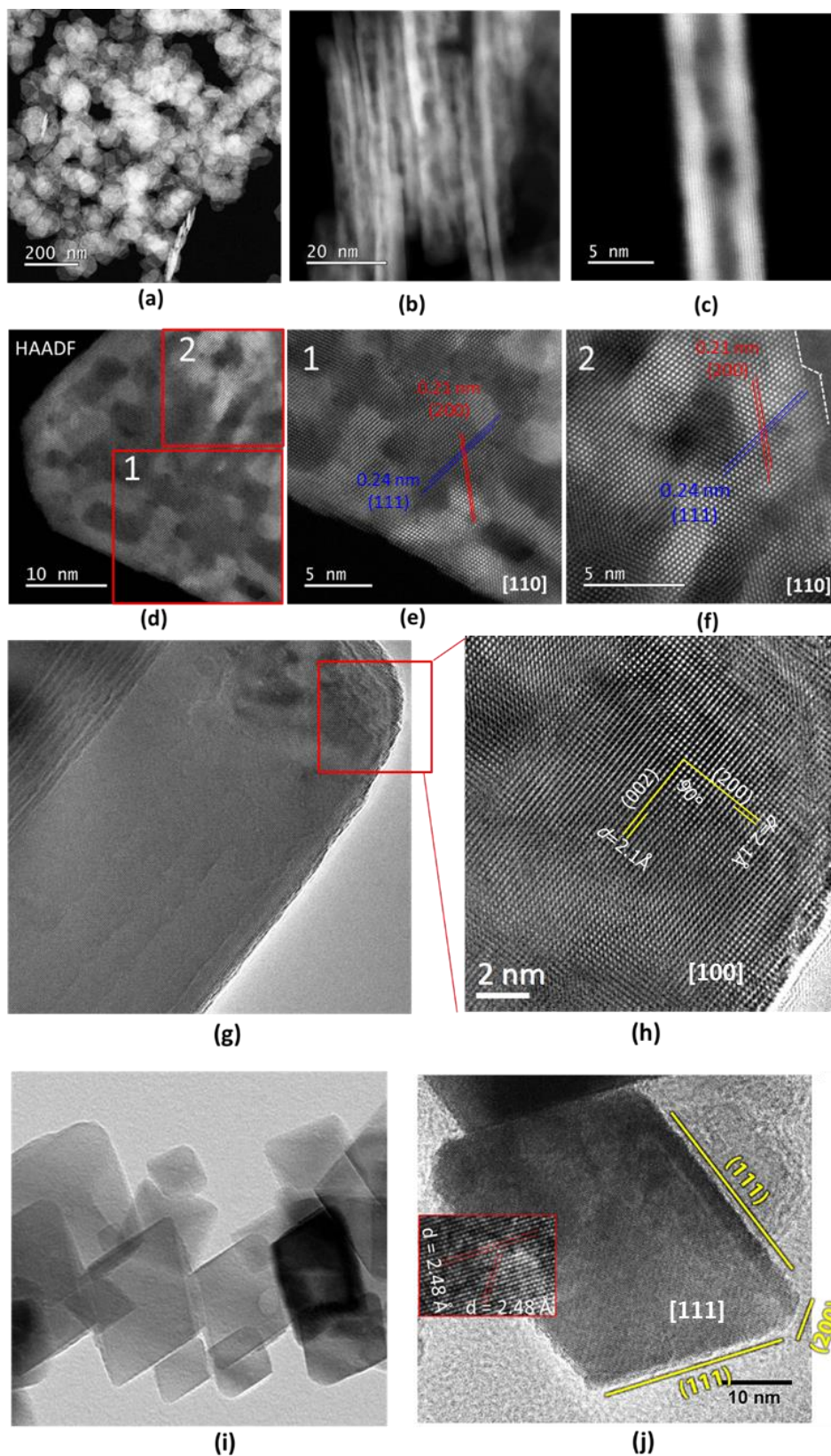


Figure 4.1 HAADF-STEM studies of morphology and lattice fringes of planar sheet NiO, cubic NiO, and octahedral NiO. (a) HAADF-STEM images of planar sheets NiO; the exposed face is (110). (b) HAADF-

STEM image of planar sheets NiO (side view). (c) HAADF-STEM image of a single planar sheet along the (110) direction which show the side view of a planar sheet. (d-f) HAADF-STEM images of planar sheet NiO; the exposed face is (110). (g, h) HAADF-STEM images of cubic NiO; the exposed face is (100). (i, j) HAADF-STEM images of octahedral NiO; the exposed face is (111).

3.2 Distinct catalytic performances of NiO(110), NiO(100) and NiO(111)

CH₄ Complete oxidation was chosen as a model reaction to explore differences in catalytic performances of (100) surface of planar sheet NiO, (100) surface of cubic NiO, and (111) surface of octahedral NiO. The detailed measurements of catalysis of three NiO are described in Appendix B. Conversion of CH₄ on (100) surface of planar sheet NiO (100 mg) is about 8% at 300°C, 56% at 350°C and reaches 99% at 375°C and 100% at 400°C (Figure 4.2d). However, (111) surface of octahedral NiO (500 mg) with similar surface area as 100 mg planar sheet NiO is not active for complete oxidation of CH₄ in the temperature range of 250-400°C (Figure 4.2d) under the same catalytic condition as planar sheet NiO. Here surface areas of 100 mg of planar sheet NiO and 500 mg of octahedral NiO are 12.7 m² and 10.75 m², respectively. The lack of catalytic activity on (111) surface of octahedral NiO and higher activity on (110) surface of planar sheet NiO clearly indicates the significant difference in catalytic activity between the two surfaces of NiO. In addition, as shown in Figure 4.3a, 100 mg of cubic NiO with a surface area of 0.5 m² does not show activity for this reaction at the temperature lower than 450°C under the same catalytic condition as planar sheet NiO, showing that (100) surface of cubic NiO is not active for CH₄ complete oxidation in this temperature range. These studies showed that only (110) surface of the planar sheet NiO is active for complete oxidation of CH₄. Figures 4.2a-c present structures of (110), (100) and (111) surfaces of NiO optimized with DFT. The coordination numbers of O atoms around a Ni cation on (110), (100) and (111) surfaces of NiO are 4, 5, and 6, respectively. Thus, only the surface with Ni atoms coordinating with four oxygen atoms is active for complete

oxidation of methane, suggesting a crucial role of the coordination environment of Ni in the activation of methane.

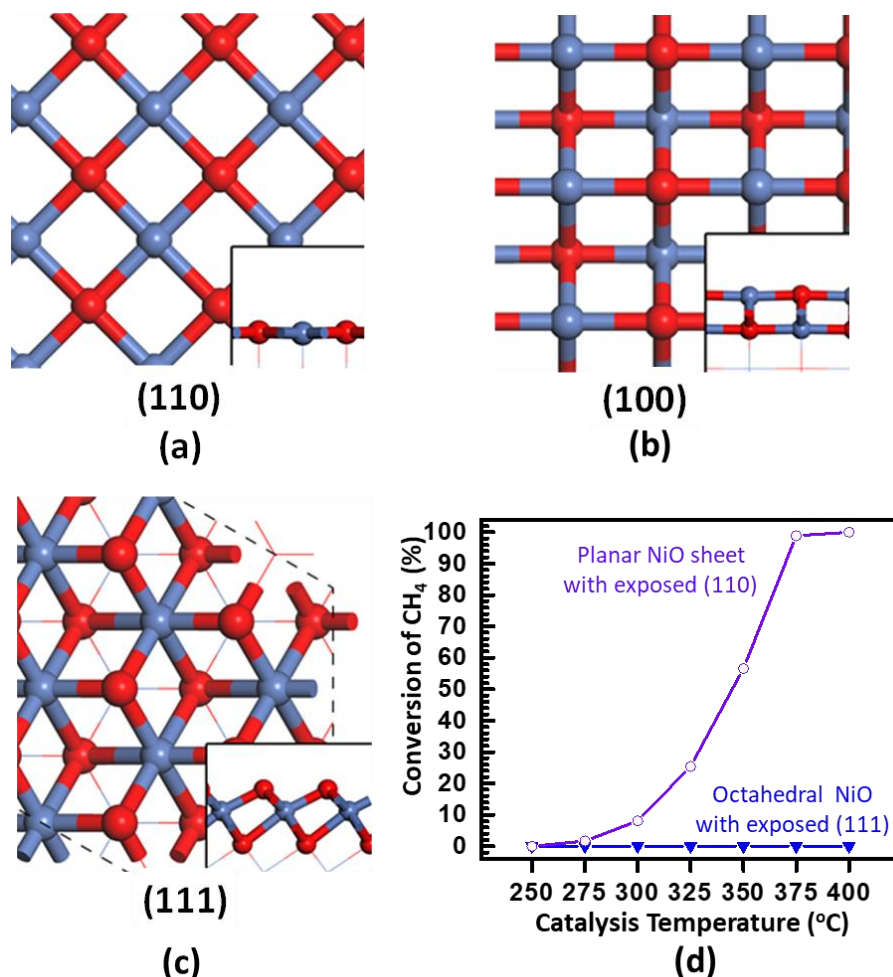


Figure 4. 2 Surface structures of NiO(110), NiO(100) and NiO(111) and experimentally measured catalytic performances of NiO. (a) (110) surface of planar sheet NiO; each Ni cation of (110) surface coordinates with four oxygen atoms. (b) (100) surface of cubic NiO; each Ni cation of (100) surface coordinates with five oxygen atoms. (c) (111) surface of octahedral NiO; each Ni cation of (111) surface coordinates with six oxygen atoms. (d) Conversion of planar sheets of NiO, cubic NiO and octahedral NiO as a function of temperature for complete oxidation of CH₄ in the temperature range of 250-500°C; 100 mg of planar sheet NiO and 500 mg of octahedral NiO was used in the measurement of catalytic performances.

To check the significance of the coordination number of O atoms around a Ni cation for complete oxidation of methane, the surface of cubic NiO was partially reduced by 5% H₂ at 225°C, 250°C, 275°C, or 300°C to generate oxygen vacancies on (100) surface of cubic NiO. These catalysts are named cubic NiO-H₂-225°C, cubic NiO-H₂-250°C, cubic NiO-H₂-275°C, and cubic

NiO-H₂-300°C. Upon such partial reductions, the potential catalytic performances of these catalysts were measured under the same condition as planar sheet NiO. As shown in Figures 4.3a-d, these partially reduced cubic NiO particles are active at temperatures higher than 375°C. Thus, a partial reduction of inert (100) surface of cubic NiO triggered the activity of methane complete oxidation for inert cubic NiO.

Ambient pressure X-ray photoelectron spectroscopy (AP-XPS), a surface-sensitive technique¹⁸³, was used to explore any potential differences on surfaces among cubic NiO without any partial reduction, cubic NiO-H₂-225°C, cubic NiO-H₂-250°C, cubic NiO-H₂-275°C, and cubic NiO-H₂-300°C. Details of the AP-XPS studies of surfaces of cubic NiO catalysts are described in Appendix B. Figure 4.3b presents the surface O/Ni atomic ratios of cubic NiO-H₂-225°C, cubic NiO-H₂-250°C, cubic NiO-H₂-275°C, and cubic NiO-H₂-300°C during catalysis. These O/Ni surface atomic ratio was calculated by setting the O/Ni surface atomic ratio of cubic NiO without any reduction to 1.0; then, the surface O/N atomic ratio of the four catalysts was calculated with

the equation, $\frac{A_{O\ 1s}(\text{cubic NiO upon partial reduction})}{A_{Ni\ 2p}(\text{cubic NiO upon partial reduction})} \div \frac{A_{O\ 1s}(\text{cubic NiO without any reduction})}{A_{Ni\ 2p}(\text{cubic NiO without any reduction})}$, where A_{O1s} and A_{Ni2p} mean peak areas of O 1s and

Ni 2p in ex-situ XPS spectra. For example, as shown in Figure 4.3b, the O/Ni surface ratio of cubic NiO that is pretreated in 5% H₂ at 225°C for 1 hour is 0.95. A cubic NiO experienced a reduction at higher temperatures in 5% H₂ for 1 hour exhibits a lower O/Ni surface atomic ratio during catalysis. In other words, these in-situ studies of surface O/Ni atomic ratio on cubic NiO suggest that more surface oxygen vacancies were generated at a higher temperature of reduction in 5% H₂. As a Ni cation of (100) surface of cubic NiO coordinates with 5 oxygen atoms, the Ni cation at an oxygen vacancy of (100) surface coordinates with only 4 oxygen atoms after losing one oxygen atom through partial reduction. Clearly, such a partial reduction turned the

stoichiometric (100) surface of cubic NiO to nonstoichiometric. This stoichiometric nature drove the observed catalysis from these catalysts (Figure 4.3a).

Significantly, as shown in Figure 4.3a-d, these partially reduced (100) surfaces of cubic NiO are active for complete oxidation of CH₄. TOFs of four modified catalysts (cubic NiO-H₂-225°C, cubic NiO-H₂-250°C, cubic NiO-H₂-275°C, and cubic NiO-H₂-300°C) at 400°C, 425°C and 450°C (catalysis temperatures) were calculated with method 1 (Figure 4.3c) and 2 (Figure 4.3d). In method 1, TOFs for complete oxidation of CH₄ on the four modified catalysts (Figure 4.3c) were calculated by dividing the number of converted CH₄ molecules per second with the number of oxygen vacancies in terms of Ni cations coordinating with 4 oxygen atoms. Thus, it is expected that TOFs at 450°C on the four catalysts (the four red bars in Figure 4.3c) are very similar, although their O/Ni surface ratios in terms of density of oxygen vacancies are quite different as shown Figure 4.3b. The nearly same TOFs of the four modified cubic NiO catalysts at the same temperature, such as 450°C, suggests that these four catalysts have the same type of active sites for complete oxidation of CH₄. On the other hand, at the same catalysis temperature such as 450°C, 100 mg of cubic NiO with a higher density of oxygen vacancies in terms of lower O/Ni surface atomic ratio (Figure 4.3b) exhibited higher conversion of CH₄ as shown in Figure 4.3a. For instance, conversions of CH₄ on cubic NiO-H₂-300°C with O/Ni ratio of 75% and cubic NiO-H₂-225°C with O/Ni ratio of 94% at 450°C are 18.3% and 3.5%, respectively. The correlation between surface densities of oxygen vacancies of the four catalysts and their activities suggests that Ni cations at oxygen vacancies are active sites for this reaction.

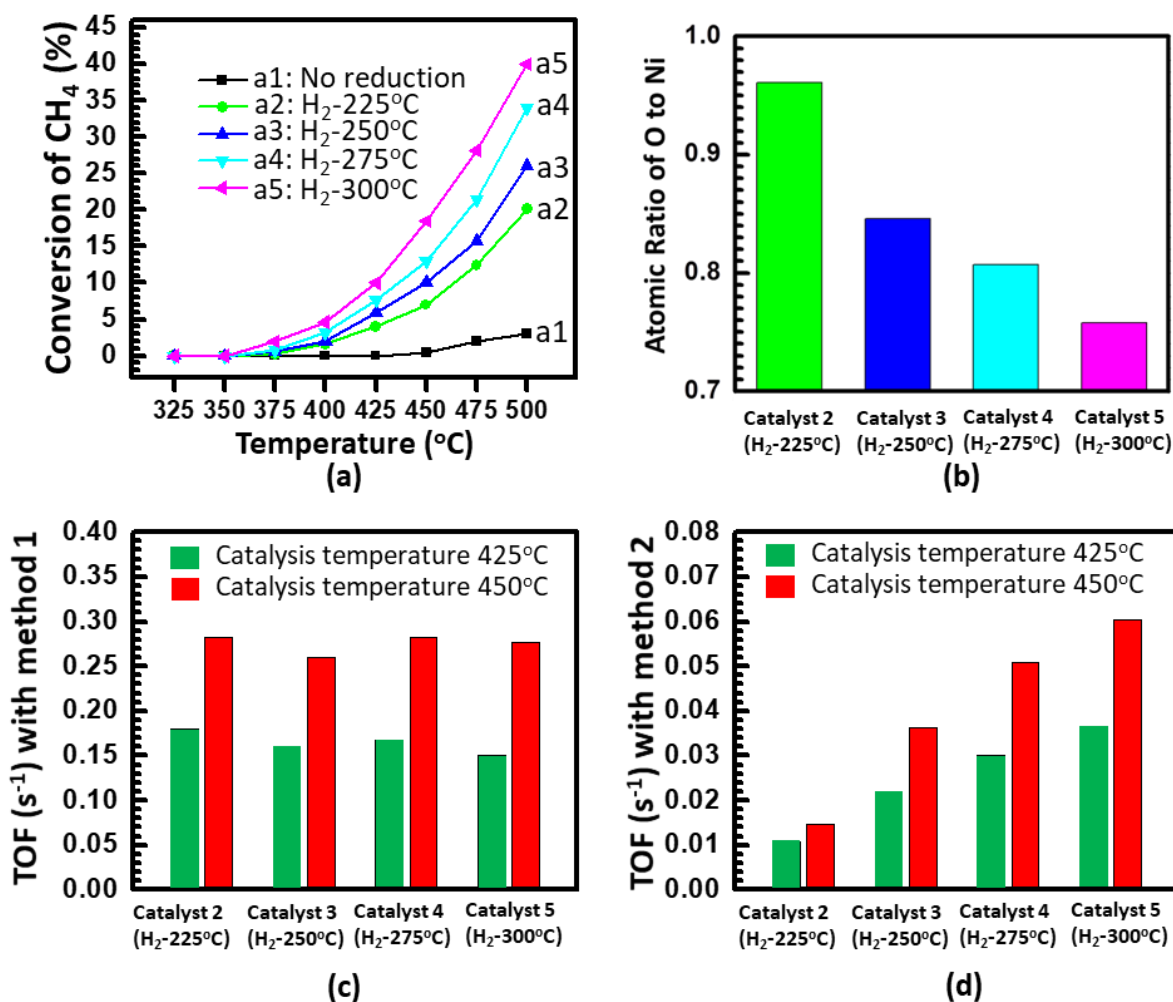


Figure 4. 3 Catalysis on the partially reduced surface of cubic NiO and their catalytic activity. (a) Catalytic performances of 100 mg of cubic NiO catalyst which was pre-reduced in 5% H₂ for 1 hour at different temperatures (225°C, 250°C, 275°C, and 300°C); thus, the four catalysts are named, cubic NiO-H₂-225°C (green), NiO-H₂-250°C (blue), NiO-H₂-275°C (cyan), and NiO-H₂-300°C (magenta). (b) Measured atomic ratios of O/Ni of the four catalysts. (c) List of TOFs of the four catalysts at catalysis temperatures 425°C and 450°C; these TOFs were calculated with Method 1 by dividing the number of consumed CH₄ molecules at a specific temperature such as 400°C or 450°C with the number of Ni atoms in oxygen vacancies on the surface measured with XPS; green and red bars are TOFs at 425°C and 450°C, respectively. (d) List of TOFs of the four catalysts at catalysis temperatures 425°C and 450°C; these TOFs were calculated with Method 2 by dividing the number of consumed CH₄ molecules at a specific temperature such as 400°C or 450°C with the number of all nickel cations on the surface measured with XPS.

Upon removal of a portion of oxygen atoms on the surface through partial reduction, some Ni cations only bonded to 4 oxygen atoms. Thus, the nonstoichiometric (100) surface of NiO consists of both Ni cations coordinating with 5 oxygen atoms and Ni cations coordinating with 4

oxygen atoms. Assuming both two types of Ni cations were active for this reaction, TOFs of the four catalysts (cubic NiO-H₂-225°C, cubic NiO-H₂-250°C, cubic NiO-H₂-275°C, and cubic NiO-H₂-300°C) were calculated by dividing the number of converted CH₄ molecules per second by the total number of the two types of Ni cations (Method 2). Figure 4.3d lists these “TOF” values calculated with Method 2. As these TOFs for catalysis on these four tailored cubic NiO catalysts at different temperatures, such as 450°C (red bars in Figure 4.3d), are quite different, the assumption that both Ni cations coordinating with 4 oxygen atoms and those with 5 oxygen atoms are active sites is not reasonable. Comparison of Figure 4.3c and Figure 4.3d confirmed that the active sites on (100) surface of cubic NiO for CH₄ complete oxidation are Ni cations next to oxygen vacancies, coordinating with 4 oxygen atoms instead of 5. This finding is highly consistent with the high activity of (110) surface of planar sheet NiO where each Ni cation coordinates with four oxygen atoms. The introduction of activity of Ni cations coordinating with 4 oxygen atoms on nonstoichiometric (100) surface of cubic NiO is further supported by our extensive DFT calculations presented in the next section.

3.3 The crucial role of the coordination environment of Ni cations on NiO in CH₄ complete oxidation

To confirm that Ni atoms on (110) surface of planar sheet NiO coordinating with 4 oxygen atoms directly participate in CH₄ complete oxidation, the surface of a planar sheet NiO catalyst performing catalysis at different temperatures was tracked via AP-XPS. Photoemission features in terms of XPS peaks of Ni 2p, O 1s, and C 1s were collected (Figures 4.4a-c). As shown in Figure 4.4a, the main peak of Ni 2p_{3/2} at 853.7 eV and the satellite peak of Ni 2p_{3/2} at 860.9 eV do not shift at all along with the increase of catalysis temperature.

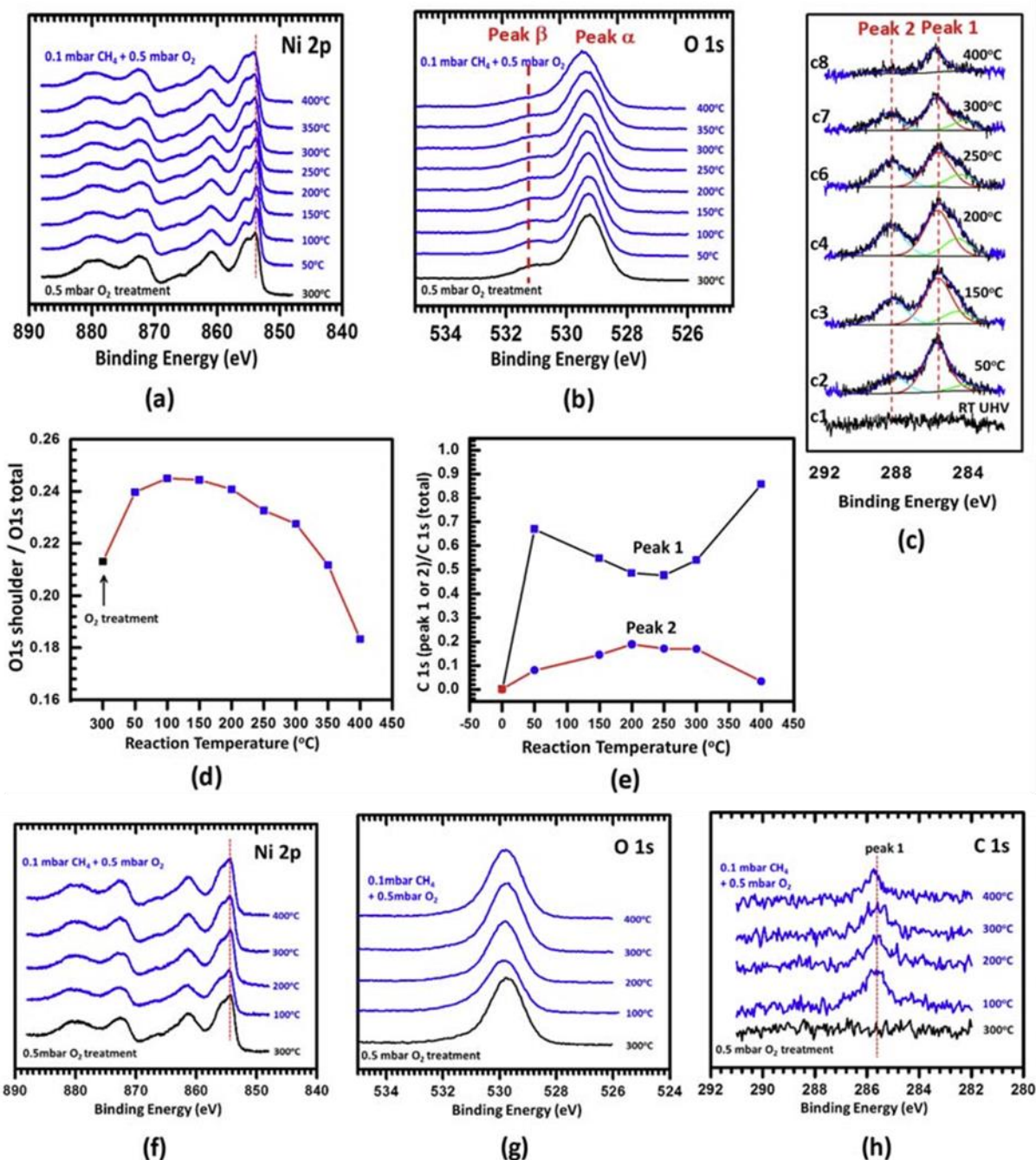


Figure 4. Operando studies of the surface of planar sheet NiO and cubic NiO during catalysis. (a) Ni 2p of planar sheet NiO in the temperature range of 25°C-400°C in the mixture of CH₄ and O₂. (b) O 1s of planar sheet NiO in the temperature range of 25°C-400°C in the mixture of CH₄ and O₂; the shoulders were marked with red dash-line. (c) C 1s of planar sheet NiO in the temperature range of 25°C-400°C in the mixture of CH₄ and O₂. Spectra were deconvoluted to peaks 1 and 2 and a minor peak at 284.3eV. (d) Plot of fraction of area of O 1s shoulder to the total area of O 1s photoemission feature. (e) Fractions of areas of peaks 1 and 2 of C 1s in total areas of peaks 1 and 2 as a function of reaction temperature. (f-h) Ni 2p, O 1s and C 1s of cubic NiO in the same temperature range of 25°C-400°C in the same mixture of CH₄ and O₂ as planar NiO sheets.

Before the introduction of the reaction mixture, O₂ was introduced to react with potential carbon contaminants on catalyst surface to form CO or CO₂, by which surface carbon contaminants, if only, were removed. The lack of carbon species on the surface of catalysts was evidenced by the lack of C 1s photoemission feature (Figure 4.4c). Upon the preparation of a carbon-free surface of planar sheet NiO, the mixture of CH₄ and O₂ with a molar ratio of 1:5 was flowing to the reactor in the AP-XPS system. While the mixture of CH₄ and O₂ was flowing through the catalyst, the peak at 285.6eV, labeled as peak 1 in Figure 4.4c, was clearly observed from the catalyst surface at 50°C (Figure 4.4c2). As CH₄ is the only reactant containing the carbon atom, peak 1 must result from activation of CH₄ on Ni cation or oxygen anion. Based on literatures,¹⁹³⁻¹⁹⁵ the peak 1 at 265.6eV observed in Figure 4.4c can be assigned to a methyl species bound to the catalyst surface. This suggests that the high capability of nickel cations in surface of a NiO for the activation of C-H bond of methane.

Other than peak 1, another peak at 288.4eV, labeled as peak 2, was clearly observed at 50°C (Figure 4.4c2). A similar C 1s peak at 288.5 eV was observed at 60°C on Co_{3-x}Ni_xO₄ in the mixture of CH₄ and O₂ in our previous work^{193, 194}, attributed to C 1s peak of an intermediate; that high binding energy peak at 288.5 eV was assigned to the photoemission features of format-like species formed on Co_{3-x}Ni_xO₄^{193, 194}. Notably, the intensity of peak 2 in Figure 4.4c changes along with the increase of catalysis temperature. The evolutions of fractions of peaks 1 and 2 of C 1s spectra were given in Figure 4.4e. The fraction of peak 2 increased first and then decreased along with the increase of catalysis temperature, exhibiting a volcano-like evolution. Such an evolution of C 1s of peak 2 (red line in Figure 4.4e) is similar to the evolution of O 1s (Figure 4.4d). Such similarity suggests that one or more intermediates containing both O and C atoms were formed and accumulated on the catalyst surface at a relatively low temperature. When they gained enough

thermal energy at higher temperatures, they transited to the next intermediate or final product. The intermediate cannot transform to the next intermediate or product at low temperatures due to the relatively high activation barrier of that rate-determining steps; sometimes, it is even called a “stable” intermediate. Based on the evaluated turning point of the intensity of peak 2 in Figure 4.4e from studies of AP-XPS, the temperature where the intermediates can transform to next intermediate till product molecules is about 250°C that is consistent with the catalytic temperature 300°C where product molecules CO₂ started to form.

Parallel studies of (100) surface of stoichiometric cubic NiO (without any reduction in 5% H₂) were performed with AP-XPS under the exact same condition as planar sheet NiO. Different from planar sheet NiO, only a weak C 1s peak at 285.6 eV (Figure 4.4h) was observed at 100°C, and its intensity and peak position remained nearly no change in the temperature range of 100°C-400°C. On (100) surface of cubic NiO (Figure 4.4h), the obvious lack of photoemission feature of intermediate at 288.5eV (peak 2) observed on planar NiO sheets (Figure 4.4c) illustrates that (100) of cubic NiO without any reduction could not take the reaction pathway of CH₄ complete oxidation adopted by (110) of planar NiO sheets. In fact, cubic NiO without any partial reduction is not active at all for complete oxidation of CH₄ in the temperature range of 300-425°C. The observed peak at 285.6eV in Figure 4.4h was assigned to a spectator. Thus, the quite different surface chemistry in terms of surface species (spectator or intermediate) formed on (100) surface of cubic NiO (without pre-reduction in 5% H₂) in contrast to (110) surface of planar sheet NiO confirms that Ni cations coordinating with 4 oxygen atoms instead of Ni cations coordinating with 5 oxygen atoms are active for CH₄ complete oxidation.

Isotope ¹⁸O atoms-labeled planar sheet Ni¹⁶O_{1-x}¹⁸O_x was used to perform complete oxidation of CH₄. A mixture of CH₄ and ¹⁶O₂ was introduced to the reaction cell that was loaded the catalyst,

$\text{Ni}^{16}\text{O}_{1-x}^{18}\text{O}_x$. Gas after the reaction was delivered to the chamber of mass spectrometer through a capillary tube of quartz with an internal diameter of 50 μm . Isotope-labeled product molecules containing ^{18}O atom, $\text{C}^{16}\text{O}^{18}\text{O}$ ($m/e=46$) and H_2^{18}O ($m/e=20$) were clearly observed when $\text{Ni}^{16}\text{O}_{1-x}^{18}\text{O}_x$ performed the catalysis at a temperature $\geq 260^\circ\text{C}$. It clearly showed that surface lattice oxygen atoms of (100) surface of planar sheet NiO directly participated in this catalysis, further supported by DFT calculations in the next section. The direct participation of surface lattice oxygen atoms was also confirmed by another set of experiments in which a mixture of $^{18}\text{O}_2$ and CH_4 was introduced to the surface of planar sheet NiO, and then $\text{C}^{16}\text{O}^{18}\text{O}$ ($m/e=46$) and H_2^{18}O ($m/e=20$) were formed during catalysis.

3.4 Mechanistic understanding of coordination number-dependent catalysis at a molecular level

To understand the origin of coordination number-specific catalytic activity on the surface of NiO, elementary reaction steps and possible reaction pathways of methane complete oxidation on (110) and (100) surfaces of NiO were investigated through DFT calculations.

Methane complete oxidation on (110) of a planar sheet NiO begins with the dissociative adsorption of first C-H of CH_4 with an activation barrier of 0.42 eV. The geometry of transition state for activating the first C-H of CH_4 on NiO(110) is shown in Figure 4.5a1, in which C atom of a CH_3 binds to a Ni cation coordinating with 4 oxygen atoms and H atom binds to a surface lattice oxygen atom, respectively. After the dissociation of methane, the C atom of $-\text{CH}_3$ is bound with two Ni atoms through a bridge-like binding configuration, as shown in Figure 4.5a2 and Figure 4.6a1.

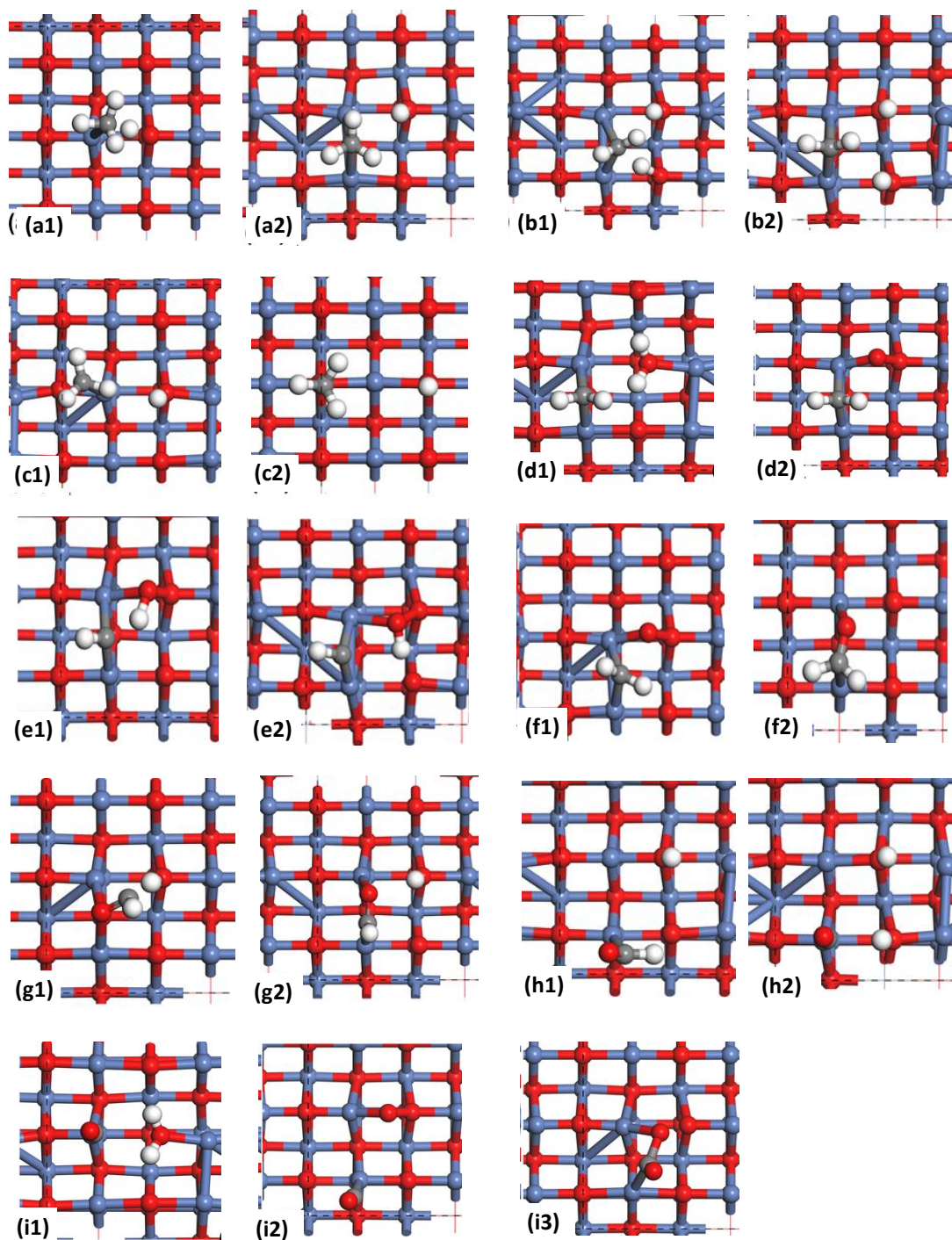


Figure 4. 5 Geometries of transition states and final states of the transformation of CH_4 and O_2 to CO_2 and H_2O on (110) surface of planar sheet NiO. (a1 and a2) Structures of transition state and final state for cleaving the first C-H of CH_4 . (b1 and b2) Structures of transition state and final state for dissociating CH_3 to CH_2 and H. (c1 and c2) Structures of transition state and final state for oxidizing CH_3 to CH_3O . (d1 and d2) Structures of transition state of hydrogen transfer and final state of water desorption and oxygen molecule adsorption. (e1 and e2) Structures of transition state and final state for dissociating CH_2 to CH and H. (f1 and f2) Structures of transition state and final state for oxidizing CH_2 to CH_2O . (g1 and g2) Structures of transition state and final state for CH_2O dehydrogenation to CHO. (h1 and h2) Structures of transition state and final state for CHO dehydrogenation to CO and H. (i1, i2, and i3) Structures of transition

state and final state for water desorption and oxygen molecule adsorption, and transition state of CO oxidation to form CO₂.

The formed CH₃ could further dissociate to CH₂ and H or be oxidized to CH₃O. A further dissociation of CH₃ is most likely found on metal oxides such as nickel doped cobalt oxide¹⁹⁶, while oxidization of CH₃ is a common path to transfer to the next intermediate in the oxidation of CH₄ on metal catalysts^{197, 198}. Here both dissociation of CH₃ to CH₂ and H and oxidation of CH₃ to CH₃O were considered for (100) surface of NiO. The activation barriers and enthalpy changes of the two possible paths in terms of dissociation and oxidation for transforming CH₃ were calculated. The optimized geometries of the transition states and final states for the two paths are presented in Figures 4.5b and c, respectively. DFT calculations show that the activation barrier for directly dissociating C-H of CH₃ is 1.04 eV (Figure 4.6b), and the activation energy of oxidation of CH₃ is 1.87 eV. Therefore, dissociation of C-H of CH₃ to CH₂, also called dehydrogenation, is a kinetically favorable pathway on (110) of NiO.

Upon the formation of CH₂ (Figure 4.6a2), both further oxidation of CH₂ to form CH₂O and dissociation of C-H of CH₂ to form CH were investigated. The specific geometries of transition states and final states are presented in Figures 4.5e and f. The activation barriers for the oxidation and dissociation are 0.43 eV and 1.18 eV, respectively; thereby, the oxidation of CH₂ to CH₂O (Figure 4.6a4) is the favorable path for activating CH₂ on (110) of NiO in contrast to dissociation of CH₂ to form CH.

For the formed CH₂O, it is found that a further dehydrogenation to CHO and H is favorable thermodynamically and kinetically, with a barrier of only 0.05 eV and enthalpy change of -1.03 eV, respectively (Figure 4.6b). The transition state for dehydrogenation of CH₂O to CHO and H is shown in Figure 4.5g1 in which one H atom of CH₂O transfers to a surface lattice O atom on (100) of NiO. Upon the formation of CHO (Figures 4.5g2 and 4.6a5), dehydrogenation of the

CHO is found to be not as easy as CH₂O in the early step. As shown in Figure 4.5h, the dissociation of the C-H bond of CHO to CO and H on (100) of NiO is facilitated by a lattice oxygen of (110) surface. This step has the highest activation barrier among all steps of this pathway on (110) surface, 1.08 eV (Figure 4.6b), suggesting that the CHO should be a “stable” intermediate which is formed at low temperature but is only able to be transformed to next intermediate or product at a reasonably high temperature. That is consistent with the high binding energy of peak 2 of C 1s observed in AP-XPS studies (Figure 4.4c).

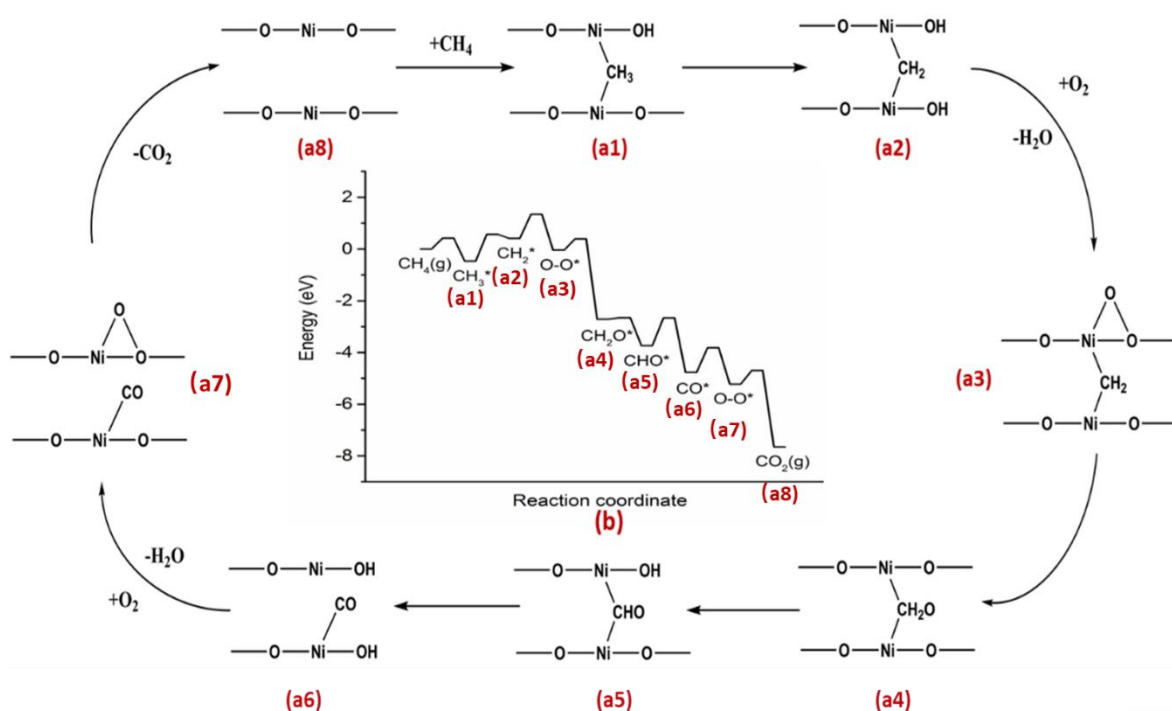


Figure 4. 6 The most favorable reaction pathway of CH₄ complete oxidation on (110) surface of planar sheet NiO proposed by DFT calculations (a) and its corresponding energy profile (b).

Based on these calculations, Figures 4.6a and b present the most favorable pathway of CH₄ complete oxidation on (110) surface of planar sheet NiO and its corresponding energy profile, respectively. The biggest energy drops in the overall pathway are the two oxidation steps, referring to the oxidation of CH₂ to CH₂O and the oxidation of CO to CO₂ (Figure 4.6b). The highest activation barrier among all elementary steps of the catalytic cycle is 1.08 eV in the dissociation

of CHO to CO and H. Furthermore, all activation barriers in the most favorable pathway in Figure 4.6a are less than 1.08, showing that (110) surface of NiO is quite active for CH₄ complete oxidation as experimentally observed in Figure 4.2d. As Ni cations of (110) of NiO are the sites of CH₄ activation, Ni cation coordinating with 4 oxygen atoms is the active site of CH₄ complete oxidation.

Other than the molecular mechanism of CH₄ complete oxidation on (110) surface of NiO, reaction pathway on (100) surface of cubic was explored. Similar to (110) surface of NiO, oxidation of CH₄ starts with methane activation on (100) surface of NiO. The geometries of the transition state and the final state for activating the first C-H bond of CH₄ are shown in Figures 4.7a1 and a2, respectively. The activation energy and enthalpy change of this step are 1.41eV and 1.38eV, respectively (Figure 4.8b). Thus, activation of the first C-H bond of CH₄ through dissociation of the C-H bond on (100) of NiO is quite unfavorable kinetically.

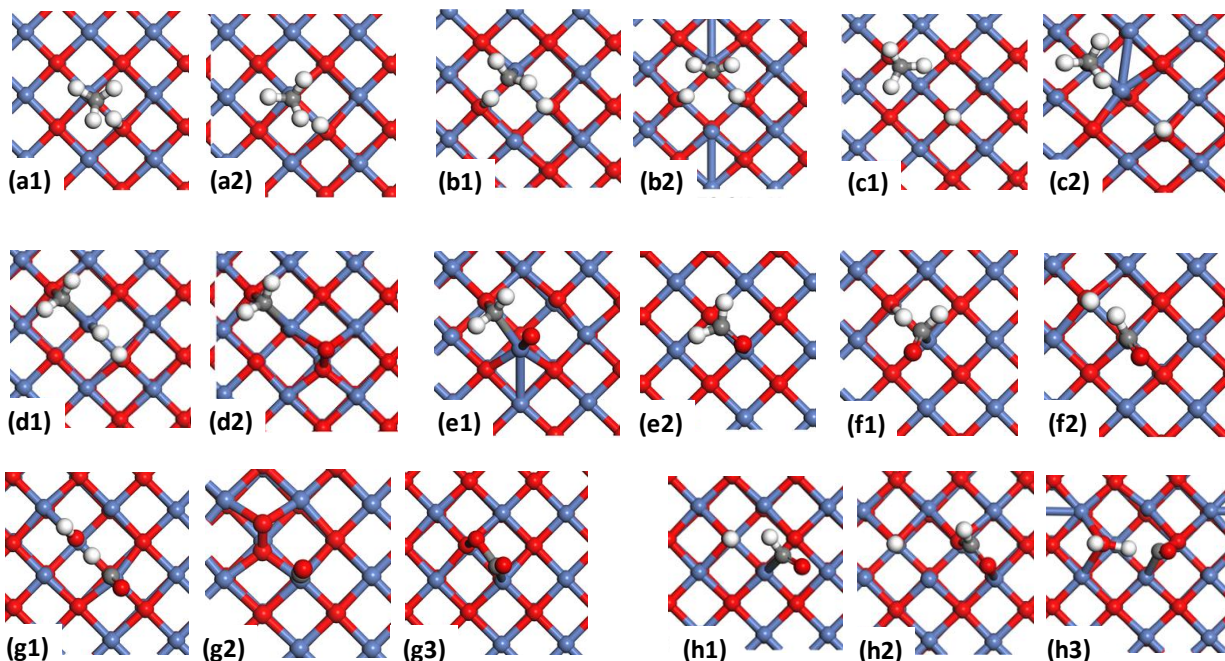


Figure 4. 7 Geometries of transition states and final states of CH₄ complete oxidation on (100) surface of cubic NiO. (a1 and a2) Structures of transition state and final state for activation of CH₄. (b1 and b2) Structures of transition state and final state for dissociating CH₃ to CH₂ and H. (c1 and c2) Structures of transition state and final state for oxidizing CH₃ to CH₃O. (d1 and d2) Structures of transition state of hydrogen transfer and final state of CH₃O dehydrogenation. (e1 and e2) Structures of transition state and

final state for oxidizing CH_2 to CH_2O . (f1 and f2) Structures of transition state and final state for dehydrogenation of CH_2O . (g1, g2 and g3) Structures of transition state of CHO dehydrogenation, final state of water desorption and oxygen molecule adsorption, and transition state of CO oxidation of pathway A (h1, h2 and h3) Structures of transition state and final state of CHO oxidation, and transition state of CHO_2 dehydrogenation.

The stabilities of surface lattice oxygen atoms of (100) and (110) surfaces of NiO in respect to a gas phase oxygen molecule were studied. It is found that the stability of a surface lattice oxygen atom of (100) of NiO is much higher than that of (110) of NiO since the energy of surface lattice oxygen atom on (100) is lower than (110) by 2.09eV. Thus, the low activity of (100) of NiO in CH_4 complete oxidation likely results from the inertness of its surface lattice oxygen. As shown later, the inertness of these surface lattice oxygen atoms of (100) of NiO makes them not readily participate in these dehydrogenation steps since binding H atom to surface lattice oxygen atoms can largely assist these dehydrogenation steps (Figure 4.7e-g). However, the surface lattice oxygen atoms of (110) of NiO largely assisted those dehydrogenation steps on (110) surface of NiO. This is understandable since each O atom on the inert (100) surface of NiO coordinates with 5 Ni atoms but each O atom on (110) surface of NiO coordinates with only 4 Ni atoms.

After the formation of CH_3 , the CH_3 could be dehydrogenated or oxidized on (100) of NiO. The two potential paths of transforming CH_3 on (100) of NiO are not favorable due to their extremely high barriers of 2.37 eV for dehydrogenation and 2.28 eV for oxidation, respectively. Figures 4.7b and c present the transition and final states of the dehydrogenation of CH_3 to CH_2 and H and the oxidation of CH_3 to CH_3O on (100) of NiO. DFT calculation shows that there are two potential paths to transform CHO to CO_2 , namely the path A and path B. In path A, the CHO firstly dissociates into CO and the H atom from CHO couples with the surface hydroxyl group of the surface to form one H_2O molecule. Then, an oxygen molecule is adsorbed and dissociated on the surface to oxidize the CO into CO_2 (Figure 4.7g2). In path B, the oxidation of CHO is performed

through a transition state, O-CHO. Then, the O-CHO dehydrogenates to form CO₂. From the calculated energy profile, path A is kinetically favorable over path B, so that path A was chosen to achieve the overall transformation as displayed in Figure 4.8b.

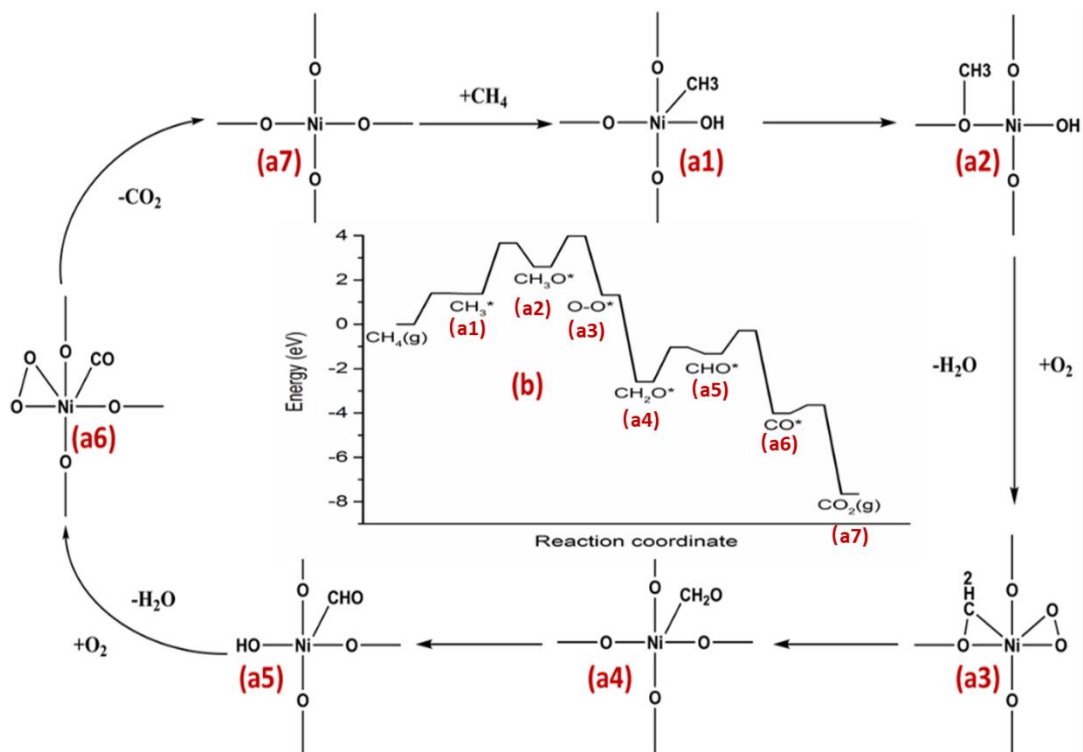


Figure 4. 8 The most favorable pathway of CH₄ complete oxidation on (100) surface of cubic NiO proposed by DFT calculations (a) and its corresponding energy profile (b).

The energy profiles of (100) of NiO and (110) of NiO in the landscape of free energy at 400°C were compared. From the energy profiles and the calculation results presented above, the following conclusions can be drawn. (110) surface of a planar sheet NiO is much more active than (100) surface of NiO for complete oxidation of methane. On (110) of NiO, all the barriers are lower than 1.10 eV. However, most of the activation barriers of C-H on (100) of NiO are quite high, especially for the dehydrogenation steps with barriers of 2.37 eV. The low activity of (100) of NiO is actually correlated with the high stability of surface lattice oxygen atoms. Compared to (110) of NiO, surface lattice oxygen atoms of (100) of NiO coordinating with 5 Ni atoms cannot

assist the dehydrogenation of CH_x steps due to their high stability. The activation energy of methane activation on (110) of planar sheet NiO is only 0.42 eV, which is much lower than most catalysts reported catalysts.^{197, 199-204} Thus, planar sheet NiO, mainly exposed (100) surfaces, is expected to be an excellent candidate for catalyzing the complete oxidation of methane.

4. Conclusion

In this work, three NiO catalysts with different surface structures, including (110) of planar sheet NiO, (100) of cubic NiO, and (111) of octahedral NiO, exhibited distinguished catalytic activity in CH_4 complete oxidation.

Experimental explorations demonstrated that the activities of three NiO catalysts strongly depended on the number of coordinated oxygen atoms around a Ni cation on the surface of NiO. Ni cation coordinating with four oxygen atoms of (110) surface of planar sheet NiO is highly active for the complete oxidation of methane, reaching almost 100% conversion of methane at 375°C or higher temperature. In contrast, there is a lack of activity of CH_4 complete oxidation on (111) surface of octahedral NiO where each Ni cation coordinates with six oxygen atoms. Moreover, the conversion of methane on (100) surface of cubic NiO is increased to approximately 40% by modifying the coordination environment of Ni atoms on this surface via the partial reduction in H_2 . Computational studies indicated that a Ni cation coordinating with four oxygen atoms on (110) of planer sheet NiO is the active site to catalyze elementary steps of CH_4 complete oxidation with lower activation barriers than those on (100) of cubic NiO on which a Ni cation coordinates with five oxygen atoms.

Consequently, this work demonstrates the coordination number-dependent catalysis of transition metal oxide and suggests a new method of designing catalysts through the modification of the coordination environment around a cation on the surface of transition metal oxide.

Contributions of the project:

The catalytic performances of prepared catalyst were mainly done by Yuting Li; Characterizations of catalysts were done by Luan Nguyen and collaborators from Arizona State University; DFT calculation was done with collaboration work from Queen's University.

Chapter 5: Catalytic oxidation of ethane to carboxylic acids in the liquid phase at near room temperature and near ambient pressure

1. Introduction

Ethane is the second most abundant component in shale gas^{5, 205}. Catalytic transformation of ethane to intermediates such as carboxylic acids is significant for chemical industries since it is an alternative approach for filling chemical feedstock of chemical industries. That is particularly important under the circumstance of switching raw materials of chemical industries from crude oil to shale gas components. Partial oxidation^{30, 206-208}, steam reforming²⁰⁹⁻²¹³, dry reforming²¹⁴⁻²¹⁶, and oxidative dehydrogenation (ODH)^{50, 51, 217-220} of ethane at high temperatures were studied for utilizing this inexpensive resource^{44, 56, 65, 221}. These catalytic transformations are typically performed at a temperature higher than 600°C^{50, 51, 217-220, 222, 223}, thus requiring a large energy supply. Other than these processes, an alternative transformation of ethane is direct dehydrogenation (DDH) to produce ethylene^{224, 225}; unfortunately, due to the endothermic nature of this reaction, a higher catalysis temperature (>750°C) is requested for achieving a reasonable conversion.

Compared to these high-temperature catalytic transformations, low-temperature oxidation leading to the production of organic oxygenates such as alcohol and the carboxylic acid is an alternative process since low-temperature oxidation is thermodynamically allowed.^{53, 65, 226} Hutchings and coworkers reported that partial oxidation of ethane to oxygenates on 2.5%Fe/ZSM-5(30) could convert 56% ethane to oxygenates; the TOF of their catalysis at 50°C is 150.7 mol of total products per mol of metal per hour⁵³. A significant advantage of the low-temperature oxidation process is its inexpensive footprint of the transformation of ethane without using any high-temperature reactors⁶⁵.

Formic acid and acetic acid are important intermediate compounds of chemical industries. For instance, formic acid is a preservative and antibacterial agent used in the livestock feed and the substitution of mineral acids for various cleaning products²²⁷⁻²³⁰. Acetic acid is widely applied in several important fields including the medical use in cervical cancer screening²³¹, the production of ether, the synthesis of vinyl acetate monomer and the formation of vinegar. Currently, acetic acid is mainly produced through thermal catalysis and fermentation. More than 75% of acetic acid was produced from carbonylation of methanol at around 200-300°C^{25,230}, which reached 90% yield of acetic acid under 6.0-8.0 MPa CO with cobalt organic complexes produced by BASF and even 99% yield of acetic acid under 3.0-6.0 MPa CO when the Monsanto process catalyst, rhodium organic complex was used. Although the production of methanol from syngas is performed at an intermediate temperature, the reactant syngas is usually produced at high temperatures through steam reforming of methane or partial oxidation of methane^{202,206,212,232}. It would be ideal if formic acid or acetic acid could be directly synthesized from shale gas components, methane or ethane without the involvement of any high-temperature catalysis.

Thus, this work explored the synthesis of carboxylic acid at near room temperature by using H₂O₂ instead of O₂ was used as the oxidant to transform ethane into oxygenates. The single-atom Rh catalyst was prepared and used to activate the ethane. It was found that approximately 37% of ethane was converted into acetic acid and formic acid at 50°C with 1.5 bar ethane. It is expected that the single-atom catalyst could exhibit a good performance of ethane oxidation at near room temperature and near ambient pressure.

2. Experiment

2.1 Synthesis of catalysts

H-ZSM-5 with loaded Rh cations was prepared with a method integrating vacuum pumping and a following incipient wetness impregnation (IWI). H-ZSM-5 was prepared by annealing NH₄-ZSM-5 (SiO₂:Al₂O₃ = 23:1, Alfa Aesar) at 450°C in air for 12h. Rhodium cations were introduced into the micropores of H-ZSM-5 through ion exchange in IWI and the followed calcination. Before anchoring single Rh atoms on the wall of micropores of H-ZSM-5, H-ZSM-5 was loaded to a sealed flask. The air in the flask was evacuated through a vacuum pump to decrease the pressure in the flask from 760 Torr to 0.75 Torr. A certain amount of Rh(NO₃)₃ solution was slowly added to H-ZSM-5 by a syringe pump. The needle of the syringe pump was inert to reach the bottom of the flask containing a certain amount of ZSM-5 powder so that the injected solution can diffuse to micropores of ZSM-5 readily in the vacuum. Then, the H-ZSM-5 containing Rh(NO₃)₃ was dried at room temperature for 12h. The dried powder, H-ZSM-5 loaded with a certain amount of Rh cations was calcined in air at 550°C for 3h with a ramping rate of 2°C/min. 2.0wt% Rh/ZSM-5 were prepared with the same method. The loading is defined as the mass ratio of Rh of the added Rh(NO₃)₃ solution to the aluminosilicate of H-ZSM-5. As Brønsted acid sites of H-ZSM-5 are singly dispersed on the internal surface of micropores of H-ZSM-5, it is expected that these Rh³⁺ sites anchored through ion exchange are dispersed on the wall of micropores of ZSM-5 in the format of a single atom.

2.2 Characterization of catalysts

Crystal structures of the prepared H-ZSM-5 and 0.10wt%Rh/ZSM-5 were checked with X-ray powder diffraction (XRD) on a Bruker diffractometer equipped with a Mo sealed-tube X-ray

source, a graphite monochromator, Mono Cap collimator and a SMART APEX charge-coupled device (CCD) area detector. Morphologies of parent H-ZSM-5, 0.10wt%Rh/ZSM-5 and 2.0wt%Rh/ZSM-5 were examined with transmission electron microscopy (TEM) (FEI, Titan 80-300). Surface compositions of catalyst particles of 0.10wt%Rh/ZSM-5 and 2.0wt%Rh/ZSM-5 were characterized with X-ray photoelectron spectroscopy on a PHI5000 VersaProbe Spectrometer using monochromatic Al K α as X-ray source. Surface area and pore volume of H-ZSM-5 and 0.10wt%/ZSM-5 were measured by BET instrument (Quantachrome Autosorb iQ). Rh concentrations of catalysts and the leaching amount of Rh in solution after catalysis were detected through ICP-AES (JY 2000 2 made by HORIBA) by building standard curves. Details of ICP tests are described in Appendix C.

XANES and EXAFS studies was performed at SSRL national lab with NSLS-II. About 100mg 0.10wt%Rh/ZSM-5 samples were loaded to the EXAFS reactor. The reactor was specifically made for EXAFS studies readily installed between synchrotron radiation and detectors of XANES and EXAFS. The EXAFS data of 0.10wt%Rh/ZSM-5, rhodium metal foil, and rhodium oxide nanoparticles supported on alumina were analyzed by Demeter software^{153, 233}.

2.3 Measurements of catalytic performances

Oxidation of ethane by hydrogen peroxide with 0.10wt%Rh/ZSM-5 was performed in a 25 ml stainless steel high-pressure and high-temperature Parr reactor (Series 4790, Parr). It is a batch reactor sealing gas through a Viton gasket. A glass beaker with a volume of 15ml was placed in the Parr reactor. 10 ml aqueous solution of H₂O₂ (typically 3.4% w/w containing 10mmol H₂O₂) was prepared by diluting a commercial solution of H₂O₂ (30% w/w aqueous solution) from Sigma Aldrich with deionized water. 30 mg of 0.10wt%Rh/ZSM-5 was dispersed in the 10 ml solution

of H₂O₂ (3.4% w/w) through sonication for 15 mins. Then, both this mixture and a magnetic stirring bar were added into the glass beaker to be placed in the Parr reactor. The remained volume inside of the Parr reactor for reactant gases is about 10 ml. Before experiments, air in the reactor was removed by repeating a process of flowing ethane and then purging it several times. Then, the reactor was pressurized with pure ethane (99.99% purity, Matheson) to an ideal pressure such as 1.5 bar.

The Parr stainless steel reactor was put in an oil bath (typically 50°C). Temperatures of the solution in the Parr reactor were directly measured with a K-type thermocouple which was inserted into the aqueous solution. This K-type thermocouple directly measures the temperature of a solution containing solvent, dissolved CH₄ and dispersed catalyst powder. Appropriate heating power was applied to heat the oil bath based on the feedback loop of temperature measurement of the VWR heater. It is noted that the temperature reading reported in the following is the actual temperature of the aqueous solution containing the stirred catalyst in the Parr reactor. In other words, in this work, the temperature of aqueous solution and the catalyst dispersed in it were always directly measured with the thermocouple. Once the aqueous solution reaches a set temperature, the stirring bar started to stir the solution to a certain speed. When the reaction was finished, the reactor was taken out from the oil bath immediately and put into an ice-water bath to cool down to 10°C or lower for collecting the majority of formed products. The cold reactor was connected to the ten-way valve of our GC equipped with FID-methanizer to detect the composition of components in gas phase above the solution after catalysis. Then, the mixture of solution and catalyst particles was filtered after catalysis; the clear aqueous solution was collected after filtration. Typically, it contained acetic acid, formic acid, a small amount of CH₃OH, CH₃CH₃OH,

H₂O, and a small amount of surplus H₂O₂. The amounts of the formed acetic acid and formic acid in the collected solution were measured through ¹H-NMR.

¹H-NMR spectra were collected from a Bruker AVANCE III HD 400 spectrometer. 4,4-dimethyl-4-silapentane-1-sulfonic acid (DSS) was added into samples as reference ($\delta=0.0$ ppm) for calibration. Before the NMR test, 0.540 ml of collected liquid after filtration and 0.060 ml of DSS solution (0.02wt% DSS dissolved in D₂O) were mixed in an NMR test tube. Similar to our previous studies^{86,90}, a water suppression program was applied in all NMR measurements of this work for minimizing the signal generating from H₂O. The main oxygenated products, acetic acid and formic acid can be qualitatively identified by checking its chemical shift $\delta=2.08$ ppm for acetic acid and $\delta=8.25$ ppm for formic acid. Figure S5.2 in Appendix C is an exemplified ¹H-NMR spectrum. By-products including methanol and ethanol in liquid phase after filtration of solid were also detected. They were quantitatively identified on the basis of the chemical shift $\delta=3.35$ ppm associated with -CH₃ of methanol and chemical shift at $\delta=1.16-1.19$ ppm (triplet) assigned to -CH₃ of ethanol.

The quantitative analyses of carboxylic acids and alcohols were done by building standard curves. They were established by building the correlation *between* the ratio of peak area of products to peak area of DSS *and* the amount of carboxylic acid and alcohol in the tested solutions. Test solutions were prepared by mixing (1) 0.540 ml of a standard solution containing the known amounts of standard products such as acetic acid or formic acid, with (2) 0.060 ml of DSS solution (0.020wt% DSS dissolved in D₂O). For instance, to establish a standard curve of a specific product such as acetic acid, a series of 10 ml aqueous solutions with different concentrations of acetic acid were prepared. They are called standard acetic acid solutions. 540 μ l of a standard acetic acid solution was mixed with 60 μ l DSS solution before the measurement of ¹H-NMR. Ratios of the

area of acetic acid ($\delta=2.08$ ppm) peak to the area of DSS peak in $^1\text{H-NMR}$ spectra were plotted as a function of the amount of acetic acid in the unit of μmol . The unknown concentration of acetic acid in the solution after catalysis was determined by using the standard curve. With the same method, standard curves of formic acid, ethanol, and methanol were established, presented in Figure S5.3 in Appendix C. Notably, for a product with an amount lower than $10 \mu\text{mol}$ of this study, no turn-over rate was calculated for it since the error bar of measurement of the amount of these carboxylic acids and alcohols is $\pm 5 \mu\text{mol}$ even larger.

3. Result and Discussion

3.1 Characterization of Rh catalyst structure

As shown in Figure 5.1b, the diffraction pattern of 0.10wt%Rh/ZSM-5 is the same as H-ZSM-5 (Figure 5.1a). Thus, the prepared 0.10wt%Rh/ZSM-5 remains the microporous structure of the original H-ZSM-5, supported by the preservation of pore volume after introducing 0.10wt% Rh to micropores (shown in Table 5.1). XPS examined compositions of surface regions of 0.10wt%Rh/ZSM-5 and 2.0wt%Rh/ZSM-5 in a high vacuum (shown in Figure 5.2). Although Rh 3d photoemission feature was observed clearly (Figure 5.2c) when the loading of Rh on ZSM-5 is 2.0wt%, no signal of Rh 3d was observed from the surface region of 0.10wt%Rh/ZSM-5 (Figure 5.2b). ICP measurement of the as-synthesized 0.10wt%Rh/ZSM-5 confirmed that the actual weight ratio of Rh to aluminosilicate in 0.10wt%Rh/ZSM-5 is approximately 0.10wt% (Table 5.2). Thus, the majority of these Rh atoms of 0.10wt%Rh/ZSM-5 must have anchored in micropores of H-ZSM-5 instead of on the external surface of H-ZSM-5 particles since no Rh 3d photoemission feature was observed in XPS studies. The lack of photoemission features of Rh 3d for 0.10wt%Rh/ZSM-5 is further supported by the lack of dark dots on the representative TEM images

of 0.10wt%Rh/ZSM-5 (Figures 5.3a and b). Under the same TEM imaging condition, however, rhodium oxide nanoparticles were clearly observed on 2.0wt%Rh/ZSM-5 (Figures 5.3c-f). This TEM observation is consistent with the observation of Rh 3d5/2 peak at 308.8 eV which is in agreement with the values of Rh₂O₃ reported in literature²³⁴.

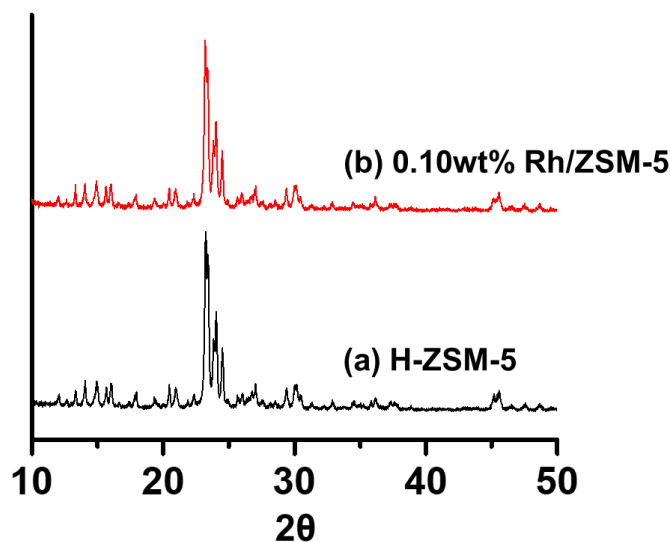


Figure 5. 1 XRD patterns of (a) pure H-ZSM-5 and (b) 0.10wt%Rh/ZSM-5. No any diffraction peaks of rhodium oxide nanoclusters were observed.

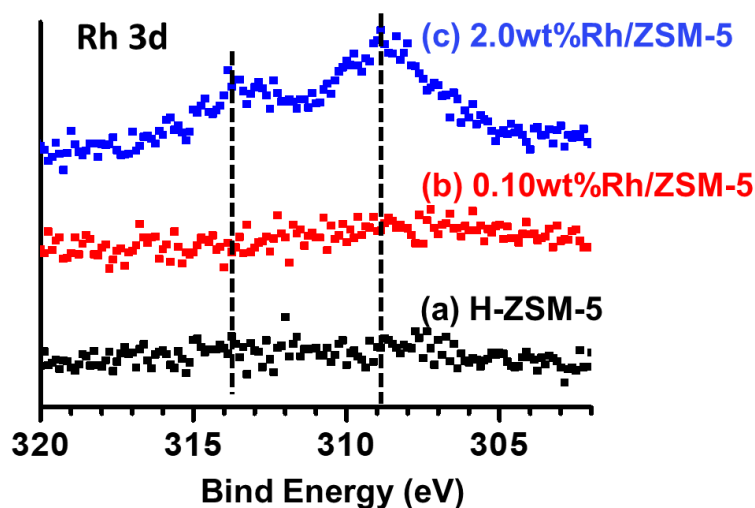


Figure 5. 2 Photoemission features of (a) H-ZSM-5, (b) 0.10wt%Rh/ZSM-5 and (c) 2.0wt%Rh/ZSM-5. Rh 3d photoemission features were not observed from 0.10wt%Rh/ZSM-5, but clearly shown on 2.0wt%Rh/ZSM-5.

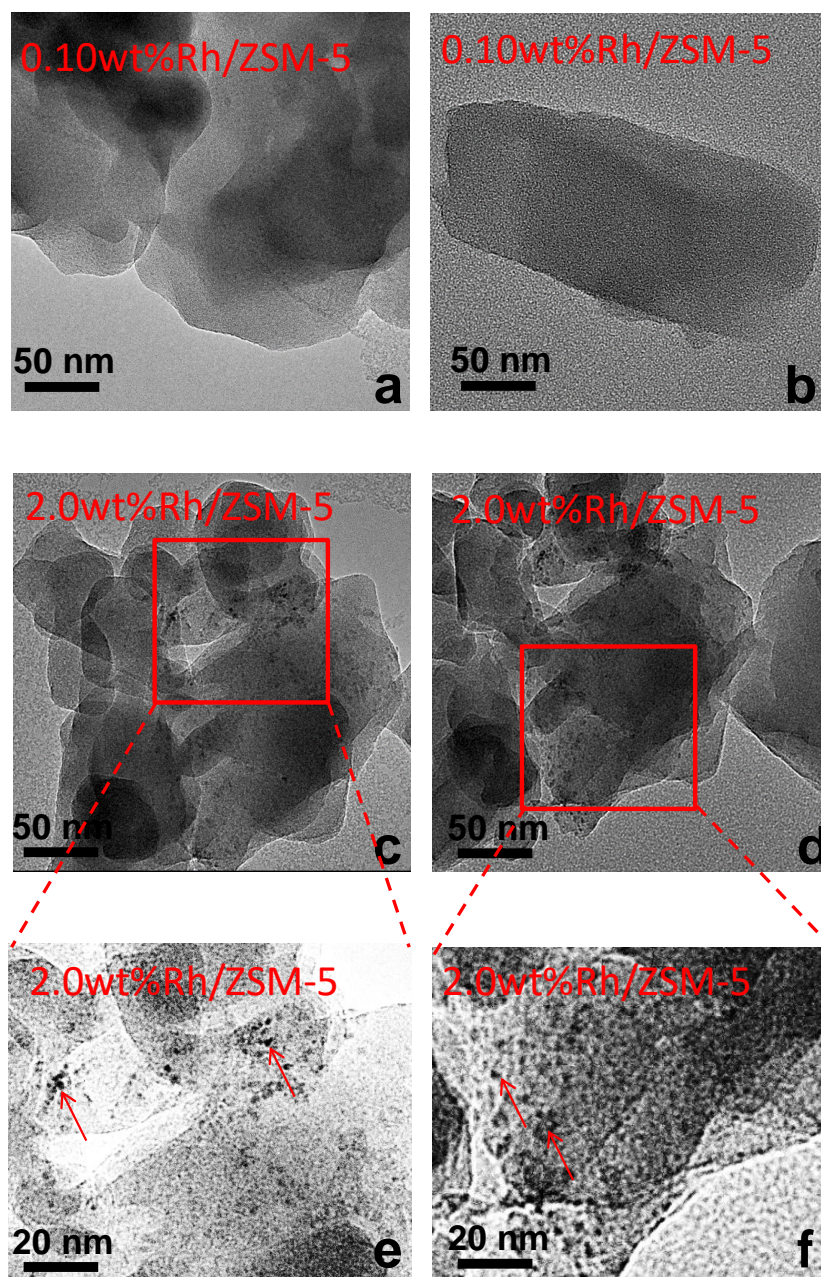


Figure 5. 3 TEM images of 0.10wt%Rh/ ZSM-5 (a and b) and 2.0wt%Rh/ZSM-5 (c-f). There are no dark spots on the external surface of 0.10wt%Rh/ZSM-5. Rhodium oxide nanoclusters on 2.0wt%Rh/ZSM-5 were readily observed in Figures 5.6c-f.

Table 5. 1 Surface area and pore volume of the catalysts

Sample	Surface area (cm ² /g)	Pore volume (cm ³ /g)
H-ZMS-5	433.5	0.1881
0.10wt%Rh/ZSM-5	441.3	0.1995

Table 5. 2 Rhodium concentration of fresh and used 0.10wt%Rh/ZSM-5

	Fresh Rh/ZSM-5	Used Rh/ZSM-5
Rh concentration (wt%)	0.10wt%	0.093wt%

Oxidation state and coordination environment of Rh atoms anchored in micropores of 0.10wt%Rh/ZSM-5 were studied with XANES and EXAFS, respectively. H₂O molecules in the ambient environment could readily adsorb on Rh atoms of 0.10wt%Rh/ZSM-5 during a process of cooling the calcinated catalyst from 550°C to 25°C in air. If water molecules are adsorbed on the Rh atoms anchored in the micropores of 0.10wt%Rh/ZSM-5, the measured coordination number of oxygen atoms to Rh atom is different from that during catalysis. To exclude the contribution of adsorbed water molecules of air to the coordination number of oxygen atoms to the anchored Rh atom, 0.10wt%Rh/ZSM-5 was heated to 150°C in flowing dry helium and remained at 150°C for one hour before data acquisition of XANES and EXAFS, by which weakly adsorbed H₂O molecules can be removed. Thus, the EXAFS data are assumed to provide information on binding between Rh atoms and native oxygen atoms of the wall of micropores of aluminosilicates. Rh K-edge was recorded when the catalyst was annealed at 150°C in He and remained at 150°C in the flowing He. As shown in Figure 5.4a, the K-edge of Rh atoms of 0.10wt%Rh/ZSM-5 located at 23.22 keV clearly suggests that Rh atoms are at a cationic state. Rhodium metal foil and rhodium oxides on alumina were used as references and their XANES spectra were shown as blue line and red line in Figure 5.4a, respectively. Compared with the shapes of rhodium metal foil and rhodium oxides spectra, XANES studies suggest that Rh atoms of 0.10wt%Rh/ZSM-5 are at oxidized states based on the similarity between shapes of edge features of Rh K-edges of Rh₂O₃ and 0.10wt%Rh/ZSM-5. Figures 5.4b and c are R-space spectra of Rh K-edge of Rh metal foil (reference sample) and 0.10wt%Rh/ZSM-5, respectively. As shown in Figure

5.4b, the main peak of the R-space of Rh K-edge of Rh foil was contributed from the first coordination shell of Rh atoms bonded to Rh atoms (Rh-Rh). It appears at 2.46Å before a phase correction, assigned to the Rh-Rh bond of Rh foil (2.72Å) in the FCC lattice of Rh metal. Compared to the peak in the R-space of Rh metal foil, the position of Rh K-edge of 0.10wt%Rh/ZSM-5 is in fact at 1.46Å before phase correction (Figure 5.4c) and 2.00Å after phase correction consistent with Rh-O bond of Rh₂O₃^{160, 235, 236}. Figure 5.4d is the R-space of Rh K-edge of Rh₂O₃ nanoparticles supported on Al₂O₃. One obvious peak appeared at 2.67Å, which is assigned to the second shell of rhodium oxide (Rh-O-Rh)^{160, 235, 236}. Compared to the observed peak at 2.67Å of Rh-O-Rh (before phase correction) in the R-space of Rh K-edge of Rh₂O₃ nanoparticles, the R-space of Rh K-edge of 0.10wt%Rh/ZSM-5 in Figure 5.4c does not have any peak at 2.67 Å. Thus, EXAFS studies of R-space of Rh K-edge of 0.10wt%Rh/ZSM-5 clearly show no rhodium oxide nanoclusters or rhodium nanoparticles formed in 0.10wt%Rh/ZSM-5. Fitting of the R-space of Rh K-edge gives the coordination number of oxygen atoms around a Rh atom of 0.10wt%Rh/ZSM-5 on average, CN(O-Rh) = 5.38±0.89 (Table 3). Therefore, these EXAFS studies suggest that single Rh atom sites are presented in micropores of 0.10wt%Rh/ZSM-5 particles through bonding with about five oxygen atoms.

Table 5. 3 Coordination number and bond length of Rh atoms in 0.10wt%Rh/ZSM-5 at 150oC in flowing helium

Sample	CN(O-Rh)	R(O-Rh) (Å)	σ ² (Å ²)
0.10wt%Rh/ZSM-5	5.38±0.89	2.001±0.014	0.0030

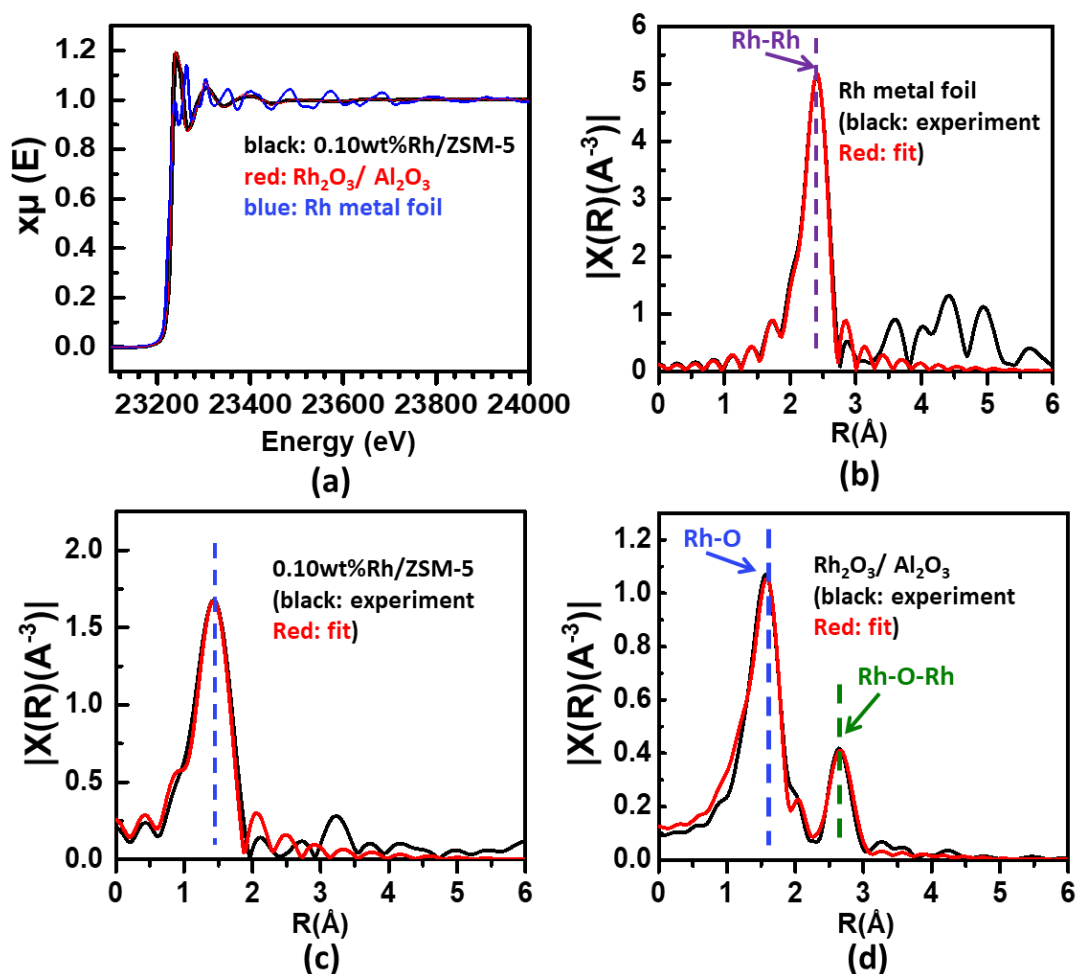


Figure 5.4 XANES and EXAFS studies of 0.10wt%Rh/ZSM-5, Rh foil and Rh₂O₃ nanoparticles supported on Al₂O₃. (a) Energy space of 0.10wt%Rh/ZSM-5 in flowing He at 150°C obtained by XANES technique. (b) R-space of Rh K-edge of Rh metal foil obtained by EXAFS technique. (c) R-space of Rh K-edge of 0.10wt%Rh/ZSM-5 in flowing He at 150°C obtained by EXAFS technique; obviously, there is a lack of the second shell of Rh K-edge of Rh-O-Rh. (d) R-space of Rh-edge of Rh₂O₃/Al₂O₃ obtained by EXAFS technique. The lack of peak of Rh-Rh bond and the lack of Rh-O-Rh (the second coordination shell of rhodium oxide) in the R-space of Rh K-edge of 0.10wt%Rh/ZSM-5 suggests the lack of formation of rhodium oxide or metal rhodium nanoclusters.

3.2 Identification of the role of Rh atoms

Oxidation of ethane by H₂O₂ is chosen as a reaction model to fundamentally understand the oxidative transformation of shale gas components on single Rh atoms anchored on the internal surface of micropores of 0.10wt%Rh/ZSM-5. A certain amount of H₂O₂ was added to deionized water to prepare a solution of H₂O₂ with a total volume of 10.0 ml. Then, 30mg of H-ZSM-5 or

0.10wt%Rh/ZSM-5 was dispersed into 10ml H₂O₂ solution through sonication. Pure C₂H₆ was introduced into the Parr reactor to reach certain pressure (1.5 bar, 5 bar, or 15 bar). The solution was continuously stirred during catalysis. The aqueous solution obtained after catalysis was analyzed with ¹H-NMR as described in the experimental section. Gas in the head part of the Parr reactor was analyzed by the FID detector of GC instrument with FID-methanizer to identify whether CO or CO₂ or ethene could be products formed under this mild reaction condition.

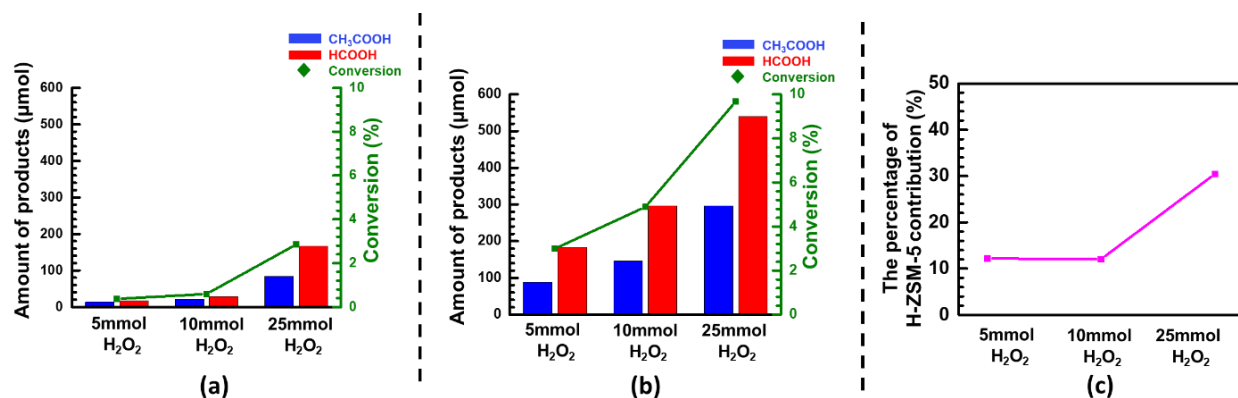


Figure 5. Influence of amount of H₂O₂ dissolved in deionized water (the volume of the H₂O₂ solution is always 10 ml) on the amounts of formed acetic acid and formic acid on 30 mg of pure H-ZSM-5 or 30 mg of 0.10wt%Rh/ZSM-5. (a) Amounts of formic acid and acetic acid formed on 30 mg of pure H-ZSM-5 in 15 bar ethane by oxidation with different amounts of H₂O₂ at 50°C for 2h. (b) Amounts of acetic acid and formic acid formed on pure 0.10wt%Rh/ZSM-5 in 15 bar ethane by oxidation with different amounts of H₂O₂ at 50°C for 2h. (c) The molar fraction of all products generated by 30 mg of pure H-ZSM-5 among all products formed by 30 mg of 0.10wt% Rh/ZSM-5. The contribution of H-ZSM-5 in formation of acetic acid and formic acid is minor in contrast to Rh₁O₅ sites of 0.10wt% Rh/ZSM-5 when the amount of H₂O₂ is 10 mmol or less. Thus, the amount of H₂O₂ is 10 mmol in 10 ml H₂O.

Based on the NMR measurements, the main products of oxidation of ethane with H₂O₂ in the liquid phase are acetic acid and formic acid. After a typical oxidation reaction with 1.5 bar C₂H₆ at 50°C for 2h, the gas in the head part of the Parr reactor was analyzed with gas chromatography. Upon qualitative identification and quantitative analyses, the carbon balance of this reaction was checked. As mentioned in Appendix C, products and their amounts were listed in Table S5.1 by introducing 1.5 bar C₂H₆ and Table S5.2 by using 15 bar C₂H₆, respectively. The carbon balances for the transformation of C₂H₆ of 1.5 bar and 15 bar were 97-98%. After a reaction,

the used 0.10wt%Rh/ZSM-5 was separated from the liquid and dried in an oven at 120°C for 3h. The concentration of rhodium in the used catalyst measured by ICP-AES is 0.093% (Table 2), suggesting that most Rh cations remain in catalyst 0.10wt%Rh/ZSM-5 after catalysis at 50°C.

Figures 5.5a and b present the yields (left axis) of products and conversion (right axis) of ethane by using pure H-ZSM-5 (Figure 5.5a) and 0.10wt%Rh/ZSM-5 (Figure 5.5b) as catalysts, respectively. As shown in Figure 5.5a, the amounts of products including acetic acid and formic acid produced from pure H-ZSM-5 are nearly zero when 15 bar ethane and 5 mmol H₂O₂ were used for catalysis at 50°C for 2h. The amount of produced acetic acid on H-ZSM-5 significantly increase to 87 μmol when the amount of H₂O₂ was 25 mmol. Compared to the pure H-ZSM-5 zeolite (Figure 5.5a), the yields of the formed acetic acid and formic acid on 0.10wt%Rh/ZSM-5 are much higher in any amounts of H₂O₂ used in experiments (Figure 5.5b). It suggests that the single-atom sites Rh₁O₅ do catalyze the activation of C-H bond and oxidize ethane to acetic acid and formic acid. In order to explicitly present the contribution of Rh₁O₅ sites of 0.10wt%Rh/H-ZSM-5 to the oxidative transformation of ethane to formic and acetic acids, the amounts of acetic acid and formic acid produced from pure H-ZSM were subtracted in all the reported amounts of acetic acid and formic acid in the following Figures 5.6-5.9. Each reaction in Figures 5.6-5.9 was performed twice, one on 30 mg of pure H-ZSM-5 and the other on 30 mg of 0.10wt%Rh/ZSM-5. The difference in yield between pure H-ZSM-5 and 0.10wt%Rh/ZSM-5 is the net amounts of acetic acid and formic acid, presented in Figures 5.6-5.9. In other words, the given amounts of acetic acid and formic acid in Figures 5.6-5.9 are these solely contributed from these anchored Rh₁O₅ sites.

In this ethane oxidation, TOF was calculated as the molecules of products (acetic acid or formic acid) per rhodium sites per second or per hour. Thus, TOFs for the oxidation of ethane at

50°C are 0.060 acetic acid molecules per Rh₁O₅ site per second (or 216 moles of acetic acid from 1 mol of Rh₁O₅ sites per hour), and 0.127 formic acid molecules per Rh₁O₅ site per second (or 457 moles of formic acid from 1 mol of Rh₁O₅ sites per hour), respectively.

3.3 Influence of pressure of ethane on amounts of products and conversion of ethane

To explore potential influence of ethane pressure on amounts of products and conversion of ethane, parallel studies using ethane of 1.5 bar, of 5 bar and of 15 bar were performed. As shown in Figure 5.6, the amounts of produced acetic acid and formic acid are about 110 μmol and 210 μmol for the oxidation of ethane on 30 mg 0.10wt% Rh/ZSM-5 dispersed in 10 ml solution of H₂O₂ with 1.5 bar ethane; the reaction was performed at 50°C for 2h. Based on the gas volume (10 ml), the introduced 1.5 bar C₂H₆ at 25°C is about 6.0 mmol. Thus, 30 mg of 0.10wt% Rh/ZSM-5 at 50°C can transform ~ 37% of ethane (6.0 mmol) within 2 hours. As shown in Figure 5.6, the conversion of ethane was decrease when operating the reaction at a higher temperature. However, along with the increase of pressure of ethane, the amount of produced formic acid (red bar) was increased to some extent but not significantly. Thus, the relationship of yields of these two carboxylic acids and pressure of ethane is not proportional. Additionally, the amount of acetic acid marked with blue bar remains no obvious change with the increase of the pressure of ethane. Notably, the conversion of ethane is obviously decreased along with the increase of pressure of ethane (the green line in Figure 5.6). The lack of an obvious increase of the amounts of acetic acid and formic acid suggests that the dissolution of ethane in liquid H₂O has nearly saturated even at 1.5 bar. To increase amounts of products (acetic acid and formic acid), the solubility and reaction rate should be promoted. Thus, it is expected to achieve a higher reaction rate of producing acetic acid and formic acid if a solvent with higher solubility of ethane could be used to replace H₂O.

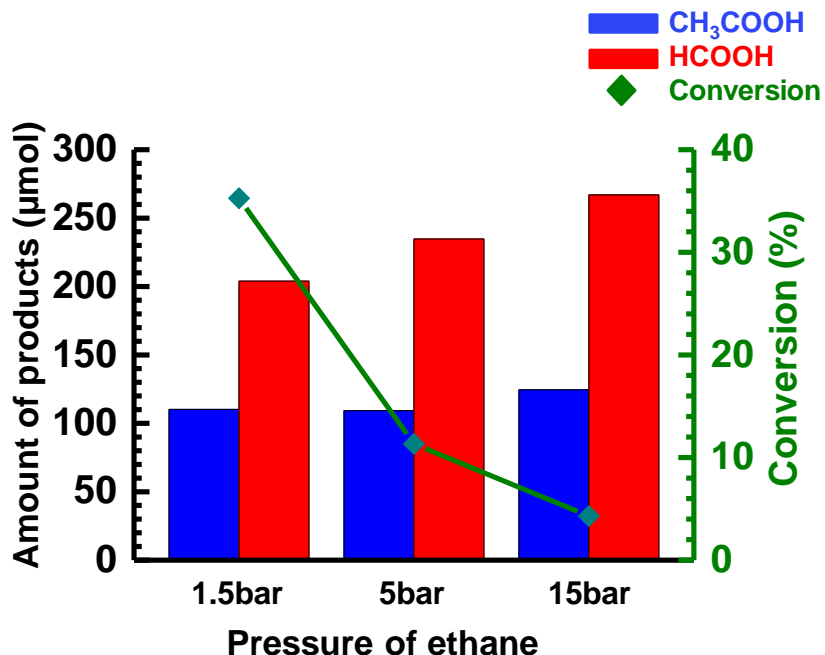


Figure 5. 6 Influence of pressure of ethane on amounts of acetic acid and formic acid formed by oxidizing ethane at 1.5, 5, or 15 bar with 10mmol H₂O₂ in 10ml H₂O at 50°C for 2h. 30mg 0.1%Rh/ZSM-5 was used as the catalyst in each experiment.

3.4 Influence of temperature on amounts of products and conversion of ethane

To investigate the influence of reaction temperature on the catalytic performance, catalytic reactions on 30 mg of 0.10wt%Rh/ZSM-5 at 50°C, 57.5°C, 65°C, and 80°C were performed when the pressure of the introduced ethane was 15 bar. Each reaction was performed with 30 mg fresh catalyst with 10mmol H₂O₂ under 15 bar ethane at one of those specific temperatures for 2h. The conversions of ethane at different temperatures were plotted in Figure 5.7. An obvious increase of conversion of ethane was found in the temperature range of 50°C-65°C. However, there is little increase of conversion of ethane when catalysis temperature was increased from 65°C to 80°C. The lack of increase of conversion of ethane at 80°C likely results from the decomposition of H₂O₂ at 80°C or the decrease of solubility of ethane in water at the relatively high temperature, 80°C.

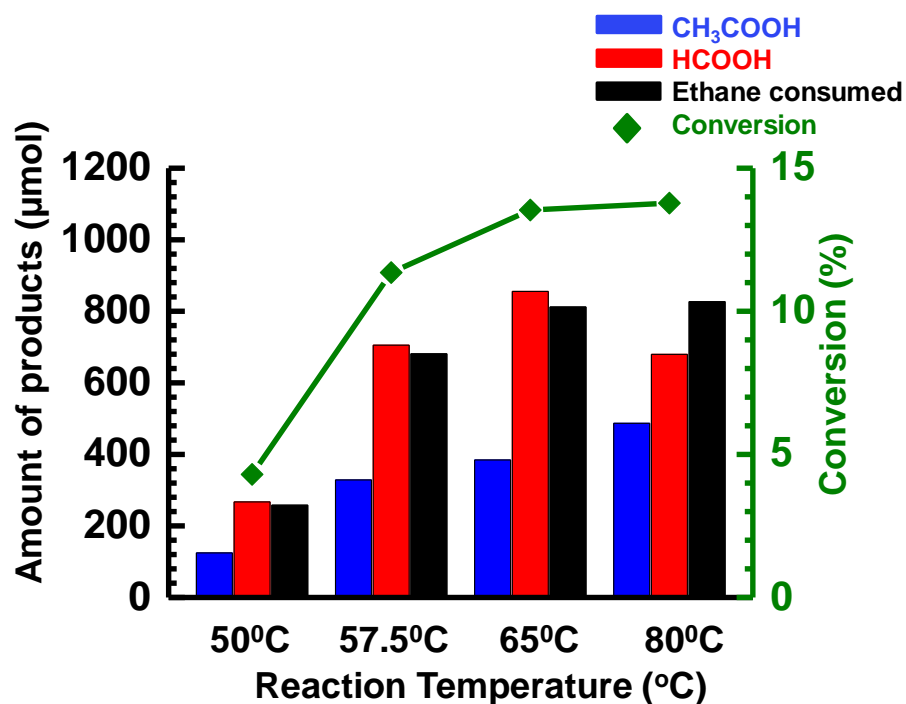


Figure 5. 7 Influence of temperature of catalysis on conversion of ethane and amounts of acetic acid and formic acid formed by oxidizing 15 bar ethane with 10mmol H₂O₂ in 10ml DI H₂O at 50°C, 57.5°C, 65°C, and 80°C for 2h. Fresh 30mg 0.1%Rh/ZSM-5 was used in catalysis at each temperature.

3.5 Reaction pathway and kinetics

Formic acid and acetic acid are the main products of oxidation of ethane with H₂O₂. To investigate whether acetic acid is formed from formic acid or not, time-dependent catalytic oxidation reactions were performed by performing parallel catalysis for different durations (30 min, 60 min, 90 min, 120 min, 180 min, or 360 min). In each independent experiment, the catalytic condition including pressure of ethane, amount of H₂O₂, amount of catalyst, and stirring rate are exact same. After performing each experiment of the parallel studies for a specific amount of time at 50°C, the Parr reactor was taken out from the heating bath immediately and was then placed to an ice bath to stop the reaction immediately by cooling the reactor to 10°C with ice water. Typically, cooling from 50°C to 10°C took about 10 minutes. Such a fast cooling can reduce the error of the

analysis of products. Each of these parallel experiments used 30 mg of fresh catalyst and 0.10wt%Rh/ZSM-5, respectively.

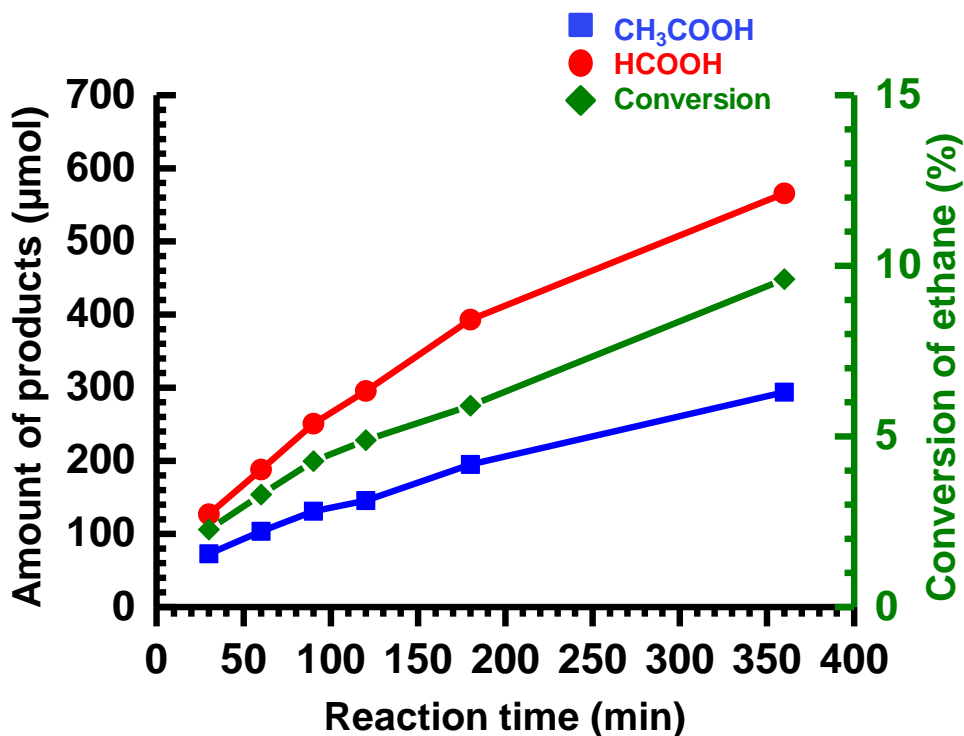


Figure 5. 8 Amounts of acetic acid and formic acid formed from 15bar C₂H₆ oxidized by 10mmol H₂O₂ at 50°C in different duration. The data of at each time (30 min, 60 min, 90 min, 12 min, 180 min, or 360 min) was achieved from an independent experiment using the same amount of fresh catalyst (30 mg 0.10wt%Rh/ZSM-5). In other words, six experiments with different reaction times were performed. Each of the six experiments was performed under the same condition on fresh 30 mg of 0.10wt%Rh/ZSM-5.

The amounts of formed acetic acid and formic acid were measured and then plotted as a function of reaction time (Figure 5.8). As shown in Figure 5.8, both acetic acid and formic acid continuously increase along the prolongation of reaction time from 0.5 to 6 hours. If acetic acid was formed through formic acid or even formic acid was produced from acetic acid, the evolutions of formic acid and acetic acid should follow of the evolution of a classic sequential reaction, A→B→C in which A is a reactant (C₂H₆ and H₂O₂), B is the intermediate product (acetic acid or formic acid), and C is a final product (formic acid or acetic acid) formed from the intermediate product B. In other words, the amount of formic acid should have increased as a function of

reaction time and then should have decreased along the prolongation of reaction time if acetic acid (or formic acid) was formed from formic acid (or acetic acid). For example, the amount a final product should have been low at the beginning of the catalysis but increase fast when the intermediate product (formic acid here) is produced. However, there are no such evolutions of formic acid and acetic acid observed along with the increase of reaction time. Thus, we prefer to think that formations of acetic acid and formic acid take their own reaction pathway instead of a sequential reaction.

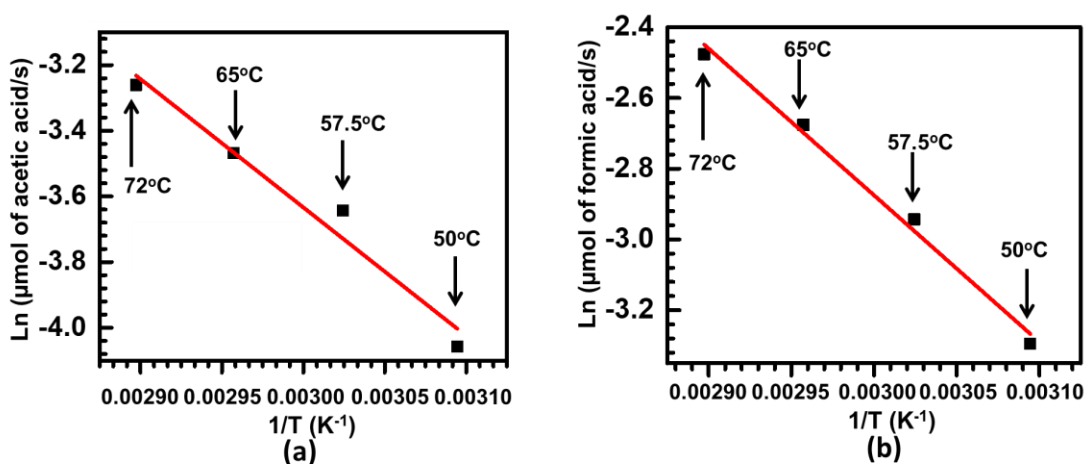


Figure 5.9 Arrhenius plot of Ln r (reaction rate) versus 1/T in the temperature range of 50°C-72°C. The activation barriers for productions of (a) acetic acid and (b) formic acid are 32.5 kJ/mol and 35.5 kJ/mol, respectively.

Since the formations of acetic acid and formic acid follow independent reaction pathways, we can evaluate their activation barriers based on kinetics studies, individually. Based on the measured amounts of acetic acid and formic acid at 50°C, 57.5°C, 65°C and 72°C, we calculated the reaction rate for producing acetic acid and formic acid by equation (1) and (2), respectively.

$$r_{acetic\ acid} = \frac{\Delta n_{consumed\ ethane\ for\ forming\ acetic\ acid}}{\Delta t\ (second)} = \frac{\Delta n_{produced\ acetic\ acid}}{\Delta t\ (second)} \quad (1)$$

$$r_{formic\ acid} = \frac{\Delta n_{consumed\ ethane\ for\ forming\ formic\ acid}}{\Delta t\ (second)} = \frac{\Delta n_{produced\ formic\ acid}}{\Delta t\ (second)} \quad (2)$$

Thus, Arrhenius plots for the formation of acetic acid or formic acid can be generated. Figures 5.9a and b present the Arrhenius plots which represent the kinetics for the formation of acetic acid and formic acid, respectively. As the conversions of ethane at these temperatures were lower than 10%, we evaluated the overall activation barriers for production of acetic acid or formic acid from the slope of the Arrhenius plots (Figures 5.9a and b). The overall activation barriers for the production of acetic acid and formic acid are 32.5 kJ/mol and 35.5 kJ/mol, respectively.

4. Conclusion

This work demonstrated that the catalyst of singly dispersed Rh sites anchored in micropores of H-ZSM-5 exhibited high activity for oxidation of ethane with H₂O₂ at 50°C. The conversion of ethane (1.5bar) to acetic acid and formic acid at 50°C for 2h is about 37%. The TOFs for the oxidation of ethane at 50°C are 0.060 acetic acid molecules per Rh₁O₅ site per second (or 216 moles of acetic acid from 1 mol of Rh₁O₅ sites per hour), and 0.127 formic acid molecules per Rh₁O₅ site per second (or 457 moles of formic acid from 1 mol of Rh₁O₅ sites per hour), respectively. This study suggests that oxidation of ethane with the heterogeneous single-atom catalyst at near ambient temperature in aqueous solution is a prospective approach for achieving the efficient transformation of ethane into acetic acid and formic acid under mild conditions.

Contributions of the project:

The synthesis of catalysts, characterization of catalysts and the evaluation of catalytic performances of prepared catalysts were mainly done by Yuting Li.

Chapter 6: Fundamental understanding of Pd promoted Zn-loaded microporous catalysts for ethane dehydrogenation

1. Introduction

Dehydrogenation of ethane has attracted significant attention in the last decades due to the increasing availability of inexpensive ethane from shale gas⁹⁵. Transformation of ethane can be done under harsh conditions such as thermal cracking²³⁷, requiring to be performed at extremely high temperatures as high as 800-1000°C. Compared to the current high-temperature thermal cracking, synthesis of ethylene through catalytic dehydrogenation of ethane with or without the participation of oxygen exhibits advantages in catalytic conditions including ambient pressure of reactants and relatively low catalysis temperature (<700°C). These mild catalytic conditions of ethane dehydrogenation are beneficial to the efficient utilization of inexpensive shale gas components to generate useful chemicals.

Driven by the advantages of performing transformation of ethane to ethylene at relatively low temperatures, many efforts have been made in the last few decades. Various types of catalysts consisting of Zn, Pd, Mo and other metal species were reported active for the dehydrogenation of short alkanes^{73, 95, 238-241}. Among these reported catalysts, Zn supported on zeolite has drawn increasing attention due to its high activity in the activation of the C-H bond of ethane^{50, 72, 242}. However, the activity and thermal stability of current studied Zn-based catalysts for the catalytic dehydrogenation of ethane to ethylene are not comparable to the thermal cracking process. Thus, it would be ideal for developing the stable catalyst exhibiting good activity of production of ethylene from ethane dehydrogenation. From studies in publications, it is reported that the activity of Zn catalyst could be significantly enhanced by adding a noble metal such as platinum^{74, 243}.

In ethane dehydrogenation, H₂ is one of the main products and stoichiometrically its amount is equal to ethylene (C₂H₆→C₂H₄+H₂). These H₂ molecules are formed through the coupling of atomic H that is generated through C-H cleavage in the activation of ethane molecules. As known, the oxidizing or reducing capability of a reactant gas could restructure the surface of a bimetallic catalyst. It was reported that reducing reactants such as CO and oxidizing reactants such as NO could alternatively reduce an oxide and oxidize a metal and thus result in the restructuring of the surface of a bimetallic catalyst in catalytic oxidation of CO with NO¹⁵⁸. In terms of ethane dehydrogenation (C₂H₆→C₂H₄+H₂), the only reactant ethane is neither an oxidizing nor a reducing chemical. However, one of the products of the dehydrogenation of ethane is H₂. It is reported that molecular H₂ is typically formed through coupling H atoms produced in elementary steps of the dehydrogenation of ethane. Thus, we hypothesized that these intermediate atomic H could readily reduce the surface of the catalyst during the dehydrogenation of ethane. At high temperature, these highly active H atoms could directly couple with oxygen atoms bonding to a metal atom of a catalytic site to form an OH group. Then OH group could couple with another intermediate H atom to form an H₂O molecule, by which oxygen atoms of a catalytic site can be removed from the catalyst surface through the formation of H₂O and then desorption. Such removal of oxygen atoms from the surface of a catalyst is expected to dramatically restructure chemical and coordination environments of metal atoms of catalytic sites. This hypothesized restructuring here is different from the reported restructuring resulted from segregation and migration of metal atoms of a bimetallic catalyst such as Rh_{0.5}Pd_{0.5} bimetallic reported in literature^{158, 244}. The proposed restructuring would play an essential role in the catalytic performance of zinc catalysts.

Consequently, in this work, catalysts including 2.0wt%Zn/silicalite-1, 1.0wt%Pd/silicalite-1, and 2.0wt%Zn/1.0wt%Pd/silicalite-1 were prepared to conduct the dehydrogenation of ethane.

Moreover, fundamental studies of the prepared catalysts at a molecular level were explored by using realistic operando studies of X-ray absorption near edge structure (XANES) and extended X-ray absorption fine structure (EXAFS). This work would reveal: (1) if the H₂ generated during ethane dehydrogenation can readily restructure catalytic sites, resulting in the rapid deactivation of the original catalyst; and (2) how the addition of Pd atoms could promote the activity of Zn-based catalyst.

2. Experiment

2.1 Catalyst preparation

The silicalite-1 supports were prepared by the hydrothermal method reported in literature²⁴⁵. The starting gel contains the Si source and templates with the molar composition of 1.0 SiO₂: 0.4 TPAOH: 35 H₂O. In a typical protocol, 13g TPAOH solution (Sigma Aldrich) was mixed with the deionized water with vigorously stirring for 10 min. Then, 8.32 g TEOS was dropwise added into the above mixture, with a followed stirring for 6 h. When TEOS was fully hydrolyzed and the mixture became clear, the reaction mixture was transferred into a 100 ml Teflon-lined stainless-steel autoclave for crystallization in a conventional oven at 170 °C for 4 days under static conditions. After centrifuging, washing with water and ethanol for several times, the as-synthesized solid powders were dried at 80 °C in the oven overnight and followed calcination at 550 °C for 8 h. Thus, the high crystalline silicate-1 was obtained, named as S-1. The three types of S-1 supported metal catalysts were continued prepared by an IWI method employed in other literatures^{86, 94}.

Silicate-1 supported Zn catalyst is named as Zn/S-1. 93 mg of Zn (NO₃)₂ (Sigma Aldrich, 98%) was dissolved in 1.0 ml of deionized water and then the mixed solution was sonicated about

10 mins to form a transparent $\text{Zn}(\text{NO}_3)_2$ solution. 1.00 gram of silicate-1 was added to a 50 ml beaker, and the prepared $\text{Zn}(\text{NO}_3)_2$ solution was gradually dropped to the porous silica powder placed in the beaker. In the meantime, the silica powder in the beaker was stirred vigorously to make a well-dispersed slurry. The gained slurry was further stirred at room temperature overnight and then was dried at 80°C in air for 3 h, followed by calcination in Muffle furnace at 650°C in air for 6 h with a ramping rate of $2^\circ\text{C}/\text{min}$.

The catalyst of silicate-1 with supported Pd (1.0wt%Pd/S-1) was prepared with the same method as that of 2.0wt%Zn/S-1 described above. 25.0 mg of Pd (NO_3)₂ (Sigma Aldrich, ~40% metal basis) was dissolved in 1.0 ml of deionized water to make a transparent Pd (NO_3)₂ aqueous solution. Then, the prepared Pd (NO_3)₂ solution was gradually added to the silicate-1 placed in a 50 ml beaker while the powder in the beaker was stirred vigorously to make a well-dispersed slurry. The gained slurry was continuously stirred at room temperature overnight and then was dried at 80°C in air for 3 h, followed by calcination in Muffle furnace at 650°C in air for 6 h with a ramping rate of $2^\circ\text{C}/\text{min}$.

In terms of 2.0wt%Zn/1.0wt%Pd/S-1, the anchoring of Zn and Pd was conducted sequentially. Firstly, the precursor of Zn^{2+} , $\text{Zn}(\text{NO}_3)_2$ solution was introduced to support powders through the same IWI method as that used for the preparation of 2.0wt%Zn/S-1. Upon drying and calcining steps, the catalyst precursor was cooled to room temperature in air, forming 2.0wt%Zn/S-1. Then, the prepared 2.0wt%Zn/S-1 was used as the catalyst precursor to be transferred to a 50 ml beaker. A prepared Pd (NO_3)₂ solution was introduced to the well-prepared 2.0wt%Zn/S-1 placed in the beaker drop by drop. After drying at 25°C overnight and then at 80°C in air for 3 h with a followed calcination at 650°C in air for 6 h, the catalyst 2.0wt%Zn/1.0wt%Pd/S-1 was prepared.

2.2 Catalyst characterization

Concentrations of zinc and palladium introduced to silicate-1 were measured through ICP-AES (JY 2000-2, HORIBA). Surface area and pore volume of silicate-1 before and after loading zinc or/and palladium were measured with BET (Quantachrome Autosorb iQ). Crystal phases of the support of these catalysts were checked with powder X-ray diffraction (XRD) performed on a Bruker SMART APEX diffractometer.

Chemical and coordination environments of Zn and Pd of these catalysts during catalysis were studied with a realistic operando approach. Here, a realistic operando approach is referred to a study where data of characterization was being collected while it is catalyzing a reaction at a specific catalytic temperature under a realistic catalytic condition. Certainly, gaseous reactant(s) must flow through the catalyst bed that was remained at the catalytic temperature when the characterization of the catalyst was being performed.

Operando studies of 2.0wt%Zn/S-1, 1.0wt%Pd/S-1, and 2.0wt%Zn/1.0wt%Pd/S-1 using XANES and EXAFS were performed at SPring-8 in Japan and Argonne National Laboratory in the United States. The typical experimental steps of an operando study of 2.0wt%Zn/S-1 catalyst were taken as an example to be described in the following so that these operando characterizations can be readily repeated. About 40mg of catalyst, 2.0wt%Zn/S-1, was added to a quartz tube with an internal diameter ID of 2.0 mm; then the quartz tube was installed in an XAS reaction cell for performing operando studies of XANES and EXAFS. As reported, this quartz tube can be heated up to 850°C and remain at 850°C for at least 6 h when reactant gasses with a pressure up to 3 bars is flowing through a catalyst bed in the quartz tube. Scanning of energy window covering Zn K-edge was performed at room temperature while 5mL/min N₂ (Matheson, 99.99%) was flowing

through the catalyst bed. Then, 5mL/min N₂ was continuously flowing through the catalyst bed in the quartz tube while the catalyst was gradually heated to a specific temperature such as 650°C. Once the temperature of the catalyst bed reached 650°C, the pure N₂ was replaced by 10% ethane (balanced with argon) to perform catalysis. Then, 5mL/min 10% ethane was flowing through the catalyst bed while the catalyst bed remained at 650°C. After maintaining at 650°C for 1h, XAS data was started to be collected. Notably, the catalyst bed was maintained at 650°C and 5mL/min 10% ethane was flowing through the catalyst bed when XAS data was being collected.

For operando characterization of 2.0wt%Zn/1.0wt%Pd/S-1, the exactly identical protocol of 2.0wt%Zn/S-1 was used to collect XAS spectra. Scans of Zn K-edge and Pd K-edge of the bimetallic catalyst will be collected separately by using two sets of the fresh catalyst, 2.0wt%Zn/1.0wt%Pd/S-1. Generally, each scan of the spectrum of Zn K-edge or Pd K-edge containing both XANES and EXAFS regimes takes 20mins. Typically, a few scans of Zn K-edge or Pd K-edge were collected for hours.

XAS spectra containing XANES and EXAFS regions were analyzed by Demeter software, a front end to Feff6, Larch, and IFEFFIT, providing the proper fitting of R-space spectra and sensible parameters of coordination environment of Zn and Pd atoms, including the coordination number of atoms surrounding the core atom and the radius of each coordinating bond also known as the distance between surrounding atoms and the core atom.

2.3 Evaluation of catalytic performances of ethane dehydrogenation

Catalytic performance including catalytic activity in conversion of ethane and selectivity for producing ethylene on these catalysts were performed on a fixed-bed flow reactor that was connected to an on-line GC equipped with a flame ionization detector (FID). The temperature of

the catalyst bed was measured with a K-type thermocouple inserted to the middle of the catalyst bed and controlled by the PID temperature controller. Specifically, the PID controller measures actual temperature and transfers the difference between the measured temperature and the programmed set temperature to a signal to a relay, so that relay can apply an appropriate voltage to the heater of the reactor. In this way, the catalyst can be heated or cooled down with a certain ramping rate or remained at a required catalysis temperature for a certain amount of time. This operating system was used to measure catalytic activity and selectivity for all catalysts discussed in this work and to evaluate the durability of catalytic performance of catalysts at a specific temperature for certain amount of time.

In each measurement of catalytic performance, 0.100 g of catalyst was diluted with 0.500 g of quartz sand. The quartz sand was purified by being soaked in aqua regia solution and stirred for 24h and then being washed with deionized water several times until the pH of the left solution after washing to 6.5-7. After being purified, the quartz sand was dried at 120°C for 5 h. The mixture of catalyst powder and the purified quartz sand was loaded into the middle of a quartz tube with OD of 9.0 mm. After the tube being installed to the reactor, 10 mL/min N₂ (99.99%, Matheson) was flowing through the catalyst bed while heating the reactor to a certain catalytic temperature such as 650°C with a ramping rate of 10°C/min. After maintaining the catalyst at that temperature under the atmosphere of inert gas for 30mins, the nitrogen was replaced with 10 mL/min of 10% ethane balanced with argon (Matheson). The stainless-steel tube connecting the outlet of the downstream of the fixed-bed flow reactor to the inlet of the ten-way valve of online GC was always kept at 150°C during measurements of catalytic performance for the complete delivery of all products of this catalysis.

The gas leaving from the outlet of the fixed-bed flow reactor contained both unreacted reactants and formed products which were separated by a HayeSep D (6' × 1/8") packed column, a molecular sieve 13 × (6' × 1/8") packed column and then analyzed with a flame ionization detector (FID). The conversion of ethane and the selectivity for producing ethylene were calculated with the following equations. The mole flow rate of unreacted ethane was calculated by dividing the measured peak area of the unreacted ethane with a sensitivity factor of ethane. The mole flow rate of produced ethylene was calculated by dividing the measured peak area of the produced ethylene with a sensitivity factor of ethylene.

$$\text{Conversion (X)} = \frac{\text{Mole flow rate of introduced ethane} - \text{Mole flow rate of unreacted ethane}}{\text{Mole flow rate of introduced ethane}} \times 100\%$$

$$\text{Selectivity (S)} = \frac{\text{Mole flow rate of produced ethylene}}{\text{Mole flow rate of introduced ethane} - \text{Mole flow rate of unreacted ethane}} \times 100\%$$

$$\text{Yield (Y)} = \text{Conversion (X)} \times \text{Selectivity (Y)}.$$

In the time-on-stream studies, the gas leaving from the downstream of the reactor was continuously flowing into the ten-way valve of GC. It was automatically injected to GC columns every 40 minutes in a period of a total time of 15 h or longer.

3. Result and Discussion

3.1 Structural characterization of as-synthesized catalysts

The measured concentrations of zinc or palladium of the prepared catalysts were listed in Table 6.1. They are consistent with the nominal concentrations of the introduced precursors of zinc or palladium. Based on the BET measurements, these catalysts remained surface area and volume similar to those of the support, parent S-1 (Table 6.2), suggesting that these preparations did not modify the microporous structure. Additionally, as shown in Figure 6.1, the crystal phase of these catalysts was identified through powder XRD. These XRD patterns are associated with the

crystalline structure of the MFI framework, reported in literatures^{245, 246}. The similarity of XRD patterns of S-1 before and after loading metals indicates the preservation of the crystalline structure of these prepared catalysts. The lack of diffraction peaks of metallic or oxidic species of zinc and palladium in these XRD patterns suggests that there were no large particles formed on these catalysts.

Table 6. 1 Loading of Zn or Pd to catalysts measured with ICP-AES

Catalysts	Zinc concentration (wt%)	Palladium concentration (wt%)
2.0wt%Zn/S-1	1.92wt%	
1.0wt%Pd/S-1		1.08wt%
2.0wt%Ga/1.0wt%Pd/S-1	1.89wt%	0.95wt%

Table 6. 2 Surface area and pore volume of catalysts measured with BET

Catalysts	Surface area (m ² /g)	Pore volume (cm ³ /g)
S-1	330.3	0.2128
2.0wt%Zn/S-1	312.7	0.2101
1.0wt%Pd/S-1	300.9	0.2077
2.0wt%Zn/1.0wt%Pd/S-1	281.3	0.2081

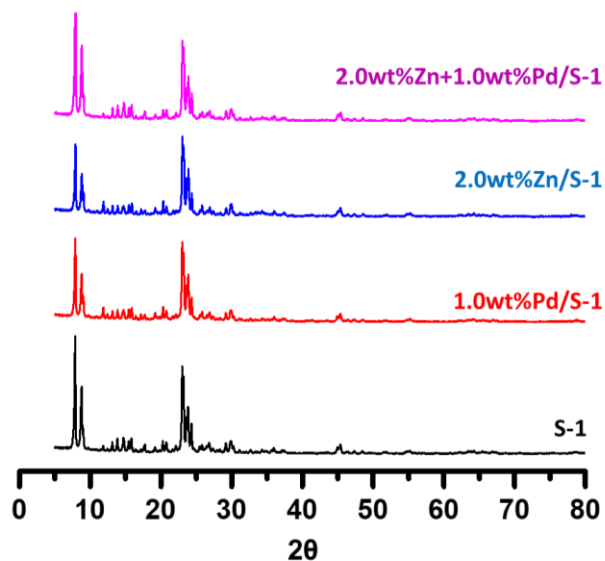


Figure 6. 1 XRD patterns of S-1 (black), 1.0wt%Pd/S-1 (red) 2.0wt%Zn/S-1 (blue), and 2.0wt%Zn/1.0wt%Pd/S-1 (purple).

3.2 Catalytic performance of S-1 supported with Zn and studies of its active sites

Catalytic performances of S-1 and 2.0wt%Zn/S-1 for ethane dehydrogenation in the temperature range of 500-650°C were measured. As shown in Figure 6.2a, pure S-1 was basically not active in the dehydrogenation of ethane, whereas 2.0wt%Zn/S-1 exhibited much higher activity (Figure 6.2b) at the same temperature. It suggests that Zn-based sites are active for the activation of ethane and dehydrogenation of ethane. Notably, the conversion of 2.0wt%Zn/S-1 increased along with the increase of catalysis temperature from 500°C to 650°C (blue line in Figure 6.2b), while its selectivity for producing ethylene obviously decreased along with the increase of catalysis temperature (red line in Figure 6.2b).

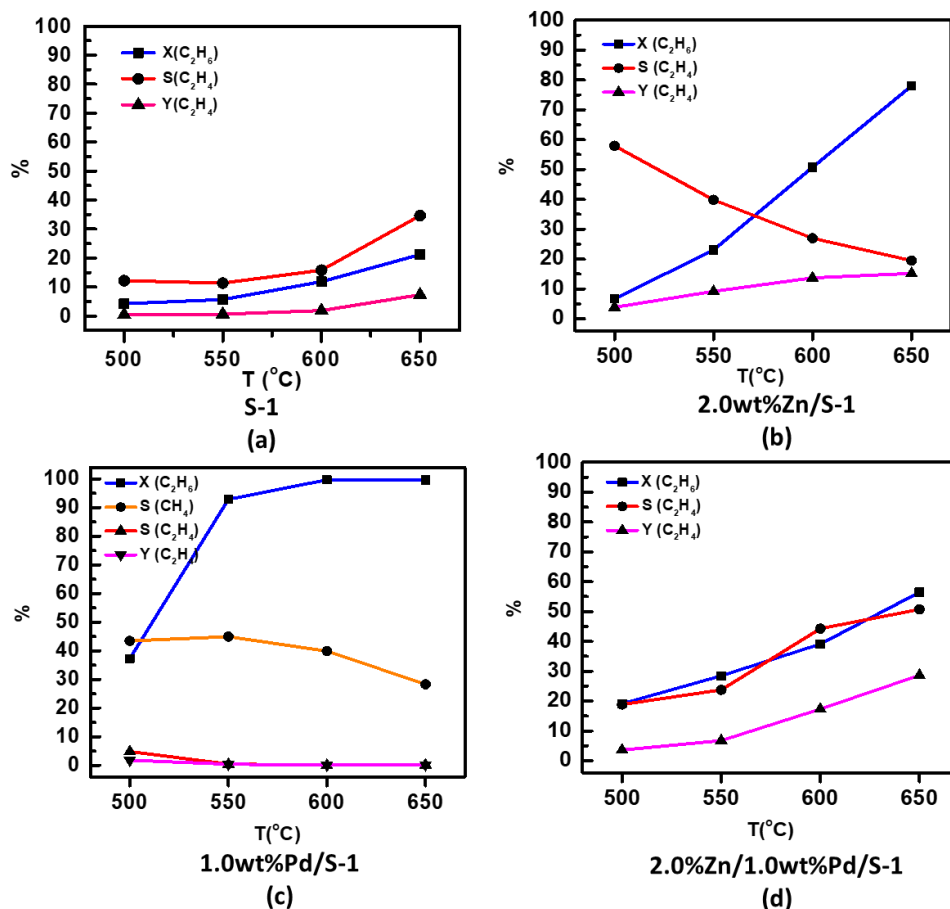


Figure 6. 2 Catalytic performance of (a) S-1, (b) 2.0wt%Zn/S-1, (c) 1.0wt%Pd/S-1 and (d) 2.0wt%Zn/1.0wt%Pd/S-1 in the temperature range of 500-650°C. 100 mg of the catalyst was used. It was diluted by 500 mg purified quartz 10 ml/min 10% ethane was flowing through the catalyst bed.

As shown in Figure 6.3a, operando studies of the Zn K-edge show that Zn atoms of 2.0wt%Zn/S-1 are in the oxidic state since the energy position of Zn K-edge is different from the edge position of Zn foil (9659eV) but quite close to that of ZnO²⁴⁷. In the R-space spectrum of Zn K-edge collected before catalysis at 25°C (Figure 6.3b), the main peak of Zn-O bonds at 2.04 Å (after phase correction) was observed, which is consistent with the Zn-O bond length of ZnO species²⁴⁸. Compared to the strong peak of Zn-O-Zn bonds at about 3.30 Å in R-space spectrum of Zn K-edge of ZnO species²⁴⁸, the quite weak peak of Zn-O-Zn bonds of the catalyst 2.0wt%Zn/S-1 in Figure 6.3b suggests (1) few ZnO nanoparticles were formed, or (2) size of ZnO nanoparticles is smaller than 1 nm even if they were formed. Notably, the peak of Zn-O-Si was also observed before catalysis at 25°C since these cationic Zn atoms were anchored on the support, S-1. These Zn cations anchored on the micropores S-1 are proposed to be active for the ethane activation.

Figure 6.3c is the R-space spectrum of Zn K-edge of 2.0wt%Zn/S-1 collected at 650°C during catalysis. The observed peak of Zn-O bonds was still the main peak, and the weak peak of Zn-O-Zn bonds was still observed during catalysis at 650°C. No peak of Zn-Zn bonds of Zn metal nanoparticles was observed, suggesting that no metal Zn nanoparticles were formed during catalysis at 650°C. Additionally, similar to the catalysis before catalysis at 25°C, the peak of Zn-O-Si was still observed during catalysis at 650°C. Although some of the introduced Zn atoms were removed through reduction and immediate vaporization, the rest of the loaded Zn atoms could have migrated to the framework of S-1. Thus, the peak of Si-O-Zn was still observed in Figure 6.3c. The correlation of the loss of Zn atoms and the migration of Zn atoms in 2.0wt%Zn/S-1 during catalysis at high temperatures will be further discussed in the following sections.

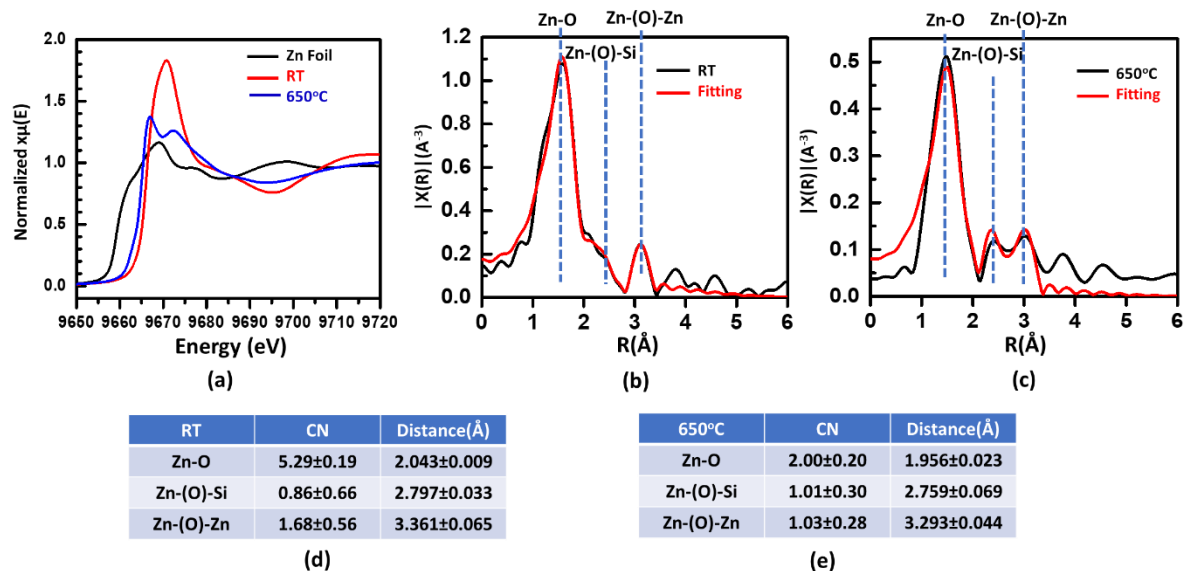


Figure 6. 3 Operando studies of Zn K-edge of 2.0wt%Zn/ S-1 using XANES and EXAFS. (a) Energy space spectra of Zn K-edge of Zn foil (as reference), 2.0wt%Zn/ S-1 at 25°C before catalysis and catalyst during catalysis at 650°C. (b) R-space spectra of Zn K-edge of 2.0wt%Zn/ S-1 before catalysis at 25°C. (c) R-space spectrum of Zn K-edge of 2.0wt%Zn/ S-1 during catalysis at 650°C. (d) List of parameters used in fitting R-space spectra of Zn K-edge in (b). (e) List of parameters used in fitting R-space spectra of Zn K-edge in (c).

3.3 Rapid deactivation of catalytic performance of S-1 supported with Zn and intermediate-driven restructuring of Zn-based sites of the catalyst

The durability of the catalytic performance, referring to the evolution of activity and selectivity of 2.0wt%Zn/S-1 as a function of time, was studied with a time-on-steam mode. As shown in Figure 6.4a, although the selectivity of ethylene raised to almost 50% at the 8th hour, the conversion of ethane was considerably decreased to reach less than 10% at the 10th hour. Thus, the maximum yield of ethylene was approximately 22%. As demonstrated in Figure 6.2a, S-1 can convert about 18% of ethane to methane and carbon species. It suggests that the conversion of ethane on 2.0wt%Zn/S-1 at 650°C at the 10th hour (Figure 6.4a) would be largely contributed from the support S-1 instead of Zn-related species or from the thermal cracking.

Although a limited amount of ZnO nanoparticles was observed on the external surface of S-1 during catalysis at 650°C (Figure 6.3c), these species did not contribute to the rapid

deactivation of the catalytic activity for converting the ethane and selectivity for producing ethylene.

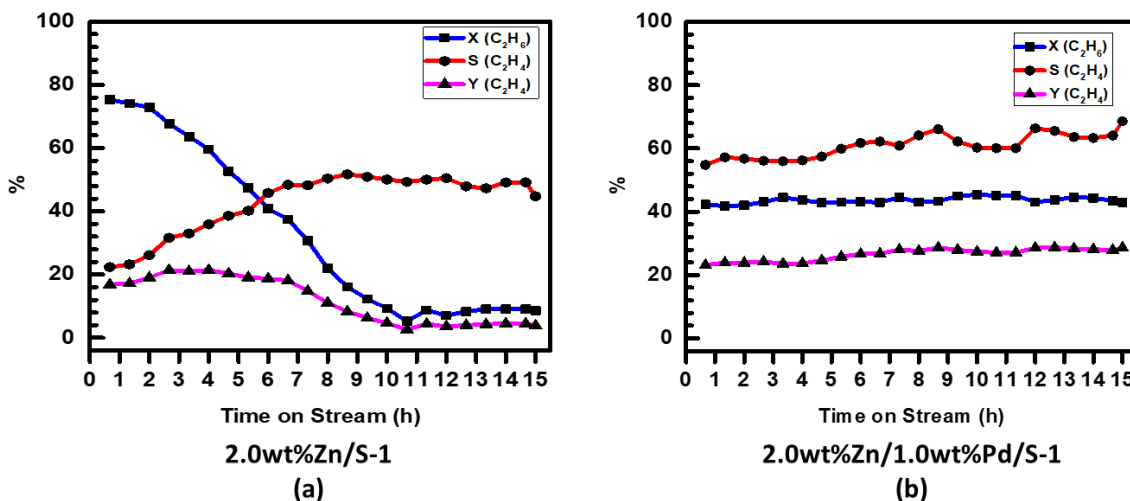


Figure 6. 4 Durability of catalytic performance based on time-on-stream examination under the same catalytic condition at 650°C. (a) 0.200 gram of 2.0wt%Zn/S-1 at 650°C, and (b) 0.200 gram of 2.0wt%Zn/1.0wt%Pd/S-1 at 650°C.

The rapid decay of catalytic performance on 2.0wt%Zn/S-1 must result from the restructuring of active sites during catalysis at high temperatures. ICP-AES studies suggest that a large amount of Zn atoms loaded to 2.0wt%Zn/S-1 lost after catalysis at 650°C for 15 hours. Although a certain amount of Zn atoms remained in the catalyst after catalysis at 650°C for 15 hours, they were not active for producing ethylene any more. Thus, the restructuring consists of loss of Zn atoms through vaporization and variation of chemical or/and coordination environments of the catalytic active Zn cationic sites.

It is well known that ZnO has a higher melting point at 1975°C^{249, 250}, in contrast to many early transition metal oxides such as Fe₂O₃ (mp, 1565°C)²⁴⁹, FeO (mp, 1377°C)²⁵¹, Co₃O₄ (mp, 895°C)²⁵¹, CuO (mp, 1326°C)²⁵¹ and any oxides of all 4d metals and 5d metals²⁵². ZnO exhibits high thermal stability up to almost 2000°C. However, the metal Zn, the reduced product of ZnO, has the second lowest melting point, 419.5°C, among all d-block metals. Correspondingly, it

exhibits a much higher vapor pressure than all d-block metals except Hg at the same temperature. Vapor pressures of a solid and liquid Zn can be calculated with the following equations²⁵³: $\log(p/atm) = 6.102 - \frac{6776}{T}$ (for solid Zn) and $\log(p/atm) = 5.378 - \frac{6286}{T}$ (for liquid Zn); here T is the temperature of solid or liquid zinc. Based on these equations, the vapor pressure of metal Zn at the melting point (419.5°C) is as high as 0.16 Torr. Vapor pressure of liquid Zn at a catalysis temperature (650°C) used in literature is as high as 28.3 Torr. It is even higher than the vapor pressure of liquid water at 40°C. Obviously, this is an extremely high vapor pressure for a liquid metal. Thus, It is expected that 0.100 g liquid Zn at 650°C could be vaporized in a few seconds, although no specific kinetic data of the vaporization of liquid metal zinc was reported. The extremely high vapor pressure of metal Zn at high temperature could result in a rapid deactivation during catalysis.

Other than the final product molecular H₂, atomic H are formed during the process from activating C-H bonds of reactant ethane molecules to the formation of product ethylene molecules. These atomic H can readily reduce Zn cations of active sites to form metallic Zn atoms and then these metallic Zn atoms sinter to form small Zn nanoparticles. As Zn nanoparticles have a quite low melting point at 495°C, these Zn nanoparticles formed at 650°C are at a state of liquid Zn which has a very high vapor pressure. Thus, metal Zn nanoparticles immediately vaporize at 650°C once they are formed.

Operando XANES and EXAFS spectra could not observe the formation of liquid metal Zn nanoparticles. That may result from (1) liquid metal Zn nanoparticles are expected to have a very short lifetime due to its high vapor pressure at 650°C (28.3 Torr) and (2) the high disordering of Zn atoms in liquid Zn nanoparticles at 650°C makes them invisible in XAS even if they have a long lifetime. The immediate vaporization after the formation of liquid Zn nanoparticles is

supported by the decrease of intensity of the Zn-O peak in R-space spectrum collected during catalysis at 650°C as a function of time (Figure 6.5). Based on the R-space spectrum of Zn K-edge during catalysis at 650°C (Figure 6.3c), these Zn atoms were bonded with O atoms. As catalytic measurements suggest that these remained Zn species did not contribute to the formation of ethylene at 650°C, we deduce that these remained Zn atoms migrated to the framework of S-1 instead of anchored on the internal wall of the micropores. These embedded Zn atoms survived under the catalytic condition at 650°C.

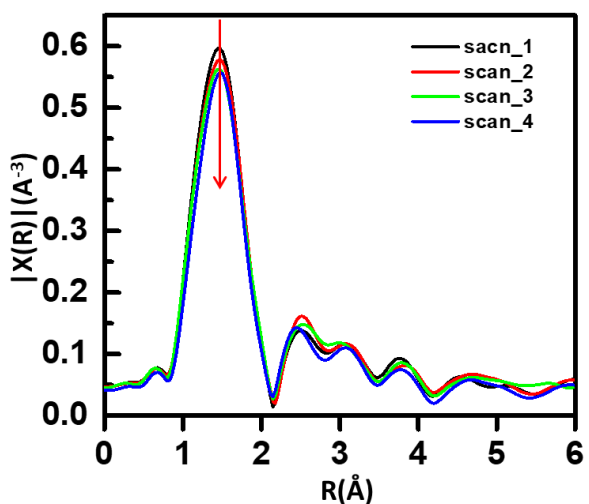


Figure 6. 5 Sequential R-space spectra of Zn K-edge of 2.0wt%Zn/S-1 studied with EXAFS technique during catalysis at 650°C (Scan #1 is the first spectrum and scan #4 is the last one).

The loss of Zn atoms during catalysis at 650°C was supported by the decrease of the intensity $|\chi(R)|$ of the peak of Zn-O bonds in the R-space spectrum of Zn K-edge of the 2wt%Zn/S-1 catalyst at 600°C as a function of time (Figure 6.5). In Figure 6.5, the intensity of a scan collected early, such as scan #1, is larger than the one collected later, such as scan #4. Notably, all scans in Figure 6.5 were collected under the same catalytic condition with the same data acquisition parameters of XAS; thereby, they are comparable.

3.4 Enhancement of activity and durability of Zn-base catalyst by adding Pd

As reported from the publication²⁵⁴, Pd presents a good capability for the dissociation of C-H bond of short alkanes. In addition, the metallic Pd is pretty stable at high temperatures since it exhibits a much higher melting point, 1555°C and correspondingly much lower vapor pressure than metallic Zn. Vapor pressures of solid and liquid Pd can be calculated with the following equations²⁵³: $\log(p/atm) = 9.502 - \frac{19813}{T} - 0.9258 \times \log(T)$ (for solid Pd) and $\log(p/atm) = 5.426 - \frac{17899}{T}$ (for liquid Pd). At 650°C, the vapor pressure of metal Pd is 1.50×10^{-12} Torr which is lower than 28.3 Torr of metal Zn by 13 orders of magnitude. The formation of Zn-based alloy could stabilize the Zn-based sites since PdZn alloy has a melting point much higher than pure Zn²⁵⁵.

Thus, Pd was introduced to 2.0wt%Zn/S-1. Before evaluating the catalytic performance of 2.0wt%Zn/1.0wt%Pd/S-1, the Pd-modified S-1, 1.0wt%Pd/S-1 was prepared with the same method as that of 2.0wt%Zn/S-1 as a reference. Figure 6.2c presents the catalytic performance of 0.100 g of 1.0wt%Pd/S-1. Here, the conversion of ethane at 550°C was over 90% and did not further increase when the temperature increased to 600°C and 650°C. Unfortunately, the selectivity for producing ethylene was quite low, near to zero. It suggests that Pd-based sites of this catalyst are active for the activation of ethane, but the selectivity for the production of ethylene is quite low. As demonstrated in Figure 6.2d, the activity of ethane dehydrogenation into ethylene with 2.0wt%Zn/1.0wt%Pd/S-1 were considerably increased along with the temperature elevated from 500°C to 650°C, reaching more than 55% conversion of ethane and over 30% selectivity of the production of ethylene. The yield of ethylene reached approximately 30% at 650°C. These findings confirmed that the addition of Pd promotes the catalytic activity of dehydrogenation of ethane into ethylene.

Moreover, Figure 6.4b presents the time-on-stream catalytic performance of 2.0wt%Zn/1.0wt%Pd/S-1 for ethane dehydrogenation for 15 h. In terms of the durability of catalytic performance, it is much different from that of 2.0wt%Zn/S-1. As shown in Figure 6.4b, the 2.0wt%Zn/1.0wt%Pd/S-1 provided a 30% yield of ethylene for over 15 hours. Thus, the addition of 1.0wt%Pd to 2.0wt%Zn/S-1 obviously enhanced the durability of catalytic performance of 2.0wt%Zn/S-1. The observation of constant yield of 2.0wt%Zn/1.0wt%Pd/S-1 for over 15 hours demonstrated that the addition of the second metal could enhance the durability of catalytic performance of another metal. Through operando studies of chemical and coordination environment of these metals during catalysis at 650°C, the fundamental understanding of the effect of Pd to Zn was achieved and will be discussed in the following sections.

3.5 Formation of Pd-Zn alloy in the proposed catalyst

XANES and EXAFS studies of 2.0wt%Zn/1.0wt%Pd/S-1 before catalysis and during catalysis at 650°C. As shown in Figure 6.6a, the edge feature of Pd K-edge before catalysis at 25°C is quite different from that of Pd foil. Compared to Pd foil, the energy position of Pd K-edge of this catalyst during catalysis at 650°C was up-shifted, suggesting that Pd atoms of this catalyst before catalysis were in the oxidic state. On the contrary, the shape and energy position of Pd K-edge of this catalyst during catalysis at 650°C was close to that of Pd foil, indicating that Pd atoms were reduced during catalysis at 650°C.

Figure 6.6b is the R-space spectrum of Pd K-edge of 2.0wt%Zn/1.0wt%Pd/S-1 before catalysis. Two main peaks were observed at 2.00 Å, and 2.92 Å, attributed to Pd-O and Pd-O-Pd, respectively, which is supported by the observation of peaks at 2.06 Å for Pd-O and 3.00 Å for Pd-O-Pd in literature^{256, 257}. Compared to 2.0wt%Zn/1.0wt%Pd/S-1 before catalysis at 25°C

(Figure 6.6b), R-space spectrum of this catalyst during catalysis at 650°C (Figure 6.6c) is distinct. Based on the position of the peak of Pd-Zn bonds in Pd-Zn alloy nanoparticles reported in literature^{258, 259}, the main peak at 2.52 Å observed in 2.0wt%Zn/1.0wt%Pd/S-1 during catalysis at 650°C is assigned to Pd-Zn bonds. It clearly shows that most Pd atoms alloyed with Zn atoms. Probably, this peak could cover a small portion of Pd-Pd bonds since the peak position of Pd-Pd bonds of a Pd metal nanoparticles is at 2.78 Å (after phase correction) based on literature²⁶⁰. Consequently, the R-space spectrum of the catalyst during catalysis at 650°C provided solid evidence for the formation of Pd-Zn alloy under this catalytic condition. It is understandable since H₂ is the product of ethane dehydrogenation ($C_2H_6 \rightarrow C_2H_4 + H_2$). Molecular H₂ is typically formed through the coupling of H atoms. In ethane dehydrogenation, H atoms are intermediate formed in C-H cleavage of ethane and dehydrogenation of ethane to form ethylene. The formed H atoms could directly bond with oxygen anions to form a hydroxyl group; a hydroxyl group can bond with another H atom to form an H₂O molecule. With desorption of H₂O molecules, oxygen atoms coordinating with some metal atoms of the catalyst surface are removed. The removal of oxygen atoms through the formation of H₂O molecules results in a reduction of surface cationic Pd atoms bonding with oxygen atoms into Pd atoms at metallic state. Similarly, oxygen atoms bonding to Zn cations can be removed through the formation of H₂O molecules, by which Zn cations were reduced to Zn atoms at metallic state. These reduced Pd and Zn atoms can readily form Pd-Zn alloy during catalysis at 650°C.

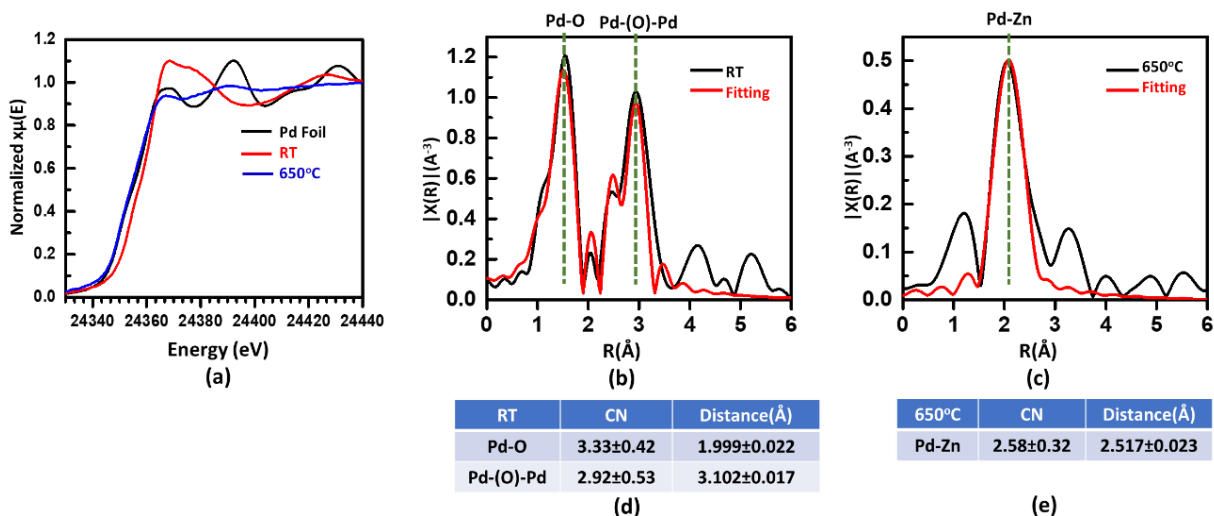


Figure 6.6 Operando studies of Pd K-edge of 2.0wt%Zn/1.0wt%Pd/S-1 using XANES and EXAFS. (a) Energy space spectra of Pd K-edge of Pd foil, catalyst before catalysis at 25°C and catalyst during catalysis at 650°C. (b) R-space spectra of Pd K-edge before catalysis at 25°C. (c) R-space spectrum of Pd K-edge of the catalyst during catalysis at 650°C. (d) List of parameters used in fitting R-space spectra of Pd K-edge in (b). (e) List of parameters used in fitting R-space spectra of Pd K-edge in (c).

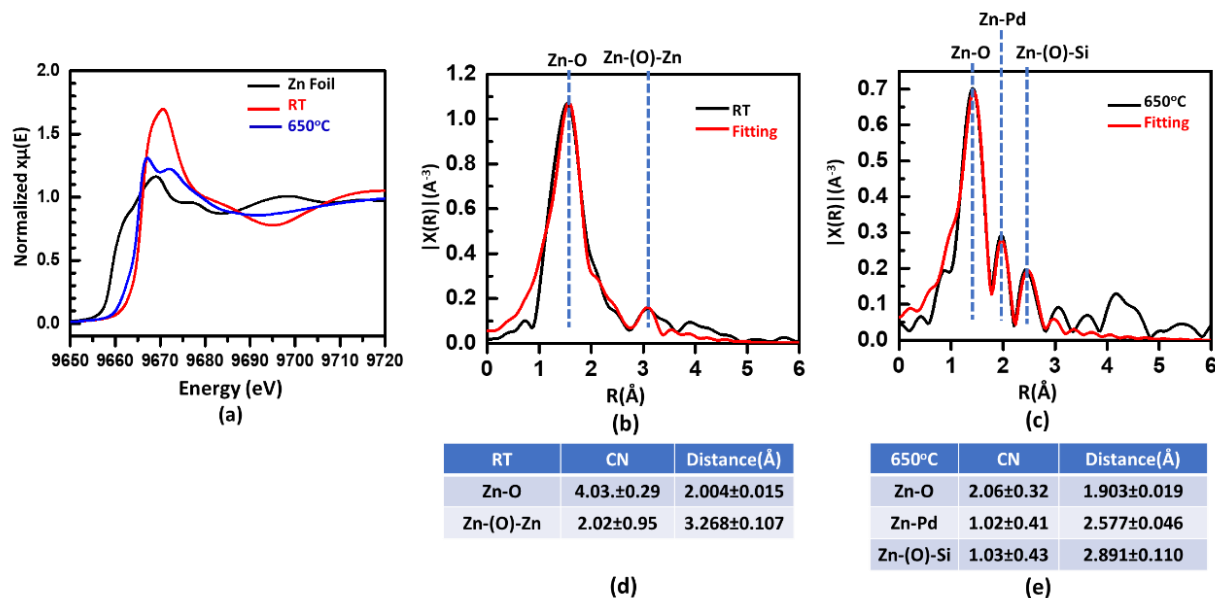


Figure 6.7 Operando studies of Zn K-edge of 2.0wt%Zn/1.0wt%Pd/S-1 using XANES and EXAFS. (a) Energy space spectra of Zn K-edge of Zn foil, the catalyst before catalysis at 25°C and the catalyst during catalysis at 650°C. (b) R-space spectra of Zn K-edge of the catalyst before catalysis at 25°C. (c) The R-space spectrum of Zn K-edge of the catalyst during catalysis at 650°C. (d) List of parameters used in fitting R-space spectra of Zn K-edge in (b). (e) List of parameters used in fitting R-space spectra of Zn K-edge in (c).

The formation of Pd-Zn alloy nanoparticles was further supported by studies of Zn K-edge of 2.0wt%Zn/1.0wt%Pd/S-1 before catalysis at 25°C and during catalysis at 650°C. Figure 6.7a is

the energy space spectra of Zn foil and 2.0wt%Zn/1.0wt%Pd/S-1 before catalysis at 25°C and during catalysis at 650°C. Obviously, the edge feature of the catalyst before catalysis at 25°C was different from Zn foil, suggesting that Zn atoms of the catalysts before catalysis is not in the metallic state. The energy position of the Zn K-edge (red spectrum) at 25°C indicated that Zn atoms of the catalyst were in the oxidic state²⁴⁸. In contrast, the edge feature of 2.0wt%Zn/1.0wt%Pd/S-1 collected during catalysis at 650°C (blue spectrum in Figure 6.7a) was quite different with either Zn foil or ZnO nanoparticles, suggesting that the cationic Zn atoms of the catalyst before catalysis at 25°C were reduced during catalysis at 650°C to some extent.

The R-space spectrum of Zn K-edge of 2.0wt%Zn/1.0wt%Pd/S-1 before catalysis at 25°C (Figure 6.7b) has a main peak at 2.00 Å and a quite weak peak at 3.27 Å, corresponding to Zn-O and Zn-O-Zn, respectively based on R-space spectrum of ZnO nanoparticles²⁴⁸. The intensity of the weak peak of Zn-O-Zn at 3.27 Å is probably negligible, suggesting that the size of ZnO clusters is extremely small even if a minimum portion of Zn atoms are in the second shell of Zn atoms. In fact, the major peak of Zn-O and the negligible peak of Zn-O-Zn in R-space spectrum suggest that most Zn atoms are at the cationic state and mainly singly dispersed in this catalyst.

Compared to the catalyst 2.0wt%Zn/1.0wt%Pd/S-1 before catalysis at 25°C (Figure 6.7b), the catalyst 2.0wt%Zn/1.0wt%Pd/S-1 during catalysis at 650°C exhibits a quite different R-space spectrum of Zn K-edge (Figure 6.7c). Although the peak of Zn-O was still the main peak, two additional peaks at 2.58 Å and 2.89 Å in Figure 6.7c were obviously observed from this catalyst during catalysis at 650°C. Based on the Zn-Pd bond length of Pd-Zn alloy reported in literature^{258, 259}, the peak at 2.58 Å in Figure 6.7c is associate with Zn-Pd bonds. This clearly shows the formation of Pd-Zn alloy for 2.0wt%Zn/1.0wt%Pd/ S-1, which is consistent with the peak of Pd-Zn bonds in R-space spectrum of Pd K-edge of the same catalyst during catalysis at 650°C (Figure

6.6c). This consistency makes us safely conclude that Pd and Zn did form alloy during catalysis on 2.0wt%Zn/1.0wt%Pd/ S-1 at 650°C. In addition, the peak at 2.89 Å in Figure 6.7c was observed and assigned to Zn-O-Si. It seems that the peak of Zn-O-Si in catalyst before catalysis at 25°C was quite weak (Figure 6.7b). Probably, working at 650°C for a few hours had made some of the Zn atoms migrate to the framework of S-1. This migration increased the ordering of the atoms (Si) in the second shell of Zn atoms since Zn atoms could be embedded in the framework at 650°C instead of capping on the internal surface of the micropore at 25°C. The high ordering of Si atoms in the second shell of these embedded Zn atoms, thus results in a relatively higher intensity of the peak of Zn-O-Si in the R-space spectrum of Zn K-edge of 2.0wt%Zn/1.0wt%Pd/S-1.

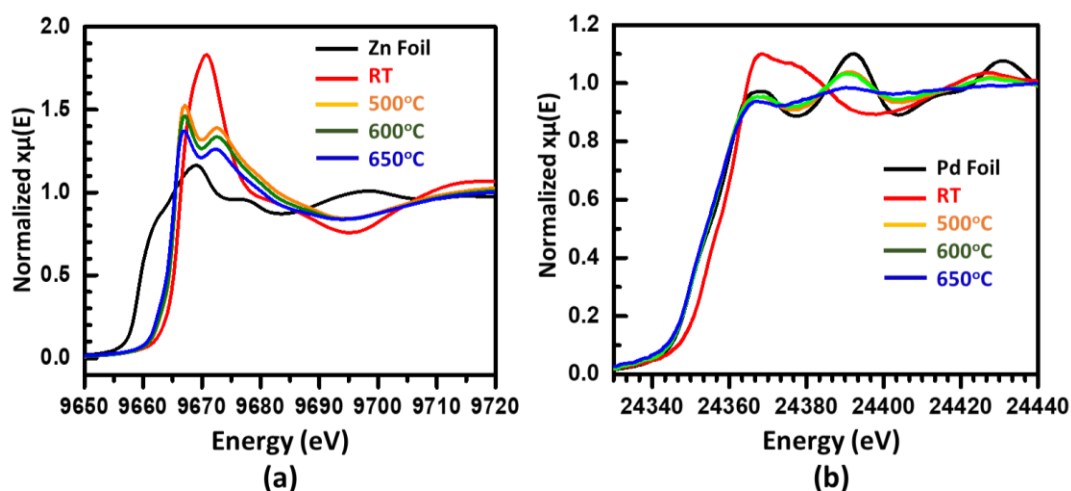


Figure 6. 8 Evolutions of energy space spectra of (a) Zn K-edge and (b) Pd K-edge of 2.0wt%Zn/1.0wt%Pd/S-1 before catalysis at 25°C (red), during catalysis at 500°C (yellow), during catalysis at 600°C (green), and during catalysis at 650°C (blue) studied with operando XANES.

Temperature-dependent evolutions of edge features of Zn K-edge and Pd K-edge of 2.0wt%Zn/1.0wt%Pd/S-1 are presented in Figure 6.8. Clearly, chemical environments in terms of oxidation states of Zn atoms at 500-650°C are significantly different from that before catalysis at 25°C. A certain amount of Zn atoms was reduced during catalysis. At 650°C (blue spectrum in Figure 6.8a), the pre-edge of metallic Zn atoms was basically seen. It suggests that a certain amount

of metallic Zn was formed; based on studies of R-space of Pd K-edge in Figure 6.9a, these metallic Zn atoms are from Pd-Zn alloy. Figure 6.8b presents the evolution of edge features of Pd K-edge of 2.0wt%Zn/1.0wt%Pd/S-1 during catalysis at different temperatures. Before catalysis at 25°C, Pd atoms were at oxidic state (red spectrum in Figure 6.8b). A major change of edge features of Pd K-edge occurred at 500°C, showing Pd atoms were turned to the metallic state (yellow spectrum).

On the other hand, the obvious transition of the oxidation state of Pd atoms of 2.0wt%Zn/1.0wt%Pd/S-1 to a metallic state can be readily seen from the evolution of R-space feature of Pd K-edge of 2.0wt%Zn/1.0wt%Pd/S-1 during catalysis (Figure 6.9). At 500°C, the peak of Pd-Pd bonds in the R-space spectrum of Pd K-edge was the main peak, while the peak of Pd-Zn bonds was also obvious obtained (Figure 6.9a). Notably, there was a lack of peak of Pd-O bonds during catalysis at 500°C, showing that all Pd atoms during catalysis at 500°C were at a metallic state, although a portion of Zn atoms coordinates with oxygen atoms (Figure 6.10a). Reduction of all Pd atoms to the metallic state during catalysis at 500°C or even at a lower temperature is reasonable as the conversion and selectivity of this catalyst at 500°C are 20% and 22%, respectively (Figure 6.2d). Along with the rising of catalysis temperature, the intensity of the peak of Pd-Zn bonds increased and even almost became the dominant peak during catalysis at 600°C (Figure 6.9b). This increase of relative intensity of the peak of Pd-Zn bonds suggests that more Pd atoms directly bond with Zn atoms at 600°C; in other words, higher catalysis temperature led to better alloying between metallic Pd atoms and metallic Zn atoms. Interestingly, the peak of Pd-Pd bonds disappeared at 650°C (Figure 6.9c). As Pd does not vaporize at 650°C, the disappearance of the peak of Pd-Pd bonds at 650°C suggests that all Pd atoms fully mixed with metallic Zn atoms to form Pd-Zn alloy. In principle, the intensity of the peak of Pd-Zn bonds at

650°C in Figure 6.9c should be higher than that of 500°C or 600°C (Figures 6.9a and 6.9b) since more Pd-Zn bonds formed at 650°C than 500°C or 600°C. It is deduced that the larger thermal factor at 650°C probably decreased the intensity of the peak of Pd-Zn bonds even though the number of Pd-Zn bonds at 650°C is larger than that during catalysis at 500°C or 600°C.

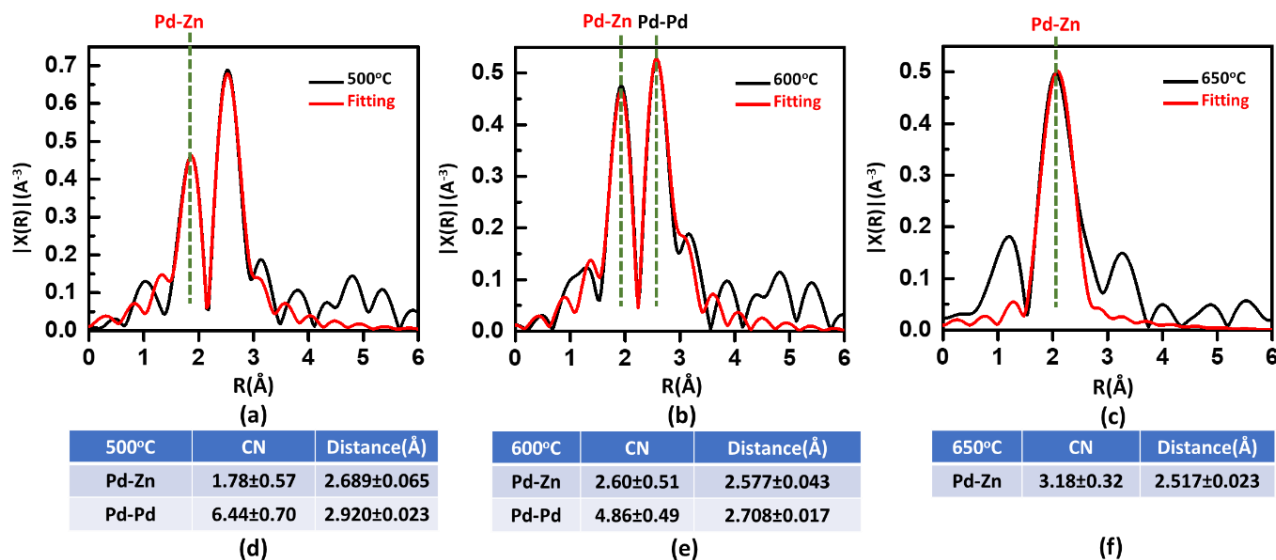


Figure 6. 9 Evolutions of R-space spectra of Pd K-edge of 2.0wt%Zn/1.0wt%Pd/S-1 (a) during catalysis at 500°C, (b) during catalysis at 600°C, and (c) during catalysis at 650°C. (d) List of parameters used in fitting R-space spectra of Pd K-edge in (a). (e) List of parameters used in fitting R-space spectra of Pd K-edge in (b). (f) List of parameters used in fitting R-space spectra of Pd K-edge in (c).

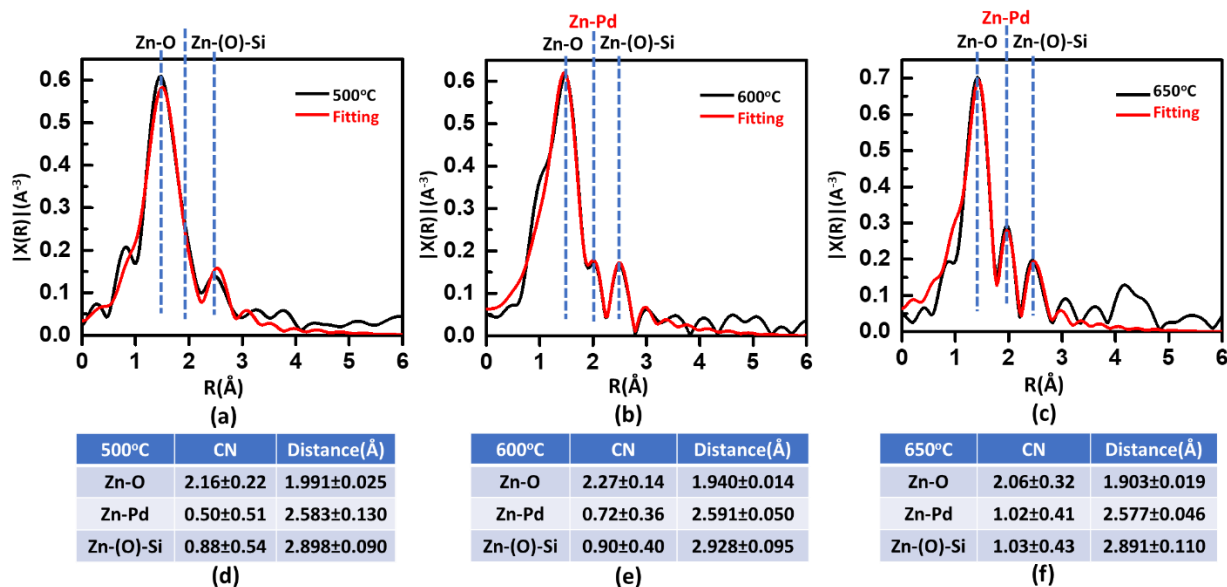


Figure 6. 10 Evolutions of R-space spectra of Zn K-edge of 2.0wt%Zn/1.0wt%Pd/S-1 (a) during catalysis at 500°C, (b) during catalysis at 600°C, and (c) during catalysis at 650°C. (d) List of parameters used in

fitting R-space spectra of Zn K-edge in (a). (e) List of parameters used in fitting R-space spectra of Zn K-edge in (b). (f) List of parameters used in fitting R-space spectra of Zn K-edge in (c).

Better alloying at a higher temperature is also supported by the evolution of features of the R-space spectrum of Zn K-edge of 2.0wt%Zn/1.0wt%Pd/S-1 along with the increase of catalysis temperature from 500°C to 650°C (Figure 6.10). As shown in Figure 6.10a, the peak of Zn-O bonds was the dominant peak during catalysis at 500°C. The contribution of Zn-Pd bonds to the R-space spectrum of Zn K-edge (Figure 6.10a) did not appear as a separate peak, although the contribution of Pd-Zn bonds to R-space spectrum of Pd K-edge was quite obvious at a higher temperature shown in Figure 6.9c.

In terms of the evolution of the R-space spectrum from 25°C to 500°C, the feature of R-space of Zn K-edge of 2.0wt%Zn/1.0wt%Pd/S-1 during catalysis at 500°C (Figure 6.10a) is similar to that before catalysis at 25°C (Figure 6.7b). However, in the case of the evolution of energy space spectrum from 25°C to 500°C, the feature of energy space spectrum of Zn K-edge of 2.0wt%Zn/1.0wt%Pd/S-1 during catalysis at 500°C (yellow spectrum in Figure 6.8a) is different from that before catalysis at 25°C (red spectrum in Figure 6.8a). The inconsistency between the evolution of the R-space spectrum of Zn K-edge and the evolution of the energy space spectrum of Zn K-edge for the same catalyst 2.0wt%Zn/1.0wt%Pd/S-1 remains unknown here. Considered this unsolved inconsistency, the invisibility of peak of Zn-Pd bonds of 2.0wt%Zn/1.0wt%Pd/S-1 at 500°C in R-space spectrum of Zn K-edge (Figure 6.10a) would not be taken as evidence to against the formation of Pd-Zn bonds firmly evidenced in the clear observation of Pd-Zn bonds in R-space spectrum of Pd K-edge of 2.0wt%Zn/1.0wt%Pd/S-1 during catalysis at 500°C (Figure 6.9a). Along with the increase of catalysis temperature to 600°C, the contribution of Pd-Zn bonds became a visible shoulder at 2.59 Å (Figure 6.10b). Compared to the shoulder at 600°C, a separate peak of Pd-Zn bonds was clearly observed during catalysis at 650°C (Figure 6.10c). Thus, the

evolution of the contribution of Pd-Zn bonds in the R-space spectra of Zn K-edge supports the better extent of alloying at a higher temperature.

4. Conclusion

This work investigated the Pd promoted Zn-based catalysts exhibiting decent activity and durability of the production of ethylene from ethane dehydrogenation at high temperatures. Compared to the rapid decay of catalytic activity of 2.0wt%Zn/S-1 for ethane conversion within the first few hours, 2.0wt%Zn/1.0wt%Pd/S-1 exhibited a constant yield of ethylene (about 30%) at 650°C for at least 15h. The fundamental studies of two catalysts by using operando XAS techniques explored the following understandings of catalysts:

- (1) The deactivation of Zn-based catalysts. It was found that active sites of 2.0wt%Zn/S-1 were restructured at a high temperature during catalysis via two routes. One is the formation of Zn metal nanoparticles with a followed immediate vaporization since metal zinc has a quite low melting point and liquid metallic Zn at high temperatures has extremely high vapor pressure. Another is the migration of Zn atoms to the framework of micropores of the catalyst. These findings indicate that the significant restructuring of catalytic sites could be derived from product molecules or intermediates of a reaction during the catalysis.
- (2) The role of Pd in the Pd-Zn catalyst. The in-situ XAS experiments confirmed the formation of Pd-Zn alloy during catalysis. Such alloy, associated with active sites for the production of ethylene, could effectively prevent Zn from being lost through vaporization. The demonstration of the enhancement of activity and durability of catalytic performance of Zn-based catalytic sites through the formation of Pd-Zn alloy suggests a potential path

toward developing a catalyst with high selectivity and durability of catalytic performance at high temperature.

Contributions of the project:

The synthesis of catalysts, characterizations of catalysts, evaluation of catalytic performances of prepared catalysts and in-situ EXAFS studies were mainly done by Yuting Li.

Chapter 7: Synthesis of Na@nanoFAU zeolite catalyst and catalysis for production of formic acid with Na@nanoFAU

1. Introduction

Microporous aluminosilicates are widely used in chemical and energy industries^{56, 66, 75-82}. These supports can be used to anchor catalytic metal atoms/sites for the transformation of CH₄ to intermediates of chemical industries such as methanol or acetic acid in liquid phase at a relatively low temperature⁸⁶⁻⁹³. Sizes of particles of porous aluminosilicate are typically a few hundreds of nanometers or even larger. In other words, the lengths of these porous channels are typically a few hundreds of nm or longer. In petrochemical industries, this type of microporous material was used to catalyze reactions performed at high temperature (>500°C)^{16, 78, 83, 84}. At a high temperature, reactant and product molecules can diffuse in micropores at a reasonable rate. When such microporous materials are at a low temperature (<200°C) or are in liquid phase^{53, 65, 226}, unfortunately, slow molecular diffusion in the confined micropores (<1 nm) with a long travel of a few hundred nanometers in a liquid media could largely limit the rate of reaction performed in the micropores. In this case, molecules of reactant in liquid at a low temperature (<200°C) have to diffuse through the confined liquid environment in microporous channels to reach the catalytic sites in the micropores; in addition, product molecules have to diffuse from catalytic sites immobilized in micropores to the external surface of an aluminosilicate particle to enter the solution. The long diffusion paths are schematically shown in Figures 7.1a and 7.1b.

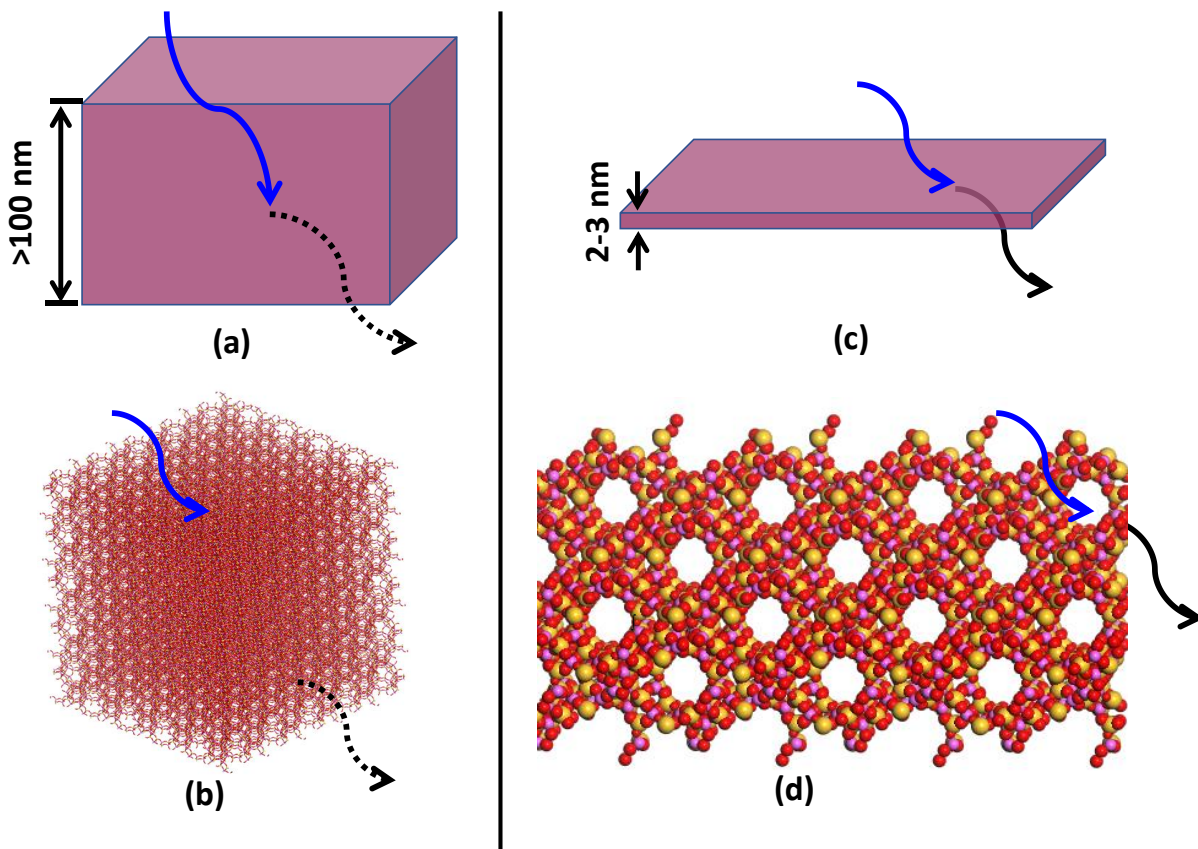


Figure 7. 1 Schematic showing molecular diffusion in micropores of FAU (a and b) and nanoFAU (c and d). At a relatively low temperature, there could be a diffusion limit of reactant and product molecules in regular FAU particles (a and b) due to both the small micropores with a diameter of subnanometer and the long channels with a length of a few hundreds of nm. Such diffusion (a and b) could be minimized by the synthesis of nanoFAU (c and d) which has a thickness of a few nanometers.

To avoid such a mass diffusion limit of reactants and products of catalysis performed at a low temperature in liquid, here we synthesized nanosheets of zeolite^{261, 262} as schematically shown in Figures 7.1c and 7.1d. Figure 7.2a is a schematic of the precursor used for synthesizing Na@nanoFAU. The first step is the crystallization of aluminosilicate in a limited space between adjacent graphene oxide layers. The lamellar graphene oxide structure²⁶³⁻²⁶⁶ acts as a scaffold. After the formation of aluminosilicate in the confined interlayer spaces formed by layered graphene oxide (Figure 7.2a), the graphene layers were removed through the formation of CO₂ and H₂O by calcination of the graphene oxide layers in air at a high temperature. It is found that the as-synthesized Na@nanoFAU with a thickness of 2-3 nm can catalyze the synthesis of formic

acid from CO and H₂O in aqueous solution at 150°C while the regular FAU anchored with Na⁺ (Na@FAU) is not active for this reaction under the same catalytic condition. This difference suggests that the synthesis of ultrathin zeolite can provide a platform for promoting catalytic reactions performed in micropores in the liquid environment at a relatively low temperature. Notably, there is no commercially direct catalytic route of synthesizing formic acid from CO. The well-known catalytic process developed by BASF and Kemira^{229, 267, 268} involves the reaction of pure methanol and CO of 5 MPa to form methyl formate at high temperature and a followed hydrolysis of methyl formate with an excess of water at 200°C to form formic acid-methanol-methyl formate aqueous mixture. Compared to the industrial process of synthesis of formic acid with a starting material methanol, here a direct synthesis of formic acid from CO and H₂O on nanosheets FAU with anchored Na⁺ (Na@nanoFAU) was demonstrated.

2. Experiment

2.1 Synthesis and characterizations of Na@nanoFAU

Na@nanoFAU was synthesized through using layered graphene oxide²⁶³⁻²⁶⁵ as a lamellar template. By filling precursor of aluminosilicate²⁶⁹ in the space between graphene oxide layers, NaOH_{aq} and Al powder were reacted to form low molecular weight sodium aluminate species, and NaOH_{aq} and Ludox HS-30 colloidal silica were employed as a source of low molecular weight sodium silicate species. The total gel composition was 9Na₂O: 0.7Al₂O₃: 10SiO₂: 180H₂O. Graphene oxide GO-Na@nanoFAU composite was formed via hydrothermal synthesis at 50 °C for 50 h under autogenous pressure. High-temperature combustion of the graphene oxide in air removed the graphene layers, forming nanosheet-like Na@nanoFAU.

The formed Na@nanoFAU was identified with the scanning electron microscope (SEM) and transmission electron microscope (TEM) techniques. SEM images were taken by Zeiss Ultraplus thermal field emission scanning electron microscope with ~5 nm sputtered gold coating. Transmission electron microscope (TEM) JEOL 2100F 200 kV FEG-STEM/TEM microscope was equipped with a CEOS Cs corrector on the illumination system. High angle annular dark-field (HAADF) images were acquired with a Fischione Model 3000 HAADF detector.

The thickness of the prepared nanosheet FAU was also estimated by the AFM technique. AFM images were obtained on TT-AFM system under vibration mode with a 10 nm wide tip and analyzed by Gwyddion 2.41 software.

Dynamic light scattering (DLS) measurements: the average hydrodynamic diameter of the nanocrystals in suspensions was determined with a Malvern Zetasizer Nano in the backscattering mode with the scattering angle 173° , HeNe laser with 3 mW output power at 632.8 nm wavelength.

X-ray Diffraction (XRD) measurements: XRD spectra were collected by a Rigaku D/Max 2100 Powder X-ray Diffractometer (Cu $K\alpha$ radiation) in increments of 0.02 degrees and an exposure time of 1.2 s/step in the angular range of 5-60 degrees.

The surface area of the as-synthesized Na@nanoFAU was measured with BET. Nitrogen adsorption isotherms were measured on Micrometrics ASAP 2020 BET analyzer. Samples were degassed at 250°C under vacuum for 5 hours prior to the measurement. The external surface area was calculated using the t-plot method.

2.2 The evaluation of catalysis via Na@nanoFAU

Catalysis on nanoFAU in terms of synthesis of formic acid from CO and H₂O was performed in a standard Parr batch reactor. 30 mg Na@nanoFAU catalyst was dispersed in 10 mg

deionized water in a beaker which was placed in the Parr reactor. Gas was introduced from a high-pressure gas cylinder of CO. It was sealed in the Parr reactor. CO pressure in the Parr reactor was read and monitored through a pressure gauge installed on the cap of the reactor. The liquid containing Na@nanoFAU was heated to a certain temperature by placing the main body of the stainless reactor to a heated silicon oil bath. The oil bath was heated with a VWR heating plate with a function of tuning output power through the feedback gained from thermocouple through a proportional-integral-derivative controller. The thermocouple probe was directly inserted into liquid near to the bottom of the glass beaker containing H₂O and catalyst particles.

The liquid containing a catalyst below gas phase of CO was vigorously, continuously stirred by a stirring magnetic bar coated with Teflon. The stirring motion of the stirring bar was driven through the magnetic force applied by the VWR heating/stirring plate. Most catalytic reactions were performed at 150°C. When the temperature reached 150°C, the stirring bar started to stir; the moment of starting to stir was considered as the starting time of experiments. After a certain amount of time, typically 3h, the reaction was stopped by immediately removing it from the hot oil bath to a water/ice bath.

3. Result and Discussion

3.1 The formation of Na@nanoFAU

The Na@nanoFAU was synthesized through the following steps. The zeolite synthesis gel was prepared from colloidal silica precursor and Al powder as a source of aluminate anions²⁶⁹. The gel was mixed with lamellar graphene oxide layers. A thorough insertion of the gel into the spacing between graphene oxide layers was done through centrifugation. After centrifugation, the precursor of zeolite was trapped into the space between graphene layers²⁶⁶. It was demonstrated

that the approximate spacing between the layers of swelled graphene oxide is in the range of 1 nm (unswelled) and 7 nm (fully swelled). This confined space likely limits the thickness of zeolite crystals to be grown²⁶⁶. Then, preparation was then performed at 50°C with regular synthesis gel of FAU (physically separated from the GO-FAU composite), forming the nanocomposite consisting of graphene oxide and FAU. Figure 7.2a schematically shows the nanocomposite formed at this step. Its morphology can be seen from the SEM image of the integrated nanoFAU crystal and graphene oxide (Figure 7.2b). Compared to widths of diffraction peaks of XRD of typical FAU crystals^{246, 270}, the broadened width of peaks in Figure 7.2c suggest that the crystals in the GO-zeolite nanocomposite are nanosized. Subsequently, this nanocomposite was purified by ten successive centrifugation/redistribution cycles in deionized water. Then, the scaffold-like graphene oxide layers were removed by calcination in air at 400°C. Figure 7.3a-d is the morphology of Na@nanoFAU after the removal of graphene oxide.

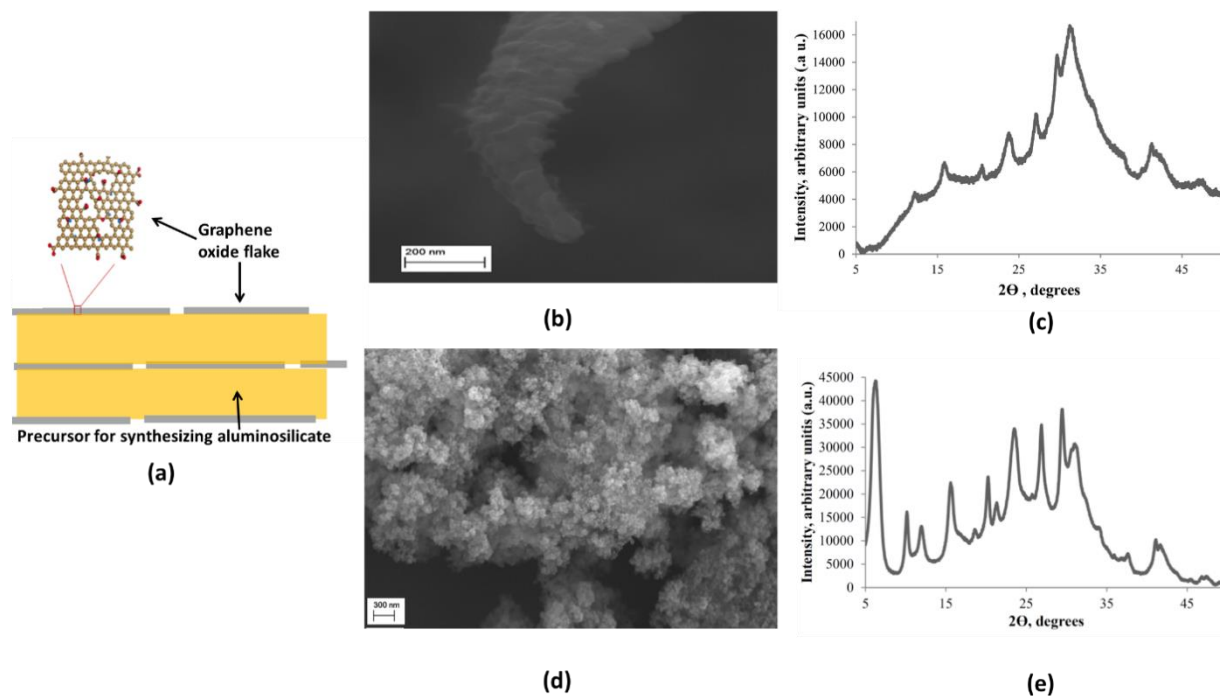


Figure 7. 2 Schematic of synthesis and SEM images of nanocomposite of graphene oxide and precursor of synthesizing aluminosilicate. (a) Schematic showing the formation of nanosheets of FAU by filling precursor to the limited space confined by graphene oxide layers. (b and c) SEM image and XRD of the nanocomposite of graphene oxide and precursor before calcination at 400°C. (d and e) SEM image and XRD of the nanocomposite after calcination at 400°C.

XRD of as-synthesized Na@nanoFAU formed after calcination at 400°C in air to remove graphene oxide flake.

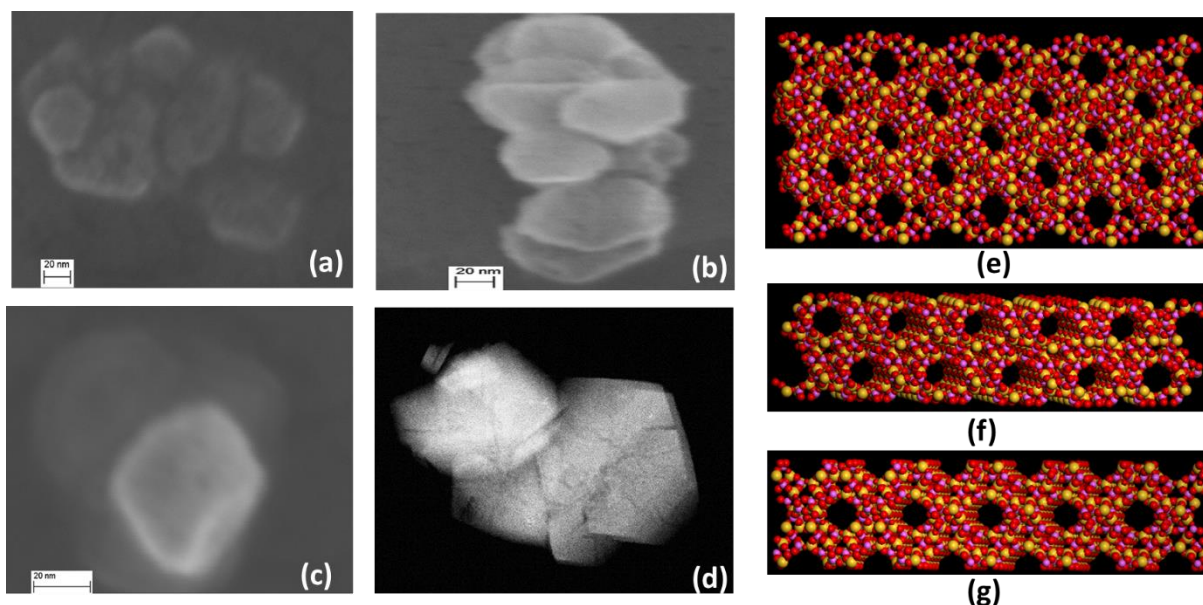


Figure 7.3 TEM images and structural model of Na@nanoFAU. (a-c) Representative SEM images of the sonicated dilute colloidal suspension of Na@nanoFAU (after graphene oxide was removed) after being dried on the TEM grid and then being sputtered with a gold film (60 seconds sputtering, ~5-10 nm thickness). These images show that these well-defined Na@nanoFAUs were successfully synthesized. (d) Representative SEM image of the commercial FAU crystals with a lateral dimension and thickness of 300-500 nm. (e-g) View of a Na@nanoFAU with a thickness of a single unit cell (2-3 nm) along Z-direction.

The synthesized nanoFAU species have nanosheet-like morphology (Figure 7.3). Based on TEM images, the sizes of nanosheets are in the range of 20-40 nm. Thickness of these nanosheets of FAU was measured with AFM. Line profiles of the three nanosheets of Na@nanoFAU in Figure 7.4a were plotted in Figure 7.4b. These line-profiles of AFM measurements show that these nanosheets have thicknesses of about 2-3 nm. These characterizations allow us to conclude that nanoFAU was successfully synthesized with this new method. Here we call these nanosheets Na@nanoFAU. Notably, this nanoFAU is distinctly different from the commercial FAU^{82, 271} which typically has a thickness of a few hundreds of nanometers in all directions. The sizes measured with AFM in Figure 7.4 are relatively smaller than the sizes measured with SEM in

Figure 7.3. This is understandable since AFM typically has the convolution effect in measuring sizes of particles.^{272, 273}

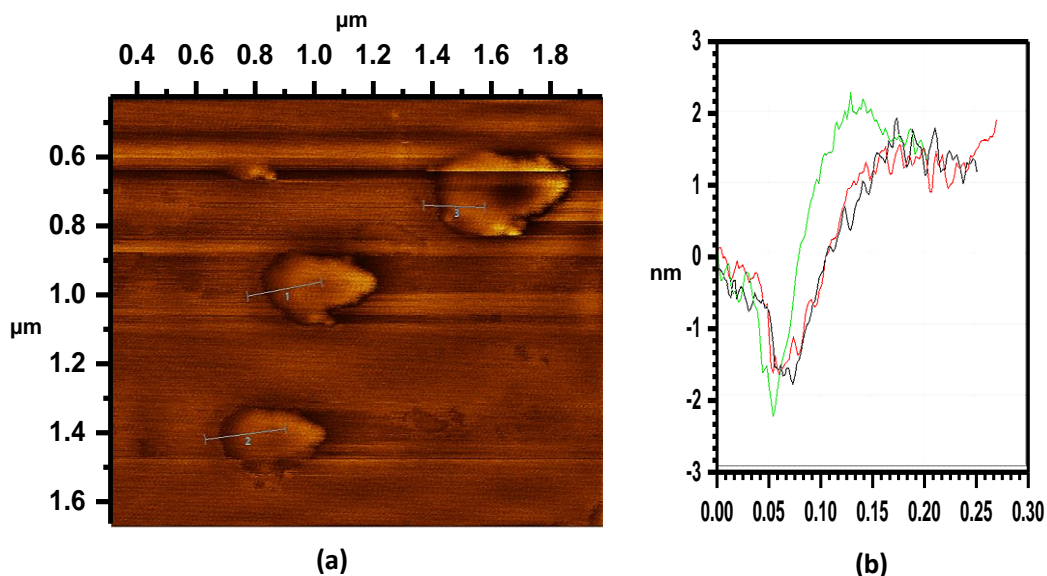


Figure 7. 4 Size and thickness of Na@nanoFAU studied with AFM. (a) AFM images of three pieces of Na@nanoFAU; their two-dimensional size is in the range of 200-300 nm. (b) Line profile of the height of the three Na@nanoFAUs of (a); the Y-axis of (b) gives the thickness of these Na@nanoFAUs; it is about 2-3 nm, only a unit cell of a regular FAU crystal.

The crystallization of as-synthesized nanoFAU sheets was confirmed with high-resolution cryogenic TEM at Electron Microscopy Center at Arizona State University. In TEM image (Figure 7.5), there are many “aggregates”. Each “aggregate” is a Na@nanoFAU particle consisting of several stacked nanosheets. The size of an aggregate measured with high-resolution TEM images (20-40 nm) is quite consistent with the average size of Na@nanoFAU suggested from the dynamic light scattering profile of dilute colloidal suspension of Na@nanoFAU (Figure 7.6a). Nitrogen physisorption shows that the external and total surface areas are 430 and 820 m²/gram, respectively (Figure 7.6b). The amount of loaded Na cations in the catalyst was calculated according to the molar ratio of the composition gel. It is 10.05±0.25wt%. In the following paragraph, Na@nanoFAU or 10wt%Na@nanoFAU was used to denote this catalyst.

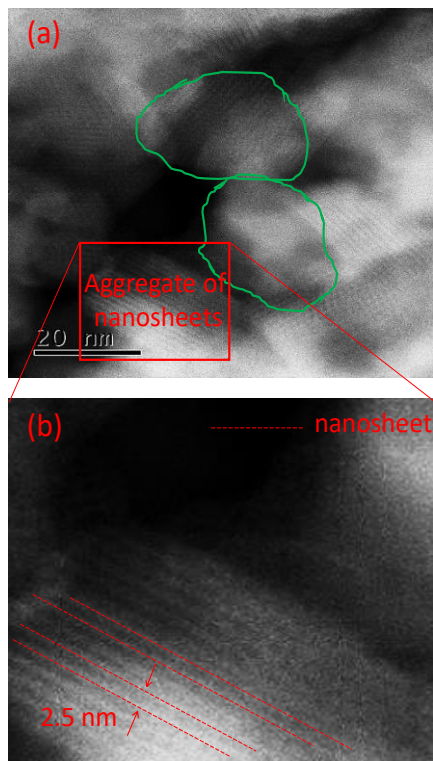


Figure 7. 5 HAADF-STEM images of Na@nanoFAU. (a) Image consisting of several Na@nanoFAU aggregates (or called nanoparticles); in each aggregate, several Na@nanoFAU sheets are stacked in parallel; the green circles mark aggregates; morphologies of these nanosheets can be seen well. (b) Enlargement of the section marked with red box in (a); each dashed line marks a nanosheets. The distance between two nanosheets is about 2.5 nm. The successful observation of these nanosheets shows the successful synthesis of Na@nanoFAU with a thickness of a single unit cell of a FAU crystal.

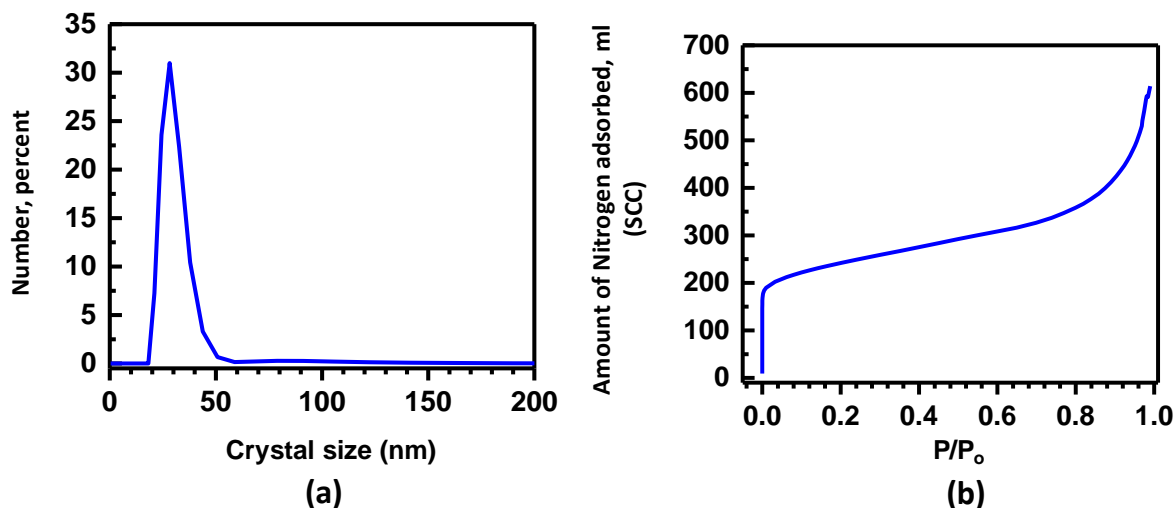


Figure 7. 6 Dynamic light scattering profile of dilute colloidal suspension of Na@nanoFAU (a) and N₂ physisorption isotherm on Na@nanoFAU (b).

3.2 The production of formic acid via Na@nanoFAU

The formation of formic acid from CO and H₂O on Na@nanoFAU in aqueous solution in a Parr reactor under high-pressure CO was studied. Before examining the potential activity of Na@nanoFAU for the synthesis of formic acid from CO and H₂O, a series of control experiments were performed. The yields of HCOOH in these control experiments were presented in Table 7.1. In the first control experiment (A in Table 7.1), no catalyst was added; 10 ml deionized water was added to the Parr reactor, 10 bar CO was introduced to the reactor and the reactor was heated to 150°C for 3h. As shown in Table 7.1, the yield of formic acid in the control experiment was almost 0 μmol. To test whether free-standing Na⁺ cations in water could be catalytic sites for the formation of formic acid from CO and H₂O, the same amount of Na⁺ cations as that of 30 mg 10wt%Na@nano-FAU (1.3×10^{-4} mol Na⁺) was dissolved in 10 ml deionized water (no heterogeneous catalyst was added). Here, 7.6 mg of NaCl (1.3×10^{-4} mol Na⁺) was added to simulate the amount of Na⁺ of 30 mg 10wt%Na@nanoFAU (1.3×10^{-4} mol Na⁺); the control experiment (B in Table 7.1) was performed under the same condition as the control experiment A; only 2 μmol of formic acid was observed in this control experiment (B in Table 7.1). It suggests that free-standing Na⁺ cations in aqueous solutions are not active for the synthesis of formic acid from CO and H₂O.

To check whether Brønsted acid sites (H) in Na@nanoFAU could be active for the synthesis of formic acid or not, H@nanoFAU was prepared through ion exchange. 30 mg H-nanoFAU was used in this control experiment under the same condition as the control experiment A. As shown in C of Table 7.1, there were about 10 μmol formic acid formed from H-nanoFAU. It suggests that the Brønsted sites of H@nanoFAU are not very active for the synthesis of formic acid from CO and H₂O. In addition, we also checked whether the Brønsted sites of a regular H-

FAU could be active for the formation of formic acid or not. 30 mg H-FAU was examined under the same condition; less than 5 μmol formic acid was found (D in Table 7.1). To test whether the Brønsted acid sites of commercial NH_4^+ -FAU are active sites or not, the same control experiments were done on 30 mg 10.0wt% NH_4^+ -FAU (E in Table 7.1). Only 5 μmol of formic acid was formed in control experimental E. Another control experiment was done by using 30 mg 5.0wt%Na@ZSM-5. However, only 3 μmol formic acid was observed.

Table 7. 1 Control experiments performed under specific reaction parameters described in the following.

Reaction condition	A	B	C	D	E	F
Amount of formic acid (μmol)	0.5	1.7	10.7	4.8	5.9	3.4

All the six control experiments were performed under a common condition of 10 bar CO, 10 ml deionized H_2O , 150°C for 3 h. (A) Experiment A did not use any catalyst. (B) Experiment B used 7.62 mg NaCl (1.3×10^{-4} mol Na^+) which has the same amount of Na^+ as 30 mg 10wt%Na@nanoFAU (1.3×10^{-4} mol Na^+). (C) Experiment C used 30 mg nanoFAU which does not have any Na^+ . (D) Experiment D used 30 mg H@FAU which does not have any Na^+ . (E) Experiment E used 30 mg of commercial NH_4 @FAU. (F) Experiment F used 30 mg 5.0wt%Na@ZSM-5.

30 mg of the as-synthesized Na@nanoFAU was used as a catalyst in each of the following experiments. The mass concentration of Na^+ in Na@nanoFAU is 10wt%. Its activity was examined under the same condition as these control experiments of Table 7.1. When the pressure of CO was 10 bar, about 108.5 μmol HCOOH was synthesized (Figure 7.7a) after the catalysis of 3h. By increasing the pressure of CO to 50 bar, the amount of formic acid was increased to 221.6 μmol (Figure 7.7a). The increase of the amount of formic acid is probably due to the increased amount of CO dissolved in water at a higher pressure of CO. This finding suggests that the enhancement of CO pressure is favored to the formation of formic acid in this equilibrium reaction. In addition, as shown in Figure 7.7b, the increase of reaction time from 3h to 9h has definitely increased the amount of formic acid. After a reaction of 9h at the CO pressure of 10 bar, 291.0 μmol formic acid

was synthesized. It is nearly 3 times of the amount of formic acid formed in regular reaction time, 3h.

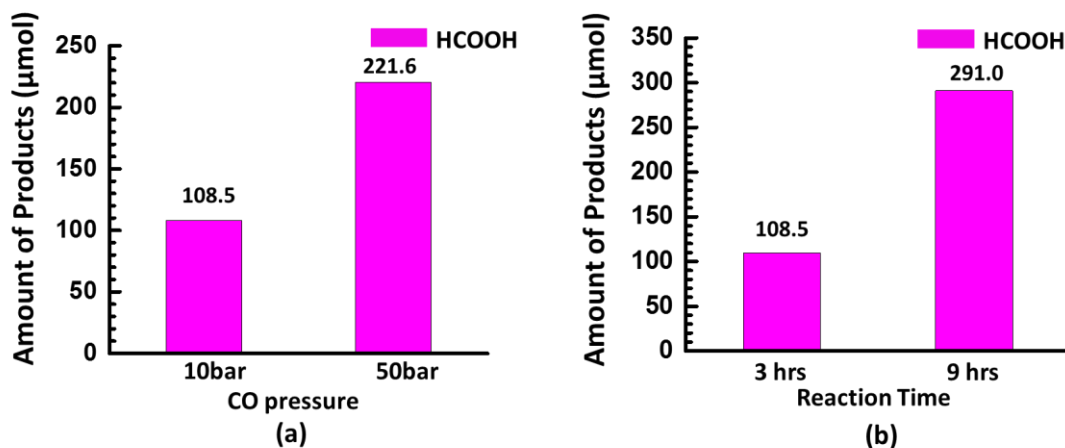


Figure 7. Catalytic performance of 30 mg Na@nanoFAU (10wt%Na@nanoFAU) at 150°C dispersed in 10 ml deionized water under 10 or 50 bar CO sealed in a Parr reactor. (a) Yields of formic acid formed on 30 mg 10wt%Na@nanoFAU at 10 bar and 50 bar CO; 10 bar or 50 bar CO was introduced into a Parr reactor which loaded with 10 ml deionized water, respectively. Each reaction was performed at 150°C for 3 h; the catalyst was vigorously stirred during catalysis. (b) Yields of formic acid catalyzed by 30 mg 10wt%Na@nanoFAU in 10 ml deionized water under 10 bar CO for 3 h and 9 h; the reaction was performed at 150°C.

A major concern is that Na cations could detach from the Al sites to form a free-standing Na^+ sites and the detached Na^+ cations could act as active sites for the formation of formic acid from CO and H_2O . ICP-AES analyses of the concentration of Na^+ in the solution after the synthesis of formic acid were performed at the University of South Carolina. Only 10%-15% of the anchored Na^+ cations of Na@nanoFAU was found in the solution after three cycles of the reaction of 3 h at 150°C. The Na^+ observed by ICP-AES may come from two sources. The portion of the Na^+ cations anchored in the 30 mg Na@nanoFAU could have detached into the aqueous solution during catalysis at 150°C. In addition, the Na@nanoFAU could have degraded into smaller pieces of Na@nanoFAU; this degradation could accelerate the detachment of Na^+ to the aqueous solution. To check whether the Na^+ cations were still remained in the potentially degraded Na@nanoFAU or not, the catalyst was used for catalysis of 3 h; its precipitate was collected; the precipitate was

washed with deionized water for removing Na^+ cations adsorbed on potentially degraded Na@nanoFAU and then it was centrifuged again before a final collection. The catalyst gained in the final collection was dissolved with HNO_3 before ICP-AES measurements. In fact, the ICP-AES measurements showed that 96% of all Na^+ cations still remained in the collected catalyst. In other words, the majority of Na^+ anchored in Na@nanoFAU did not detach to the solution to become free-standing cations. In fact, based on the control experiment B in Table 7.1, free-standing Na^+ cations in aqueous solution contribute very less to the synthesis of formic acid. Thus, the 4% of the anchored Na^+ cations of 30 mg Na@nanoFAU detached from the Na-nanoFAU after catalysis of 3 h at 150°C did not contribute to the formation of formic acid.

A possible explanation to the detachment of 4% of Na^+ cations from Na@nanoFAU to solution is that protons of the aqueous solution could replace 4% of Na^+ cations anchored in micropores of Na@nanoFAU. If 4% of Na^+ cations were replaced by H^+ cations of the aqueous solution, such a potential replacement of 4% of all Na^+ cations (1.3×10^{-4} mol) should have consumed 5.2×10^{-6} mol of protons. To provide 5.2×10^{-6} mol of protons, 5.2×10^{-6} mol H_2O molecules should have been hydrolyzed. Thus, hydrolysis should have formed 5.2×10^{-6} mol of OH^- . Then, the concentration of OH^- in the 10 ml solution could have been 5.2×10^{-4} mol/l. Then, the pH value of the solution should have been 11-12. By carefully checking the pH of the solution after the catalytic reaction, it is in fact 7.0-8.0. It suggests that the explanation of the replacement of Na^+ cations by H^+ during catalysis is not reasonable.

Another study was done to test whether a potential exchange between the anchored Na^+ cations and free H^+ in solution could happen at 150°C . 30 mg Na@nanoFAU with a concentration of Na^+ at 10% was added to 10 mg deionized water and then 10 bar N_2 was introduced to a Parr reactor; then, the reactor was heated to 150°C and remained at 150°C for 3h. Upon this control

experiment, the solution was cooled to 25°C and pH was measured. It is 7.5. Clearly, the measured pH, 7.5 is much different from the expected 11-12. Thus, a potential replacement of Na⁺ by H⁺ in solution at 150°C was excluded. The detached Na⁺ cations could be the Na⁺ weakly physisorbed either in microspores or on the external surface of the as-synthesized nanoFAU sheets since Na⁺ was used in the preparation of this catalyst. Alternatively, it could be Na⁺ cations anchored on broken or degraded Na@nanoFAU.

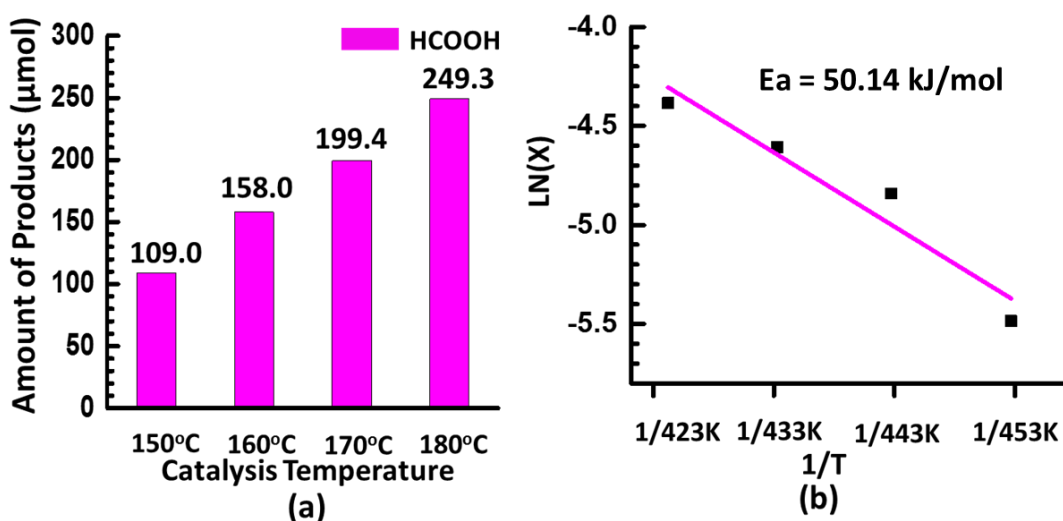


Figure 7. 8 Kinetics studies of the formation of formic acid from CO and H₂O on 30 mg Na@nanoFAU in the temperature range of 150-180°C. (a) Amount of formic acid formed through catalysis on 30 mg Na@nanoFAU (10wt%Na@nanoFAU) at different temperatures. (b) Arrhenius plot for the formation of formic acid under kinetics control regime.

Yields of formic acid at 160°C, 170°C, and 180°C were measured under the same condition (30 mg Na@nanoFAU in 10 ml deionized water under CO gas of 10 bar). As shown in Figure 7.8a, the yields of formic acid at 150°C, 160°C, 170°C, and 180°C are 109.0, 158.0, 199.4 and 249.3 μmol, respectively. The formation of formic acid from CO and H₂O is exothermic^{229, 274}, so pressure increase and temperature decrease could shift the equilibrium of this reaction in favor of the production of formic acid. From the kinetic point of view, the high temperature could enhance the reaction rate. The obviously increased yields of formic acid in Figure 7.8a, along with the

increase of temperature, would result from the catalyst-driven kinetics instead of temperature-promoted kinetics. By plotting the $\ln[X]$ as a function of $1/T$, an Arrhenius plot was generated in Figure 7.8b. Here X is the conversion of CO which is definitely lower than 10% under the current catalytic condition²⁷⁵. The apparent activation barrier calculated from the slope of this Arrhenius plot is 50.1 kJ/mol.

4. Conclusion

In this work, Na@nanoFAU was prepared by synthesizing FAU at a nanoscale via a template of layered graphene oxide. The catalyst is active for the formation of formic acid from CO and H₂O by introducing 10 bar CO into the aqueous solution at 150°C. The apparent activation barrier for the synthesis of formic acid from carbon monoxide and water catalyzed by Na@nanoFAU is 50.1 kJ/mol in the temperature range of 150°C-180°C. The lack of contribution from the Brønsted acid sites of Na@nanoFAU or detached Na⁺ cations to the formation of formic acid suggested that the anchored Na⁺ sites in the Na@nanoFAU are essential in the catalysis. This study demonstrated a direct synthesis of formic acid from CO with the microporous heterogeneous catalysts and suggested a potential application of nanosheet zeolitic material in the transformation of small carbon-containing molecules.

Contributions of the project:

The synthesis of catalysts and characterizations of catalysts were done with collaboration work from Rensselaer Polytechnic Institute. The evaluation of catalytic performances of prepared catalysts was done by Yuting Li.

Chapter 8: Summary

1. Conclusion

Overall, this dissertation includes five distinct projects investigating the efficient transformation of the main components of shale gas, methane and ethane, by using novel catalysts and performing different catalytic processes. The designed catalysts exhibited remarkable activity of conversions of methane or ethane into the ideal products. Additionally, the fundamental understandings of proposed catalysts used in different catalytic processes were explored by characterizing local structures of catalysts at a molecular level through multiple techniques. Upon the integration of experimental explorations and fundamental understandings, these studies provide insights into 1) the design of novel catalysts with high activation of the C-H bond of short-chain alkanes, and 2) the advance of heterogeneous catalytic transformations of light hydrocarbons into value-added materials. Significant findings from each project are concisely summarized in the following section:

1.1 Single rhodium atoms anchored in micropores for efficient transformation of methane under mild conditions

- Singly dispersed heterogeneous catalyst 0.10wt%Rh/ZSM-5, consisting of singly dispersed Rh_1O_5 sites anchored in the micropores of H-ZSM-5, exhibit unprecedented catalytic activity in the synthesis of acetic acid by directly converting methane under the presence of carbon monoxide and oxygen (low-cost oxidant) at a relatively low temperature of 150°C
- The TOR for the formation of total oxygenates over the single-atom Rh catalyst at 150°C is 0.10 moles of total products per mole Rh_1O_5 sites per second with a selectivity of ~70%, higher than that of free Rh^{3+} in aqueous solution by >1000 times under mild conditions.

- The mechanism of production of acetic acid from the direct coupling of three reactants (CH_4 , CO and O_2) over the Rh_1O_5 active sites catalyst was revealed by the integration of isotope experiments and theoretical simulations, suggesting that C-H bond of methane could be activated and dissociated by single Rh atom sites.
- This heterogeneous catalytic process is a promising alternative of conventional two-step production of acetic acid, to synthesize acetic acid directly from methane under a mild condition.

1.2 Coordination number-dependent catalysis on transition metal oxide for methane complete oxidation

- The complete oxidation of methane was conducted with three NiO catalysts with different shapes exposing the various surfaces, namely (110) facet in planar sheet NiO, (100) facet in cubic NiO, and (111) facet in octahedral NiO. The planar sheet NiO exhibited the highest activity of the complete oxidation of methane, reaching >99% conversion at 375°C , while cubic NiO and octahedral NiO were not active for conversion of methane.
- The enhancement of the catalytic activity on cubic NiO could be derived from the decrease of the coordination number of O atoms around a Ni in (100) face of cubic NiO from five to four by creating oxygen vacancies in (100) face through the reduction of cubic NiO in H_2 at a temperature $\geq 225^\circ\text{C}$,
- It is found that Ni cations coordinating with four oxygen atoms are active sites with the lowest activation barrier for catalyzing the complete oxidation of methane. That is confirmed by the high activity on (110) surface of planar sheet NiO where each Ni cation coordinates with four

O atoms and the inertness on (111) surface of octahedral NiO on which each Ni cation coordinates with six O atoms.

- An intrinsic correlation at a molecular level between the coordination environment of active sites on transition metal oxide and their corresponding catalytic performances was established through the AP-XPS experiments and computational studies.
- The demonstrated coordination number-dependent catalysis of transition metal oxide suggests a new method of designing catalysts by modulating the coordination environment around an atom of active sites on a catalyst.

1.3 Catalytic oxidation of ethane to carboxylic acids in the liquid phase at near room temperature and near ambient pressure

- The single-atom Rh catalyst presented good performance of the oxidation of ethane to acetic acid at near room temperature (50°C) with 1.5 bar ethane and 10mmol H₂O₂, reaching about 37% of conversion of ethane.
- TOFs for the oxidation of ethane to produce acetic acid and formic acid at 50°C are 0.060 acetic acid molecules per Rh₁O₅ site per second (or 216 moles of acetic acid from 1 mol of Rh₁O₅ sites per hour), and 0.127 formic acid molecules per Rh₁O₅ site per second (or 457 moles of formic acid from 1 mol of Rh₁O₅ sites per hour), respectively.
- It indicates that the singly dispersed Rh sites in the single-atom catalyst could activate the C-H bond of ethane, and this heterogeneous catalysis could open a new route of the transformation of short alkanes under mild conditions.

1.4 Fundamental understanding of Pd promoted Zn-loaded microporous catalysts for ethane dehydrogenation

- The Zn-based catalyst with the introduction of Pd (Pd/Zn/S-1) demonstrated a significantly enhanced selectivity and durability of dehydrogenation of ethane into ethylene, exhibiting a ~30% yield of ethylene at 650°C for more than 15 hours. In contrary, the activity of the reaction on Zn supported on silicate-1 without the addition of Pd (Zn/S-1) dramatically decreased within 9 hours to reach less than 10% conversion of ethane at 650 °C at the 10th hour and present maximum 22% yield of ethylene in the overall time-on-stream study.
- The rapid decay of catalytic activity and complete deactivation for producing olefin on monometallic Zn/S-1 was understood by operando XAS studies, which presumably results from the significant reconstruction of catalytic sites by atomic H or molecular H₂ generated during the dehydrogenation of ethane.
- The cationic Zn species were confirmed as active sites of 2.0wt%Zn/S-1 for dehydrogenation of ethane. They were restructured at a high temperature during catalysis through two pathways: (1) to form the small Zn nanoparticles with a followed immediate vaporization; and (2) to migrate into the framework of micropores of the support S-1.
- The promotion effect of added Pd in Zn/S-1 resulting from the formation of Pd-Zn alloy during catalysis at high temperatures was explored by XAS studies, which is because that the formation of Pd-Zn alloy could effectively prevent Zn sites from being restructured.
- The promotion of activity and durability of catalytic performance at high temperatures by the introduction of Pd atoms to form alloy suggests a promising route of developing efficient heterogeneous catalysts with the thermal stability at high temperatures.

1.5 Synthesis of Na@nanoFAU zeolite catalyst and catalysis for production of formic acid with Na@nanoFAU

- A new type of nanosheet zeolite, namely Na@nanoFAU, was prepared through a novel synthetic methodology by crystalizing FAU nanosheet via a template of layered graphene oxide.
- The nanosheet zeolitic catalyst is active for the formation of formic acid from 10bar CO by direct reaction with water at 150°C.
- The contribution from the Brønsted acid sites of Na@nanoFAU or detached Na⁺ cations to the formation of formic acid are small, thus confirming the catalytic role of the anchored Na⁺ in the Na@nanoFAU.
- Compared with the conventional microporous materials, the nanosheet or 2-D zeolite are proposed to improve the reaction rate by diminishing the diffusion limitation of the reactants and products during catalysis in liquid at low temperature.
- This nanoFAU zeolitic catalyst is expected to be applied in the efficient transformation of small molecules in liquid at low temperatures.

2. Recommendations

The findings of these studies imply several important following-up works:

2.1 The improvement of selectivity of ideal products formed by converting methane or ethane via single-atom catalysts in the gas-liquid-solid reaction system

As demonstrated in projects 1 and 3, one challenge of these reactions is that the selectivity of the acetic acid, ideal product, was lower than that of the formic acid by converting methane or ethane in liquid under mild conditions. As known, the separation of acetic acid and formic

acid cannot be easily obtained via distillation due to the closeness of the vapor pressures of two materials. The extraction distillation can be performed to remove the formic acid in the acetic acid, but that process requires to use acids or organic solvent. Thus, to avoid the challenge of separation, it would be essential to significantly improve the selectivity of one product, either acetic acid or formic acid, during the coupling of methane with carbon monoxide and oxygen as well as the oxidation of ethane by hydrogen peroxide.

From the catalyst point of view, the properties of a catalyst will affect the performance of the catalyst in reactions. As the ZSM-5 with a low ratio of Si/Al used in studied works provides a large amount of Brønsted acid sites, the acidity of such ZSM-5 is strong. Such strong acidity is possible to promote the cleavage of the C-C bond in acetic acid resulting in the formation of formic acid. Thus, one potential approach for improving the selectivity of acetic acid in studied reactions is to choose the ZSM-5 with a relatively weaker acidity in terms of a higher ratio of Si/Al to be the support anchoring the singly dispersed metal atoms.

On the other hand, in the study of the oxidation of ethane into acetic acid, the hydrogen peroxide was used as an oxidizing agent. However, the oxidizing property of hydrogen peroxide is quite strong; thereby, it is possible to promote the activation of the C-C bond of the acetic acid. Therefore, the alternative of hydrogen peroxide by a relatively soft oxidizing agent should be explored. Moreover, in recent research, one in-situ formation of the H_2O_2 method, referring to simultaneously generating hydrogen peroxide/hydroxyl radicals during the oxidation process, could be attempted to replace the addition of high-cost hydrogen peroxide.

2.2 The enhancement of activities of transformations of light alkanes

One main challenge of the studied projects is the activity obtained from current catalytic processes via proposed catalysts are limited, especially for the transformations of methane or ethane under mild conditions. To tackle this challenge, some potential strategies could be considered.

One promising approach is to enhance the number of active sites in the proposed catalysts. In general, the number of active sites in proposed catalysts, including the single-atom metal catalyst, transition metal oxide exposing specific surface where a metal cation has the low coordination number, and the bimetallic catalyst, is limited. For example, the amount of all Rh atoms anchored in 0.1wt%Rh/ZSM-5 is only 2.8×10^{-7} mol. To increase the number of active sites on catalysts, the development of useful synthetic methodologies is critical.

- Regarding the catalyst consisting of singly dispersed metal sites, the post-synthesis thermal treatment method was reported in publications to achieve the high concentration of single-atom active sites on supports.
- In terms of transition metal oxide, more oxygen vacancies could be created by the high-temperature reduction or the doping of a second metal.
- As for bimetallic catalysts, the bimetallic nanoparticles should be controlled in small size by using appropriate synthesis protocols. From the exploration in publications^{103, 108}, the small size of nanoparticles would provide sites with lower coordination numbers, which could lead to a decrease of the activation barrier of a certain reaction pathway.

On the other hand, for transformation of methane or ethane in liquid at low temperatures, the reaction system, in fact, has a significant influence on the kinetics of the reaction. The affected

factors include the solubility of methane or ethane gas in the liquid and the diffusion of reactants and products in the channels of microporous materials.

- A solvent effect on the gas-liquid-solid reaction system is crucial to be investigated. An inert organic solvent is considered to perform the reaction to improve the solubility of methane or ethane, leading to a higher concentration of reactants participated in the reaction.
- For reducing the limitation of internal diffusion in the micropores reaching active sites, one approach is using the 2D zeolitic materials in reactions. However, the nanosheet FAU zeolite needs to be modified to provide the necessary active sites for the activation and conversion of short-chain alkanes into value-added materials.

2.3 The understanding of reaction mechanisms of ethane transformations

The mechanism of a reaction is essential for the design of novel catalysts and the development of advanced processes. Here, reaction mechanisms of ethane oxidation and dehydrogenation are expected to be revealed.

In terms of the fundamental study of ethane oxidation into formic acid in aqueous solution, it is difficult to perform in-situ X-ray characterization experiments in the gas-liquid-solid system, due to the complexity of the complicated interaction between X-ray photos with various materials such as reactants in gas, solvent as well as products in liquid, and catalyst powders. It is challenging to obtain convinced signals presenting useful information of catalyst. Therefore, the computational simulations or kinetics modeling approaches can be applied to understand the reaction pathway of ethane oxidation in gas-liquid-solid via a single-atom Rh catalyst. In the theoretical study of the

ethane oxidation, several significant attributes are necessary to know for the understanding of the overall reaction pathway:

- 1) How single atom Rh sites activate the C-H bond of ethane.
- 2) The overall reaction pathway for the oxidation of ethane to produce carboxylic acids (acetic acid and formic acid) could be uncovered.
- 3) If the radicals were generated and involved in the reaction.
- 4) If the Brønsted acid sites participated in the reaction.

On the other hand, in the investigation of ethane dehydrogenation to produce ethylene, the local structure of the bimetallic catalyst was uncovered from the in-situ XAS studies. Thus, it would be feasible to utilize the DFT calculation method to understand how bimetallic sites performed the overall dehydrogenation of ethane. In the theoretical study of the ethane dehydrogenation, the following information could be explored from the understanding of the overall reaction pathway:

- 1) How bimetallic Pd-Zn sites activate the C-H bond of ethane.
- 2) The promotion effect of bimetallic sites could be explored by calculating the adsorption energy of reactants, intermediates and products on Zn sites and Pd-Zn sites, respectively.
- 3) The sites exhibiting the best catalytic performance could be found by screening elements in the periodic table to form the bimetallic alloy.

References

1. Iea (2019), "Global Energy & CO₂ Status Report 2018", Iea, Paris <https://www.iea.org/reports/global-energy-co2-status-report-2018>.
2. Artz, J.; Muller, T. E.; Thenert, K.; Kleinekorte, J.; Meys, R.; Sternberg, A.; Bardow, A.; Leitner, W., Sustainable Conversion of Carbon Dioxide: An Integrated Review of Catalysis and Life Cycle Assessment. *Chemical Reviews* 2018, 118 (2), 434-504.
3. Speight, J. G., The Chemistry and Technology of Petroleum. 2014.
4. Mokhatab, S.; Poe, W. A.; Mak, J. Y., Chapter 1 - Natural Gas Fundamentals. In *Handbook of Natural Gas Transmission and Processing (Third Edition)*, Mokhatab, S.; Poe, W. A.; Mak, J. Y., Eds. Gulf Professional Publishing: Boston, 2015; pp 1-36.
5. Liss, W. E., Impacts of Shale Gas Advancements on Natural Gas Utilization in the United States. *Energy Technology* 2014, 2 (12), 953-967.
6. Jing, W.; Huiqing, L.; Rongna, G.; Aihong, K.; Mi, Z., A New Technology for the Exploration of Shale Gas Reservoirs. *Petroleum Science and Technology* 2011, 29 (23), 2450-2459.
7. Rahm, D., Regulating Hydraulic Fracturing in Shale Gas Plays: The Case of Texas. *Energy Policy* 2011, 39 (5), 2974-2981.
8. Soeder, D. J., The Successful Development of Gas and Oil Resources from Shales in North America. *Journal of Petroleum Science and Engineering* 2018, 163, 399-420.
9. <http://naturalgas.org/>.
10. Bae, J. H.; Park, J. K.; Lee, J. W., Patents Trend Analysis on Unconventional Oil and Gas Technologies. *Economic and Environmental Geology* 2015, 48 (4), 361-369.

11. Karakaya, C.; Kee, R. J., Progress in the Direct Catalytic Conversion of Methane to Fuels and Chemicals. *Progress in Energy and Combustion Science* 2016, 55, 60-97.
12. Schwach, P.; Pan, X. L.; Bao, X. H., Direct Conversion of Methane to Value-Added Chemicals over Heterogeneous Catalysts: Challenges and Prospects. *Chemical Reviews* 2017, 117 (13), 8497-8520.
13. Grant, J. T.; Venegas, J. M.; McDermott, W. P.; Hermans, I., Aerobic Oxidations of Light Alkanes over Solid Metal Oxide Catalysts. *Chemical Reviews* 2018, 118 (5), 2769-2815.
14. Xue, X.-S.; Ji, P.; Zhou, B.; Cheng, J.-P., The Essential Role of Bond Energetics in C–H Activation/Functionalization. *Chemical Reviews* 2017, 117 (13), 8622-8648.
15. Deutschmann, O.; Knözinger, H.; Kochloefl, K.; Turek, T., *Heterogeneous Catalysis and Solid Catalysts, 3. Industrial Applications. In Ullmann's Encyclopedia of Industrial Chemistry.*
16. Usman, M.; Daud, W.; Abbas, H. F., Dry Reforming of Methane: Influence of Process Parameters-a Review. *Renewable & Sustainable Energy Reviews* 2015, 45, 710-744.
17. Tang, P.; Zhu, Q. J.; Wu, Z. X.; Ma, D., Methane Activation: The Past and Future. *Energy & Environmental Science* 2014, 7 (8), 2580-2591.
18. Kondratenko, E. V.; Peppel, T.; Seeburg, D.; Kondratenko, V. A.; Kalevaru, N.; Martin, A.; Wohlrab, S., Methane Conversion into Different Hydrocarbons or Oxygenates: Current Status and Future Perspectives in Catalyst Development and Reactor Operation. *Catalysis Science & Technology* 2017, 7 (2), 366-381.
19. Schwach, P.; Pan, X.; Bao, X., Direct Conversion of Methane to Value-Added Chemicals over Heterogeneous Catalysts: Challenges and Prospects. *Chemical Reviews* 2017, 117 (13), 8497-8520.

20. Gao, P.; Li, S.; Bu, X.; Dang, S.; Liu, Z.; Wang, H.; Zhong, L.; Qiu, M.; Yang, C.; Cai, J.; Wei, W.; Sun, Y., Direct Conversion of Co₂ into Liquid Fuels with High Selectivity over a Bifunctional Catalyst. *Nature Chemistry* 2017, 9 (10), 1019-1024.
21. Acetic Acid. In *Ullmann's Encyclopedia of Industrial Chemistry*, pp 1-34.
22. Paulik, F. E.; Roth, J. F., Novel Catalysts for the Low-Pressure Carbonylation of Methanol to Acetic Acid. *Chemical Communications (London)* 1968, (24), 1578a-1578a.
23. Grewer, T.; Schmidt, A., Dampf/Flüssigkeits-Gleichgewichte Mit Assoziation Im Dampf. *Chemie Ingenieur Technik* 1973, 45 (17), 1063-1067.
24. Common Nomenclature and Units in Catalysts. In *Applied Industrial Catalysis*, Leach, B. E., Ed. Academic Press: 1983; pp 297-299.
25. "Reportlinker Adds Global Acetic Acid Market Analysis and Forecasts". *Market Research Database. June 2014. P. Contents.*
26. Methanol. In *Ullmann's Encyclopedia of Industrial Chemistry*.
27. Hydrocarbons from Petroleum and Natural Gas. In *Hydrocarbon Chemistry*, 2003; pp 30-84.
28. Higman, C.; Tam, S., Advances in Coal Gasification, Hydrogenation, and Gas Treating for the Production of Chemicals and Fuels. *Chemical Reviews* 2014, 114 (3), 1673-1708.
29. Tao, F. F.; Shan, J. J.; Nguyen, L.; Wang, Z. Y.; Zhang, S. R.; Zhang, L.; Wu, Z. L.; Huang, W. X.; Zeng, S. B.; Hu, P., Understanding Complete Oxidation of Methane on Spinel Oxides at a Molecular Level. *Nature Communications* 2015, 6, 10.
30. Vadrine, J. C., Heterogeneous Catalytic Partial Oxidation of Lower Alkanes (C-1 - C-6) on Mixed Metal Oxides. *Journal of Energy Chemistry* 2016, 25 (6), 936-946.

31. Schwach, P.; Frandsen, W.; Willinger, M. G.; Schlogl, R.; Trunschke, A., Structure Sensitivity of the Oxidative Activation of Methane over Mgo Model Catalysts: I. Kinetic Study. *Journal of Catalysis* 2015, 329, 560-573.
32. Fung, V.; Tao, F.; Jiang, D. E., Trends of Alkane Activation on Doped Cobalt (II,III) Oxide from First Principles. *Chemcatchem* 2018, 10 (1), 244-249.
33. Tao, F. F.; Shan, J.-j.; Nguyen, L.; Wang, Z.; Zhang, S.; Zhang, L.; Wu, Z.; Huang, W.; Zeng, S.; Hu, P., Understanding Complete Oxidation of Methane on Spinel Oxides at a Molecular Level. *Nature Communications* 2015, 6, 7798.
34. Papadatos, K.; Shelstad, K. A., Catalyst Screening Using a Stone DTA Apparatus: I. Oxidation of Toluene over Cobalt-Metal-Oxide Catalysts. *Journal of Catalysis* 1973, 28 (1), 116-123.
35. Baussart, H.; Delobel, R.; Le Bras, M.; Leroy, J. M., Oxidation of Propene on Mixed Oxides of Copper and Cobalt. *Journal of the Chemical Society, Faraday Transactions 1: Physical Chemistry in Condensed Phases* 1979, 75 (0), 1337-1345.
36. Prasad, R.; Sony, Singh, P., Low Temperature Complete Combustion of a Lean Mixture of Lpg Emissions over Cobaltite Catalysts. *Catalysis Science & Technology* 2013, 3 (12), 3223-3233.
37. Gélin, P.; Primet, M., Complete Oxidation of Methane at Low Temperature over Noble Metal Based Catalysts: A Review. *Applied Catalysis B: Environmental* 2002, 39 (1), 1-37.
38. Cargnello, M.; Delgado Jaen, J. J.; Hernandez Garrido, J. C.; Bakhmutsky, K.; Montini, T.; Calvino Gamez, J. J.; Gorte, R. J.; Fornasiero, P., Exceptional Activity for Methane Combustion over Modular Pd@CeO₂ Subunits on Functionalized Al₂O₃. *Science* 2012, 337 (6095), 713-717.

39. Farrauto, R. J., Low-Temperature Oxidation of Methane. *Science* 2012, 337 (6095), 659.
40. Chin, Y.-H.; Buda, C.; Neurock, M.; Iglesia, E., Consequences of Metal–Oxide Interconversion for C–H Bond Activation During CH₄ Reactions on Pd Catalysts. *Journal of the American Chemical Society* 2013, 135 (41), 15425-15442.
41. Honkanen, M.; Kärkkäinen, M.; Viitanen, V.; Jiang, H.; Kallinen, K.; Huuhtanen, M.; Vippola, M.; Lahtinen, J.; Keiski, R.; Lepistö, T., Structural Characteristics of Natural-Gas-Vehicle-Aged Oxidation Catalyst. *Topics in Catalysis* 2013, 56 (9), 576-585.
42. Gélin, P.; Urfels, L.; Primet, M.; Tena, E., Complete Oxidation of Methane at Low Temperature over Pt and Pd Catalysts for the Abatement of Lean-Burn Natural Gas Fuelled Vehicles Emissions: Influence of Water and Sulphur Containing Compounds. *Catalysis Today* 2003, 83 (1), 45-57.
43. Dou, J.; Tang, Y.; Nie, L. H.; Andolina, C. M.; Zhang, X. Y.; House, S.; Li, Y. T.; Yang, J.; Tao, F. F., Complete Oxidation of Methane on Co₃O₄/CeO₂ Nanocomposite: A Synergic Effect. *Catalysis Today* 2018, 311, 48-55.
44. Banares, M. A., Supported Metal Oxide and Other Catalysts for Ethane Conversion: A Review. *Catalysis Today* 1999, 51 (2), 319-348.
45. Chen, J. H.; Arandiyan, H.; Gao, X.; Li, J. H., Recent Advances in Catalysts for Methane Combustion. *Catalysis Surveys from Asia* 2015, 19 (3), 140-171.
46. Hashiguchi, B. G.; Bischof, S. M.; Konnick, M. M.; Periana, R. A., Designing Catalysts for Functionalization of Unactivated C-H Bonds Based on the CH Activation Reaction. *Accounts of Chemical Research* 2012, 45 (6), 885-898.
47. Choudhary, T. V.; Banerjee, S.; Choudhary, V. R., Catalysts for Combustion of Methane and Lower Alkanes. *Applied Catalysis a-General* 2002, 234 (1-2), 1-23.

48. Aramouni, N. A. K.; Touma, J. G.; Abu Tarboush, B.; Zeaiter, J.; Ahmad, M. N., Catalyst Design for Dry Reforming of Methane: Analysis Review. *Renewable & Sustainable Energy Reviews* 2018, 82, 2570-2585.
49. Peneau, V.; Shaw, G.; Armstrong, R. D.; Jenkins, R. L.; Dimitratos, N.; Taylor, S. H.; Zanthoff, H. W.; Peitz, S.; Stochniol, G.; Hutchings, G. J., The Partial Oxidation of Propane under Mild Aqueous Conditions with H₂O₂ and ZSM-5 Catalysts. *Catalysis Science & Technology* 2016, 6 (20), 7521-7531.
50. Gartner, C. A.; van Veen, A. C.; Lercher, J. A., Oxidative Dehydrogenation of Ethane: Common Principles and Mechanistic Aspects. *Chemcatchem* 2013, 5 (11), 3196-3217.
51. Cavani, F.; Ballarini, N.; Cericola, A., Oxidative Dehydrogenation of Ethane and Propane: How Far from Commercial Implementation? *Catalysis Today* 2007, 127 (1-4), 113-131.
52. Li, X.; Iglesia, E., Support and Promoter Effects in the Selective Oxidation of Ethane to Acetic Acid Catalyzed by Mo-V-Nb Oxides. *Applied Catalysis A: General* 2008, 334 (1), 339-347.
53. Forde, M. M.; Armstrong, R. D.; Hammond, C.; He, Q.; Jenkins, R. L.; Kondrat, S. A.; Dimitratos, N.; Lopez-Sanchez, J. A.; Taylor, S. H.; Willock, D.; Kiely, C. J.; Hutchings, G. J., Partial Oxidation of Ethane to Oxygenates Using Fe- and Cu-Containing ZSM-5. *Journal of the American Chemical Society* 2013, 135 (30), 11087-11099.
54. Ruth, K.; Burch, R.; Kieffer, R., Mo-V-Nb Oxide Catalysts for the Partial Oxidation of Ethane - II. Chemical and Catalytic Properties and Structure Function Relationships. *Journal of Catalysis* 1998, 175 (1), 27-39.
55. Xiang, Y. Z.; Wang, H.; Cheng, J. H.; Matsubu, J., Progress and Prospects in Catalytic Ethane Aromatization. *Catalysis Science & Technology* 2018, 8 (6), 1500-1516.

56. Hagen, A.; Roessner, F., Ethane to Aromatic Hydrocarbons: Past, Present, Future. *Catalysis Reviews-Science and Engineering* 2000, 42 (4), 403-437.
57. Sinev, M. Y., Free Radicals in Catalytic Oxidation of Light Alkanes: Kinetic and Thermochemical Aspects. *Journal of Catalysis* 2003, 216 (1-2), 468-476.
58. Thorsteinson, E. M.; Wilson, T. P.; Young, F. G.; Kasai, P. H., The Oxidative Dehydrogenation of Ethane over Catalysts Containing Mixed Oxides of Molybdenum and Vanadium. *Journal of Catalysis* 1978, 52 (1), 116-132.
59. Tessier, L.; Bordes, E.; Gubelmann-Bonneau, M., Active Specie on Vanadium-Containing Catalysts for the Selective Oxidation of Ethane to Acetic Acid. *Catalysis Today* 1995, 24 (3), 335-340.
60. Roy, M.; Gubelmann-Bonneau, M.; Ponceblanc, H.; Volta, J.-C., Vanadium-Molybdenum Phosphates Supported by TiO₂-Anatase as New Catalysts for Selective Oxidation of Ethane to Acetic Acid. *Catalysis Letters* 1996, 42 (1), 93-97.
61. Roussel, M.; Bouchard, M.; Karim, K.; Al-Sayari, S.; Bordes-Richard, E., Movo-Based Catalysts for the Oxidation of Ethane to Ethylene and Acetic Acid: Influence of Niobium and/or Palladium on Physicochemical and Catalytic Properties. *Applied Catalysis A: General* 2006, 308, 62-74.
62. Ueda, W.; Oshihara, K., Selective Oxidation of Light Alkanes over Hydrothermally Synthesized Mo-V-M-O (M=Al, Ga, Bi, Sb, and Te) Oxide Catalysts. *Applied Catalysis A: General* 2000, 200 (1), 135-143.
63. Linke, D.; Wolf, D.; Baerns, M.; Timpe, O.; Schlögl, R.; Zeyß, S.; Dingerdissen, U., Catalytic Partial Oxidation of Ethane to Acetic Acid over Mo₁V_{0.25}Nb_{0.12}Pd_{0.0005}O_x: I. Catalyst Performance and Reaction Mechanism. *Journal of Catalysis* 2002, 205 (1), 16-31.

64. Linke, D.; Wolf, D.; Baerns, M.; Zeyss, S.; Dingerdissen, U., Catalytic Partial Oxidation of Ethane to Acetic Acid over $\text{Mo}_1\text{V}_{0.25}\text{Nb}_{0.12}\text{Pd}_{0.0005}\text{O}_x$: II. Kinetic Modelling. *Journal of Catalysis* 2002, 205 (1), 32-43.
65. Armstrong, R. D.; Hutchings, G. J.; Taylor, S. H., An Overview of Recent Advances of the Catalytic Selective Oxidation of Ethane to Oxygenates. *Catalysts* 2016, 6 (5), 19.
66. Rahimi, N.; Karimzadeh, R., Catalytic Cracking of Hydrocarbons over Modified ZSM-5 Zeolites to Produce Light Olefins: A Review. *Applied Catalysis a-General* 2011, 398 (1-2), 1-17.
67. Elkins, T. W.; Hagelin-Weaver, H. E., Characterization of Mn- $\text{Na}_2\text{WO}_4/\text{SiO}_2$ and Mn- $\text{Na}_2\text{WO}_4/\text{MgO}$ Catalysts for the Oxidative Coupling of Methane. *Applied Catalysis a-General* 2015, 497, 96-106.
68. Arndt, S.; Laugel, G.; Levchenko, S.; Horn, R.; Baerns, M.; Scheffler, M.; Schlogl, R.; Schomacker, R., A Critical Assessment of Li/MgO-Based Catalysts for the Oxidative Coupling of Methane. *Catalysis Reviews-Science and Engineering* 2011, 53 (4), 424-514.
69. Arndt, S.; Otremba, T.; Simon, U.; Yildiz, M.; Schubert, H.; Schomacker, R., Mn- $\text{Na}_2\text{WO}_4/\text{SiO}_2$ as Catalyst for the Oxidative Coupling of Methane. What Is Really Known? *Applied Catalysis a-General* 2012, 425, 53-61.
70. Li, S. B., Oxidative Coupling of Methane over W-Mn/ SiO_2 Catalyst. *Chinese Journal of Chemistry* 2001, 19 (1), 16-21.
71. Arndt, S.; Uysal, B.; Berthold, A.; Otrebma, T.; Aksu, Y.; Driess, M.; Schomacker, R., Supported ZnO Catalysts for the Conversion of Alkanes: About the Metamorphosis of a Heterogeneous Catalyst. *Journal of Natural Gas Chemistry* 2012, 21 (5), 581-594.
72. Frash, M. V.; van Santen, R. A., Activation of Ethane in Zn-Exchanged Zeolites: A Theoretical Study. *Physical Chemistry Chemical Physics* 2000, 2 (5), 1085-1089.

73. Mehdad, A.; Gould, N. S.; Xu, B. J.; Lobo, R. F., Effect of Steam and CO₂ on Ethane Activation over Zn-Zsm-5. *Catalysis Science & Technology* 2018, 8 (1), 358-366.
74. Yu, Z.; Sawada, J. A.; An, W.; Kuznicki, S. M., PtZn-ETS-2: A Novel Catalyst for Ethane Dehydrogenation. *Aiche Journal* 2015, 61 (12), 4367-4376.
75. Sun, L. Y.; Zhang, Y. F.; Gong, Y. J., Structural Features and Application of Micro-Microporous Composite Zeolites. *Acta Physico-Chimica Sinica* 2016, 32 (5), 1105-1122.
76. Mortensen, P. M.; Grunwaldt, J. D.; Jensen, P. A.; Knudsen, K. G.; Jensen, A. D., A Review of Catalytic Upgrading of Bio-Oil to Engine Fuels. *Applied Catalysis a-General* 2011, 407 (1-2), 1-19.
77. Mitchell, S.; Pinar, A. B.; Kenvin, J.; Crivelli, P.; Kaerger, J.; Perez-Ramirez, J., Structural Analysis of Hierarchically Organized Zeolites. *Nature Communications* 2015, 6.
78. Kubicka, D.; Kubickova, I.; Cejka, J., Application of Molecular Sieves in Transformations of Biomass and Biomass-Derived Feedstocks. *Catalysis Reviews-Science and Engineering* 2013, 55 (1), 1-78.
79. Bastani, D.; Esmaeili, N.; Asadollahi, M., Polymeric Mixed Matrix Membranes Containing Zeolites as a Filler for Gas Separation Applications: A Review. *Journal of Industrial and Engineering Chemistry* 2013, 19 (2), 375-393.
80. Mravec, D.; Hudec, J.; Janotka, I., Some Possibilities of Catalytic and Noncatalytic Utilization of Zeolites. *Chemical Papers* 2005, 59 (1), 62-69.
81. Xuan Hoan, V.; Armbruster, U.; Martin, A., Micro/Mesoporous Zeolitic Composites: Recent Developments in Synthesis and Catalytic Applications. *Catalysts* 2016, 6 (12).
82. Auerbach, S. C., K.; Dutta, P., *Handbook of Zeolite Science and Technology* Boca Raton: CRC Press., 2003.

83. Gerhard Ertl, H. K., Ferdi Schuth, Jens Weitkamp, *Handbook of Heterogeneous Catalysis*. 2008; p 2.
84. Galadima, A.; Muraza, O., Stability Improvement of Zeolite Catalysts under Hydrothermal Conditions for Their Potential Applications in Biomass Valorization and Crude Oil Upgrading. *Microporous and Mesoporous Materials* 2017, 249, 42-54.
85. Gläser, R.; Weitkamp, J., The Application of Zeolites in Catalysis. In *Basic Principles in Applied Catalysis*, Baerns, M., Ed. Springer Berlin Heidelberg: Berlin, Heidelberg, 2004; pp 159-212.
86. Tang, Y.; Li, Y. T.; Fung, V.; Jiang, D. E.; Huang, W. X.; Zhang, S. R.; Iwasawa, Y.; Sakata, T.; Nguyen, L.; Zhang, X. Y.; Frenkel, A. I.; Tao, F., Single Rhodium Atoms Anchored in Micropores for Efficient Transformation of Methane under Mild Conditions. *Nature Communications* 2018, 9, 11.
87. Xu, J.; Armstrong, R. D.; Shaw, G.; Dummer, N. F.; Freakley, S. J.; Taylor, S. H.; Hutchings, G. J., Continuous Selective Oxidation of Methane to Methanol over Cu- and Fe-Modified ZSM-5 Catalysts in a Flow Reactor. *Catalysis Today* 2016, 270, 93-100.
88. Hammond, C.; Forde, M. M.; Ab Rahim, M. H.; Thetford, A.; He, Q.; Jenkins, R. L.; Dimitratos, N.; Lopez-Sanchez, J. A.; Dummer, N. F.; Murphy, D. M.; Carley, A. F.; Taylor, S. H.; Willock, D. J.; Stangland, E. E.; Kang, J.; Hagen, H.; Kiely, C. J.; Hutchings, G. J., Direct Catalytic Conversion of Methane to Methanol in an Aqueous Medium by Using Copper-Promoted Fe-ZSM-5. *Angewandte Chemie-International Edition* 2012, 51 (21), 5129-5133.
89. Le, H. V.; Parishan, S.; Saaltchik, A.; Gobel, C.; Schlesiger, C.; Malzer, W.; Trunschke, A.; Schomacker, R.; Thomas, A., Solid-State Ion-Exchanged Cu/Mordenite Catalysts for the Direct Conversion of Methane to Methanol. *Acs Catalysis* 2017, 7 (2), 1403-1412.

90. Huang, W. X.; Zhang, S. R.; Tang, Y.; Li, Y. T.; Nguyen, L.; Li, Y. Y.; Shan, J. J.; Xiao, D. Q.; Gagne, R.; Frenkel, A. I.; Tao, F., Low-Temperature Transformation of Methane to Methanol on Pd₁O₄ Single Sites Anchored on the Internal Surface of Microporous Silicate. *Angewandte Chemie-International Edition* 2016, 55 (43), 13441-13445.
91. Narsimhan, K.; Iyoki, K.; Dinh, K.; Roman-Leshkov, Y., Catalytic Oxidation of Methane into Methanol over Copper-Exchanged Zeolites with Oxygen at Low Temperature. *Acs Central Science* 2016, 2 (6), 424-429.
92. Narsimhan, K.; Michaelis, V. K.; Mathies, G.; Gunther, W. R.; Griffin, R. G.; Roman-Leshkov, Y., Methane to Acetic Acid over Cu-Exchanged Zeolites: Mechanistic Insights from a Site-Specific Carbonylation Reaction. *Journal of the American Chemical Society* 2015, 137 (5), 1825-1832.
93. Shan, J. J.; Huang, W. X.; Nguyen, L.; Yu, Y.; Zhang, S. R.; Li, Y. Y.; Frenkel, A. I.; Tao, F., Conversion of Methane to Methanol with a Bent Mono(μ -oxo)Dinickel Anchored on the Internal Surfaces of Micropores. *Langmuir* 2014, 30 (28), 8558-8569.
94. Li, Y. T.; Tang, Y.; Nguyen, L.; Tao, F. F., Catalytic Oxidation of Ethane to Carboxylic Acids in the Liquid Phase at near Room Temperature at Ambient Pressure. *Acs Sustainable Chemistry & Engineering* 2019, 7 (5), 4707-4715.
95. Caeiro, G.; Carvalho, R. H.; Wang, X.; Lemos, M.; Lemos, F.; Guisnet, M.; Ribeiro, F. R., Activation of C-2-C-4 Alkanes over Acid and Bifunctional Zeolite Catalysts. *Journal of Molecular Catalysis a-Chemical* 2006, 255 (1-2), 131-158.
96. Snyder, B. E.; Vanelderen, P.; Bols, M. L.; Hallaert, S. D.; Bottger, L. H.; Ungur, L.; Pierloot, K.; Schoonheydt, R. A.; Sels, B. F.; Solomon, E. I., The Active Site of Low-Temperature Methane Hydroxylation in Iron-Containing Zeolites. *Nature* 2016, 536 (7616), 317-321.

97. Mahyuddin, M. H.; Staykov, A.; Shiota, Y.; Yoshizawa, K., Direct Conversion of Methane to Methanol by Metal-Exchanged ZSM-5 Zeolite (Metal = Fe, Co, Ni, Cu). *Acs Catalysis* 2016, 6 (12), 8321-8331.
98. Wang, S.; Agirrezabal-Telleria, I.; Bhan, A.; Simonetti, D.; Takanebe, K.; Iglesia, E., Catalytic Routes to Fuels from C1 and Oxygenate Molecules. *Faraday Discussions* 2017, 197, 9-39.
99. Ertl, G. K., H.; Schüth, F.; Weitkamp, J., *Handbook of Heterogeneous Catalysis*. Wiley-VCH: 2008.
100. Schwarz, J. A.; Contescu, C.; Contescu, A., Methods for Preparation of Catalytic Materials. *Chemical Reviews* 1995, 95 (3), 477-510.
101. Serp, P.; Kalck, P.; Feurer, R., Chemical Vapor Deposition Methods for the Controlled Preparation of Supported Catalytic Materials. *Chemical Reviews* 2002, 102 (9), 3085-3128.
102. Climent, M. J.; Corma, A.; Iborra, S., Heterogeneous Catalysts for the One-Pot Synthesis of Chemicals and Fine Chemicals. *Chemical Reviews* 2011, 111 (2), 1072-1133.
103. Cao, S. W.; Tao, F.; Tang, Y.; Li, Y. T.; Yu, J. G., Size- and Shape-Dependent Catalytic Performances of Oxidation and Reduction Reactions on Nanocatalysts. *Chemical Society Reviews* 2016, 45 (17), 4747-4765.
104. Wang, A.; Li, J.; Zhang, T., Heterogeneous Single-Atom Catalysis. *Nature Reviews Chemistry* 2018, 2 (6), 65-81.
105. Zhao, G. X.; Liu, H. M.; Ye, J. H., Constructing and Controlling of Highly Dispersed Metallic Sites for Catalysis. *Nano Today* 2018, 19, 108-125.
106. Liu, L. C.; Corma, A., Metal Catalysts for Heterogeneous Catalysis: From Single Atoms to Nanoclusters and Nanoparticles. *Chemical Reviews* 2018, 118 (10), 4981-5079.

107. Yan, H.; Su, C. L.; He, J.; Chen, W., Single-Atom Catalysts and Their Applications in Organic Chemistry. *Journal of Materials Chemistry A* 2018, 6 (19), 8793-8814.
108. Yang, X. F.; Wang, A. Q.; Qiao, B. T.; Li, J.; Liu, J. Y.; Zhang, T., Single-Atom Catalysts: A New Frontier in Heterogeneous Catalysis. *Accounts of Chemical Research* 2013, 46 (8), 1740-1748.
109. Zhang, H. B.; Liu, G. G.; Shi, L.; Ye, J. H., Single-Atom Catalysts: Emerging Multifunctional Materials in Heterogeneous Catalysis. *Advanced Energy Materials* 2018, 8 (1), 24.
110. Xia, Y.; Xiong, Y.; Lim, B.; Skrabalak, S. E., Shape-Controlled Synthesis of Metal Nanocrystals: Simple Chemistry Meets Complex Physics? *Angewandte Chemie International Edition* 2009, 48 (1), 60-103.
111. Lu, H. M.; Meng, X. K., Theoretical Model to Calculate Catalytic Activation Energies of Platinum Nanoparticles of Different Sizes and Shapes. *The Journal of Physical Chemistry C* 2010, 114 (3), 1534-1538.
112. Tao, F.; Zhang, S. R.; Nguyen, L.; Zhang, X. Q., Action of Bimetallic Nanocatalysts under Reaction Conditions and During Catalysis: Evolution of Chemistry from High Vacuum Conditions to Reaction Conditions. *Chemical Society Reviews* 2012, 41 (24), 7980-7993.
113. Li, M. M.-J.; Tsang, S. C. E., Bimetallic Catalysts for Green Methanol Production Via CO_2 and Renewable Hydrogen: A Mini-Review and Prospects. *Catalysis Science & Technology* 2018, 8 (14), 3450-3464.
114. Peng, X. H.; Pan, Q. M.; Rempel, G. L., Bimetallic Dendrimer-Encapsulated Nanoparticles as Catalysts: A Review of the Research Advances. *Chemical Society Reviews* 2008, 37 (8), 1619-1628.

115. Ferrando, R.; Jellinek, J.; Johnston, R. L., Nanoalloys: From Theory to Applications of Alloy Clusters and Nanoparticles. *Chemical Reviews* 2008, 108 (3), 845-910.
116. Ghosh Chaudhuri, R.; Paria, S., Core/Shell Nanoparticles: Classes, Properties, Synthesis Mechanisms, Characterization, and Applications. *Chemical Reviews* 2012, 112 (4), 2373-2433.
117. Alayoglu, S.; Zavalij, P.; Eichhorn, B.; Wang, Q.; Frenkel, A. I.; Chupas, P., Structural and Architectural Evaluation of Bimetallic Nanoparticles: A Case Study of Pt–Ru Core–Shell and Alloy Nanoparticles. *Acs Nano* 2009, 3 (10), 3127-3137.
118. Yang, Z.; Yang, X.; Xu, Z.; Liu, S., Structural Evolution of Pt–Au Nanoalloys During Heating Process: Comparison of Random and Core-Shell Orderings. *Physical Chemistry Chemical Physics* 2009, 11 (29), 6249-6255.
119. Ferrer, D.; Torres-Castro, A.; Gao, X.; Sepúlveda-Guzmán, S.; Ortiz-Méndez, U.; José-Yacamán, M., Three-Layer Core/Shell Structure in Au–Pd Bimetallic Nanoparticles. *Nano Letters* 2007, 7 (6), 1701-1705.
120. Heiz, U.; Sanchez, A.; Abbet, S.; Schneider, W. D., Catalytic Oxidation of Carbon Monoxide on Monodispersed Platinum Clusters: Each Atom Counts. *Journal of the American Chemical Society* 1999, 121 (13), 3214-3217.
121. Kaden, W. E.; Wu, T.; Kunkel, W. A.; Anderson, S. L., Electronic Structure Controls Reactivity of Size-Selected Pd Clusters Adsorbed on TiO₂ Surfaces. *Science* 2009, 326 (5954), 826-829.
122. Abbet, S.; Sanchez, A.; Heiz, U.; Schneider, W. D.; Ferrari, A. M.; Pacchioni, G.; Rösch, N., Acetylene Cyclotrimerization on Supported Size-Selected Pd_n Clusters (1 ≤ N ≤ 30): One Atom Is Enough! *Journal of the American Chemical Society* 2000, 122 (14), 3453-3457.

123. Gu, J.; Zhang, Y. W.; Tao, F., Shape Control of Bimetallic Nanocatalysts through Well-Designed Colloidal Chemistry Approaches. *Chemical Society Reviews* 2012, 41 (24), 8050-8065.
124. Jin, M.; He, G.; Zhang, H.; Zeng, J.; Xie, Z.; Xia, Y., Shape-Controlled Synthesis of Copper Nanocrystals in an Aqueous Solution with Glucose as a Reducing Agent and Hexadecylamine as a Capping Agent. *Angewandte Chemie International Edition* 2011, 50 (45), 10560-10564.
125. Sankar, M.; Dimitratos, N.; Miedziak, P. J.; Wells, P. P.; Kiely, C. J.; Hutchings, G. J., Designing Bimetallic Catalysts for a Green and Sustainable Future. *Chemical Society Reviews* 2012, 41 (24), 8099-8139.
126. Prech, J.; Pizarro, P.; Serrano, D. P.; Cejka, J., From 3d to 2d Zeolite Catalytic Materials. *Chemical Society Reviews* 2018, 47 (22), 8263-8306.
127. Transmission Electron Microscopy. In *Materials Characterization*, pp 79-119.
128. Siegbahn, K., Electron-Spectroscopy - Outlook. *Journal of Electron Spectroscopy and Related Phenomena* 1974, 5 (NOV-D), 3-97.
129. Moulder, J. F.; Chastain, J., *Handbook of X-Ray Photoelectron Spectroscopy: A Reference Book of Standard Spectra for Identification and Interpretation of Xps Data*. Physical Electronics Division, Perkin-Elmer Corporation: 1992.
130. Wannberg, B.; Gelius, U.; Siegbahn, K., Design Principles in Electron-Spectroscopy. *Journal of Physics E-Scientific Instruments* 1974, 7 (3), 149-159.
131. Siegbahn, K., Electron-Spectroscopy for Atoms, Molecules, and Condensed Matter. *Reviews of Modern Physics* 1982, 54 (3), 709-728.
132. Toyoshima, R.; Kondoh, H., In-Situ Observations of Catalytic Surface Reactions with Soft X-rays under Working Conditions. *Journal of Physics-Condensed Matter* 2015, 27 (8).

133. Salmeron, M.; Schlogl, R., Ambient Pressure Photoelectron Spectroscopy: A New Tool for Surface Science and Nanotechnology. *Surface Science Reports* 2008, 63 (4), 169-199.
134. Zhong, L. P.; Chen, D. K.; Zafeiratos, S., A Mini Review of in situ near-Ambient Pressure XPS Studies on Non-Noble, Late Transition Metal Catalysts. *Catalysis Science & Technology* 2019, 9 (15), 3851-3867.
135. Arble, C.; Jia, M.; Newberg, J. T., Lab-Based Ambient Pressure X-Ray Photoelectron Spectroscopy from Past to Present. *Surface Science Reports* 2018, 73 (2), 37-57.
136. Newville, M., Fundamentals of Xafs. *Reviews in Mineralogy and Geochemistry* 2014, 78 (1), 33-74.
137. Ravel, B.; Newville, M., Athena, Artemis, Hephaestus: Data Analysis for X-Ray Absorption Spectroscopy Using Ifeffit. *J Synchrotron Radiat* 2005, 12 (Pt 4), 537-541.
138. Mattos, L. V.; Jacobs, G.; Davis, B. H.; Noronha, F. B., Production of Hydrogen from Ethanol: Review of Reaction Mechanism and Catalyst Deactivation. *Chemical Reviews* 2012, 112 (7), 4094-4123.
139. Liu, Y.; Li, D. F.; Wang, T. Y.; Liu, Y.; Xu, T.; Zhang, Y., Efficient Conversion of Methane to Aromatics by Coupling Methylation Reaction. *Acs Catalysis* 2016, 6 (8), 5366-5370.
140. Ali, A.; Alvarez, W.; Loughran, C. J.; Resasco, D. E., State of Pd on H-ZSM-5 and Other Acidic Supports During the Selective Reduction of No by CH₄ Studied by EXAFS/XANES. *Applied Catalysis B-Environmental* 1997, 14 (1-2), 13-22.
141. Ali, A.; Chin, Y. H.; Resasco, D. E., Redispersion of Pd on Acidic Supports and Loss of Methane Combustion Activity During the Selective Reduction of NO by CH₄. *Catalysis Letters* 1998, 56 (2-3), 111-117.

142. Yoshizawa, K.; Shiota, Y.; Yumura, T.; Yamabe, T., Direct Methane-Methanol and Benzene-Phenol Conversions on Fe-ZSM-5 Zeolite: Theoretical Predictions on the Reaction Pathways and Energetics. *Journal of Physical Chemistry B* 2000, 104 (4), 734-740.
143. Kuroda, Y.; Mori, T.; Sugiyama, H.; Uozumi, Y.; Ikeda, K.; Itadani, A.; Nagao, M., On the Possibility of AgZSM-5 Zeolite Being a Partial Oxidation Catalyst for Methane. *Journal of Colloid and Interface Science* 2009, 333 (1), 294-299.
144. Goltl, F.; Michel, C.; Andrikopoulos, P. C.; Love, A. M.; Hafner, J.; Hermans, I.; Sautet, P., Computationally Exploring Confinement Effects in the Methane-to-Methanol Conversion over Iron-oxo Centers in Zeolites. *Acs Catalysis* 2016, 6 (12), 8404-8409.
145. Behrens, M.; Studt, F.; Kasatkin, I.; Kuhl, S.; Havecker, M.; Abild-Pedersen, F.; Zander, S.; Girgsdies, F.; Kurr, P.; Knief, B. L.; Tovar, M.; Fischer, R. W.; Norskov, J. K.; Schlogl, R., The Active Site of Methanol Synthesis over Cu/ZnO/Al₂O₃ Industrial Catalysts. *Science* 2012, 336 (6083), 893-897.
146. Labinger, J. A.; Bercaw, J. E., Understanding and Exploiting C-H Bond Activation. *Nature* 2002, 417 (6888), 507-514.
147. Lin, M.; Sen, A., Direct Catalytic Conversion of Methane to Acetic-Acid in an Aqueous-Medium. *Nature* 1994, 368 (6472), 613-615.
148. Periana, R. A.; Mironov, O.; Taube, D.; Bhalla, G.; Jones, C. J., Catalytic, Oxidative Condensation of CH₄ to CH₃COOH in One Step Via C-H Activation. *Science* 2003, 301 (5634), 814-818.
149. Copéret, C.; Comas-Vives, A.; Conley, M. P.; Estes, D. P.; Fedorov, A.; Mougél, V.; Nagaé, H.; Núñez-Zarur, F.; Zhizhko, P. A., Surface Organometallic and Coordination Chemistry

toward Single-Site Heterogeneous Catalysts: Strategies, Methods, Structures, and Activities. *Chemical Reviews* 2016, 116 (2), 323-421.

150. Qiao, B.; Wang, A.; Yang, X.; Allard, L. F.; Jiang, Z.; Cui, Y.; Liu, J.; Li, J.; Zhang, T., Single-Atom Catalysis of Co Oxidation Using Pt₁/FeO_x. *Nature Chemistry* 2011, 3, 634.

151. Zhang, S.; Nguyen, L.; Liang, J.-X.; Shan, J.; Liu, J.; Frenkel, A. I.; Patlolla, A.; Huang, W.; Li, J.; Tao, F., Catalysis on Singly Dispersed Bimetallic Sites. *Nature Communications* 2015, 6 (1), 7938.

152. Yang, X.-F.; Wang, A.; Qiao, B.; Li, J.; Liu, J.; Zhang, T., Single-Atom Catalysts: A New Frontier in Heterogeneous Catalysis. *Accounts of Chemical Research* 2013, 46 (8), 1740-1748.

153. Serna, P.; Gates, B. C., Molecular Metal Catalysts on Supports: Organometallic Chemistry Meets Surface Science. *Accounts of Chemical Research* 2014, 47 (8), 2612-2620.

154. Pelletier, J. D.; Basset, J. M., Catalysis by Design: Well-Defined Single-Site Heterogeneous Catalysts. *Acc Chem Res* 2016, 49 (4), 664-677.

155. Zhang, S. R.; Nguyen, L.; Liang, J. X.; Shan, J. J.; Liu, J. Y.; Frenkel, A. I.; Patlolla, A.; Huang, W. X.; Li, J.; Tao, F., Catalysis on Singly Dispersed Bimetallic Sites. *Nature Communications* 2015, 6.

156. Ma, T., *Ignitability and Explosibility of Gases and Vapors*. Springer, New York, NY: 2015.

157. Gas, L., Lower and Upper Explosive Limits for Flammable Gases and Vapors (LEL/UEL). *Matheson gas products* 2013.

158. Tao, F.; Grass, M. E.; Zhang, Y. W.; Butcher, D. R.; Renzas, J. R.; Liu, Z.; Chung, J. Y.; Mun, B. S.; Salmeron, M.; Somorjai, G. A., Reaction-Driven Restructuring of Rh-Pd and Pt-Pd Core-Shell Nanoparticles. *Science* 2008, 322 (5903), 932-934.

159. Mulukutla, R. S.; Asakura, K.; Namba, S.; Iwasawa, Y., Nanosized Rhodium Oxide Particles in the MCM-41 Mesoporous Molecular Sieve. *Chemical Communications* 1998, (14), 1425-1426.
160. Mulukutla, R. S.; Shido, T.; Asakura, K.; Kogure, T.; Iwasawa, Y., Characterization of Rhodium Oxide Nanoparticles in MCM-41 and Their Catalytic Performances for NO-CO Reactions in Excess O₂. *Applied Catalysis a-General* 2002, 228 (1-2), 305-314.
161. Dent, A. J.; Evans, J.; Fiddy, S. G.; Jyoti, B.; Newton, M. A.; Tromp, M., Rhodium Dispersion During No/Co Conversions. *Angewandte Chemie-International Edition* 2007, 46 (28), 5356-5358.
162. Kinnunen, T.; Laasonen, K., The Oxidative Addition and Migratory 1,1-Insertion in the Monsanto and Cativa Processes. A Density Functional Study of the Catalytic Carbonylation of Methanol. *Journal of Molecular Structure-Theochem* 2001, 542, 273-288.
163. Maitlis, P. M.; Haynes, A.; Sunley, G. J.; Howard, M. J., Methanol Carbonylation Revisited: Thirty Years On. *Journal of the Chemical Society, Dalton Transactions* 1996, (11), 2187-2196.
164. Liu, Z. Y.; Grinter, D. C.; Lustemberg, P. G.; Nguyen-Phan, T. D.; Zhou, Y. H.; Luo, S.; Waluyo, I.; Crumlin, E. J.; Stacchiola, D. J.; Zhou, J.; Carrasco, J.; Busnengo, H. F.; Ganduglia-Pirovano, M. V.; Senanayake, S. D.; Rodriguez, J. A., Dry Reforming of Methane on a Highly-Active Ni-CeO₂ Catalyst: Effects of Metal-Support Interactions on C-H Bond Breaking. *Angewandte Chemie-International Edition* 2016, 55 (26), 7455-7459.
165. Wu, J. F.; Yu, S. M.; Wang, W. D.; Fan, Y. X.; Bai, S.; Zhang, C. W.; Gao, Q.; Huang, J.; Wang, W., Mechanistic Insight into the Formation of Acetic Acid from the Direct Conversion

of Methane and Carbon Dioxide on Zinc-Modified H-ZSM-5 Zeolite. *Journal of the American Chemical Society* 2013, 135 (36), 13567-13573.

166. Huang, W.; Xie, K. C.; Wang, J. P.; Gao, Z. H.; Yin, L. H.; Zhu, Q. M., Possibility of Direct Conversion of CH₄ and CO₂ to High-Value Products. *Journal of Catalysis* 2001, 201 (1), 100-104.

167. Zhang, R. G.; Song, L. Z.; Liu, H. Y.; Wang, B. J., The Interaction Mechanism of CO₂ with CH₃ and H on Cu (111) Surface in Synthesis of Acetic Acid from CH₄/CO₂: A Dft Study. *Applied Catalysis a-General* 2012, 443, 50-58.

168. Lustemberg, P. G.; Ramirez, P. J.; Liu, Z. Y.; Gutierrez, R. A.; Grinter, D. G.; Carrasco, J.; Senanayake, S. D.; Rodriguez, J. A.; Ganduglia-Pirovano, M. V., Room-Temperature Activation of Methane and Dry Re-Forming with CO₂ on Ni-CeO₂ (111) Surfaces: Effect of Ce³⁺ Sites and Metal-Support Interactions on C-H Bond Cleavage. *Acs Catalysis* 2016, 6 (12), 8184-8191.

169. Yahi, N.; Menad, S.; Rodriguez-Ramos, I., Dry Reforming of Methane over Ni/CeO₂ Catalysts Prepared by Three Different Methods. *Green Processing and Synthesis* 2015, 4 (6), 479-486.

170. Molnar, G. A. O. a. A., *Hydrocarbon Chemistry*. Hoboken: NJ, 2003.

171. Zerella, M.; Mukhopadhyay, S.; Bell, A. T., Direct Oxidation of Methane to Acetic Acid Catalyzed by Pd²⁺ and Cu²⁺ in the Presence of Molecular Oxygen. *Chemical Communications* 2004, (17), 1948-1949.

172. Somorjai, G.; Li, Y., *Introduction to Surface Chemistry and Catalysis*. Wiley-VCH: 2010.

173. Bernasek, S. L.; Somorjai, G. A., Small Molecule Reactions on Stepped Single-Crystal Platinum Surfaces. *Surface Science* 1975, 48 (1), 204-213.

174. Bernasek, S. L.; Somorjai, G. A., Molecular-Beam Study of Mechanism of Catalyzed Hydrogen-Deuterium Exchange on Platinum Single-Crystal Surfaces. *Journal of Chemical Physics* 1975, 62 (8), 3149-3161.
175. Bernasek, S. L.; Siekhaus, W. J.; Somorjai, G. A., Molecular-Beam Study of Hydrogen-Deuterium Exchange on Low-Miller-Index Platinum Single-Crystal Surfaces. *Physical Review Letters* 1973, 30 (24), 1202-1204.
176. Ruckenstein, E.; Hul, Y. H., Methane Partial Oxidation over NiO MgO Solid Solution Catalysts. *Applied Catalysis a-General* 1999, 183 (1), 85-92.
177. Shan, W. J.; Luo, M. F.; Ying, P. L.; Shen, W. J.; Li, C., Reduction Property and Catalytic Activity of $Ce_{1-x}Ni_xO_2$ Mixed Oxide Catalysts for CH_4 Oxidation. *Applied Catalysis a-General* 2003, 246 (1), 1-9.
178. Dissanayake, D.; Rosynek, M. P.; Kharas, K. C. C.; Lunsford, J. H., Partial Oxidation of Methane to Carbon-Monoxide and Hydrogen over a Ni/ Al_2O_3 Catalyst. *Journal of Catalysis* 1991, 132 (1), 117-127.
179. Choi, S. H.; Kang, Y. C., Ultrafast Synthesis of Yolk-Shell and Cubic NiO Nanopowders and Application in Lithium Ion Batteries. *Acs Applied Materials & Interfaces* 2014, 6 (4), 2312-2316.
180. Choi, S. H.; Kang, Y. C., One-Pot Facile Synthesis of Janus-Structured SnO_2 -CuO Composite Nanorods and Their Application as Anode Materials in Li-Ion Batteries. *Nanoscale* 2013, 5 (11), 4662-4668.
181. Yin, J.; Cao, H., Synthesis and Photocatalytic Activity of Single-Crystalline Hollow Rh- In_2O_3 Nanocrystals. *Inorganic Chemistry* 2012, 51 (12), 6529-6536.

182. Wang, C.; Zhao, Y.; Su, D.; Ding, C.; Wang, L.; Yan, D.; Li, J.; Jin, H., Synthesis of NiO Nano Octahedron Aggregates as High-Performance Anode Materials for Lithium Ion Batteries. *Electrochimica Acta* 2017, 231, 272-278.
183. Nguyen, L.; Tao, F. F.; Tang, Y.; Dou, J.; Bao, X.-J., Understanding Catalyst Surfaces During Catalysis through near Ambient Pressure X-Ray Photoelectron Spectroscopy. *Chemical Reviews* 2019, 119 (12), 6822-6905.
184. Kresse, G.; Furthmüller, J., Efficient Iterative Schemes for Ab Initio Total-Energy Calculations Using a Plane-Wave Basis Set. *Physical Review B* 1996, 54 (16), 11169-11186.
185. Kresse, G.; Furthmüller, J., Efficiency of Ab-Initio Total Energy Calculations for Metals and Semiconductors Using a Plane-Wave Basis Set. *Computational Materials Science* 1996, 6 (1), 15-50.
186. Kresse, G.; Hafner, J., Ab-Initio Molecular-Dynamics Simulation of the Liquid-Metal Amorphous-Semiconductor Transition in Germanium. *Physical Review B* 1994, 49 (20), 14251-14269.
187. Kresse, G.; Hafner, J., Ab Initio Molecular Dynamics for Liquid Metals. *Physical Review B* 1993, 47 (1), 558-561.
188. Perdew, J. P.; Burke, K.; Ernzerhof, M., Generalized Gradient Approximation Made Simple. *Physical Review Letters* 1996, 77 (18), 3865-3868.
189. Kresse, G.; Joubert, D., From Ultrasoft Pseudopotentials to the Projector Augmented-Wave Method. *Physical Review B* 1999, 59 (3), 1758-1775.
190. Blöchl, P. E., Projector Augmented-Wave Method. *Physical Review B* 1994, 50 (24), 17953-17979.

191. Peck, M. A.; Langell, M. A., Comparison of Nanoscaled and Bulk NiO Structural and Environmental Characteristics by XRD, XAFS, and XPS. *Chemistry of Materials* 2012, 24 (23), 4483-4490.
192. Anspoks, A.; Kalinko, A.; Kalendarev, R.; Kuzmin, A., Atomic Structure Relaxation in Nanocrystalline NiO Studied by EXAFS Spectroscopy: Role of Nickel Vacancies. *Physical Review B* 2012, 86 (17), 174114.
193. Tanaka, K.; Matsuzaki, S.; Toyoshima, I., Photodecomposition of Adsorbed Methoxy Species by UV-Light and Formaldehyde Adsorption on Si(111) Studied by XPS and UPS. *Journal of Physical Chemistry* 1993, 97 (21), 5673-5677.
194. Houtman, C.; Barteau, M. A., Reactions of Methanol on Rh(111) and Rh(111)-(2x2)O Surfaces - Spectroscopic Identification of Adsorbed Methoxide and ETA-1-Formaldehyde. *Langmuir* 1990, 6 (10), 1558-1566.
195. Liu, Z.; Huang, E.; Orozco, I.; Liao, W.; Palomino, R. M.; Rui, N.; Duchon, T.; Nemsak, S.; Grinter, D. C.; Mahapatra, M.; Liu, P.; Rodriguez, J. A.; Senanayake, S. D., Water-Promoted Interfacial Pathways in Methane Oxidation to Methanol on a CeO₂-Cu₂O Catalyst. *Science* 2020, 368 (6490), 513-517.
196. Tao, F. F.; Shan, J. J.; Nguyen, L.; Wang, Z.; Zhang, S.; Zhang, L.; Wu, Z.; Huang, W.; Zeng, S.; Hu, P., Understanding Complete Oxidation of Methane on Spinel Oxides at a Molecular Level. *Nature Communications* 2015, 6, 7798.
197. Wang, Z.; Cao, X. M.; Zhu, J.; Hu, P., Activity and Coke Formation of Nickel and Nickel Carbide in Dry Reforming: A Deactivation Scheme from Density Functional Theory. *Journal of Catalysis* 2014, 311 (0), 469-480.

198. Zhang, S. R.; Shan, J. J.; Nie, L. H.; Nguyen, L.; Wu, Z. L.; Tao, F., In Situ Studies of Surface of NiFe₂O₄ Catalyst During Complete Oxidation of Methane. *Surface Science* 2016, 648, 156-162.
199. Ciobica, I. M.; Frechard, F.; van Santen, R. A.; Kleyn, A. W.; Hafner, J., A DFT Study of Transition States for C-H Activation on the Ru(0001) Surface. *Journal of Physical Chemistry B* 2000, 104 (14), 3364-3369.
200. Zhang, X. G.; Liyanage, R.; Armentrout, P. B., Potential Energy Surface for Activation of Methane by Pt⁺: A Combined Guided Ion Beam and DFT Study. *Journal of the American Chemical Society* 2001, 123 (23), 5563-5575.
201. Abild-Pedersen, F.; Lytken, O.; Engbaek, J.; Nielsen, G.; Chorkendorff, I.; Norskov, J. K., Methane Activation on Ni(111): Effects of Poisons and Step Defects. *Surface Science* 2005, 590 (2-3), 127-137.
202. Jones, G.; Jakobsen, J. G.; Shim, S. S.; Kleis, J.; Andersson, M. P.; Rossmeisl, J.; Abild-Pedersen, F.; Bligaard, T.; Helveg, S.; Hinnemann, B.; Rostrup-Nielsen, J. R.; Chorkendorff, I.; Sehested, J.; Norskov, J. K., First Principles Calculations and Experimental Insight into Methane Steam Reforming over Transition Metal Catalysts. *Journal of Catalysis* 2008, 259 (1), 147-160.
203. Vines, F.; Lykhach, Y.; Staudt, T.; Lorenz, M. P. A.; Papp, C.; Steinrueck, H.-P.; Libuda, J.; Neyman, K. M.; Goerling, A., Methane Activation by Platinum: Critical Role of Edge and Corner Sites of Metal Nanoparticles. *Chemistry-a European Journal* 2010, 16 (22), 6530-6539.
204. Mayernick, A. D.; Janik, M. J., Methane Oxidation on Pd-Ceria: A DFT Study of the Mechanism over Pd_xCe_{1-x}O₂, Pd, and PdO. *Journal of Catalysis* 2011, 278 (1), 16-25.

205. Furlan, C.; Mortarino, C., Forecasting the Impact of Renewable Energies in Competition with Non-Renewable Sources. *Renewable & Sustainable Energy Reviews* 2018, 81, 1879-1886.
206. Peymani, M.; Alavi, S. M.; Rezaei, M., Synthesis Gas Production by Catalytic Partial Oxidation of Methane, Ethane and Propane on Mesoporous Nanocrystalline Ni/Al₂O₃ Catalysts. *International Journal of Hydrogen Energy* 2016, 41 (42), 19057-19069.
207. Bodke, A. S.; Olschki, D. A.; Schmidt, L. D.; Ranzi, E., High Selectivities to Ethylene by Partial Oxidation of Ethane. *Science* 1999, 285 (5428), 712-715.
208. Goetsch, D. A.; Schmidt, L. D., Microsecond Catalytic Partial Oxidation of Alkanes. *Science* 1996, 271 (5255), 1560-1562.
209. Jeong, S.; Kim, S.; Lee, B.; Ryi, S. K.; Lim, H., Techno-Economic Analysis: Ethane Steam Reforming in a Membrane Reactor with H₂ Selectivity Effect and Profitability Analysis. *International Journal of Hydrogen Energy* 2018, 43 (15), 7693-7702.
210. Schadel, B. T.; Duisberg, M.; Deutschmann, O., Steam Reforming of Methane, Ethane, Propane, Butane, and Natural Gas over a Rhodium-Based Catalyst. *Catalysis Today* 2009, 142 (1-2), 42-51.
211. Graf, P. O.; Mojet, B. L.; Lefferts, L., Influence of Potassium on the Competition between Methane and Ethane in Steam Reforming over Pt Supported on Yttrium-Stabilized Zirconia. *Applied Catalysis a-General* 2008, 346 (1-2), 90-95.
212. Graf, P. O.; Mojet, B. L.; van Ommen, J. G.; Lefferts, L., Comparative Study of Steam Reforming of Methane, Ethane and Ethylene on Pt, Rh and Pd Supported on Yttrium-Stabilized Zirconia. *Applied Catalysis a-General* 2007, 332 (2), 310-317.
213. Kneale, B.; Ross, J. R. H., The Steam Reforming of Ethane over Nickel Alumina Catalysts. *Faraday Discussions* 1981, 72, 157-171.

214. Yan, B. H.; Yang, X. F.; Yao, S. Y.; Wan, J.; Myint, M.; Gomez, E.; Xie, Z. H.; Kattel, S.; Xu, W. Q.; Chen, J. G. G., Dry Reforming of Ethane and Butane with CO₂ over PtNi/CeO₂ Bimetallic Catalysts. *Acs Catalysis* 2016, 6 (11), 7283-7292.
215. Myint, M.; Yan, B. H.; Wan, J.; Zhao, S.; Chen, J. G. G., Reforming and Oxidative Dehydrogenation of Ethane with CO₂ as a Soft Oxidant over Bimetallic Catalysts. *Journal of Catalysis* 2016, 343, 168-177.
216. Porosoff, M. D.; Myint, M. N. Z.; Kattel, S.; Xie, Z. H.; Gomez, E.; Liu, P.; Chen, J. G. G., Identifying Different Types of Catalysts for Co₂ Reduction by Ethane through Dry Reforming and Oxidative Dehydrogenation. *Angewandte Chemie-International Edition* 2015, 54 (51), 15501-15505.
217. Wang, L.; Li, H.; Zhang, W.; Zhao, X.; Qiu, J.; Li, A.; Zheng, X.; Hu, Z.; Si, R.; Zeng, J., Supported Rhodium Catalysts for Ammonia–Borane Hydrolysis: Dependence of the Catalytic Activity on the Highest Occupied State of the Single Rhodium Atoms. *Angewandte Chemie International Edition* 2017, 56 (17), 4712-4718.
218. Grabowski, R., Kinetics of Oxidative Dehydrogenation of C(2)-C(3) Alkanes on Oxide Catalysts. *Catalysis Reviews-Science and Engineering* 2006, 48 (2), 199-268.
219. Heracleous, E.; Machli, M.; Lemonidou, A. A.; Vasalos, L. A., Oxidative Dehydrogenation of Ethane and Propane over Vanadia and Molybdena Supported Catalysts. *Journal of Molecular Catalysis a-Chemical* 2005, 232 (1-2), 29-39.
220. Heracleous, E.; Lee, A.; Wilson, K.; Lemonidou, A., Investigation of Ni-Based Alumina-Supported Catalysts for the Oxidative Dehydrogenation of Ethane to Ethylene: Structural Characterization and Reactivity Studies. *Journal of Catalysis* 2005, 231 (1), 159-171.

221. Jia, C. G.; Kitamura, T.; Fujiwara, Y., Catalytic Functionalization of Arenes and Alkanes Via C-H Bond Activation. *Accounts of Chemical Research* 2001, 34 (8), 633-639.
222. Liu, J.; Fung, V.; Wang, Y.; Du, K.; Zhang, S.; Nguyen, L.; Tang, Y.; Fan, J.; Jiang, D.-e.; Tao, F. F., Promotion of Catalytic Selectivity on Transition Metal Oxide through Restructuring Surface Lattice. *Applied Catalysis B: Environmental* 2018, 237, 957-969.
223. Liu, J. J.; Zhang, S. R.; Zhou, Y.; Fung, V.; Nguyen, L.; Jiang, D. E.; Shen, W. J.; Fan, J.; Tao, F. F., Tuning Catalytic Selectivity of Oxidative Catalysis through Deposition of Nonmetallic Atoms in Surface Lattice of Metal Oxide. *Acs Catalysis* 2016, 6 (7), 4218-4228.
224. Frey, F. E.; Huppke, W. F., Equilibrium Dehydrogenation of Ethane, Propane, and the Butanes. *Industrial and Engineering Chemistry* 1933, 25, 54-59.
225. Gryaznov, V. M.; Maldonad.K; Khuares, E., A Deep Dehydrogenation of Ethane on Platinum. *Doklady Akademii Nauk Sssr* 1969, 184 (5), 1135-&.
226. Armstrong, R. D.; Freakley, S. J.; Forde, M. M.; Peneau, V.; Jenkins, R. L.; Taylor, S. H.; Moulijn, J. A.; Morgan, D. J.; Hutchings, G. J., Low Temperature Catalytic Partial Oxidation of Ethane to Oxygenates by Fe- and Cu-ZSM-5 in a Continuous Flow Reactor. *Journal of Catalysis* 2015, 330, 84-92.
227. Zhang, S.; Nguyen, L.; Liang, J.-X.; Shan, J.; Liu, J.; Frenkel, A. I.; Patlolla, A.; Huang, W.; Li, J.; Tao, F., Catalysis on Singly Dispersed Bimetallic Sites. *Nature communications* 2015, 6, 7938.
228. Supronowicz, W.; Ignatyev, I. A.; Lolli, G.; Wolf, A.; Zhao, L.; Mleczko, L., Formic Acid: A Future Bridge between the Power and Chemical Industries. *Green Chemistry* 2015, 17 (5), 2904-2911.

229. Hietala, J. V., A.; Johnsson, P.; Pollari, I.; Reutemann, W.; Kieczka, H., Formic Acid. In Ullmann's Encyclopedia of Industrial Chemistry; Wiley-Vch Verlag Gmbh & Co. Kгаа. 2016.
230. Budiman, A. W.; Nam, J. S.; Park, J. H.; Mukti, R. I.; Chang, T. S.; Bae, J. W.; Choi, M. J., Review of Acetic Acid Synthesis from Various Feedstocks through Different Catalytic Processes. *Catalysis Surveys from Asia* 2016, 20 (3), 173-193.
231. Fokom-Domgue, J.; Combescure, C.; Fokom-Defo, V.; Tebeu, P. M.; Vassilakos, P.; Kengne, A. P.; Petignat, P., Performance of Alternative Strategies for Primary Cervical Cancer Screening in Sub-Saharan Africa: Systematic Review and Meta-Analysis of Diagnostic Test Accuracy Studies. *Bmj-British Medical Journal* 2015, 351.
232. Canete, B.; Gigola, C. E.; Brignole, N. B., Synthesis Gas Processes for Methanol Production Via CH₄ Reforming with CO₂, H₂O, and O₂. *Industrial & Engineering Chemistry Research* 2014, 53 (17), 7103-7112.
233. Bazin, D.; Guzzi, L., Soft X-Ray Absorption Spectroscopy in Heterogeneous Catalysis. *Applied Catalysis a-General* 2001, 213 (2), 147-162.
234. Zhang, S. R.; Nguyen, L.; Liang, J. X.; Shan, J. J.; Liu, J. Y.; Frenkel, A. I.; Patlolla, A.; Huang, W. X.; Li, J.; Tao, F., Catalysis on Singly Dispersed Bimetallic Sites. *Nature Communications* 2015, 6, 10.
235. Wang, L.; Zhang, S. R.; Zhu, Y.; Patlolla, A.; Shan, J. J.; Yoshida, H.; Takeda, S.; Frenkel, A. I.; Tao, F., Catalysis and in Situ Studies of Rh₁/Co₃O₄ Nanorods in Reduction of NO with H₂. *Acs Catalysis* 2013, 3 (5), 1011-1019.
236. Burch, R.; Loader, P. K.; Cruise, N. A., An Investigation of the Deactivation of Rh/Alumina Catalysts under Strong Oxidising Conditions. *Applied Catalysis a-General* 1996, 147 (2), 375-394.

237. Folkins, H. O., Benzene. In *Ullmann's Encyclopedia of Industrial Chemistry*, 2000.
238. Argyle, M. D.; Chen, K. D.; Bell, A. T.; Iglesia, E., Effect of Catalyst Structure on Oxidative Dehydrogenation of Ethane and Propane on Alumina-Supported Vanadia. *Journal of Catalysis* 2002, 208 (1), 139-149.
239. Takanabe, K.; Shahid, S., Dehydrogenation of Ethane to Ethylene Via Radical Pathways Enhanced by Alkali Metal Based Catalyst in Oxysteam Condition. *Aiche Journal* 2017, 63 (1), 105-110.
240. Leth, K. T.; Rovik, A. K.; Holm, M. S.; Brorson, M.; Jakobsen, H. J.; Skibsted, J.; Christensen, C. H., Synthesis and Characterization of Conventional and Mesoporous Ga-Mfi for Ethane Dehydrogenation. *Applied Catalysis A: General* 2008, 348 (2), 257-265.
241. Frash, M. V.; van Santen, R. A., Activation of Small Alkanes in Ga-Exchanged Zeolites: A Quantum Chemical Study of Ethane Dehydrogenation. *Journal of Physical Chemistry A* 2000, 104 (11), 2468-2475.
242. Samanta, A.; Bai, X.; Robinson, B.; Chen, H.; Hu, J., Conversion of Light Alkane to Value-Added Chemicals over ZSM-5/Metal Promoted Catalysts. *Industrial & Engineering Chemistry Research* 2017, 56 (39), 11006-11012.
243. Cybulskis, V. J.; Bukowski, B. C.; Tseng, H. T.; Gallagher, J. R.; Wu, Z. W.; Wegener, E.; Kropf, A. J.; Ravel, B.; Ribeiro, F. H.; Greeley, J.; Miller, J. T., Zinc Promotion of Platinum for Catalytic Light Alkane Dehydrogenation: Insights into Geometric and Electronic Effects. *Acs Catalysis* 2017, 7 (6), 4173-4181.
244. Nguyen, L.; Tao, F. F.; Tang, Y.; Doug, J.; Bao, X. J., Understanding Catalyst Surfaces During Catalysis through near Ambient Pressure X-Ray Photoelectron Spectroscopy. *Chemical Reviews* 2019, 119 (12), 6822-6905.

245. Wang, N.; Sun, Q.; Bai, R.; Li, X.; Guo, G.; Yu, J., In Situ Confinement of Ultrasmall Pd Clusters within Nanosized Silicalite-1 Zeolite for Highly Efficient Catalysis of Hydrogen Generation. *Journal of the American Chemical Society* 2016, 138 (24), 7484-7487.
246. Treacy, M. M. J. H., J. B., *Collection of Simulated XRD Powder Patterns for Zeolites, 4th Ed.; Elsevier: Amsterdam. 2001.*
247. Almutairi, S. M. T.; Mezari, B.; Magusin, P.; Pidko, E. A.; Hensen, E. J. M., Structure and Reactivity of Zn-Modified ZSM-5 Zeolites: The Importance of Clustered Cationic Zn Complexes. *Acs Catalysis* 2012, 2 (1), 71-83.
248. Jeong, E.; Yu, H. J.; Han, S. W.; An, S. J.; Yoo, J.; Kim, Y.-J.; Yi, G.-C., Local Structural Properties of ZnO Nanoparticles, Nanorods and Powder Studied by Extended X-Ray Absorption Fine Structure. *Journal of the Korean Physical Society* 2008, 53, 461-465.
249. Haynes, W. M., ed., *CRC Handbook of Chemistry and Physics*. CRC Press: 2011.
250. Takahashi, K.; Yoshikawa, A.; Sandhu, A., *Wide Bandgap Semiconductors Fundamental Properties and Modern Photonic and Electronic Devices*. 2007.
251. Patnaik, P., *Handbook of Inorganic Chemicals*. Mcgraw-Hill. 2002.
252. Schneider, S. J., *Compilation of the Melting Points of the Metal Oxides*. 1963.
253. Alcock, C. B.; Itkin, V. P.; Horrigan, M. K., Vapour Pressure Equations for the Metallic Elements: 298–2500k. *Canadian Metallurgical Quarterly* 1984, 23 (3), 309-313.
254. Fung, V.; Tao, F.; Jiang, D. E., Low-Temperature Activation of Methane on Doped Single Atoms: Descriptor and Prediction. *Physical Chemistry Chemical Physics* 2018, 20 (35), 22909-22914.
255. Hansen, M.; Anderko, K., “Constitution of Binary Alloys” 2nd Edition, Mcgraw-Hill Companies, Inc., New York,. 1958.

256. Lu, Y.; Keav, S.; Marchionni, V.; Chiarello, G. L.; Pappacena, A.; Di Michiel, M.; Newton, M. A.; Weidenkaff, A.; Ferri, D., Ageing Induced Improvement of Methane Oxidation Activity of Pd/YFeO₃. *Catalysis Science & Technology* 2014, 4 (9), 2919-2931.
257. Husin, H.; Su, W.-N.; Pan, C.-J.; Liu, J.-Y.; Rick, J.; Yang, S.-C.; Chuang, W.-T.; Sheu, H.-S.; Hwang, B.-J., Pd/Nio Core/Shell Nanoparticles on La_{0.02}Na_{0.98}TaO₃ Catalyst for Hydrogen Evolution from Water and Aqueous Methanol Solution. *International Journal of Hydrogen Energy* 2013, 38 (31), 13529-13540.
258. Gallagher, J. R.; Childers, D. J.; Zhao, H.; Winans, R. E.; Meyer, R. J.; Miller, J. T., Structural Evolution of an Intermetallic Pd–Zn Catalyst Selective for Propane Dehydrogenation. *Physical Chemistry Chemical Physics* 2015, 17 (42), 28144-28153.
259. Tew, M. W.; Emerich, H.; van Bokhoven, J. A., Formation and Characterization of PdZn Alloy: A Very Selective Catalyst for Alkyne Semihydrogenation. *The Journal of Physical Chemistry C* 2011, 115 (17), 8457-8465.
260. Sun, Y.; Frenkel, A. I.; Isseroff, R.; Shonbrun, C.; Forman, M.; Shin, K.; Koga, T.; White, H.; Zhang, L.; Zhu, Y.; Rafailovich, M. H.; Sokolov, J. C., Characterization of Palladium Nanoparticles by Using X-Ray Reflectivity, EXAFS, and Electron Microscopy. *Langmuir* 2006, 22 (2), 807-816.
261. Min, Y. Y.; Shang, Y. S.; Song, Y.; Li, G. D.; Gong, Y. J., The Synthesis of Nanosheets Zeolite and Its Catalytic Application. *Progress in Chemistry* 2015, 27 (8), 1002-1013.
262. Morales-Pacheco, P.; Alvarez, F.; Bucio, L.; Dominguez, J. M., Synthesis and Structural Properties of Zeolitic Nanocrystals Ii: FAU-Type Zeolites. *Journal of Physical Chemistry C* 2009, 113 (6), 2247-2255.

263. Li, H.; Song, Z. N.; Zhang, X. J.; Huang, Y.; Li, S. G.; Mao, Y. T.; Ploehn, H. J.; Bao, Y.; Yu, M., Ultrathin, Molecular-Sieving Graphene Oxide Membranes for Selective Hydrogen Separation. *Science* 2013, 342 (6154), 95-98.
264. Fathizadeh, M.; Tien, H. N.; Khivantsev, K.; Chen, J. T.; Yu, M., Printing Ultrathin Graphene Oxide Nanofiltration Membranes for Water Purification. *Journal of Materials Chemistry A* 2017, 5 (39), 20860-20866.
265. Zhou, F. L.; Tien, H. N.; Xu, W. W. L.; Chen, J. T.; Liu, Q. L.; Hicks, E.; Fathizadeh, M.; Li, S. G.; Yu, M., Ultrathin Graphene Oxide-Based Hollow Fiber Membranes with Brush-Like Co²⁺-Philic Agent for Highly Efficient CO₂ Capture. *Nature Communications* 2017, 8, 8.
266. Zheng, S. X.; Tu, Q. S.; Urban, J. J.; Li, S. F.; Mi, B. X., Swelling of Graphene Oxide Membranes in Aqueous Solution: Characterization of Interlayer Spacing and Insight into Water Transport Mechanisms. *Acs Nano* 2017, 11 (6), 6440-6450.
267. Improvements in the Manufacture and Production of Alkyl Esters of Formic Acid GB 252848, 1925.
268. A Process for the Preparation of Methyl Formate. GB 1047408, 1966.
269. Awala, H.; Gilson, J. P.; Retoux, R.; Boullay, P.; Goupil, J. M.; Valtchev, V.; Mintova, S., Template-Free Nanosized Faujasite-Type Zeolites. *Nature Materials* 2015, 14 (4), 447-451.
270. Zhu, G. S.; Qiu, S. L.; Yu, J. H.; Sakamoto, Y.; Xiao, F. S.; Xu, R. R.; Terasaki, O., Synthesis and Characterization of High-Quality Zeolite Lta and Fau Single Nanocrystals. *Chemistry of Materials* 1998, 10 (6), 1483-1486.
271. Severance, M.; Wang, B.; Ramasubramanian, K.; Zhao, L.; Ho, W. S. W.; Dutta, P. K., Rapid Crystallization of Faujasitic Zeolites: Mechanism and Application to Zeolite Membrane Growth on Polymer Supports. *Langmuir* 2014, 30 (23), 6929-6937.

272. Dazzi, A.; Prater, C. B., Afm-Ir: Technology and Applications in Nanoscale Infrared Spectroscopy and Chemical Imaging. *Chemical Reviews* 2017, 117 (7), 5146-5173.
273. Shan, Y. P.; Wang, H. D., The Structure and Function of Cell Membranes Examined by Atomic Force Microscopy and Single-Molecule Force Spectroscopy. *Chemical Society Reviews* 2015, 44 (11), 3617-3638.
274. Arsem, W. C. Process for the Production of Formic Acid. US1606394, 1926.
275. Tang, Y.; Ma, L. J.; Dou, J.; Andolina, C. M.; Li, Y. T.; Ma, H. B.; House, S. D.; Zhang, X. Y.; Yang, J.; Tao, F., Transition of Surface Phase of Cobalt Oxide During CO Oxidation. *Physical Chemistry Chemical Physics* 2018, 20 (9), 6440-6449.

Appendix A More experimental results of chapter 3

Setup of experiments

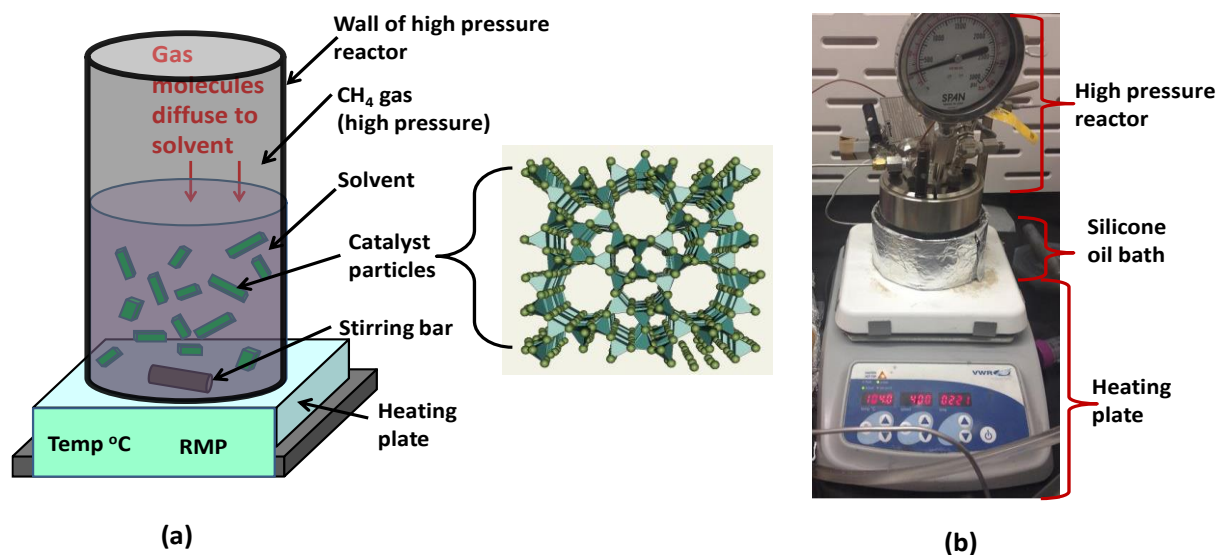


Figure S3.1 Setup of the catalytic transformation of CH₄ to acetic acid and other products in a Parr reactor. Typically, 28 mg catalyst was loaded to the catalyst and dispersed in 10 ml (aqueous water or dodecane). Gases with certain pressure were introduced and mixed. The Parr reactor containing catalyst and a mixture of reactants was loaded to an oil bath. The output power of the heating plate was modulated by the K-type thermocouple that was inserted into the liquid solution in the Parr reactor. The reading temperature during catalysis is $T \pm 1^\circ\text{C}$; here T is typically 150°C . When the temperature of the liquid in the Parr reactor reaches the set temperature such as 150°C , the stirring bar started to stir to make the solid catalyst dispersed in liquid homogeneously.

ICP-AES measurements of concentrations of Rh in catalysts

ICP-AES was used in the measurements of Rh concentration in catalysts before and after catalysis. Four standard solutions with different concentrations of Rh³⁺ (0.1ppm, 1ppm, 5ppm, 10ppm) were prepared by dissolving Rh(NO₃)₃ into de-ionized water. The volume of each solution is 40 ml. The standard curve was built through measuring the four solutions under the exactly same setup and parameters of the ICP-AES (mode: JY 2000 2 manufacture: HORIBA) and then plotting the known concentrations of the four solutions as a function of the optical emission spectrometry intensity. Figure S3.2 is the plot of the known concentration of the solution as a function of the

atomic emission spectrometry intensity. It is the standard curve for the measurements of the concentration of Rh in the fresh and used catalysts.

To prepare a test solution of ICP-AES analysis, a certain amount of fresh or used catalyst (0.10wt% Rh/ZSM-5) was dissolved in NaOH solution through simply mixing the accurately weighed catalyst into 10mL (>1M) NaOH solution and then sonication the mixture for about 12h. Then, aqua regia (a mixture of nitric acid and hydrochloric acid) was added to the solution until the pH was less than 5. After filtration, the transparent solution was diluted by adding DI water to make the volume of the diluted solution to 30 ml. All test solution was tested under the exact same setup and parameters of the same ICP-AES.

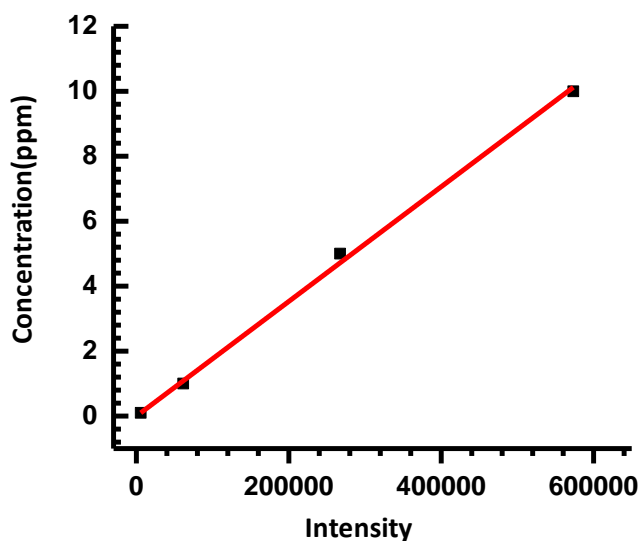


Figure S3. 2 Standard curves for measurement of the concentration of Rh cations in solution with ICP-AES.

Catalysis evaluation by NMR measurements

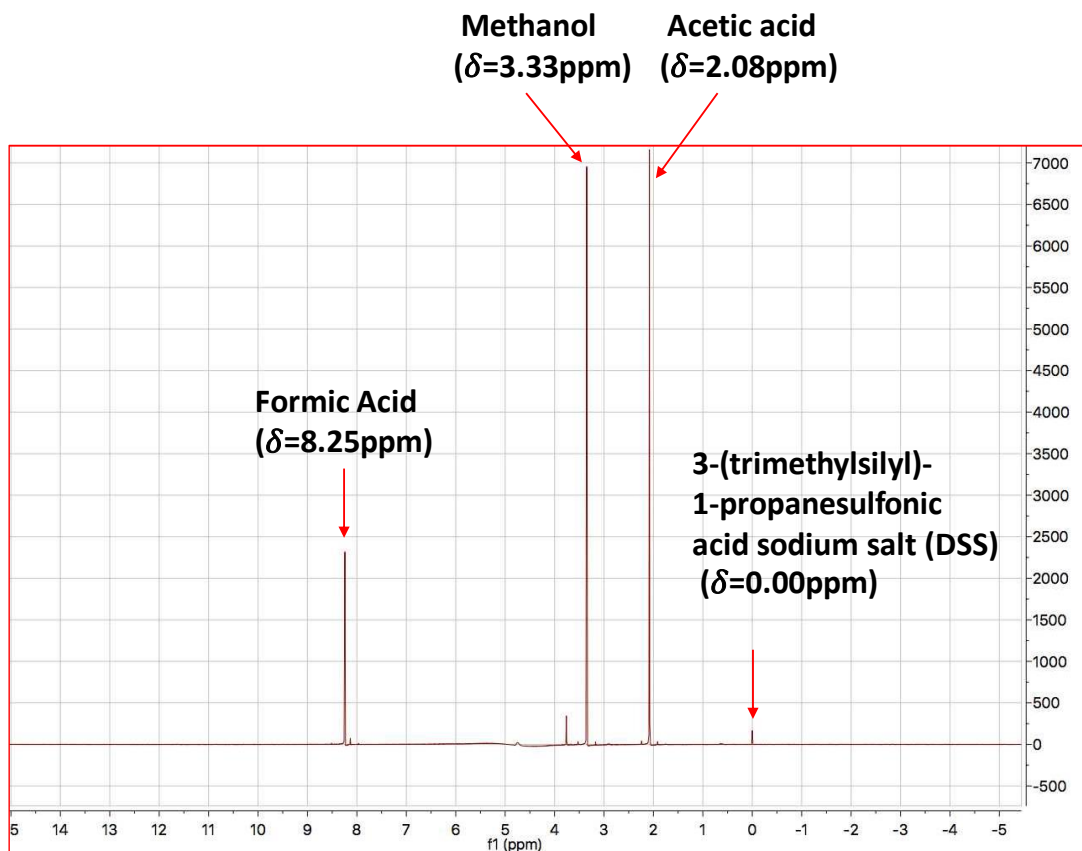


Figure S3. 3 $^1\text{H-NMR}$ spectrum of solution in Parr reactor after chemical transformation of CH_4 to acetic acid, methanol and formic acid on 0.10wt% Rh@ZSM-5.

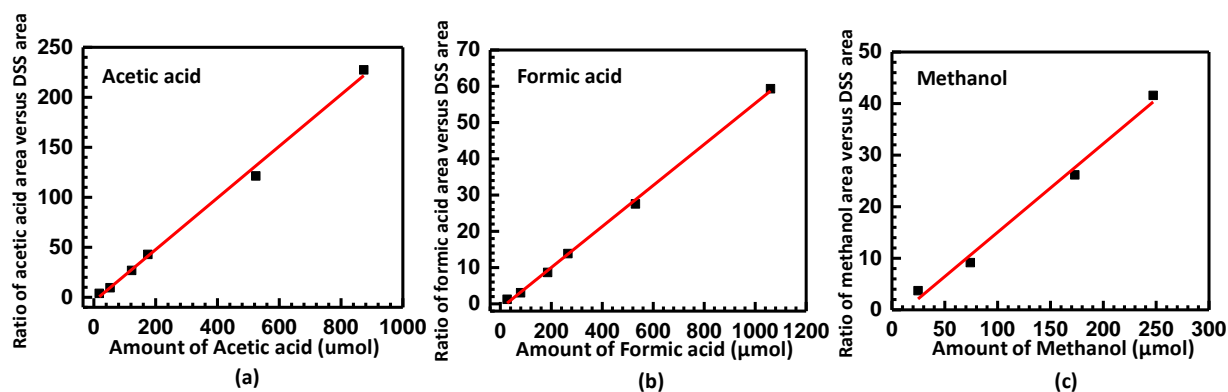


Figure S3. 4 Standard curves built for measurements of amount of acetic acid (a), formic acid (b), and methanol (c) through $^1\text{H-NMR}$ spectra.

Carbon balance and extra experiments of the transformation of methane to acetic acid

Table S3. 1 Analysis of carbon-containing reactants before the catalytic transformation of CH₄, CO and O₂ and the left carbon-containing reactants and the formed carbon-containing products in Parr reactor

	Carbon of CH ₄ (μmol)	Carbon of acetic acid (μmol)	Carbon of formic acid (μmol)	Carbon of methanol (μmol)	Carbon of CO (μmol)	Carbon of CO ₂ (μmol)	Carbon in total (μmol)
Before catalysis	20848.4				3207.4		24055.8
After catalysis	19857.2	224.2	146.3	37.0	2046.0	None	22310.7

Note: Catalytic condition: 28 mg 0.10wt%Rh/ZSM-5 in 10 ml deionized H₂O, 50 bar CH₄, 10 bar CO and 8 bar O₂, 2 h of reaction time. 112.1 μmol acetic acid, 146.3 μmol formic acid, 37 μmol of methanol were produced.

Table S3. 2 Catalytic performances of 28 mg catalysts with different loadings of rhodium. The reaction was conducted in 10 ml H₂O under gas phase of a mixture of 10 bar CH₄, 5 bar CO and 2 bar O₂ at 150°C in a Parr reactor. The reaction time is 1 h.

Entry	Catalyst	Mixture of reactants (bar)	Temperature (°C)	Methanol (μmol)	Formic acid (μmol)	Acetic acid (μmol)	Total products (μmol)
1	H-ZMS-5	CH ₄ : 10 bar CO: 5 bar O ₂ : 2bar	150	3.7±5.0	2.3±5.0	1.9±5.0	7.8±5.0
2	0.01wt%Rh/ZSM-5	CH ₄ : 10 bar CO: 5 bar O ₂ : 2 bar	150	7.4±5.0	4.6±5.0	5.7±5.0	17.6±15.0
3	0.05wt%Rh/ZSM-5	CH ₄ : 10 bar CO: 5 bar O ₂ : 2 bar	150	12.4±5.0	89.4±5.0	44.0±5.0	145.8±15.0
4	0.10wt%Rh/ZSM-5	CH ₄ : 10 bar CO: 5 bar O ₂ : 2 bar	150	14.0±5.0	153.4±5.0	58.7±5.0	246.0±15.0
5	0.50wt%Rh/ZSM-5	CH ₄ : 10 bar CO: 5 bar O ₂ : 2 bar	150	11.2±5.0	144.1±5.0	86.6±5.0	241.8±15.0

Calculations of TOF of 0.10wt%Rh/ZSM-5 and Rh(NO₃)₃

The turn-over frequency of Rh₁O₅/ZSM-5 and Rh(NO₃)₃ used in this work were calculated in terms of the number of product molecules per Rh site per second. The following paragraphs will describe how they were calculated.

For catalyst, Rh₁O₅/ZMS-5 (0.10wt%Rh/ZSM-5), as shown in entry 4 of Table S3.1, 58.7 μmol of acetic acid was formed from 28 mg of catalyst at 150°C per hr. The concentration of rhodium in the catalyst is 0.10wt%. The amount of all Rh atoms is $\frac{28 \times 10^{-3} \text{ gram} \times 0.10\%}{104 \text{ gram per mol Rh}} = 2.8 \times 10^{-7} \text{ mol}$. By assuming all Rh atoms anchored to ZSM-5 participate in this catalysis, TOF for production of acetic acid can be calculated as the following:

$$TOF = \frac{58.7 \times 10^{-6} \text{ mol} \times N_A}{2.8 \times 10^{-7} \times N_A \times 3600 \text{ second}} = 0.06 \text{ acetic molecules per Rh site per second.}$$

The TOFs of 14.0 μmol methanol and 153.4 μmol formic acid can be calculated via the same approach.

A similar experiment was performed with Rh cations without any supports in aqueous solution. 5 ml of 0.01 mol/l Rh(NO₃)₃ was added in the Parr reactor and then 50 bar CH₄, 10 bar CO and 8 bar O₂ was introduced the Parr reactor. The reaction was performed at 150°C for about 90 h. With the same calculation method, the TORs were calculated. The TORs of all organic products (CH₃COOH, CH₃OH and HCOOH) and TOR of acetic acid are 2.4×10⁻⁵ organic molecules and 6.3×10⁻⁶ acetic acid molecules per Rh site per second generated from homogeneous catalyst Rh(NO₃)₃ without any promoter.

Control experiments for confirming the participation of three reactants

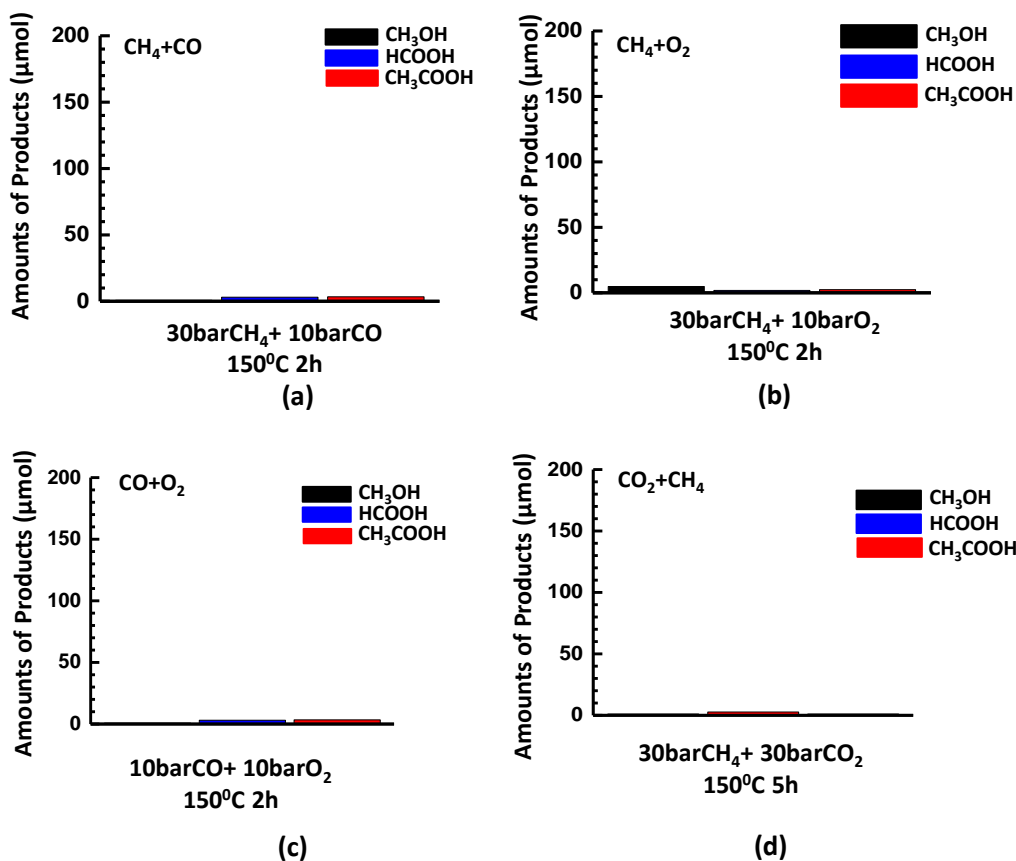


Figure S3. 5 Yields of acetic acid, formic acid and methanol from 28 mg 0.10wt% Rh/ZSM-5 in aqueous solution at 150°C for a certain amount of time as shown in figures in (a) the mixture of 30 bar CH_4 and 10 bar CO, (b) the mixture of 30 bar CH_4 and 10 bar O_2 , (c) the mixture of 10 bar CO and 10 bar O_2 , and (d) the mixture of 30 bar CO_2 and 30 bar CH_4 .

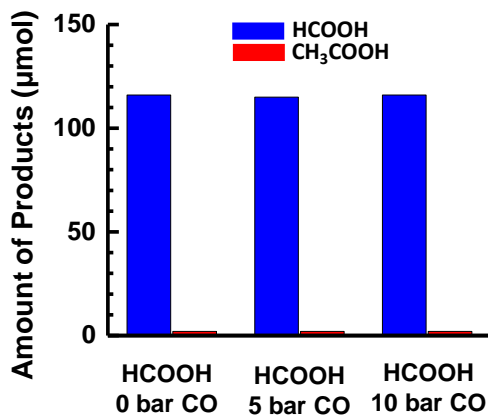


Figure S3. 6 Yields of acetic acid when 118 μmol HCOOH was mixed with different pressure of CO at 150°C for 3 h

Isotope-labeled experiments using $^{13}\text{CH}_3\text{OH}$.

To test whether acetic acid could form from carbonylation of CH_3OH on our catalyst 0.10wt%Rh/ZSM-5, 1.0 mmol isotope-labeled $^{13}\text{CH}_3\text{OH}$ (99 atom% ^{13}C , Aldrich) was added to 10 ml deionized H_2O before the introduction of 10 bar CH_4 , 5 bar CO , and 4 bar O_2 to the Parr reactor. The purpose of adding isotope-labeled $^{13}\text{CH}_3\text{OH}$ to H_2O before catalysis is to test whether $^{13}\text{CH}_3\text{OH}$ could act as an intermediate to react with CO on the catalyst to form isotope-labeled acetic acid, $^{13}\text{CH}_3\text{COOH}$. In the reaction pathway β acetic acid is formed through carboxylation of methanol; in other words, methanol should be involved definitely, while the reaction pathway α does not involve CH_3OH . There would be three sets of possible products if $^{13}\text{CH}_3\text{OH}$ was added as a probe agent. Figures 3.7c and 3.7d are a regular ^1H NMR spectrum of the solution obtained from 10 bar CH_4 , 5 bar CO and 4 bar O_2 and the ^1H NMR spectrum of the solution obtained from 10 bar CH_4 , 5 bar CO and 4 bar O_2 with added 1 mmol $^{13}\text{CH}_3\text{OH}$, respectively.

Appendix B Supplementary information of chapter 4

Measurements of catalytic performances of NiO catalysts

Catalytic performances of complete oxidation of methane on NiO catalysts were measured in a fix-bed flow reactor made of quartz. The reactant gases were a mixture of 20 ml/min 10% CH₄ balanced with Ar and 10 ml/min pure O₂ (99.99%). They were mixed before flowing into the reactor. The molar ratio of CH₄ to O₂ in the mixture is 1:5. A certain amount of catalyst powder in 40-60 mesh was used in each measurement as noted in figure captions or text. The gas mixture leaving downstream of this reactor was introduced to the introduction port of a gas chromatograph equipped with columns and FID and TCD detectors. The gas components in the mixture were separated with GC columns first and then the concentrations of CH₄, CO₂ and CO was measured with FID equipped with a methanizer. In addition, concentrations of CH₄, CO₂, and potential CO were measured with TCD as well, although the sensitivities of TCD to CH₄, particularly CO₂ and CO are low. These measurements were performed in an on-line mode. At each temperature, the catalyst was remained for about two hours for the acquisition of multiple sets of data. At least three sets of data were collected at each temperature.

The conversion of methane was calculated using the following equation: $X_{CH_4} \% = \frac{M_0 - M_t}{M_0} \times 100\%$, where M_0 is the peak area of methane without any consumption, and M_t is the peak area of unreacted methane after conversion of certain portion of CH₄ at each temperature. No CO was found in the gas mixture, showing that partial oxidation of methane was not a side reaction on NiO catalysts. Carbon balance at each temperature suggested no deposition of atomic carbon, probably due to excess O₂ in the mixture of reactants, the high molar ratio of O₂ to CH₄ in the gas mixture introduced to upstream of the fixed-bed flow reactor. Planar sheet NiO has much higher surface area (127 m²/g) than octahedral NiO (21.5 m²/g). For a fair comparison of catalytic

performances of CH₄ complete oxidation on planar sheet NiO and octahedral NiO, 100 mg planar sheet NiO and 500 mg of octahedral NiO which have some similar surface area, were used in the measurements of catalytic performance under the same catalytic condition [a mixture of reactants is the mixture of 20 ml/min 10% CH₄ balanced with Ar and 10 ml/min pure O₂ (99.99%)]. The conversions of CH₄ on the two catalysts were presented in Figure 2d in the main text. Planar sheet NiO and octahedral NiO exhibited distinctly different catalytic activity in complete oxidation of CH₄ in the temperature range of 250°C-400°C. Planar sheet NiO is highly active for CH₄ complete oxidation but octahedral NiO is not active at all

Compared to planar sheet NiO (127 m²/g), surface area of cubic NiO is much lower. It is only 5-6 m²/g due to its large size. 100 mg of cubic NiO without any pre-reduction in 5% H₂ was used as catalyst; activity in CH₄ complete oxidation on 100 mg of cubic NiO was measured under the same condition as that used for 100 mg of planar sheet NiO and 500 mg of cubic NiO.

To generate oxygen vacancies and thus to decrease the coordination environment of Ni atoms on (100) surface of cubic NiO, cubic NiO was partially reduced in 5% H₂ for one hour. Through this partial reduction at 225°C, 250°C, 275°C, and 300°C in 5% H₂, four catalysts were prepared in the fixed-bed flow reactor before immediately followed measurements of catalytic performance for CH₄ complete oxidation. The four catalysts were named, cubic NiO-H₂-225°C, cubic NiO-H₂-250°C, cubic NiO-H₂-275°C, and cubic NiO-H₂-300°C.

Appendix C Extra experimental results of chapter 5

The Rh concentration of fresh and used catalysts measured by ICP-AES

Four standard solutions with different concentrations of Rh^{3+} (0.1ppm, 1ppm, 5ppm, 10ppm) were prepared by dissolving a certain amount of $\text{Rh}(\text{NO}_3)_3$ into 40ml deionized water. The standard curve (shown in Figure S5.1) was built by plotting the known concentration of Rh in solutions as a function of the atomic emission spectrometry intensity measured by the same setup of ICP-AES. The built standard curve was used for the measurements of the concentration of Rh in the fresh and used catalysts. A test solution of ICP-AES analysis was prepared by dissolving a certain amount of fresh or used catalyst into 10ml NaOH solution (>1.0 M). In order to dissolve the framework of ZSM-5, the mixture was sonicated and heated at 50°C overnight. After the dissolution and filtration, several drops of aqua regia (a mixture of nitric acid and hydrochloric acid) were added to the solution to adjust the pH less than 5. Then, the transparent test solution was diluted by adding DI water to make the total volume of 30 ml and then was examined under the same setup of the ICP-AES as used for previous solutions used for building the standard curve.

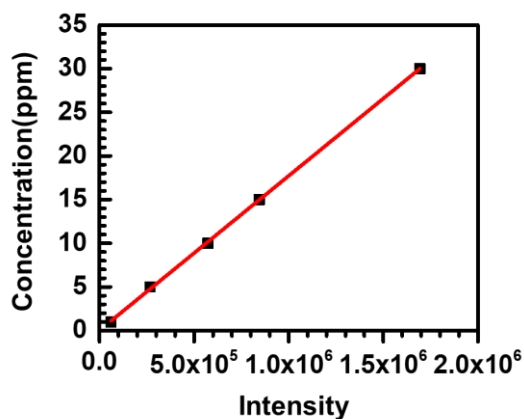


Figure S5. 1 Standard curve of ICP-AES to measure the Rh concentration of fresh and used catalysts

^1H -NMR spectrum of the filtered aqueous solution after ethane oxidation reaction by hydrogen peroxide

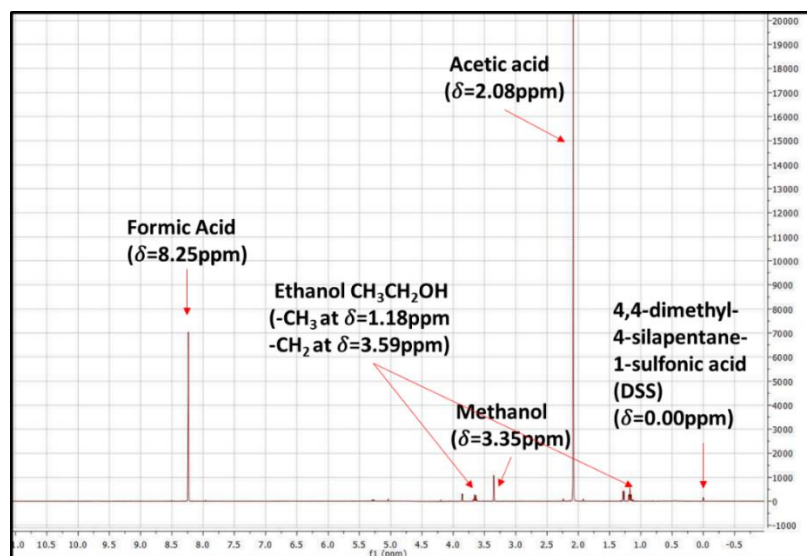


Figure S5. 2 $^1\text{H-NMR}$ spectrum of the filtered aqueous solution after ethane oxidation reaction by hydrogen peroxide.

Standard curves established for measuring amounts of acetic acid, formic acid, ethanol and methanol

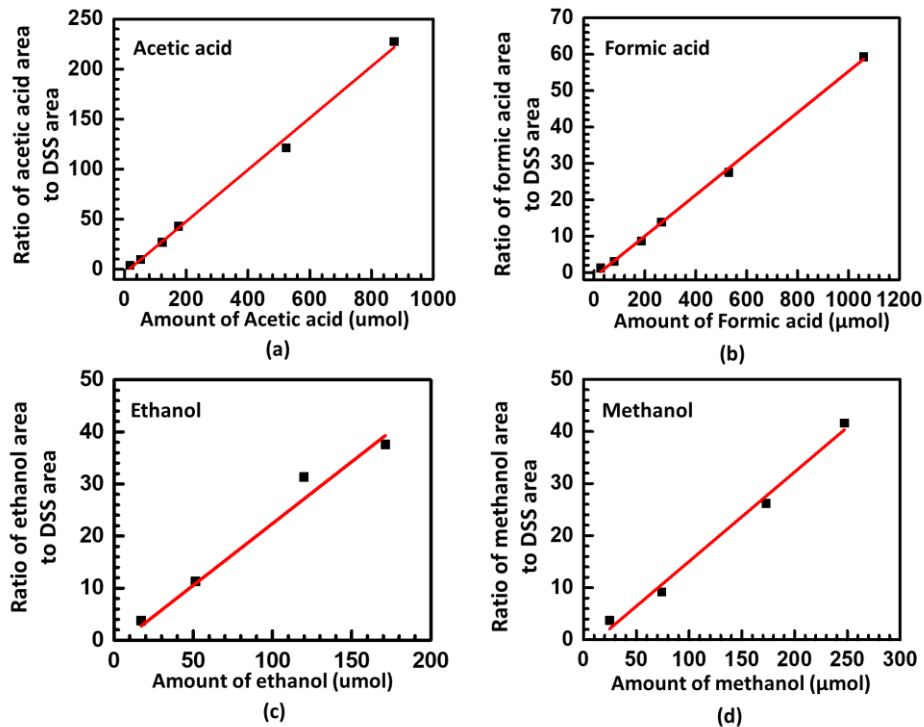


Figure S5. 3 Standard curves established for measuring amounts of (a) acetic acid, (b) formic acid, (c) ethanol and (d) methanol formed in aqueous solution through oxidation of ethane with H_2O_2 .

Catalytic performance of 3. 0.1wt%Rh/Silicalite-1

30mg 0.10wt%Rh/Silicalite-1 prepared through the same incipient wetness impregnation (IWI) method and calcination condition as that of 0.10wt%Rh/ZSM-5 was used to catalyze ethane oxidation at 50°C for 2h by introducing 15bar C₂H₆ and 10mmol H₂O₂. A significant decrease of amounts of products indicates that Rh not anchoring on ion-exchange sites would not be active to ethane partial oxidation at near room temperature.

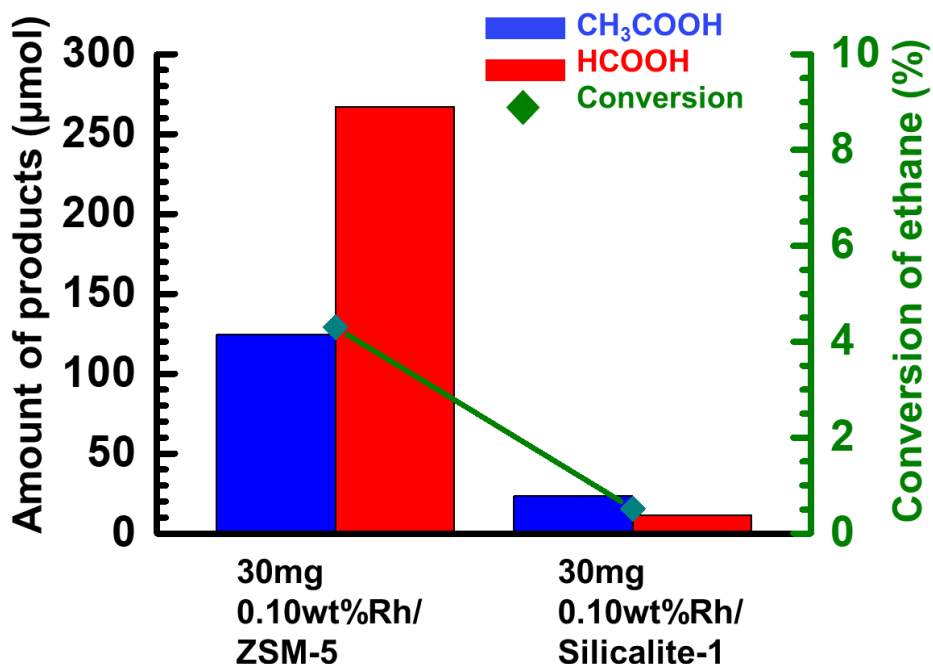


Figure S5. 4 Comparison of activities of ethane partial oxidation between 0.1wt%Rh/ZSM-5 and 0.10wt%Rh/Silicalite-1. Both reactions were performed with 30mg catalysts at 50°C for 2h by introducing 15bar C₂H₆ and 10 ml aqueous solution of 10mmol H₂O₂.

Influence of product diffusion on the amounts of the products

To check whether the formed acetic acid and formic acid experienced diffusion limits in aqueous solution during catalysis, parallel catalytic studies on 30 mg 0.10wt%Rh/ZSM-5 at 50°C dispersed in 10 ml solution of H₂O₂ under ethane of 15 bar sealed in a Parr reactor were performed at different stirring speeds, 350 rpm and 850 rpm. As shown in Figure S5.5, the amount of acetic

acid only slightly increased after the stirring rate largely rise from 350 rpm to 850 rpm although the amount of formic acid increased. It suggests there is no obvious diffusion limit.

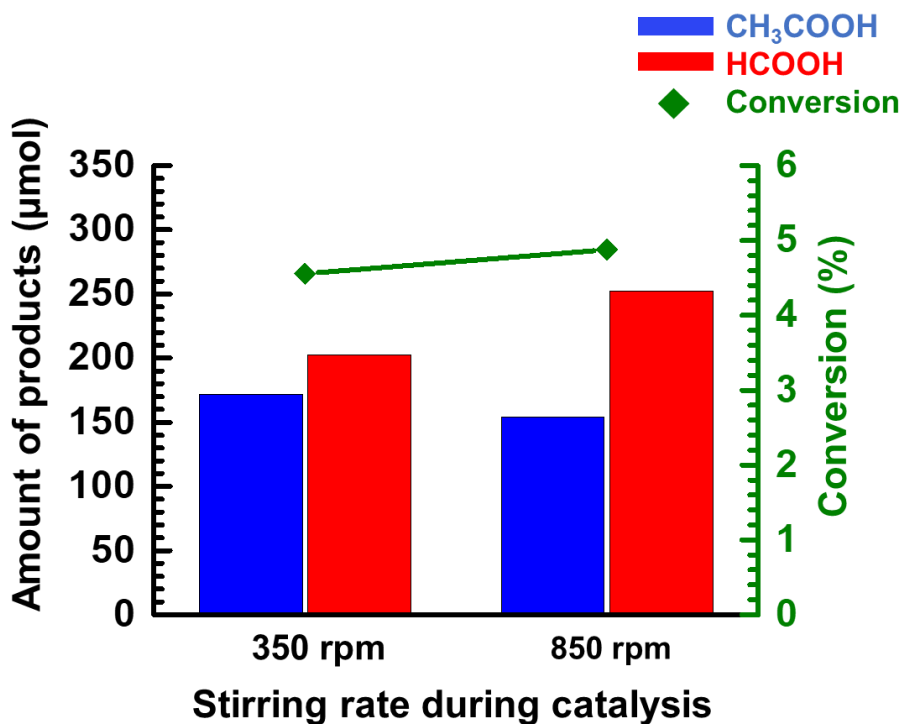


Figure S5. 5 Influence of diffusion of product molecules from catalyst particles to solution on amounts of acetic acid and formic acid by using 30 mg 0.10wt% Rh/ZSM-5, introducing 15bar C₂H₆ and 10 ml aqueous solution of 10mmol H₂O₂, heating at 50°C for 2h, at 350rpm and 850 rpm, respectively. Contribution of H-ZSM-5 to formation of acetic acid and formic acid was subtracted.

Relationship between the activity and amount of catalysts

Amounts of acetic acid and formic acid were generally proportional increased with a linear relationship when adding an amount of catalysts proportionally. This may suggest that the kinetics gained from 45-72°C is the true activation barrier of the ethane partial oxidation during this range of temperature.

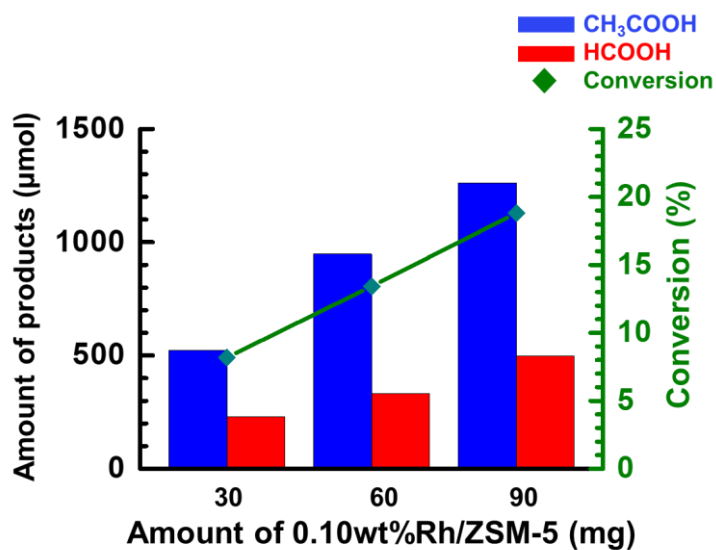


Figure S5. 6 Influence of amount of catalyst on amounts of acetic acid and formic acid by adding 30mg, 60mg and 90mg 0.10wt%Rh/ZSM-5, respectively, with 15bar C₂H₆, 10 ml aqueous solution of 10mmol H₂O₂, performed at 72°C for 2h. Contribution of H-ZSM-5 to the formation of acetic acid and formic acid was subtracted.

Carbon Balance for catalysis at 50°C and 72°C

Table S5. 1 Carbon balance of the reaction with 1.5bar ethane and 10ml of 10mmol H₂O₂ solution conducting at 50°C for 2h

	C ₂ H ₆ (μmol)	CH ₃ COOH (μmol)	HCOOH (μmol)	CH ₃ CH ₂ OH (μmol)	CH ₃ OH (μmol)	CO (μmol)	CO ₂ (μmol)	CH ₄ (μmol)	C ₂ H ₄ (μmol)	Amount of carbon (μmol)	Carbon Balance (%)
Before	610									1220	100
After	366.49	110.15	203.91	8.39	12.45	0.32	9.42	0.64	0.06	1196.90	98.11

Table S5. 2 Carbon balance of the reaction with 15bar ethane and 10ml of 10mmol H₂O₂ solution conducting at 72°C for 2h

	C ₂ H ₆ (μmol)	CH ₃ COOH (μmol)	HCOOH (μmol)	CH ₃ CH ₂ OH (μmol)	CH ₃ OH (μmol)	CO (μmol)	CO ₂ (μmol)	CH ₄ (μmol)	C ₂ H ₄ (μmol)	Amount of carbon (μmol)	Carbon Balance (%)
Before	6100.00									12200.00	100.00
After	5120.69	415.9227451	598.476809	37.00	39.25	3.32	153.89	7.58	1.20	11952.11	97.97

Publication List

1. Li, Y.; Tang, Y.; Nguyen, L. and Tao, F.* “Catalytic Oxidation of Ethane to Carboxylic Acids in the Liquid Phase at Near Room Temperature at Ambient Pressure”. *ACS Sustainable Chemistry & Engineering*, 2019, 7 (5), 4707–4715. DOI: 10.1021/acssuschemeng.8b04455.
2. Li, Y.; Khivantsev, N.; Tang, Y.; Nguyen, L., Liu, J., Yu, M.*; Tao, F.*. “Synthesis of Na@nanoFAU zeolite catalyst and catalysis for production of formic acid on in Na@nanoFAU”. *Catalysis Letters*, 2019, 149(7), 1965-1974. DOI: 10.1007/s10562-019-02702-0.
3. Eskandari, S.; Li, Y.; Tao, F.; Regalbuto, J.*. “The Use of Salts to Control Silica Supported Pt Particle Size in Charge Enhanced Dry Impregnation Syntheses”. *Catalysis Today*, 2019, 334, 187-192. DOI: 10.1016/j.cattod.2018.11.033.
4. Tang, Y.; Wei, Y.; Wang, Z.; Zhang, S.; Li, Y.; Nguyen, L.; Li, Y.; Zhou, Y.; Shen, W.; Tao, F.*, and Hu, P.*. “Synergy of Single-Atom Ni₁ and Ru₁ Sites on CeO₂ for Dry Reforming of CH₄”. *Journal of the American Chemical Society*, 2019, 141(18), 7283-7293. DOI: 10.1021/jacs.8b10910.
5. Tang, Y.; Li, Y.; Fung, V.; Jiang, D., Huang, W.; Zhang, S.; Iwasawa, Y.; Sakata, T.; Nguyen, L.; Zhang, X.; Frenkel, A.I. and Tao, F.* “Single rhodium atoms anchored in micropores for efficient transformation of methane under mild conditions”. *Nature Communications*, 2018, 9, 1231. DOI: 10.1038/s41467-018-03235-7.
6. Nguyen, L.; Tang, Y.; Li, Y.; Zhang, X.; Tao, F.* “Dual reactor for in situ/operando fluorescent mode XAS studies of sample containing low-concentration 3d or 5d metal elements”. *Review of Scientific Instruments*, 2018, 89, 054103. DOI: 10.1063/1.5022738.
7. Zhang, X.; House, S.; Tang, Y.; Nguyen, L.; Li, Y.; Opalade, A.; Yang, J.; Sun, Z.; Tao, F.,* “Complete Oxidation of Methane on NiO Nanoclusters Supported on CeO₂ Nanorods through

- Synergistic Effect*". ACS Sustainable Chemistry & Engineering, 2018, 6(5), 6467-6477. DOI: 10.1021/acssuschemeng.8b00234.
8. Dou, J.; Tang, Y.; Nie, L.; Andolina, C.M.; Zhang, X.; House, S.; **Li, Y.**; Yang, J.; Tao, F.* "Complete Oxidation of Methane on $\text{Co}_3\text{O}_4/\text{CeO}_2$ Nanocomposite: A Synergistic Effect". Catalysis Today, 2018, 311, 48-55. DOI: 10.1016/j.cattod.2017.12.027.
 9. Tang, Y.; Ma, L.; Dou, J.; Andolina, C. M.; **Li, Y.**; Ma, H.; House, S. D.; Zhang, X.; Yang, J.; Tao, F.* "Transition of Surface Phase of Cobalt Oxide during CO Oxidation". Physical Chemistry Chemical Physics, 2018, 20, 6440-6449. DOI: 10.1039/C7CP07407G.
 10. Zhang, X; Sun, Z; Wang, B; Tang, Y.; Nguyen, L.; **Li, Y.**; Tao, F.* "C-C coupling on single-atom based heterogeneous catalyst". Journal of the American Chemical Society, 2017, 140 (3), 954–962. DOI: 10.1021/jacs.7b09314.
 11. Huang, W.; Zhang, S.; Tang, Y.; **Li, Y.**; Nguyen, L.; Shan, J.; Xiao, D.; Gagne, R.; Frenkel, A. I.; Tao, F.* "Low-temperature transformation of methane to methanol on single sites anchored on internal surface of microporous silicate in liquid". Angewandte Chemie International Edition, 2016, 55(43), 13441-13445. DOI: 10.1002/anie.201604708.
 12. Tang, Y.; Nguyen, L.; **Li, Y.**; Wang, N.; Tao, F.* "Surface of a catalyst in a gas phase". Current opinion in chemical engineering, 2016, 12, 52-61. DOI: 10.1016/j.coche.2016.02.007.
 13. Cao, S.; Tao, F.*; Tang, Y.; **Li, Y.**; Yu, J.* "Size- and Shape-Dependent Catalytic Performances of Oxidation and Reduction Reactions on Nanocatalysts". Chemical Society Review, 2016, 45, 4747-4765. DOI: 10.1039/C6CS00094K.